High-Dimensional Quantum Dynamics: Method Development and Photochemical Applications

Dissertation
zur Erlangung des Doktorgrades
der Naturwissenschaften

vorgelegt beim Fachbereich 14
der Johann Wolfgang Goethe-Universität
in Frankfurt am Main

von
Pierre Eisenbrandt
aus
Frankfurt am Main

Frankfurt am Main
2017

(D30)

vom Fachbereich 14 Biochemie, Chemie und Pharmazie
der Johann Wolfgang Goethe - Universität als Dissertation angenommen.

Dekan: Prof. Dr. Michael Karas
Gutachter: Prof. Dr. Irene Burghardt
Dr. Jean Christophe Tremblay

Datum der Disputation: 20.07.2017

Abstract

This thesis is concerned with quantum dynamical propagation methods suitable for high-dimensional systems, and their application to excitation energy transfer (EET), electron transfer (ET), and intra-molecular vibrational redistribution (IVR) in molecular aggregates. The theoretical description of these processes, which are often ultrafast – with time scales in the range of femtoseconds to picoseconds – is challenging, both with regard to quantum dynamical simulations and electronic structure calculations.

The present thesis comprises two parts. The first part concerns the implementation of a novel quantum dynamical method based on Gaussian Wavepackets (GWPs): the 2-Layer Gaussian-MCTDH (2L-GMCTDH) method. This method, which has recently been proposed in [S. Römer, M. Ruckenbauer, I. Burghardt, *The Journal of Chemical Physics*, **2013**, *138*, 064106] was implemented in a Fortran90 code and applied to various high-dimensional test systems. The second part of the thesis addresses the combined electronic structure and dynamical study of a novel type of donor-acceptor systems that have been investigated in a joint project with experimental collaboration partners at Strasbourg University. In both parts, numerical applications focus on high-dimensional model Hamiltonians for EET and ET processes.

Regarding the first part, the interest of using GWP-based methods is two-fold: First, GWPs represent spatially localized basis sets that are useful for on-the-fly dynamics in conjunction with electronic structure calculations. Second, they are naturally suited for the explicit representation of quantum mechanical system-bath type problems where a large number of vibrational bath modes are weakly perturbed from equilibrium. In this context, various methods exist that are based upon classically evolving GWP bases. A major improvement results from variational methods which involve optimized, non-classical GWP trajectories. In particular, the variational Gaussian-based Multi-Configuration Time-Dependent Hartree (G-MCTDH) and its variational Multi-Configurational Gaussians (vMCG) variant were originally derived as semiclassical variants of the Multi-Configuration Time-Dependent Hartree (MCTDH) method. However, the G-MCTDH and vMCG methods mostly use Frozen Gaussian (FG) basis sets that are far less flexible than the single-particle (SPF) representation of standard MCTDH. As a consequence, a significantly larger number of GWPs are generally required to reach convergence.

To remedy the lack of flexibility of the FG basis sets, the abovementioned two-layer (2L-G-MCTDH) approach has been introduced: Here, the first layer is composed of flexible SPFs, while the second layer is composed of low-dimensional FGs. The numerical scaling properties are significantly improved as compared with the conventional G-MCTDH and vMCG schemes. The first implementation of the method in an in-house Fortran90 code is presented, along with applications to (i) a model of site-to-site vibrational energy flow in the presence of intra-site vibrational energy redistribution (IVR) and (ii) a multidimensional donor-acceptor electron transfer system described within a linear vibronic coupling model. The second system relates to a model for ET at an oligothiophene-fullerene interface relevant to organic photovoltaics. Besides the description of the implementation, a detailed assessment of the convergence properties and comparison with multi-layer MCTDH (ML-MCTDH) benchmark calculations is presented. Finally, a perspective is given on the future combination with the existing ML-MCTDH scheme; indeed, such a combination is straightforward since the first layer of the 2L-G-MCTDH approach can be chosen to be orthogonal.

Regarding the second part of the thesis, two generations of a novel donor-acceptor (DA) system for organic photovoltaics applications, involving self-assembled block co-oligomers DA dyads and triads with perylene-diimide (PDI) accepter units, are addressed within a collaborative project with S. Haacke and S. Mery (University of Strasbourg). Based upon detailed excited-state electronic structure investigations along with quantum dynamical and kinetic studies, the relevant ET formation and recombination steps are characterized quantitatively, in view of optimizing the chemical design and reducing recombination losses.

In a first-generation variant of the abovementioned DA systems, which involves liquid-crystalline triads, we were able to show that a highly efficient inter-chain ET process prevails over intra-molecular ET, leading to fast recombination. Due to the latter, this system turns out to be inefficient for photovoltaic applications. To fully understand the elementary steps, high-dimensional quantum dynamics simulations were carried out using the ML-MCTDH method, in collaboration with Matthias Polkehn from our group. In the second-generation variant, which is in the focus of the present thesis, both the nanomorphology and the chemical design were modified. The present work, focuses upon the aspect of chemical design, by characterizing a series of modified DA's, with donor units of varying length while the PDI accepter units remain unchanged. The intra-molecular ET is observed in these systems, but the processes are comparatively slow, of the order of tens to hundreds of picoseconds. Hence, a kinetic analysis using the Marcus-Levich-Jortner rate theory is employed. Among the main results of the study is that addition of an

electron donating amine unit strongly increases the lifetime of the charge-separated state, and therefore reduced recombination losses.

Overall, the present thesis shows how a combination of high-dimensional quantum dynamics, electronic structure calculations, and vibronic coupling model Hamiltonians can be employed to obtain an accurate picture of EET, ET, and IVR in high-dimensional molecular assemblies. Furthermore, the 2L-GMCTDH method paves the way for accurate and efficient on-the-fly calculations; a suitable set-up for such calculations is currently in progress.

Zusammenfassung

Diese Arbeit befasst sich einerseits mit neuen methodischen Entwicklungen im Bereich der hochdimensionalen Quantendynamik und andererseits mit der kombinierten Anwendung von Quantendynamiksimulationen und elektronischen Strukturrechnungen an hochdimensionalen molekularen Systemen. Im Anwendungsteil dieser Arbeit liegt der Fokus auf Energie- und Ladungstransferprozessen, sowie der intra-molekularen Verteilung von Schwingungsenergie in molekularen Aggregaten. Energie- und Ladungstransferprozesse spielen eine wichtige Rolle in vielen reaktiven Prozessen der Chemie, Biologie und Physik. Diese treten sowohl in isolierten Molekülen, als auch molekularen Aggregaten, wie Lichtsammelkomplexen und photo-aktiven organischen Materialien, auf. Typische Zeitskalen dieser Transferprozesse befinden sich im ultra-schnellen Bereich von Femto- bis Pikosekunden.

Die vorliegende Arbeit ist in zwei Themenbereiche gegliedert. Der erste Teil behandelt die Implementierung einer neuartigen Quantendynamikmethode, welche Gaußsche Wellenpakete (GWP) als Basis nutzt, die sogenannte 2-Layer-Gaussian-Multi-Configuration Time-Dependent Hartree (2L-G-MCTDH)-Methode. Diese Methode, die auf einer hierarchischen Darstellung der Wellenfunktion beruht, wurde in [S. Römer, M. Ruckenbauer, I. Burghardt, *The Journal of Chemical Physics*, **2013**, *138*, 064106] vorgeschlagen und in der vorliegenden Arbeit in einem Fortran90-Code umgesetzt. Anhand dieses Codes wurden erste Anwendungen an hochdimensionalen Systemen durchgeführt. Der zweite Teil dieser Arbeit befasst sich mit der Untersuchung eines neuartigen Typs von Donor-Akzeptor-Systemen mittels einer Kombination von elektronischen Strukturrechnungen, Quantendynamiksimulationen und kinetischen Simulationen. Diese Untersuchung ist Teil einer DFG/ANR-Kooperation mit den Arbeitsgruppen von Prof. S. Haacke und Dr. S. Méry (Universität Straßburg). Beide Teile konzentrieren sich auf Energie- und Ladungstransferprozesse in hochdimensionalen Systemen.

Im Rahmen der Quantendynamik sind GWP-basierte Methoden von besonderem Interesse, weil GWP-Funktionen eine lokalisierte Basis bilden und dadurch besonders für semi-klassische Dynamik in Kombination mit *on-the-fly* elektronischen Strukturrechnungen geeignet sind. Weiterhin sind GWP-Funktionen ebenfalls für die explizite Beschreibung von Schwingungs-Badmoden in System-Bad Problemen geeignet, da hier eine hohe Anzahl an schwach gekoppelten Schwingungsmoden zu behandeln ist. Verschiedene aktuell gebräuchliche Methoden verwenden im Sinne der semi-klassischen Dynamik klassisch propagierte GWP-Funktionen. Stark verbesserte Resultate liefern allerdings nicht-klassische GWP-Trajektorien, wie

sie insbesondere in der Gauß-basierten *Multi-Configuration Time-Dependent Hartree* (G-MCTDH)-Methode oder deren *variational Multiconfigurational Gaussian* (vMCG)-Variante verwendet werden. Diese Methoden wurden ursprünglich als semi-klassische Varianten der hochflexiblen *Multi-Configuration Time-Dependent Hartree* (MCTDH)-Methode konzipiert. Allerdings werden diese Methoden meist mit sogenannten *Frozen-Gaussian* (FG) basierten Basissätzen genutzt. Im Vergleich zur *single-particle* (SPF)-Basis der MCTDH-Methode sind FG-Funktionen deutlich weniger flexibel, sodass generell eine größere Anzahl an GWP-Funktionen benötigt wird, um konvergierte Rechnungen zu erhalten.

Um die mangelnde Flexibilität der GWP-Basis auszugleichen, wurde die oben erwähnte 2L-G-MCTDH Methode eingeführt. Diese basiert auf einem hierarchischen 2-Layer-Ansatz. Die erste Ebene – d.h. der erste *Layer* – ist dabei aus flexiblen SPFs aufgebaut, wohingegen der zweite *Layer* als Summe niedrigdimensionaler FG-Funktionen konstruiert wird. Infolgedessen sind die Skalierungseigenschaften der Methode im Vergleich zu den herkömmlichen G-MCTDH- und vMCG-Schemata deutlich verbessert. Eine erste Implementierung der Methode in einem Fortran90-Code wird in dieser Arbeit vorgestellt; dabei stand insbesondere auch eine Implementierung für nicht-adiabatisch gekoppelte elektronische Zustände im Vordergrund. Erste Anwendungen an zwei repräsentativen Modellsystemen betreffen zwei Typen von Prozessen: Das erste System beschreibt den intra-molekularen Schwingungsenergietransfer entlang einer Kette molekularer Einheiten (wie z.B. in einer Peptidkette), in denen als Konkurrenzprozess lokale Schwingungsenergietransferprozesse stattfinden. Das zweite System beschreibt den multidimensionalen Ladungstransfer innerhalb eines Donor-Akzeptor-Systems, das anhand eines linearen vibronischen Kopplungsmodells beschrieben wird. Neben der Anwendungsseite wird die Implementierung im Detail besprochen und die verbesserten Skalierungseigenschaften sowie der Vergleich zu ML-MCTDH-Rechnungen demonstriert. Schließlich wird eine Perspektive bezüglich der Kombination mit der ML-MCTDH Methode vorgestellt; diese ist ohne Weiteres möglich, da die SPF-Funktionen in der obersten Ebene (*first layer*) eine orthogonale Basis bilden.

Der zweite Abschnitt dieser Arbeit befasst sich mit zwei Generationen eines neuartigen Donor-Akzeptor Systems zur Anwendung in der organischen Photovoltaik, das wie oben erwähnt in den Straßburger Arbeitsgruppen von S. Méry und S. Haacke entwickelt wurde. Die relevanten Systeme basieren auf selbst-assemblierenden Co-Oligomer Donor-Akzeptor-Dyaden und -Triaden, die eine Perylendiimid-Akzeptor-Einheit verwenden. Detaillierte elektronische Strukturrechnungen, insbesondere auch für angeregte Zustände, dienen als Basis für quantendynamische und kinetische Untersuchungen, um die relevanten Ladungsseparations- und- Rekombinati-

onsschritte quantitativ zu beschreiben. Die Optimierung dieser Schritte durch ein geeignetes chemisches Design der Donor-Akzeptor-Komponenten steht im Vordergrund dieser Studie. Dabei sollen insbesondere Rekombinationsverluste reduziert werden.

Bezüglich der ersten Generation des Donor-Akzeptor-Systems wurde gezeigt, dass ein hocheffizienter inter-molekularer Ladungstransfer gegenüber dem intramolekularen Ladungstransfer innerhalb einer Donor-Akzeptor-Dyade oder -Triade deutlich bevorzugt ist. Obwohl dies zu einer ultra-schnellen initialen Ladungstrennung führt, erweist sich das System jedoch als ineffizient für die Nutzung in der Photovoltaik. Dies ist darauf zurückzuführen, dass aufgrund der dreidimensionalen Stapelanordnung des Donor-Akzeptor-Systems die relevanten Transferintegrale gegenüber der Rekombinationsrate vernachlässigbar sind. Eine quantendynamische Analyse entstand in Kooperation mit Matthias Polkehn und umfasste hochdimensionale Quantendynamiksimulationen mittels der ML-MCTDH-Methode. Die vorliegende Arbeit konzentriert sich vor allem auf die zweite Generation der Donor-Akzeptor-Materialen, bei der sowohl die Nanomorphologie als auch das chemische Design modifiziert wurden. In dieser Arbeit liegt der Fokus auf letzterem Aspekt, wobei eine systematische Untersuchung von einer Reihe modifizierter Donor-Akzeptor-Varianten durchgeführt wurde. Die beobachteten Ladungstransferprozesse in diesen Systemen sind allerdings vergleichsweise langsam - im Bereich von hunderten Pikosekunden - weshalb eine kinetische Analyse mit Hilfe der Marcus-Jortner-Levich Theorie angewendet wurde. Ein wesentliches Ergebnis dieser Studie zeigt, dass durch die Einführung einer Amin-Gruppe die Lebensdauer der ladungsseparierten Zustände stark verlängert und daher die Ladungsrekombinationen deutlich reduziert wird.

Zusammenfassend zeigt diese Arbeit, dass eine Kombination von hochdimensionalen Quantendynamiksimulationen, elektronischen Strukturrechnungen und parameterisierten Modellen ein detailliertes Bild von Energie- und Ladungstransferprozessen in hochdimensionalen molekularen Aggregaten liefern kann. Mit Blick auf die verwendeten quantendynamischen Methoden ist weiterhin hervorzuheben, dass die neue 2L-G-MCTDH-Methode im Rahmen dieser Arbeit erstmalig implementiert wurde. Neben ersten Anwendungen auf parametrisierte Modelle ebnet diese Methode den Weg für genaue und effiziente *on-the-fly* Rechnungen. Eine entsprechende Erweiterung der aktuellen Implementierung ist momentan in Arbeit.

Für Claudia

Contents

List of Figures

List of Tables

List of Abbreviations

2L-G-MCTDH	2-Layer-Gaussian-Multi-Configuration Time-Dependent Hartree
A	acceptor
ADC	Algebraic Diagrammatic Construction
ADC(2)	second-order Algebraic Diagrammatic Construction
AIMS	*ab initio* multiple spawning
BLA	bond-length alternation
BO	Born-Oppenheimer
C60	fullerene
CC	Coupled Cluster
CC2	second-order approximate Coupled Cluster
CCS	Coupled Cluster with Singles
CCSD	Coupled Cluster with Singles and Doubles
CI	Configuration Interaction
CID	Configuration Interaction with Doubles
CIS	Configuration Interaction with Singles
CISD	Configuration Interaction with Singles and Doubles
COSMO	conductor-like screening model
CS	charge separated
CT	charge transfer
D	donor
DA	donor-acceptor
DD-vMCG	Direct Dynamics variational Multi-Configurational Gaussians
DFT	Density Functional Theory
DF-VP	Dirac-Frenkel variational principle
DOF	degree of freedom
DVR	discrete variable representation
EET	excitation energy transfer

e-h	electron-hole
EOM	equations of motion
ET	electron transfer
ET-SI	electron-transfer self-interaction error
FFT	fast Fourier transform
FG	frozen Gaussian
GGA	Generalized Gradient Approximation
G-MCTDH	Gaussian-Multi-Configuration Time-Dependent Hartree
GWP	Gaussian Wavepacket
HF	Hartree Fock
HK	Hohenberg-Kohn
HOMO	highest occupied molecular orbital
IVR	intra-molecular vibrational redistribution
LC	liquid crystalline
LDSA	Local Spin-Density Approximation
LHA	Local Harmonic Approximation
LUMO	lowest unoccupied molecular orbital
LVC	Linear Vibronic Coupling
MBPT	Many-Body Perturbation Theory
MCTDH	Multi-Configuration Time-Dependent Hartree
MD	Molecular Dynamics
MLJ	Marcus-Jortner-Levich
ML-MCTDH	Multi-Layer Multi-Configuration Time-Dependent Hartree
MO	molecular orbital
MP(2)	second-order Møller-Plesset Perturbation Theory
OPV	organic photovoltaic
OT4	oligothiophene
P3HT	poly-3-hexylthiophene
PCBM	phenyl-C_{61} butyric acid methyl ester
PDI	perylene-diimide

PES	potential energy surface
QC	quantum chemical
QD	quantum dynamical
RI	resolution of the identity
RMSD	root-mean-square deviation
SCF	self-consistent-field
SCS	spin-component-scaling
SE	Schrödinger Equation
SHF	single hole function
SOP	sum-over-products
SPF	single particle function
TCE	trichloroethylene
TDA	Tamm-Dancoff-approximation
TDDFT	Time-Dependent Density Functional Theory
TDH	Time-Dependent Hartree
TDSE	time-dependent Schrödinger Equation
TISE	time-independent Schrödinger Equation
TG	thawed Gaussian
vMCG	variational Multi-Configurational Gaussians
XT	excitonic state

Deutsche Zusammenfassung

Die vorliegende Arbeit befasst sich einerseits mit neuen methodischen Entwicklungen im Bereich der hochdimensionalen Quantendynamik und andererseits mit der kombinierten Anwendung von Quantendynamiksimulationen und elektronischen Strukturrechnungen an hochdimensionalen molekularen Systemen. Im Anwendungsteil dieser Arbeit liegt der Fokus auf Energie- und Ladungstransferprozessen, sowie der intra-molekularen Verteilung von Schwingungsenergie in molekularen Aggregaten. Energie- und Ladungstransferprozesse spielen eine wichtige Rolle in vielen reaktiven Prozessen der Chemie, Biologie und Physik. Diese treten sowohl in isolierten Molekülen, als auch molekularen Aggregaten, wie Lichtsammelkomplexen und photoaktiven organischen Materialien, auf. Typische Zeitskalen dieser Transferprozesse befinden sich im ultra-schnellen Bereich von Femto- bis Pikosekunden.

Die Herausforderung einer theoretischen Studie dieser Phänomene besteht in der Notwendigkeit einer kombinierten Betrachtung von elektronischer Struktur und Quantendynamik hochdimensionaler Systeme. Problematisch ist in diesem Zusammenhang die ungünstige, exponentielle Skalierung des Rechenaufwandes beider Methoden mit steigender Anzahl an Freiheitsgraden. Die bestmögliche Kombination aus hoch-qualitativen elektronischen Strukturrechnungen und hochdimensionalen Quantendynamiksimulationen ist daher nur in seltenen Fällen anwendbar und Näherungen müssen eingeführt werden. Dem begegnet man häufig auf zwei Arten: Entweder durch die Verwendung von sogenannten *on-the-fly* Methoden, bei denen Quantendynamiksimulationen durch semi-klassische Dynamikmethoden ersetzt und mit hoch-qualitativen elektronischen Strukturrechnungen kombiniert werden, oder durch die Anwendung von parametrisierten, vorberechneten Potentialflächen, die durch passende Modell-Hamiltonians, wie Gitter- und vibronische Kopplungs-Modelle, beschrieben werden. Diese werden dann in Kombination mit genauen Quantendynamikmethoden verwendet. Im Rahmen der ersten Methode finden häufig der *Surface Hopping*-Ansatz, die *Ab Initio Multiple Spawning* (AIMS)-Methode oder klassisch und variationell propagierte Gaußsche-Wellenpakete (GWP) Anwendung. Die zweite Methode wird häufig in Kombination mit der *Multi-Configuration Time-Dependent Hartree* (MCTDH)-Methode und ihrer hierarchischen *multi-layer* (ML-MCTDH)-Variante verwendet. Bei zu großen Systemen kann es notwendig sein, auf gemischt quanten-klassische Methoden oder andere Ansätze zurückzugreifen.

Diese Arbeit behandelt beide oben genannten Näherungen und kombiniert Aspekte beider Ansätze. Sie ist dementsprechend aufgeteilt in zwei thematische Abschnitte. Der erste Teil behandelt die Implementierung eines neuen Typs einer hierarchischen Quantendynamikmethode, die auf GWPs als Basis aufbaut, die *2-Layer-Gaussian-MCTDH* (2L-G-MCTDH)-Methode. Diese Methode wurde in Ref. [1] vorgeschlagen und in dieser Arbeit in einem Fortran90-Code implementiert. Vergleichbare auf GWPs basierende Methoden sind häufig auf wenige Freiheitsgrade beschränkt. Dies trifft besonders auf die *variational Multi-Configurational Gaussian* (vMCG) Methode zu. Mit dieser können lediglich etwa 10 Freiheitsgraden behandelt werden, sofern konvergierte Ergebnisse erhalten werden sollen. Diese Arbeit zeigt, dass der neue 2L-G-MCTDH-Ansatz es erlaubt, genaue und konvergierte Ergebnisse für 100 und mehr Freiheitsgrade zu bekommen, die in ihrer Qualität an die von ML-MCTDH Rechnungen heranreichen. In Verbindung mit *on-the-fly* elektronischen Strukturrechnungen ebnet diese Methode den Weg hin zu genauen Quantendynamiksimulationen auf genauen Potentialflächen.

Der zweite Teil befasst sich mit der Studie eines neuen Typs eines Donor-Akzeptor-Systems für die organische Photovoltaik. Diese Untersuchung ist Teil eines Gemeinschaftsprojekts mit den Arbeitsgruppen von Prof. S. Haacke und Dr. S. Méry der Universität Straßburg. Die relevanten Ladungstransferprozesse, die die Ladungstrennung und -rekombination beschreiben, werden mit Hilfe von elektronischen Strukturmethoden und einer Analyse der Elektronentransferkinetik untersucht. Besonderes Augenmerk liegt dabei auf dem Einfluss des chemischen Designs um Ladungsrekombinationsverluste zu verringern. Weiterhin werden hochdimensionale Quantendynamiksimulationen des Vorgänger-System vorgestellt. Diese wurden in Kollaboration mit M. Polkehn mit der ML-MCTDH-Methode durchgeführt und eröffnen die Möglichkeit für weiterführende Untersuchungen, die die molekulare Packung in neuartigen Donor-Akzeptor-Materialen betrachten.

Die vorliegende Arbeit befasst sich zunächst mit der Beschreibung und Implementierung der neuartigen 2L-G-MCTDH-Methode in einem Fortran90-Code. Diese kombiniert in einem hierarchischen Wellenfunktions-Ansatz die flexiblen *single particle functions* (SPF) der konventionellen MCTDH-Methode mit einem zeitabhängigen GWP-Basissatz aus sogenannten *frozen Gaussians* (FGs). In dieser Arbeit ist der Ansatz auf zwei *Layer* begrenzt, lässt sich allerdings ohne Weiteres mit bereits existierenden hierarchischen Methoden, wie der *Multi-Layer*-MCTDH (ML-MCTDH)-Methode kombinieren.

Die Verwendung von FGs begründet sich in der besseren, numerischen Stabilität im Vergleich zu *thawed Gaussians* (TGs). FGs besitzen im Gegensatz zu TGs eine feste Breite, wodurch sie an Flexibilität einbüßen. Dies ist besonders bei mehreren, kombinierten Freiheitsgraden ausgeprägt ist. Beide Ansätze sind im Bezug auf die Flexibilität allerdings den sehr flexiblen SPFs der MCTDH-Methode unterlegen. Auf Grund dessen muss häufig eine große Anzahl an Basis-Funktionen (sogenannte Konfigurationen) verwendet werden, was die Konvergenz der G-MCTDH-Methode erschwert. In der vMCG-Methode, einem Spezialfall von G-MCTDH, werden alle Freiheitsgrade in einer Mode kombiniert. Um konvergierte Rechnungen zu erhalten, benötigt man daher eine große Zahl an Konfigurationen und ist in ihrer Anwendung auf etwa 10 Freiheitsgrade limitiert. Dies liegt an der ungünstigen Skalierung der rechenintensiven Propagation der GWPs, die mit der Anzahl der Freiheitsgrade (d) und der Anzahl an Konfigurationen (n) exponentiell ($\sim (dn)^3$) skaliert.

Der 2L-G-MCTDH-Ansatz verwendet im ersten *Layer* orthogonale SPFs, ähnlich denen der MCTDH-Methode. Die *first layer* SPFs werden in diesem Fall allerdings durch eine Linearkombination von nicht-orthogonalen, multidimensionalen GWPs (anstelle einer Grid-Darstellung), ähnlich des G-MCTDH-Ansatzes, ausgedrückt. Auf diese Weise bewegen sich die FGs in einem kleinen Subraum und die Propagation erfordert weniger Rechenaufwand zu Vergleich mit den vMCG- und G-MCTDH-Methoden. Die Berechnung der *mean-fields* im ersten und zweiten *Layer* erhält auf diese Weise ein stärkeres Gewicht und muss gegen diese Verbesserung ausbalanciert werden. Dies erreicht man durch eine sinnvolle Wahl der Modenaufteilung und -kombination der Freiheitsgrade des Systems. Auf diese Weise können signifikante Verbesserungen der Skalierungseigenschaften im Vergleich zu G-MCTDH und vMCG erreicht werden.

Im Rahmen dieser Arbeit wurde die Methode zur Verwendung mit nicht-adiabatischen Systemen, bestehend aus mehreren elektronischen Zuständen, erweitert. Drei Ansätze werden dazu vorgestellt: Die bereits bekannten *single-set* und *multi-set* Varianten, sowie ein Hybrid-Ansatz. Beim *single-set* Ansatz wird der elektronische Freiheitsgrad ähnlich wie die anderen Moden über ein eigenes Partikel beschrieben. Die anderen SPFs gehören hier keinem elektronischen Zustand explizit an. Der *multi-set* Ansatz hingegen stellt die Gesamtwellenfunktion als Summe über zustandsspezifische Wellenfunktionen dar, sodass jede einem elektronischen Zustand zugeordnet ist. Der Hybrid-Ansatz kombiniert die beiden ersten Ansätze. Hierbei sind die *first-layer* Moden zustandsspezifisch, allerdings gilt dies nicht für

die zugrunde liegende GWP Basis, sondern nur für die Koeffizienten im zweiten *Layer*.

Im Rahmen der Besprechung der Implementierung wird zum Einen auf den allgemeinen Programmabauf, zum Anderen allerdings auch auf tiefer gehende Details, wie das Speichermanagement und die effiziente Berechnung der Tensor-Form der Wellenfunktion über eine Multi-Summen-Struktur der Matrix-Vektor Produkte eingegangen. Hierbei wurde darauf Wert gelegt, dass das mehrmalige Berechnen von Produktintegralen vermieden wird. Um eine effiziente Anwendbarkeit dieser Methode gewährleisten zu können, ist es notwendig, dass die praktische Skalierung des Programmcodes der theoretischen nahekommt. Die Skalierungseigenschaften des implementierten Programmcodes wurden anhand zweier Modellsysteme analysiert und entsprechen sehr genau den theoretischen Vorhersagen und unterstreichen eine effiziente Implementierung.

Die Methode wurde mit dem vorgestellten Programmcode erfolgreich an zwei repräsentativen Modellsystemen angewendet. Das erste System verwendet einen intra-molekularen Schwingungstransfer-Hamiltonian um den Energietransfer entlang einer Kette von mehreren Untereinheiten (*Sites*) zu beschreiben. Der zweite Hamiltonian beschreibt den ultra-schnellen Ladungstransfer in einem Donor-Akzeptor System mit einer variablen Pointcaré-Rekurrenzzeit. Für beide Systeme wurden zum Einen eine sehr gute Übereinstimmung zu Referenzmethoden, und zum Anderen hervorragende Konvergenzeigenschaften erhalten. Eine grundlegende Erkenntnis ist, dass die Modenverteilung und -kombination entscheidend für die Qualität der Ergebnisse sein kann.

Typische Probleme, die bereits bei der G-MCTDH-Methode auftreten, bleiben allerdings bestehen. Die Methode leidet an Singularitäten in den Überlapp- und $\underline{C}$-Matrizen, die auf Grund von zu großem Überlapp der GWPs und den infolge dessen linearen Abhängigkeiten auftreten. Die Wahl der nicht besetzten GWPs kann dabei einen erheblichen Einfluss auf die numerische Stabilität und die Ergebnisse haben. Dies trifft besonders auf kombinierte Moden zu, die nur eine geringe Anzahl an physikalischen Moden enthalten.

Die gezeigten Ergebnisse des 2L-G-MCTDH sind sehr vielversprechend. Die Methode ist zudem mit bereits existierenden hierarchischen *multi-layer*-MCTDH-Methoden flexibel kombinierbar, da dort lediglich der unterste *layer* durch die

GWPs ersetzt werden muss. Die Parallelisierung des Codes sollte es zudem möglich machen, die Anzahl der zu behandelnden Freiheitsgrade deutlich zu erhöhen, sodass die Methode bis zu oder sogar mehr als 1000 Freiheitsgraden anwendbar ist. Zudem eignet sich die Methode ebenfalls zur Kombination mit *on-the-fly* elektronischen Strukturrechnungen vergleichbar zur DD-vMCG Methode, da Gauß-Funktionen eine semi-klassische Beschreibung der Trajektorien über Ort und Impuls der GWPs ermöglichen. Da die elektronischen Strukturrechnungen – man benötigt hier die Gradienten und den Hessian – der limitierende Faktor sind, ist es notwendig, ihre Anzahl zu reduzieren. Jede elektronische Strukturrechnung entspricht hierbei einer Konfiguration aus dem Wellenfunktions-Ansatz. Im 2L-G-MCTDH werden allerdings zum Teil deutlich über 10 000 Konfigurationen benötigt, wodurch es unumgänglich, ist ein *Sampling*-Schema zu entwickeln, um die Anzahl der Konfigurationen und damit den Rechenaufwand deutlich zu verringern. Dies kann zudem mit einem Datenbank-Ansatz und Fit-Schemata basierend auf neuralen Netzwerken erweitert werden.

Der zweite Abschnitt dieser Arbeit befasst sich mit zwei Generationen eines neuen Donor-Akzeptor Systems, die in den Arbeitsgruppen von S. Méry und S. Haacke der Universität Straßburg synthetisiert und spektroskopisch charakterisiert wurden. Diese Systeme haben die Eigenschaft selbst-assemblierte, flüssigkristalline Strukturen zu bilden. Die vorliegende Arbeit befasst sich hauptsächlich mit der theoretischen Untersuchung der zweiten Generation in Lösung, die eine Weiterentwicklung zur Ersten darstellt. Beide Systeme beinhalten gleiche Strukturtypen. Als Akzeptor kommt stets eine Perylendiimid-Einheit zum Einsatz. Der Donor verwendet als Grundstruktur eine Bisthiophen-Einheit, die häufig als Donor-Material Verwendung findet. Die Donor und Akzeptor Einheiten sind zudem über eine Ethylenbrücke miteinander verbunden.

Die *Steady-State*-Ergebnisse zum ersten System zeigen in Lösung (Chloroform) einen zweischrittigen Ladungstransfer (CT) mit einem vorhergehenden Energietransfer vom Donor zum Akzeptor. Der Ladungstransfer läuft mit einer Zeitkonstanten von etwa 3 ps ab. Das Bild ändert sich allerdings im flüssigkristallinen Film. Hier wird ein nur noch einschrittiger, ultra-schneller Ladungstransferprozess innerhalb von 50 fs ohne vorgeschalteten Energietransfer beobachtet. Der Grund für diesen ultra-schnell gebildeten CT-Zustand liegt in der molekularen Packung der Moleküle im Flüssigkristall, in dem die molekularen Ebenen mit einem Winkel von etwa 70° verkippt sind. Quantendynamische Rechnungen zeigen, dass es daher

nach der anfänglichen Photo-Anregung zur Bildung eines inter-molekularen CT-Zustands, einem ladungsgetrennten CS-Zustand, zwischen benachbarten Molekülen (CS(-1)) kommt. Es zeigt sich, dass dieser sehr stabil ist und ein quasi-stationärer Zustand erreicht wird. Dies wird zum Einen durch sehr kleine Transferintegrale und zum Anderen durch die resultierende Coulomb-Barriere für weiter entfernte CS-Zustände bedingt. Sowohl das System in Lösung, als auch das System im Flüssigkristall zeigen eine sehr kurze Lebensdauer von nur etwa 50 fs, sodass die mögliche Anwendung in der organischen Photovoltaik limitiert ist.

Die zweite Generation wurde mit dem Ziel entwickelt, die Lebensdauer des CT-Zustandes stark zu verlängern. Um dies zu erreichen, wurde das System modular aufgebaut. Die zentrale Donor-Einheit ist variabel in ihrer Länge und besteht aus Fluoren- und Thiophen-Einheiten (D_n). Zwischen Donor und Akzeptor ist zudem eine Verknüpfungs-Einheit eingefügt, die entweder eine Benzothiadiazol-Gruppe (δ_+) oder eine simple Phenyl-Gruppe (δ) beinhaltet. Die spektroskopische Charakterisierung der Systeme mit elektronischen Strukturmethoden offenbart zwei verschiedene photo-chemische Prozesse für die δ- und δ_+-Gruppen. Die δ-Variante zeigt einen Verlauf vergleichbar mit den Ergebnissen der ersten Generation in Lösung, bei dem der Ladungstransfer auf einen Energietransfer vom Donor auf den Akzeptor folgt. Die Zeitskalen sind allerdings um eine Größenordnung langsamer. Bei der δ_+-Variante zeigt sich stattdessen ein langsamer, direkter Ladungstransfer innerhalb von 90 ps. Die Lebensdauer des CT-Zustandes steigt in beiden Systemen dabei um den Faktor 10. Einen noch stärkeren Einfluss auf die Lebensdauer hat allerdings die Einführung einer Amin-Gruppe (δ_-) am anderen Ende der Donor-Einheit. Diese verlängert die Lebensdauer in Kombination mit einer optimalen Donorlänge von $n = 1$ insgesamt um den Faktor 50. Auf den photo-chemischen Prozess des Ladungstransfers hat sie aber keinen Einfluss.

Untersuchungen mit zeitabhängiger Dichtefunktionaltheorie (TDDFT) zeigen, dass bei der δ-Variante drei Zusände beteiligt sind, während es bei der δ_+-Variante vier sind. Beiden gemeinsam sind die lokalen, angeregten Donor- bzw. Akzeptorzustände und der CT-Zustand. Bei der δ_+-Variante findet sich ein zusätzliche lokale Donorzustand, der hauptsächlich auf der Benzothiadizol-Gruppe lokalisiert ist. Während man mit der δ-Variante einen exzitonisch gekoppelten Zustand der beiden lokalen Donor- bzw. Akzeptorzustände findet, ist dies bei der δ_+-Variante nicht der Fall.

Eine Analyse der Elektron- und Lochdichten zeigt, dass durch die δ_-Gruppe der Abstand der Schwerpunkte der Dichten vergrößert wird. Um die längere CT-Lebensdauer durch das Anfügen der δ_-Gruppe genauer zu charakterisieren, wurde eine kinetische Analyse mit Hilfe der Marcus-Jortner-Levich Theorie durchgeführt. Dazu wurden sowohl experimentelle, als auch TDDFT Ergebnisse miteinbezogen. Es zeigt sich, dass durch die δ_-Gruppe die Dichte-Schwerpunkte um bis zu 3 Å weiter voneinander entfernt sind und es damit einhergehend zu einer Verringerung der elektronischen Kopplung kommt.

Weitergehende Untersuchungen der zweiten Generation des Donor-Akzeptor Systems behandeln die photo-chemischen Eigenschaften und Prozesse in selbst-organisierten, flüssigkristallinen Strukturen und sind aktuell in Arbeit. Die Ergebnisse der vorgestellten Untersuchung der beiden Donor-Akzeptor Systeme zeigen, dass das chemische Design bezüglich einer Eigenschaft lediglich als ein Baustein im gesamten Entwicklungsprozess betrachtet werden kann, um die Lebensdauer von CT-Zuständen in funktionellen Materialien zu steigern.

Die im Rahmen der vorliegenden Arbeit erhaltenen Ergebnisse zeigen, dass die Kombination von elektronischen Strukturrechnungen und hochdimensionalen Quantendynamiksimulationen entscheidend für die Beschreibung von Energie- und Ladungstransferprozessen ist. Die richtige Wahl der Methode und notwendigen Näherungen spielt dabei eine entscheidende Rolle im Bezug auf die Qualität und Anwendbarkeit der Ergebnisse. In diesem Zusammenhang wurde eine neuartige Methode implementiert und erfolgreich angewendet. Diese, auf Gaußschen Wellenpaketen basierende, hierarchische Methode ist zudem nicht nur im Zusammenhang mit Modell-Hamiltonians – wie in der vorliegenden Arbeit gezeigt –, sondern auch mit *on-the-fly* elektronischen Strukturrechnungen anwendbar. Diesbezüglich befinden sich weiterführende Entwicklungen momentan in Bearbeitung.

1 | Introduction

Excitation energy transfer (EET) and electron transfer (ET) processes play an important role in many areas of chemistry, biology, and physics. EET and ET are crucial steps in many reactive processes involving isolated molecules as well as molecular aggregates like light harvesting complexes, and various types of functional materials employed in photovoltaics and as light emitting diodes.[2–7] To the extent that photoinduced processes are considered, EET and ET kinetics are often ultrafast, with characteristic time scales in the femtosecond and picosecond regime. From the point of view of the theoretical description, the challenge is twofold, since both quantum dynamical simulations and electronic structure calculations need to be performed in many dimensions. Therefore, one needs to choose appropriate methods in order to describe both aspects with sufficient accuracy. As shown in Fig. 1.1, the optimal choice would lead one to combine accurate potentials from high-level *ab initio* electronic structure methods and accurate high-dimensional quantum dynamics. However, this combination cannot be realized in practice, due to the unfavorable scaling properties of both electronic structure and dynamics methods with the number of degrees of freedom. In a real-world example, one therefore needs to employ approximations. These need to be chosen judiciously, such that the chemical and physical properties of interest are described correctly.

To achieve reasonable approximations for high-dimensional molecular systems, two types of approximations are currently employed. First, in the so-called direct dynamics, or "on-the-fly" methods, one approximates the quantum dynamics by performing semi-classical dynamics in combination with high-level electronic

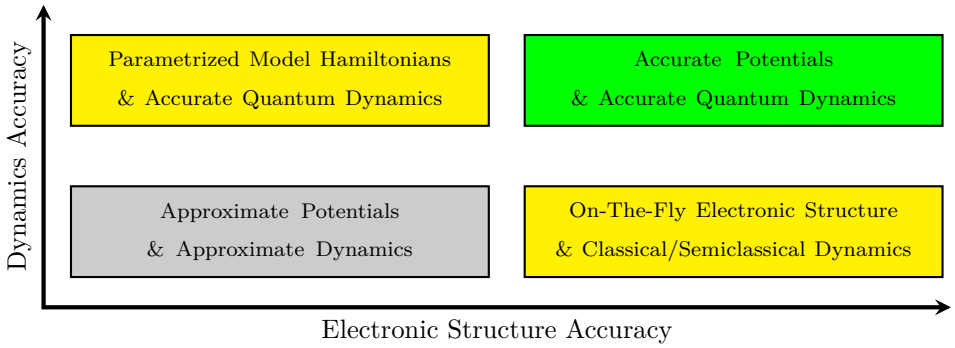

Figure 1.1: Sketch about the different levels of accuracy employable in the theoretical investigation of a molecular system with quantum dynamic simulations and electronic structure calculations.

structure methods, as exemplified by the surface hopping approach,[8] the *ab initio* multiple spawning method (AIMS),[9–11] or classically or variationally evolving Gaussian Wavepackets.[12–18] Second, one can resort to parametrized, pre-computed potential energy surfaces represented by suitable model Hamiltonians, e.g., vibronic coupling models[19–21] or lattice models.[22–24] These can be combined with accurate quantum dynamical approaches, in particular multi-configurational methods of the Multi-Configuration Time-Dependent Hartree (MCTDH)[25] family and its hierarchical multi-layer (ML-MCTDH) variants.[26,27] If the systems are too large, one might need to resort to mixed quantum-classical methods or reduced-dynamics approaches.

This thesis addresses both types of approaches mentioned above, and combines quantum dynamical and electronic structure aspects. The two main parts of the thesis concern the following topics:

- First, the implementation of a novel hierarchical quantum dynamical method based on Gaussian wavepackets (GWPs): the 2-Layer-Gaussian-MCTDH (2L-G-MCTDH) method. This method, which has been proposed in Ref. [1], has been implemented in a Fortran90 code. This method breaks the bottleneck of currently available GWP-based approaches, especially regarding the vMCG method which essentially cannot be converged for systems beyond ∼10-15 degrees of freedom. As shown in this thesis, the 2L-G-MCTDH method ensures an accurate, convergeable representation for ∼ 100 degrees of freedom and more, that is close to ML-MCTDH methods. While on-the-fly calculations have not yet been carried out in the framework of this thesis, a suitable set-up based upon the 2L-G-MCTDH approach is currently in preparation.

- Second, a novel type of donor-acceptor systems for organic photovoltaics is investigated, within a joint project in collaboration with Prof. S. Haacke and Dr. S. Méry (University of Strasbourg). Using electronic structure methods and a kinetic analysis, the relevant ET formation and recombination steps are characterized, in view of optimizing the chemical design and reducing recombination losses. In a first-generation variant of this system, high-dimensional quantum dynamical studies were performed using the ML-MCTDH method in collaboration with M. Polkehn.[28] These studies pave the way for follow-up investigations addressing the molecular packing of novel class of DA materials.

Against this background, the thesis is organized as follows. In part I the fundamental methods and concepts that are needed for the description and understanding of the two main projects are introduced. First, an introduction to electronic structure theory (chapter 3) is given. Second, quantum-dynamical techniques are introduced, with a focus on multi-configurational techniques and GWP-based approaches (chapter 4). Last, several types of model Hamiltonians are introduced that are suitable to describe EET and ET phenomena (chapter 5). The remaining two parts address the implementation of the hierarchical 2L-G-MCTDH approach and its application to EET and ET processes in many dimensions (Part II), and the investigation of the above mentioned donor-acceptor systems (Part III).

Part I

Theoretical Background and Methods

2 | The Born-Oppenheimer Approximation and Beyond

2.1 The Schrödinger Equation and the Molecular Hamiltonian

Unlike very large molecular systems like proteins or nucleic acids, which are usually studied with classical approaches such as Molecular Dynamics (MD) simulations, for small molecular systems one is able to employ methods accounting for quantum effects. To this end, the time-dependent Schrödinger Equation (TDSE)[29] is solved numerically,

$$\hat{H}\Psi(\vec{r},\vec{R},t) = i\hbar\frac{\partial}{\partial t}\Psi(\vec{r},\vec{R},t) \tag{2.1}$$

The high-dimensional wave function is a function of electronic ($\vec{r}$) and nuclear ($\vec{R}$) coordinates and time (t). $\hat{H}$ represents the Hamiltonian of the system and contains all information and interactions for the description of the system of interest. This equation treats the dynamics and time-dependent properties of a given system. If the Hamiltonian of the system is time-independent, it is possible to separate the spatial variables ($\vec{r},\vec{R}$) from the temporal dependence on t according to a separation ansatz,

$$\Psi(\vec{r},\vec{R},t) = \phi\left(t\right)\psi\left(\vec{r},\vec{R}\right) \tag{2.2}$$

After inserting Eqn. 2.2 in Eqn. 2.1 and rearranging the equation, the time-independent SE (TISE) is obtained,

$$\hat{H}\psi(\vec{r},\vec{R}) = E\psi(\vec{r},\vec{R}) \tag{2.3}$$

Here, the discussion is focused on molecular systems employing the molecular Hamiltonian which depends on the electronic and nuclear degrees of freedom as follows,[30,31]

$$\begin{aligned}\hat{H}_{tot} = &-\sum_{A=1}^{M}\frac{1}{2M_A}\nabla_I^2 - \sum_{i=1}^{N}\frac{1}{2}\nabla_i^2 - \sum_{i=1}^{N}\sum_{A=1}^{M}\frac{Z_A}{|r_i - R_A|} \\ &+ \sum_{A=1}^{M}\sum_{B>A}^{M}\frac{Z_A Z_B}{|R_A - R_B|} + \sum_{i=1}^{N}\sum_{j>i}^{N}\frac{1}{|r_i - r_j|}\end{aligned} \tag{2.4}$$

M_A represents the ratio of the masses of nucleus A and an electron (such that the electron mass is set to $m_e = 1$) and Z_A is the charge of nucleus A. The first two terms contain the kinetic energy of the system. The third term represents the Coulomb attraction between electrons and nuclei, whereas the last two terms denote the repulsion between pairs of nuclei and pairs of electrons. A molecule is characterized by the number of nuclei M and electrons N ($3\,(M+N)$ spatial degrees of freedom in total). Additionally, electrons feature an additional quantum number to account for the spin (noting that nuclear spin will be disregarded in the present context).

2.2 The Born-Oppenheimer Approximation

The Born-Oppenheimer (BO) approximation is one of the key approximations in quantum chemistry. Since the nuclei are much heavier than the electrons, one can assume that the electronic degrees of freedom respond instantaneously to changes in the nuclear configuration.[30,31] Following this approximation, the first term of Eqn. 2.4, the kinetic energy of the nuclei, can be neglected and the fourth term, the repulsion between the nuclei can be considered to be constant for a given molecular structure. The third term, the Coulomb attraction, only depends parametrically on the nuclei. The resulting Hamiltonian is called the electronic Hamiltonian (Eqn. 2.5),[32]

$$\hat{H}_{el}(R) = -\sum_{i=1}^{N}\frac{1}{2}\nabla_i^2 - \sum_{i=1}^{N}\sum_{A=1}^{M}\frac{Z_A}{|r_i - R_A|} + \sum_{i=1}^{N}\sum_{j>i}^{N}\frac{1}{|r_i - r_j|} + V\,(R) \tag{2.5}$$

where $V\,(R) = \sum_{A=1}^{M}\sum_{B>A}^{M}\frac{Z_A Z_B}{|R_A - R_B|}$ is an additive term for the nuclear repulsion, which is assumed to be constant for a specific nuclear geometry. Considering this Hamiltonian, the electronic Schrödinger equation is constructed as follows,

$$\hat{H}_{el}\Psi_{el}\left(\vec{r};\vec{R}\right) = E_{el}(\vec{R})\Psi_{el}\left(\vec{r};\vec{R}\right) \tag{2.6}$$

where the electronic wave function and the electronic energy depend parametrically on the nuclear geometry. This is also true for the total energy,

$$E_{tot}(\vec{R}) = E_{el}(\vec{R}) + \sum_{A=1}^{M}\sum_{B>A}^{M}\frac{Z_A Z_B}{|R_A - R_B|} \tag{2.7}$$

The nuclear Hamiltonian $\hat{H}_{nuc}$ can be generated using the same assumptions. The electronic coordinates are replaced by their average values, such that the nuclei move in the average field of the electrons,

$$\hat{H}_{nuc} = \hat{T}_{nuc} + E_{tot}\left(\{\vec{R}\}\right) \tag{2.8}$$

with $\hat{T}_{nuc} = -\sum_{A=1}^{M} \frac{1}{2M_A}\nabla_I^2$. The total wave function can be written as a product of a nuclear and an electronic wave function.,

$$\Psi\left(\vec{r},\vec{R}\right) = \Theta_{nuc}\left(R\right)\Psi_{el}\left(\vec{r};\vec{R}\right) \tag{2.9}$$

From this expression the nuclear and the electronic Schrödinger Equations may be solved separately,

$$\hat{H}_{el}\Psi_{el}\left(\vec{r};\vec{R}\right) = E_{el}(\vec{R})\Psi_{el}\left(\vec{r};\vec{R}\right) \tag{2.10}$$

$$i\frac{\partial}{\partial t}\Theta_{nuc}\left(\vec{R}\right) = \left[\hat{T}_{nuc} + E_{tot}(\vec{R})\left(\{\vec{R}\}\right)\right]\Theta_{nuc}\left(\vec{R}\right) \tag{2.11}$$

where $E_{el}(\vec{R})$ from the first equation determines the potential $E_{tot}(\vec{R})$ appearing in the second equation for the nuclei.

The Born-Oppenheimer approximation is an adiabatic approximation, where nuclear motion takes place on a single Born-Oppenheimer potential energy surface (PES) defined by a single $\vec{R}$-dependent eigenvalue of the electronic Schrödinger equation. The Born-Oppenheimer approximation is no longer valid when two or more electronic states are nearly degenerate, which is known as "breakdown of the Born-Oppenheimer approximation". In this case, so-called non-adiabatic coupling matrix elements cannot be neglected. This is typically the case in regions exhibiting conical intersections or avoided crossings.

2.3 Beyond Born-Oppenheimer: Non-Adiabatic Effects

As indicated in the last section, the BO approximation breaks down when two or more electronic states become degenerate. Many phenomena appearing in molecular physics, especially in photochemistry and photophysics, cannot be described correctly within the BO approximation. These phenomena include dynamics at avoided crossings and conical intersection. In order to be able to describe the excited state quantum dynamics of a molecular system, one has to go beyond the Born-Oppenheimer approximation and a more general ansatz is needed.

The solution of Eqn. 2.10 yields a set of electronic eigenfunctions $\psi_i\left(\vec{r};\vec{R}\right)$ parametrically depending on the nuclear coordinates. The total wave function $\Psi(\vec{r},\vec{R},t)$

is then written as linear combination of these electronic eigenfunctions and nuclear wave functions $\varphi_i\left(\vec{R}\right)$,[33]

$$\Psi(\vec{r},\vec{R},t)=\sum_i \psi_i\left(\vec{r};\vec{R}\right)\varphi_i\left(\vec{R}\right) \tag{2.12}$$

Inserting Eqn. 2.12 into the TDSE (Eqn. 2.1) and integrating over the electronic coordinates yields coupled equations for the nuclear wave functions $\varphi_j\left(\vec{R}\right)$,

$$\left[\hat{T}_{nuc}+E\left(R\right)\right]\varphi_j\left(\vec{R}\right)-\sum_i \hat{\Lambda}_{ji}\varphi_i\left(\vec{R}\right)=i\hbar\frac{\partial}{\partial t}\varphi_j\left(\vec{R}\right) \tag{2.13}$$

with the off-diagonal matrix elements $\hat{\Lambda}_{ji}$, defining the non-adiabatic coupling operators,[33]

$$\hat{\Lambda}_{ji}=-\left\langle\psi_j\left(\vec{r};\vec{R}\right)|\hat{T}_{nuc}|\psi_i\left(\vec{r};\vec{R}\right)\right\rangle \tag{2.14}$$

Within the BO-approximation these coupling operators are neglected. As one can see from Eqn. 2.14, $\hat{\Lambda}_{ji}$ describes the coupled motion and dynamical interaction of the electronic and nuclear degrees of freedom.[33] For a two-state model using a more intuitive matrix representation one obtains,

$$i\hbar\frac{\partial}{\partial t}\begin{pmatrix}\varphi_1\left(\vec{R}\right)\\ \varphi_2\left(\vec{R}\right)\end{pmatrix}=\begin{pmatrix}\hat{T}_{nuc}+E_1\left(\vec{R}\right) & \hat{\Lambda}_{12}\left(\vec{R}\right)\\ \hat{\Lambda}_{21}\left(\vec{R}\right) & \hat{T}_{nuc}+E_2\left(\vec{R}\right)\end{pmatrix}\begin{pmatrix}\varphi_1\left(\vec{R}\right)\\ \varphi_2\left(\vec{R}\right)\end{pmatrix} \tag{2.15}$$

Eqn. 2.15 is still formulated in an adiabatic representation. But for quantum dynamical simulations, it is often more intuitive and preferable from a numerical point of view to use a so-called diabatic representation of the matrix formulation. By applying an appropriate unitary transformation to the electronic wave functions, a diabatic representation is formulated ($\Phi^{\text{dia}}\left(\vec{r};\vec{R}\right)$), such that the kinetic energy couplings $\hat{\Lambda}_{ji}$ are replaced by potential-type couplings,

$$\Phi^{\text{dia}}\left(\vec{r};\vec{R}\right)=S\left(\vec{R}\right)\psi^{\text{adia}}\left(\vec{r};\vec{R}\right) \tag{2.16}$$

Using these diabatic electronic wave functions, Eqn. 2.15 changes to,

$$i\hbar\frac{\partial}{\partial t}\begin{pmatrix}\tilde{\varphi}_1\left(\vec{R}\right)\\ \tilde{\varphi}_2\left(\vec{R}\right)\end{pmatrix}=\begin{pmatrix}\hat{T}_{nuc}+V_1^{\text{dia}}\left(\vec{R}\right) & V_{12}\left(\vec{R}\right)\\ V_{21}\left(\vec{R}\right) & \hat{T}_{nuc}+V_2^{\text{dia}}\left(\vec{R}\right)\end{pmatrix}\begin{pmatrix}\tilde{\varphi}_1\left(\vec{R}\right)\\ \tilde{\varphi}_2\left(\vec{R}\right)\end{pmatrix} \tag{2.17}$$

This representation is in general more convenient as the calculations of the derivative couplings is avoided, which can be ill-behaved exhibiting a singularity at conical intersections. Furthermore, the diabatic states have a well defined electronic character, giving a more intuitive understanding than the adiabatic representation. For special cases such as diatomics and isolated two-state systems the unitary transformation can be determined analytically. However, in general a strictly diabatic basis

does not exist.[34] Therefore, in order to perform the unitary transformation, several methods have been developed to perform a quasi-diabatization procedure, where the derivative couplings are approximately eliminated.[35–37] For more information and a more detailed discussion, see Refs. [21] and [33].

3 | Electronic Structure Theory

This chapter aims to give an overview about the electronic structure methods that are employed in this work. The methods in this chapter are introduced against the background of the fundamental concepts and approximations in the previous chapter. As one of the basic approximate methods, the Hartree-Fock (HF) method[32] is described. Before introducing the very efficient Density Functional theory (DFT)[38] and its time-dependent variant (TDDFT),[39] more accurate methods such as Configuration Interaction (CI),[32] second-order Møller-Plesset Perturbation Theory MP(2),[40,41] second-order approximate Coupled Cluster (CC2)[42] and the second-order Algebraic Diagrammatic Construction (ADC(2))[43,44] are presented, which often serve as a high-level benchmark for DFT functionals. If not stated differently, all equations are given in atomic units (the Planck constant $\hbar$, the elementary charge e, the electron mass m_e and the speed of light c are set to 1). Small indices indicate the electronic coordinates and capital indices indicate the nuclear coordinates.

3.1 Hartree-Fock Approximation

The Hartree-Fock approximation is one important step towards modern quantum chemistry. To tackle many-electron problems, solving the Schrödinger Equation for only two interacting electrons is the fundamental problem in quantum chemistry. A significant contribution to a solution to this problem is the approach of D. R. Hartree and V. A. Fock developed in the 1930s.

A simple, but insufficient *ansatz* for the N-electron wave function is the Hartree-Product $\Psi_{el}(x_1, x_2, \ldots, x_N; R) = \chi_i(x_1)\,\chi_j(x_2)\cdots\chi_k(x_N)$. The Hartree-Product is simply the product of one-particle spin orbitals $\chi_j(x_i)$ for each electron.[32] However, this does not satisfy the antisymmetry principle by Pauli, meaning that two electrons must be distinguishable by at least one quantum number. The Pauli principle can be fulfilled by using a Slater determinant to build an antisymmetric wave function,

$$\Psi_0\left(x_1, x_2, \ldots, x_N; R\right) = \frac{1}{\sqrt{N!}} \begin{vmatrix} \chi_i(x_1) & \chi_j(x_1) & \cdots & \chi_k(x_1) \\ \chi_i(x_2) & \chi_j(x_2) & \cdots & \cdots \\ \cdot & \cdot & \cdot & \cdot \\ \cdot & \cdot & \cdot & \cdot \\ \chi_i(x_N) & \cdots & \cdots & \chi_k(x_N) \end{vmatrix}$$

$$= |\chi_i(x_1)\chi_j(x_2)...\chi_k(x_N)\rangle \tag{3.1}$$

Eqn. 3.1 depicts the simplest antisymmetric wave function, which can be used to describe the ground state of an N-electron system. The Hartree-Fock approach is based on the variational principle, which in turn ensures that the best wave function of a given functional form yields the lowest possible ground state energy for this form. Using the exact wave function and the exact Hamiltonian would yield the exact minimum energy,[32]

$$E_0 \geq \left\langle \Psi_0 \middle| \hat{H} \middle| \Psi_0 \right\rangle \tag{3.2}$$

With this one can minimize the energy E_0 of the system with respect to the spin orbitals and derive an equation (the Hartree-Fock equation) that takes the form of an eigenvalue problem,

$$\hat{f}\left(i\right)\chi_i(x_i) = \epsilon\chi_i(x_i) \tag{3.3}$$

where $\hat{f}\left(i\right)$ is an effective one-electron operator, the Fock operator, and is given as,

$$\begin{aligned} \hat{f}\left(1\right) &= \hat{h}\left(1\right) + v^{\mathrm{HF}}\left(1\right) \\ &= -\frac{1}{2}\nabla_1^2 - \sum_{A=1}^{M}\frac{Z_A}{r_{1A}} + \sum_{j\neq i}^{N}\left[\hat{J}_j\left(1\right) - \hat{K}_j\left(1\right)\right] \end{aligned} \tag{3.4}$$

Here, $h\left(i\right)$ represents the one-particle Hamiltonian and $v^{\mathrm{HF}}\left(i\right)$ the average potential experienced by electron i. $v^{\mathrm{HF}}\left(i\right)$ includes a Coulomb operator ($\hat{J}$) and an Exchange ($\hat{K}$) operator,

$$\hat{J}_j\left(1\right)\chi_i\left(1\right) = \left[\int \chi_j^*\left(2\right) r_{12}^{-1}\chi_j\left(2\right) dx_2\right]\chi_i\left(1\right) \tag{3.5}$$

$$\hat{K}_j\left(1\right)\chi_i\left(1\right) = \left[\int \chi_j^*\left(2\right) r_{12}^{-1}\chi_i\left(2\right) dx_2\right]\chi_j\left(1\right) \tag{3.6}$$

The Coulomb operator describes the average local potential at x_1 arising from an electron in χ_j, whereas the exchange operator describes the exchange of electron 1 in spin-orbital χ_j with electron 2 in spin-orbital χ_i.[32] Hence, the many-electron problem has been replaced by an one-electron problem, where one electron moves in the mean field of all other electrons. Thus the potential for one electron depends

on the spin orbitals of all other electrons and Eqn. 3.3 is non-linear. This equation has to be solved iteratively by a self-consistent-field (SCF) method. This is accomplished by making an initial guess for the spin orbitals calculating the average potential $v^{\mathrm{HF}}(i)$ for each electron. Then, by solving the eigenvalue problem a new set of spin orbitals is obtained. These can be used to repeat the procedure until the orbitals and the field do not change any more, they reach self-consistency.

3.2 Post Hartree-Fock Methods

As shown in the previous section 3.1 Hartree-Fock does not describe the electron electron correlation explicitly, but it treats it as an average interaction. With a sufficiently large basis set the HF wave function can cover approximately 99% of the total energy. But the remaining 1% are very often the most important part for the description of chemical phenomena. The electron-electron correlation energy is therefore defined as the difference between the exact energy of the system and the HF energy E_0 obtained in the limit of a complete basis set,[32]

$$E_{corr} = E_{exact} - E_0 \tag{3.7}$$

Several methods have been developed to account for the electron electron correlation. In the following, the Configuration Interaction (CI), the Møller-Plesset Perturbation Theory (MP(2)), Coupled Cluster (CC2) and Algebraic Diagrammatic Construction (ADC(2)) method are introduced. All these methods use HF as a starting point for improving the wave function, since already ~99% of the problem are described correctly.

3.2.1 Configuration Interaction

Hartree-Fock determines the energetically best trial wave function using a single determinant. In order to improve this wave function a multi-determinant description may be chosen. In Configuration Interaction the wave function is given as a linear combination of Slater determinants, where the expansion coefficients are obtained by requiring that the energy should be a minimum. As basis for determinants it is suitable to use *excited* determinants, such that for a singly excited determinant $|\Psi_i^a\rangle$ one spin orbital is replaced by another spin orbital, for a doubly excited determinant two spin orbitals are replaced by two other spin orbitals, etc. up to n-tuply excited determinants,[32]

$$|\Psi\rangle = c_0 |\Psi_0\rangle + \left(\frac{1}{1!}\right)^2 \sum_{i,a} c_i^a |\Psi_i^a\rangle + \left(\frac{1}{2!}\right)^2 \sum_{\substack{ab \\ ij}} |\Psi_{ij}^{ab}\rangle + \left(\frac{1}{3!}\right)^2 \sum_{\substack{abc \\ ijk}} |\Psi_{ijk}^{abc}\rangle + \cdots \quad (3.8)$$

The factor $\left(\frac{1}{n!}\right)^2$ ensures that every individual excitation is counted only once. To obtain the corresponding energy the (linear) variational method is employed, where a matrix representation of the Hamiltonian in the basis of the N-electron functions of Eqn. 3.8 is built. This is referred to as the full CI matrix.[32] The structure of the hermitian full CI matrix is shown in Eqn. 3.9. As simplification the singly/doubly excited determinants are denoted as $|S\rangle$ and $|D\rangle$,

$$\begin{pmatrix} \left\langle \Psi_0 \middle| \hat{H} \middle| \Psi_0 \right\rangle & \left\langle \Psi_0 \middle| \hat{H} \middle| S \right\rangle & \left\langle \Psi_0 \middle| \hat{H} \middle| D \right\rangle & \cdots \\ \left\langle S \middle| \hat{H} \middle| \Psi_0 \right\rangle & \left\langle S \middle| \hat{H} \middle| S \right\rangle & \left\langle S \middle| \hat{H} \middle| D \right\rangle & \cdots \\ \left\langle D \middle| \hat{H} \middle| \Psi_0 \right\rangle & \left\langle D \middle| \hat{H} \middle| S \right\rangle & \left\langle D \middle| \hat{H} \middle| D \right\rangle & \cdots \\ \vdots & \vdots & \vdots & \ddots \end{pmatrix} \quad (3.9)$$

From the variational method one obtains the matrix equation,

$$(\mathbf{H} - E\mathbf{I})\,\mathbf{c} = \mathbf{0} \quad (3.10)$$

Solving this secular equation is equivalent to diagonalizing the CI matrix. The lowest eigenvalue corresponds to the CI energy.[32] Although this method is conceptually rather simple, it is computationally very expensive already for small systems. In practice one therefore often uses a truncated excited determinant basis by limiting the excitation level.

According to Brillouin's Theorem, stating that singly excited determinants $|S\rangle$ will not interact directly with the reference determinant $|\Psi_0\rangle$ (resulting in $\left\langle S \middle| \hat{H} \middle| \Psi_0 \right\rangle = 0$), truncating the excitation level to one (CI *with Singles* (CIS)) does not give an improvement to the ground state HF energy.[32] The first level of improvement is therefore obtained by including double excitations. This is referred to as either CI *with Doubles* (CID) or CI *with Singles and Doubles* (CISD). The Computational effort of CISD scales with N^6 and typically covers 80-90% of the correlation energy. One major drawback asides the bad scaling behavior for truncated CI methods is the fact that they are not size consistent and size extensive. They therefore recover less electron correlation with growing system size.

3.2.2 MP(2)

A different non-variational but size consistent (and size extensive) method is the Many-Body Perturbation Theory (MBPT).[41] The underlying concept behind the MBPT is the assumption that the problem that is to be solved differs only slightly from a problem, where a solution is known. Therefore, the solution to the new problem should be somehow closely related to the solution of the existing and solved problem. The system Hamiltonian is then be expressed by two parts: A reference Hamiltonian($\hat{H}_0$) and the perturbation Hamiltonian ($\hat{H}'$). As a requirement the perturbation operator should be small compared to the reference,

$$\hat{H} = \hat{H}_0 + \lambda \hat{H}' \tag{3.11}$$

$$\hat{H}_0 \Phi_i = E_i \Phi_i \qquad i = 0, 1, 2, \ldots, \infty \tag{3.12}$$

λ is the perturbation parameter determining the strength of the perturbation. The solution to the Schrödinger Equation for the reference Hamiltonian $\hat{H}_0$ ($\lambda = 0$) is known and forms a complete set. For the sake of simplicity only the lowest energy state will be considered and the perturbation is time-independent in the following. The perturbed Schrödinger equation is given by,[41]

$$\hat{H}\Psi = E_{MBPT}\Psi \tag{3.13}$$

By setting $\lambda = 0$ one obtains $H = H_0$, $\Psi = \Phi_0$ and $E_{MBPT} = E_0$. The wave function and the energy are now expanded as a Taylor expansion in λ:

$$\Psi = \lambda^0\Psi_0 + \lambda^1\Psi_1 + \lambda^2\Psi_2 + \lambda^3\Psi_3 + \ldots \tag{3.14}$$

$$E_{MBPT} = \lambda^0 E_0 + \lambda^1 E_1 + \lambda^2 E_2 + \lambda^3 E_3 + \ldots \tag{3.15}$$

Inserting these expressions in Eqn. 3.13 yields,

$$\begin{aligned} &\left(\hat{H}_0 + \lambda\hat{H}'\right)\left(\lambda^0\Psi_0 + \lambda^1\Psi_1 + \lambda^2\Psi_2 + \ldots\right) = \\ &= \left(\lambda^0 E_0 + \lambda^1 E_1 + \lambda^2 E_2 + \ldots\right)\left(\lambda^0\Psi_0 + \lambda^1\Psi_1 + \lambda^2\Psi_2 + \ldots\right) \end{aligned} \tag{3.16}$$

This is correct for any value of λ, therefore we can gather all terms of λ with the same power,

$$\begin{aligned}
\lambda^0 &: \hat{H}_0\Psi_0 = E_0\Psi_0 \\
\lambda^1 &: \hat{H}_0\Psi_1 + \hat{H}'\Psi_0 = E_0\Psi_1 + E_1\Psi_0 \\
\lambda^2 &: \hat{H}_0\Psi_2 + \hat{H}'\Psi_1 = E_0\Psi_2 + E_1\Psi_1 + E_2\Psi_0 \\
&\cdots \\
\lambda^n &: \hat{H}_0\Psi_n + \hat{H}'\Psi_{n-1} = \sum_{i=0}^{n} E_i\Psi_{n-1}
\end{aligned} \tag{3.17}$$

These are the zero-, first-, second- and nth-order perturbation equations. Where the zeroth-order equation is just the Schrödinger equation for the unperturbed case.[41]

Since the goal is to use MBPT to calculate the correlation energy, one has to choose an appropriate reference Hamiltonian. This leads to the Møller-Plesset-MBPT.[40,41] In 1934 C. Møller and M.S. Plesset applied the MBPT to the calculation of the correlation energy by using a sum over Fock operators. In the sum of Fock operators the average electron electron repulsion $\left\langle \hat{V}_{ee} \right\rangle$ is counted twice and the perturbation becomes $\hat{V}_{ee} - 2\left\langle \hat{V}_{ee} \right\rangle$. This is also known as the fluctuation potential,

$$\begin{aligned}
\hat{H}_0 &= \sum_{i=1}^{N} \hat{F}_i = \sum_{i=1}^{N} \left(\hat{h}_i + \sum_{j=1}^{N} (\hat{J}_j - \hat{K}_j) \right) \\
&= \sum_{i=1}^{N} \hat{h}_i + \sum_{i=1}^{N}\sum_{j=1}^{N} \left\langle \hat{g}_{ij} \right\rangle = \sum_{i=1}^{N} \hat{h}_i + 2\left\langle \hat{V}_{ee} \right\rangle \\
\hat{H}' &= \hat{H} - \hat{H}_0 = \sum_{i=1}^{N}\sum_{j>i}^{N} \hat{g}_{ij} - \sum_{i=1}^{N}\sum_{j=1}^{N} \left\langle \hat{g}_{ij} \right\rangle = \hat{V}_{ee} - 2\left\langle \hat{V}_{ee} \right\rangle
\end{aligned} \tag{3.18}$$

This choice is furthermore the only one which gives a size extensive, and therefore preferable, method. The zeroth-order wave function is given by the HF determinant and the zeroth-order energy is just the sum of the molecular orbital (MO) energies. The first order energy correction yields the negative of the average of the electron-electron repulsion $\left\langle \hat{V}_{ee} \right\rangle$ and accounts for the double counting in zeroth-order. One therefore obtains the HF energy as first order energy,

$$\mathrm{MP}(0) : E_{MP(0)} = \left\langle \Phi_0 \middle| \hat{H}_0 \middle| \Phi_0 \right\rangle = \sum_{i=1}^{N} \epsilon_i \tag{3.19}$$

$$\mathrm{MP}(1) : E_{MP(0)} + E_{MP(1)} = \left\langle \Phi_0 \middle| \hat{H}_0 \middle| \Phi_0 \right\rangle + \left\langle \Phi_0 \middle| \hat{H}' \middle| \Phi_0 \right\rangle = E\,(HF) \tag{3.20}$$

Accordingly, the first contribution to the electron correlation energy is given by the second order term,

$$E_2 = \sum_{i<j}^{occ} \sum_{a<b}^{virt} \frac{\left\langle \Phi_0 \middle| \hat{H}' \middle| \Phi_{ij}^{ab} \right\rangle \left\langle \Phi_{ij}^{ab} \middle| \hat{H}' \middle| \Phi_0 \right\rangle}{E_0 - E_{ij}^{ab}} \tag{3.21}$$

The matrix elements between the HF and a doubly excited state are given by two-electron integrals over MOs. In accordance with Koopmans' theorem the difference of the total energy between two Slater determinants becomes a difference in MO energies. The MP(2) energy is given as,[41]

$$E_{MP(2)} = \sum_{i<j}^{occ} \sum_{a<b}^{virt} \frac{\left(\left\langle \varphi_i \varphi_j \middle| \varphi_a \varphi_b \right\rangle - \left\langle \varphi_i \varphi_j \middle| \varphi_b \varphi_a \right\rangle \right)}{\epsilon_i + \epsilon_j - \epsilon_a - \epsilon_b} \tag{3.22}$$

Since MP(2) is not variational, a lower energy does not correspond to a better description. Typically MP(2) often overestimates the electron electron correlation. To account for that the spin-component scaling (SCS) approach can be used. This has first been introduced by Grimme[45] and improvements are especially observed for molecules which contain pitfalls for MP(2). In the SCS approach an individual scaling factor is used for the same-spin contributions of the correlation energy.

3.2.3 CC2

Further improvements towards the description of the electron electron correlation can be achieved with the Coupled Cluster (CC) method. Like MBPT, it is non-variational but size-consistent (and size extensive). But contrary to MBPT, which adds all types of corrections up to a given order, CC is intended to include all corrections of a given type to infinite order.[42,46]

In CC an excitation operator (also called cluster operator) is defined,

$$\hat{T} = \hat{T}_1 + \hat{T}_2 + \hat{T}_3 + \cdots + \hat{T}_N \tag{3.23}$$

The operator $\hat{T}_i$ acting on a HF reference wave function Ψ_0 generates all ith excited Slater determinants,

$$\hat{T}_1 \Psi_0 = \sum_{i}^{occ} \sum_{a}^{virt} t_i^a \Psi_{ij}^{ab} \tag{3.24}$$

$$\hat{T}_2 \Psi_0 = \sum_{i<j}^{occ} \sum_{a<b}^{virt} t_i^a \Psi_{ij}^{ab} \tag{3.25}$$

The corresponding Coupled Cluster wave function is defined with the exponential operator $e^{\hat{T}}$ in Eqn. 3.26.[46] The exponential operator is furthermore expanded in a Taylor expansion,

$$\Psi_{CC} = e^{\hat{T}}\Psi_0 \tag{3.26}$$

$$e^{\hat{T}} = 1 + \hat{T} + \frac{1}{1}\hat{T}^2 + \frac{1}{6}\hat{T}^4 + \cdots = \sum_{k=0}^{\infty} \frac{1}{k!}T^k \tag{3.27}$$

Using Eqn. 3.26 the Schrödinger equation can be written as,

$$\hat{H}e^{\hat{T}}\Psi_0 = Ee^{\hat{T}}\Psi_0 \tag{3.28}$$

The CC energy is then evaluated by projecting the the CC Schrödinger equation onto the reference wave function.[46] After expanding out the exponential terms one obtains the CC energy,

$$E_{CC} = \left\langle \Psi_0 \middle| \hat{H}e^{T} \middle| \Psi_0 \right\rangle \tag{3.29}$$

Again to reduce computational effort usually a truncated second-order approach (CCSD) is applied. But in contrast to truncated CI, truncated CC is size consistent and size extensive.[46] To save further computation time an additional approximation can be used. In the Second-Order Approximate Coupled-Cluster (CC2) method only a subset of the full CCSD equation is included by approximating the doubles contributions to first order only.[42,46] CC2 scales with N^5 and typically gives better results as CIS or CCS.

3.2.4 ADC(2)

The Algebraic Diagrammatic Construction (ADC) scheme can be derivated from the intermediate state representation (ISR).[43] As a starting point the exact N-electron ground state $|\Psi_0^N\rangle$ is used. The excitation operators are represented by pairs of creation and annihilation operators,

$$\{\hat{C}_J\} = \{c_a^\dagger c_i; c_a^\dagger c_b^\dagger c_i c_j, i < j, a < b\} \tag{3.30}$$

By applying excitation operators $\hat{C}_J$ one obtains a set of correlated excited states,

$$|\Psi_J^N\rangle = \hat{C}_J\,|\Psi_0^N\rangle \tag{3.31}$$

The resulting states can than be allocated to the various excitation classes (singles, doubles, etc.).However, these excited states do not form an orthonormal basis. One therefore needs to orthogonalize by employing the Gram-Schmidt orthogonalization scheme. This yields the basis of intermediate states $\{|\tilde{\Psi}_J^N\rangle\}$ which can be used to represent the hermitian ADC matrix (which is shifted by the exact ground state energy E_0^N),

$$M_{IJ} = \left\langle \tilde{\Psi}_I^N \middle| \hat{H} - E_0^N \middle| \tilde{\Psi}_J^N \right\rangle \tag{3.32}$$

Diagonalizing the ADC matrix will, in principle, result in the exact excitation energies.

Up to this point no approximation according the exact N-electron ground state wave function has been employed. Since the exact N-electron ground state wave function is not known, one needs a suitable approximation. This is done by using the Møller-Plesset-MBPT up to a specific order as ground state wave function, i.e. MP(2) results in ADC(2). ADC(2) typically scales with N^5 similar to CC2 and gives qualitatively similar results.

3.3 Density Functional Theory

Density Functional Theory (DFT) represents a different approach towards solving the SE. Due to its high efficiency, DFT is a widely used method. In general DFT is an exact method, but in order to apply DFT as a quantum chemical method, approximations have to be utilized. As a consequence, the just presented methods often serve as a benchmark for DFT calculations. In the following, the basics of Ground-State DFT are introduced. Thereupon, the extension to excited states, the Linear Response Time Dependent DFT is presented.

3.3.1 Ground-State Density Functional Theory

The basic idea behind Density Functional Theory is to express the energy of an electronic system not by a wave function, but as a functional of the electron density. The main advantage of using the electron density is in the reduction of dimensionality. Instead of solving a $4N$-dimensional wave function (including the spin) one uses a single three-dimensional function to describe a N-electron molecule.

The basis of DFT as used nowadays are the Hohenberg-Kohn theorems (HK). In 1964 P. Hohenberg and W. Kohn provided a proof that the electronic ground state energy and its properties are related uniquely to the electron density (HK1). The second theorem establishes a density-based analogue of the variation principle. The energy functional $E_0[\rho']$ for a trial density function $\rho'(r)$ is always greater or equal the exact ground state energy (HK2).[38]

The next step in the progression of DFT was done by W. Kohn and L.J. Sham in 1965[47] by considering a system consisting of N non-interacting electrons in an external potential $v_{ext}(r)$. This is selected such that the electron density $\rho_{ref}(r)$ of a reference system is identical to its exact electron density $\rho_{exact}(r)$,

$$\rho_{ref}(r) = \sum_{i=1}^{N} |\psi_i^{KS}|^2 = \rho_{exact}(r) \tag{3.33}$$

The energy functional E_{DFT} is given as,

$$\begin{aligned} E_{DFT}[\rho(r)] = &\sum_{i=1}^{N} \left\langle \psi_i^{KS} \left| -\frac{1}{2}\nabla_i^2 \right| \psi_i^{KS} \right\rangle - \left\langle \psi_i^{KS} \left| \sum_{A}^{M} \frac{Z_A}{|r_i - R_A|} \right| \psi_i^{KS} \right\rangle \\ &+ \sum_{i=1}^{N} \left\langle \psi_i^{KS} \left| \frac{1}{2} \int \frac{\rho(r')}{|r_i - r'|} dr' \right| \psi_i^{KS} \right\rangle + E_{xc}[\rho(r)] \end{aligned} \tag{3.34}$$

where the first term describes the kinetic energy, the electron nuclear attraction is given by the second term, the third term depicts the coulomb repulsion and the last term defines the exchange-correlation energy. The exchange-correlation energy contains the kinetic energy correction for the interacting system, terms that compensate the non-classical effects of self-interaction, exchange and correlation. In other words, everything that is unknown or not given in an exact form. For an exact $E_{xc}[\rho(r)]$ functional DFT would yield the exact energy.

Similar to the HF approach one has to solve the Kohn-Sham equation,

$$\hat{h}_i^{KS} \psi_i^{KS} = \epsilon_i^{KS} \psi_i^{KS} \tag{3.35}$$

with the Kohn-Sham Hamiltonian $\hat{h}_i^{KS}$, given as,

$$h_i^{KS} = -\frac{1}{2}\nabla_i^2 - \sum_{A=1}^{M} \frac{Z_A}{|r_i - R_A|} + \int \frac{\rho\langle r' \rangle}{|r_i - r_j|} dr' + V_{xc}[\rho(r)] \tag{3.36}$$

where $V_{xc}[\rho(r)]$ is the exchange-correlation functional. In turn, finding a suitable exchange-correlation potential is the key to solve the Kohn-Sham equation. Many functionals have been developed and many (improved) variants are available today (functionals using the Local Spin-Density Approximation (LDSA) like the Slater exchange functional,[48] the Generalized Gradient Approximation (GGA) like the Perdew, Burke, and Ernzerhof (PBE) functionals[49,50] or meta-GGA functionals as the Tao, Perdew, Staroverov, and Scuseria functional (TPSS). One of the most famous functionals is represented by the B3LYP functional by Becke and Lee, Young and Parr.[51] B3LYP is a hybrid functional which mixes a certain amount Hartree-Fock exchange into the computation. It is also possible to add certain amounts of PT(2) correction for dynamic correlation ("double hybrid" functionals

e.g. B2PLYP[52]) into the calculation. The choice of the functional depends on the problem at hand. Therefore, a thoroughly performed benchmark against post-HF ab-initio methods should be done before choosing a specific functional.

3.3.2 Linear Response Density Functional Theory

So far, the presented Kohn-Sham equations are limited to time-independent problems. Further the Hohenberg-Kohn theorems are only formulated for these systems and need to be reformulated for time-dependent problems. The Runge-Gross theorem[39] fills this gap and can be seen as the time-dependent analogue of the HK theorems. It states that a one-to-one mapping between time-dependent potentials and time-dependent functionals exist. With this and by the introduction of the action functional it is possible to derive a set of working equations, the time-dependent Kohn-Sham equations,

$$i\frac{\partial}{\partial t}\psi_i^{KS}(r,t) = \hat{F}^{KS}\psi_i^{KS}(r,t) \tag{3.37}$$

with the time-dependent Kohn-Sham orbitals $\psi_i^{KS}(r,t) = \sum_{j=1}^{M} c_{i,j}(t)\,\chi_j^{KS}(r)$. Eqn. 3.37 can be expressed in a density matrix form,

$$\sum_q \left[\mathbf{F}_{pq}\mathbf{P}_{qr} - \mathbf{P}_{pq}\mathbf{F}_{qr}\right] = i\frac{\partial}{\partial t}\mathbf{P}_{pr} \tag{3.38}$$

where $\mathbf{F}_{pq}$ represents the time-independent Kohn-Sham Hamiltonian matrix with the Kohn-Sham orbitals as basis. Furthermore, the density matrix is related to the electron density by Eqn. 3.39

$$\begin{aligned}\rho(r,t) &= \sum_{p,q}^{M} c_p(t)\,c_q^*(t)\,\chi_p^{KS}(r)\,\chi_q^{*KS}(r)\\ &= \sum_{p,q}^{M} \mathbf{P}_{pq}\chi_p^{KS}(r)\,\chi_q^{*KS}(r)\end{aligned} \tag{3.39}$$

Now, a small time-dependent perturbation g_{pq} (via an oscillating external field) is applied (effectively making the external potential time-dependent). Then, the first order (linear) response to the density matrix and the time-dependent Kohn-Sham Hamiltonian is given as ,

$$\mathbf{P}_{pq} = \mathbf{P}_{pq}^{(0)} + \mathbf{P}_{pq}^{(1)} \tag{3.40}$$

$$\mathbf{F}_{pq} = \mathbf{F}_{pq}^{(0)} + \mathbf{F}_{pq}^{(1)} \tag{3.41}$$

Insertion of Eqns. 3.40 and 3.41 into Eqn. 3.38 yields,

$$\sum_q \left[\mathbf{F}^{(0)}_{pq}\mathbf{P}^{(1)}_{qr} - \mathbf{P}^{(1)}_{pq}\mathbf{F}^{(0)}_{qr} + \mathbf{F}^{(1)}_{pq}\mathbf{P}^{(0)}_{qr} - \mathbf{P}^{(0)}_{pq}\mathbf{F}^{(1)}_{qr}\right] = i\frac{\partial}{\partial t}\mathbf{P}^{(1)}_{pr} \tag{3.42}$$

where the first order change in the KS Hamiltonian is given by,

$$\mathbf{F}^{(1)}_{pq} = g_{pq} + \Delta\mathbf{F}^{(0)}_{pq} \tag{3.43}$$

For the first order change of the density matrix $\mathbf{P}^{(1)}_{qp}$ it turns out that it is only different from zero, when q corresponds to an occupied and p to a virtual orbital. One therefore obtains two coupled equations and by Fourier transformation one obtains the TDDFT working equations. For convenience, occupied orbitals are labeled i, j and virtual orbitals are labeled a, b,

$$\begin{aligned}\omega\Delta P_{ia}(\omega) = (\epsilon_a - \epsilon_i)\Delta P_{ia}(\omega) &+ \sum_{jb}\left[\langle aj\,|\,ib\rangle + \langle aj\,|\,\delta v_{xc}\,|\,ib\rangle\right]\Delta P_{jb}(\omega) \\ &+ \sum_{jb}\left[\langle ab\,|\,ij\rangle + \langle ab\,|\,\delta v_{xc}\,|\,ij\rangle\right]\Delta P_{bj}(\omega) \qquad (3.44)\\ -\omega\Delta P_{ia}(\omega) = (\epsilon_a - \epsilon_i)\Delta P_{ai}(\omega) &+ \sum_{jb}\left[\langle ib\,|\,aj\rangle + \langle ib\,|\,\delta v_{xc}\,|\,aj\rangle\right]\Delta P_{jb}(\omega) \\ &+ \sum_{jb}\left[\langle ij\,|\,ab\rangle + \langle ij\,|\,\delta v_{xc}\,|\,ab\rangle\right]\Delta P_{jb}(\omega) \qquad (3.45)\end{aligned}$$

These equations can be transformed into a non-hermitian eigenvalue equation, the TDDFT or Casida[53] equation,

$$\begin{pmatrix} A & B \\ B^* & A^* \end{pmatrix}\begin{pmatrix} \Delta P_{ia} \\ \Delta P_{ai} \end{pmatrix} = -\omega\begin{pmatrix} 1 & 0 \\ 0 & -1 \end{pmatrix}\begin{pmatrix} \Delta P_{ia} \\ \Delta P_{ai} \end{pmatrix} \tag{3.46}$$

The Elements **A** and **B** are given as,

$$A_{ia,jb} = (\epsilon_a - \epsilon_i)\,\delta_{ij}\delta_{ab} + \langle ia\,|\,jb\rangle + \langle ia\,|\,\delta v_{xc}\,|\,jb\rangle \tag{3.47}$$

$$B_{ia,jb} = \langle ia\,|\,bj\rangle + \langle ia\,|\,\delta v_{xc}\,|\,bj\rangle \tag{3.48}$$

Here, the first term of $A_{ia,jb}$ represents the difference of orbital energies for ϵ and ϵ_a. The second term stems from the linear response of the Coulomb Operator. The last term depicts the response to the exchange-correlation functional.

One substantial problem of TDDFT is the description of charge transfer states. Not only are the excitation energies obtained usually dramatically too low, but also TDDFT does not recover the correct $\frac{1}{r}$ dependence along the charge separating coordinate. If a long-range charge transfer excited state is considered the overlap between the occupied and virtual orbitals is assumed to be equal to zero, as a consequence, all terms except the first one of Eqn. 3.47 vanish. This excitation energy is solely determined by the difference of the orbital energies. This is, in

general, a poor estimate. As all terms of B vanish they do not contribute at all to charge transfer states. This problem is also known as electron-transfer self-interaction error (ET-SI).[54]

One option to overcome this problem is to include HF exchange in the exchange-correlation potential. To this end the corresponding equation are given in Eqns. 3.49 and 3.50,

$$A_{ia,jb} = (\epsilon_a - \epsilon_i)\,\delta_{ij}\delta_{ab} + \langle ia\,|\,jb\rangle - c_{HF}\,\langle ij|ab\rangle + (1 - c_{HF})\,\langle ia\,|\,\delta v_{xc}\,|\,jb\rangle \quad (3.49)$$

$$B_{ia,jb} = \langle ia\,|\,bj\rangle - c_{HF}\,\langle ib\,|\,aj\rangle + (1 - c_{HF})\,\langle ia\,|\,\delta v_{xc}\,|\,bj\rangle \quad (3.50)$$

Now, the terms comprising c_{HF} do not vanish. By adding more HF exchange the correct $\frac{1}{r}$ long-range behavior is recovered. Another approach is provided by the so called range-separated functionals. Here, depending on the distance the amount of HF exchange is modulated in the exchange correlation functional. Functionals using this approach are for example the CAM-B3LYP[55] or ωB97XD[56] functionals.

4 | Quantum Dynamical Methods

A well established method to study the dynamics of large molecular systems like proteins or nucleic acids is to run Molecular Dynamics (MD) simulations. Here, classical equations of motion (EOM) are numerically integrated in order to learn about the properties of such systems. This does not work if one wants to describe a non-relativistic molecular system, including quantum effects as tunneling and non-adiabatic transitions, e.g. for the interpretation of experiments in the femtosecond regime. For the description of such systems, one needs to solve the Schrödinger equation. This can be done in two ways:

- in the time-independent picture by diagonalising the Hamiltonian (for more details, methods and references see chapter 3),
- in the time-dependent picture by propagation of a wave packet (focus of this chapter).

The time-dependent form of the Schrödinger equation (TDSE) is given by):[29]

$$i\hbar\frac{\partial\Psi}{\partial t} = \hat{H}\Psi \tag{4.1}$$

Unfortunately this equation can only be solved analytically for up to two particles, e.g. the hydrogen atom. However, several approximations have been developed to solve the Schrödinger equation numerically. A key step, as already mentioned in more detail in chapter 2.2, towards this was the Born-Oppenheimer approximation, by separating nuclear and electronic motion. The nuclei of a molecular system can now be described as point masses moving on a potential energy surface (PES), where the electrons react instantaneously to the new nuclear configuration. However, this approximation breaks down at certain areas on the PES, e.g. when two electronic configurations (states) are strongly coupled as it is the case at conical intersections or avoided crossings. Then, the nuclei have to be described by moving on several, coupled electronic states (non-adiabatic picture). The PES can be obtained by employing quantum chemical (QC) methods (c.f. chapter 3) along selected molecular coordinates, which have to be pre-selected appropriately. With these cuts one is able to parametrize a Hamiltonian that can be used in the quantum dynamic (QD) simulation. The QC methods are then also able to provide further information (gradients, Hessian, molecular properties like polarizabilaties, charge distribution, etc.) of critical or important points on the PES of the investigated system.

Several methods have been developed in parallel to study quantum molecular dynamics. In the 1970s and 1980s, mainly methods based on many classical trajectories, which represent the wave packet, were employed. Since the classical treatment introduces a quite significant error, semi-classical and mixed quantum-classical approaches have been developed, where the simple, trajectory based picture remains and quantum wavefunctions are represented by trajectory ensembles that are "dressed" with quantum phase information. In mixed quantum-classical methods, the system is split into a classical and a quantum part (where the latter represents, e.g., electronic degrees of freedom (DOFs)). These methods have the advantage to study systems with many DOFs, as the dynamics of the nuclei is still described classically. A prominent representative for semiclassical methods is the Gaussian wavepacket (GWP) method introduced by Heller in the 1970s.[57,58] A prominent example of mixed quantum-classical schemes is the mean-field Ehrenfest method.[59,60]

One of the first full QD simulations was performed for $H + H_2$.[61,62] In combination with grid based methods like the discrete variable representation (DVR) of Light in the 1980s[63–65] and the Dirac-Frenkel variational principle (DF-VP)[48,66,67] a method was introduced which is able to provide exact quantum dynamics, the so-called standard method. However, this method suffers from an exponential scaling with the number of degrees of freedom (both for the computational effort and the memory requirements) and is therefore only applicable to small systems, typically up to 5-6 DOFs.

In order to extend the range of feasible numbers of DOFs, approximate wave function approaches were developed using the variational principle to derive approximate solutions to the TDSE.

A rather simple ansatz is the use of a Hartree product with one basis function for each DOF in the Time-Dependent Hartree (TDH) method.[48,68,69] For TDH the computational cost is drastically reduced, but with the drawback that correlations between den DOFs are not treated correctly anymore. An extension to TDH was to use several Hartree products instead of only one. This led to the famous Multi-configuration Time-Dependent Hartree (MCTDH) method.[25,70] While MCTDH is an extension to TDH it has a similar structure as the standard method, with the difference that time-dependent rather than time-independent basis functions are used, resulting in a more flexible basis such that fewer basis functions are needed.

A further development was the use of combined particles, where several modes were comprised into a multidimensional particle. Due to these developments and further tweaks, e.g. regarding the numerical integration, MCTDH is able to treat up to 100 DOF.

As an extension to MCTDH, the Gaussian-MCTDH (G-MCTDH) method combining the GWP approach of Heller with the multi-configurational setup of MCTDH was developed.[14] While it was first thought of as a way to split the system into *primary* and *secondary* modes (e.g., for system-bath type dynamics), where the secondary modes are combined into a multidimensional GWP to describe environmental near-harmonic modes, the G-MCTDH method in its general form replaces partially or completely the basis functions with GWPs in a sum of products like fashion.[15]

A special variant of the G-MCTDH approach is the variational multi-configuration Gaussian (vMCG) method. vMCG uses a multidimensional GWP where all DOFs are combined into a multidimensional GWP, and the wavefunction is constructed from superpositions of such multidimensional GWPs.[14] Although this method shows a very bad convergence behavior, convergence can only be achieved for very few DOFs. vMCG is especially useful in conjunction with on-the-fly electronic structure calculations, such that there is no necessity to pre-compute the PES.

In the following, some of these developments will be presented and explained in more detail, including the standard method, Time-Dependent Hartree, MCTDH and its Gaussian variants (G-MCTDH and vMCG). Atomic units are assumed throughout, such that $\hbar = 1$.

4.1 The Standard Method

The *standard* approach to solve the time-dependent Schrödinger equation (Eqn. 4.1) is to expand the wave function in a time-independent direct-product basis, whose coefficients are then propagated numerically. A p-dimensional wave function is then written as,

$$\Psi\left(x_1, \ldots, x_p, t\right) = \sum_{j_1}^{N_1} \cdots \sum_{j_p}^{N_p} A_{j_1,\ldots,j_p}(t) \prod_{\kappa=1}^{p} \chi_{j_\kappa}^{(\kappa)}(x_\kappa) \tag{4.2}$$

where A_{j_κ} are the time-dependent coefficients, $\chi_{j_\kappa}^{(\kappa)}$ are the time-independent basis functions and N_κ denotes the number of basis functions used for the kth degree of

freedom (DOF). The equations of motion (EOMs) are obtained by applying the Dirac-Frenkel variational principle:

$$\langle \delta\Psi | ih\frac{\partial}{\partial t} - \hat{H}|\Psi\rangle = 0 \tag{4.3}$$

This leads to the EOMs,

$$\begin{aligned} i\dot{A}_{j_1,\ldots,j_p} &= \sum_{l_1,\ldots,l_p} \langle \chi^{(1)}_{j_1} \cdots \chi^{(p)}_{j_p} | \hat{H} | \chi^{(1)}_{l_1} \cdots \chi^{(p)}_{l_p} \rangle \, A_{l_1,\ldots,l_p} \\ i\dot{\mathbf{A}} &= \mathbf{H}\mathbf{A} \end{aligned} \tag{4.4}$$

This set of coupled linear first-order differential equations can then be solved by using numerical integration techniques like split-propagator[71–73] or Lanczos[74] methods. The computational effort (typically measured by the number of floating point operations) for this method increases exponentially with the number of degrees of freedom p and is therefore proportional to fN^{p+1}. The effort for the time-independent Hamiltonian matrix can be neglected, since it is only needed to be calculated once. A further, even more striking, bottleneck is the memory requirement, which also increases exponentially with the number of DOFs proportional to fN^p. For example with $p = 6$ DOFs and $N = 20$ basis functions per DOF, one gets $64 \cdot 10^6$ functions in total and a coefficient vector requiring already 1 GB of memory. Since several of these coefficient vectors have to be stored during the integration, even on typical workstations not more than 6 DOF can be treated with this method.

4.2 Time-Dependent Hartree

To overcome the limitations of the standard method, approximate methods for solving the TDSE have been developed. One of the simplest approaches is the Time-Dependent Hartree (TDH) approach.[69,75] In this ansatz (Eqn. 4.5) the wave function is written as a product of one-dimensional functions $\left(\varphi_j\right)$, which are called single particle functions (SPFs), forming a Hartree product (c.f Hartree-Fock in section 3.1). To keep it short and simple the ansatz will be presented for only two dimensions, but the expansion to higher dimensions is straightforward,

$$\Psi\left(x_1, x_2, t\right) = a\left(t\right) \varphi_1\left(x_1, t\right) \varphi_2\left(x_2, t\right) \tag{4.5}$$

This ansatz is not unique, because the phase and normalization factors can be moved between the SPFs. Therefore the (redundant) coefficient $a\left(t\right)$ is introduced in order to be able to freely choose the phase of the SPFs. In differential form the introduced constraints are written as,

$$\langle\varphi_1|\dot{\varphi}_2\rangle = \langle\varphi_2|\dot{\varphi}_1\rangle = 0 \tag{4.6}$$

This ensures that the norm of the SPFs does not change and that they stay normalized during the whole propagation, if they have been normalized initially. By applying the DF-VP one can again derive the equations of motion. While the equation for the coefficients is very similar to the one for the standard method, one now gets an additional equation for the single particle functions,

$$i\dot{a} = Ha \tag{4.7}$$

$$i\dot{\varphi}_j = \left(H^{(j)} - H\right)\varphi_j \tag{4.8}$$

where the Hamiltonian is expressed as $H = \langle\varphi_1\varphi_2|\hat{H}|\varphi_1\varphi_2\rangle$ and the mean-field operator is written as $H^{(j)} = \langle\varphi_i|\hat{H}|\varphi_j\rangle$.
The computational effort for this is rather small and scales linearly. However, the performance of this method is often very poor due to the simplistic ansatz. Due to the use of only one configuration, it is not able to capture the correlations between coupled DOFs sufficiently.

4.3 Multi-Configuration Time-Dependent Hartree (MCTDH)

A natural improvement for TDH is to use multiple configurations rather than only one. An improved multi-configurational method as a tool for accurate quantum dynamics is the Multi-Configuration Time-Dependent Hartree (MCTDH)[25] method. As an ansatz for the wave function one uses a linear combination of Hartree products (sum over products ansatz) which is expanded in a direct product of f sets of orthonormal, time-dependent, basis functions φ_κ, the single particle functions:[25]

$$\Psi\left(\vec{X}_1, \vec{X}_2, \ldots, \vec{X}_f, t\right) = \sum_J A_J(t)\,\Phi_J\left(\vec{X}_1, \vec{X}_2, \ldots, \vec{X}_f, t\right) \tag{4.9}$$

$$= \sum_{j_1}^{n_1}\sum_{j_2}^{n_2}\cdots\sum_{j_f}^{n_f} A_{j_1,j_2,\ldots,j_f}(t)\prod_{\kappa=1}^{f}\varphi_{j_\kappa}^{(\kappa)}\left(\vec{X}_\kappa, t\right) \tag{4.10}$$

In Eqn. 4.9 a multi-index notation is used $\left(J = j_1, j_2, \ldots, j_f\right)$. Eqn. 4.10 is, at first sight, very similar to the ansatz of the standard method. However, there are two major differences. The orthonormal basis functions or SPFs $\varphi_{j_\kappa}^{(\kappa)}$, are now time-dependent. Hence, the basis is more flexible and fewer basis functions are needed in order to converge the calculations. As second difference, the coordinates $\vec{X}_\kappa$ are now combined/composite coordinates, where several degrees of freedom

are combined within a d-dimensional particle $\vec{X}_\kappa = \left(x_1^{(\kappa)}, x_2^{(\kappa)}, \ldots, x_d^{(\kappa)}\right)$. As a consequence, less particles (f) are needed and more degrees of freedom can be investigated. Typically MCTDH is feasible with up to 50-100 DOFs.

As for TDH, the representation of the wave function is not unique. Two different sets of SPFs (with different sets of coefficients) can span the same Hilbert subspace $\mathscr{H}^{(\kappa)}$ and one can freely alternate by linearly transforming between these two sets of $\mathscr{H}^{(\kappa)}$. As a consequence, the Dirac-Frenkel variational principle fixes only the time evolution of $\mathscr{H}^{(\kappa)}$, leaving some freedom to the time evolution of the SPFs $\varphi_{j_\kappa}^{(\kappa)}$, which can lead to singularities during the propagation.[25] Therefore, to ensure singularity-free propagation, the initial SPFs are chosen orthonormal (Eqn. 4.11) and their individual time-evolution is fixed such, that they stay orthonormal during the propagation at all times. This is achieved by a constraint operator $\hat{g}^{(\kappa)}$ (Eqn. 4.12),[25]

$$\langle \varphi_{j_\kappa}^{(\kappa)} | \varphi_{j'_\kappa}^{(\kappa)} \rangle = \delta_{j_\kappa j'_\kappa} \tag{4.11}$$

$$\langle \varphi_{j_\kappa}^{(\kappa)} | \dot{\varphi}_{j'_\kappa}^{(\kappa)} \rangle = -i \, \langle \varphi_{j_\kappa}^{(\kappa)} | \hat{g}^{(\kappa)} | \dot{\varphi}_{j'_\kappa}^{(\kappa)} \rangle \tag{4.12}$$

This constraint operator is a hermitian but otherwise arbitrary operator which acts exclusively on the κth mode. Complementary to the single-particle functions, one can define so called single hole functions (SHF) $\psi_{l_\kappa}^{(\kappa)}$. They arise when expanding the total wave function in the SPFs of a single mode κ,

$$\Psi = \sum_{l_\kappa=1}^{n_\kappa} \psi_{l_\kappa}^{(\kappa)} \cdot \varphi_{l_\kappa}^{(\kappa)} \tag{4.13}$$

$$\psi_{l_\kappa}^{(\kappa)} = \sum_{j_1}^{n_1} \cdots \sum_{j_{\kappa-1}}^{n_{\kappa-1}} \sum_{j_{\kappa+1}}^{n_{\kappa+1}} \cdots \sum_{j_f}^{n_f} A_{j_1,\ldots,j_{\kappa-1},l_\kappa,j_{\kappa+1},\ldots,j_f}(t) \prod_{\kappa' \neq \kappa,}^{f} \varphi_{j'_\kappa}^{(\kappa')} \tag{4.14}$$

As for the ansatz, one can define a reduced multi-index for the SHF, where the κth index is missing $J_{(\kappa)} = j_1, \ldots, j_{\kappa-1}, j_{\kappa+1}, \ldots, j_f$, or where the κth index is replaced by index l_κ, $J_{(\kappa:l_\kappa)} = j_1, \ldots, j_{\kappa-1}, l_\kappa, j_{\kappa+1}, \ldots, j_f$. The SHF can then be written in a shorter notation:

$$\psi_{l_\kappa}^{(\kappa)} = \sum_{J_{(\kappa)}} A_{J_{(\kappa:l_\kappa)}} \prod_{\kappa' \neq \kappa}^{f} \varphi_{j_{\kappa'}}^{(\kappa')} \tag{4.15}$$

With the single hole functions one is able to define so called mean-field Hamiltonian operators,

$$\hat{H}_{jl}^{(\kappa)} = \langle \psi_{j_\kappa}^{(\kappa)} | \hat{H} | \psi_{l_\kappa}^{(\kappa)} \rangle \tag{4.16}$$

and density matrices,

$$\rho_{jl}^{(\kappa)} = \langle \psi_{j_\kappa}^{(\kappa)} | \psi_{l_\kappa}^{(\kappa)} \rangle \tag{4.17}$$

4.3.1 Equations of Motion

The equations of motion for the ansatz (Eqn. 4.9) can be derived, again, by applying the Dirac-Frenkel variational principle (Eqn. 4.3).[25] The variation of the wave function $\delta\Psi$ is expressed as,

$$\delta\Psi = \sum_J \delta A_J \Phi_J + \sum_J A_J \delta\Phi_J \tag{4.18}$$

The variation of the configurations $\delta\Phi_J$ is expanded in a sum of products where one SPF is varied at a time, with the A_J and the remaining SHFs being untouched,

$$\sum_J A_J \delta\Phi_J = \sum_\kappa \left\{ \sum_{j_1} \cdots \sum_{j_\kappa} \cdots \sum_{j_f} \left(A_{J_{(\kappa:j_\kappa)}} \delta\varphi_{j_\kappa}^{(\kappa)} \prod_{\kappa' \neq \kappa} \varphi_{j_{\kappa'}}^{(\kappa')} \right) \right\} \tag{4.19}$$

$$= \sum_{\kappa=1}^{f} \sum_{j_\kappa=1}^{n_\kappa} \delta\varphi_{j_\kappa}^{(\kappa)} \psi_{j_\kappa}^{(\kappa)} \tag{4.20}$$

Inserting this in the variational principle yields:

$$\sum_J \left[\delta A_J \langle \Phi_J | i\frac{\partial}{\partial t} - \hat{H} | \Psi \rangle \right] + \sum_{\kappa=1}^{f} \sum_{j_\kappa=1}^{n_\kappa} \left[\langle \delta\varphi_{j_\kappa}^{(\kappa)} \psi_{j_\kappa}^{(\kappa)} | i\frac{\partial}{\partial t} - \hat{H} | \Psi \rangle \right] = 0 \tag{4.21}$$

In order to solve this equation both terms have to be equal to zero. Since the A coefficients and the SPFs can be varied independently, one can treat these terms separately,[25]

$$\delta A_J \left\langle \Phi_J \middle| i\frac{\partial}{\partial t} - \hat{H} \middle| \Psi \right\rangle = 0 \quad \forall J \tag{4.22}$$

$$\left\langle \delta\varphi_{j_\kappa}^{(\kappa)} \psi_{j_\kappa}^{(\kappa)} \middle| i\frac{\partial}{\partial t} - \hat{H} \middle| \Psi \right\rangle = 0 \quad \forall j, \kappa \tag{4.23}$$

Additionally, the expression for the time derivative of the total wave function Ψ is needed:

$$\frac{\partial\Psi}{\partial t} = \sum_J \frac{dA_J}{dt} + \sum_J A_J \frac{\partial\Phi_J}{\partial t}$$

$$= \sum_J \frac{dA_J}{dt} + \sum_\kappa \sum_{j_\kappa} \frac{\partial\varphi_{j_\kappa}^{(\kappa)}}{\partial t} \psi_{j_\kappa}^{(\kappa)} \tag{4.24}$$

4.3.1.1 Variation of the Coefficients

First, the time derivative of the coefficients $\frac{\partial A}{\partial t}$ is determined with Eqn. 4.22. Since the variation of the coefficients δA_J is arbitrary, the bracket has to become zero and one does not need to consider δA_J. Inserting the derivative of the wave function (Eqn. 4.24) in the remainder gives:

$$\begin{aligned} 0 =& i\left(\sum_L \frac{dA_L}{dt}\langle\Phi_J\,|\,\Phi_L\rangle + \sum_\kappa \sum_{l_\kappa}\left\langle\Phi_J\left|\frac{\partial\varphi_{l_\kappa}^{(\kappa)}}{\partial t}\right.\right\rangle + \left\langle\Phi_J\left|\hat{H}\sum_L A_L\Phi_L\right.\right\rangle\right) \\ 0 =& i\frac{dA_J}{dt} + \sum_L\left\{A_L\left\langle\Phi_J\left|\sum_\kappa \hat{g}^{(\kappa)}\Phi_L\right.\right\rangle - A_L\left\langle\Phi_J\left|\hat{H}\right|\Phi_L\right\rangle\right\}\forall J \\ i\frac{dA_J}{dt} =& \sum_L\left\langle\Phi_J\left|\hat{H}-\hat{g}^{(\kappa)}\right|\Phi_L\right\rangle \end{aligned} \tag{4.25}$$

Here, the orthonormality of the SPFs and the relation from Eqn. 4.12 have been used.[25]

4.3.1.2 Variation of the Single Particle Functions

Second, the time derivatives of the SPFs are derived by beginning with Eqn. 4.23. Inserting Eqn. 4.24 yields:

$$\begin{aligned} i\Bigg\{&\sum_L\left\langle\delta\varphi_{j_\kappa}^{(\kappa)}\psi_{j_\kappa}^{(\kappa)}\left|\frac{dA_L}{dt}\Phi_L\right.\right\rangle + \sum_{\kappa'}\sum_{l_{\kappa'}}\left\langle\delta\varphi_{j_\kappa}^{(\kappa)}\psi_{j_\kappa}^{(\kappa)}\left|\frac{\partial\varphi_{j_\kappa}^{(\kappa)}}{\partial t}\psi_{l_\kappa}^{(\kappa)}\right.\right\rangle - \\ &-\left\langle\delta\varphi_{j_\kappa}^{(\kappa)}\psi_{j_\kappa}^{(\kappa)}\left|\hat{H}\right|\Psi\right\rangle\Bigg\} = 0 \qquad \forall j,\kappa \end{aligned} \tag{4.26}$$

From this equation one can obtain the EOMs on two different paths. The more traditional way is to substitute the result for $\frac{dA_J}{dt}$ (Eqn. 4.25). The second, alternative way, is more elegant though and preferable. Here, the variation of the SPFs is split into two parts with the help of a new orthogonal projector $\hat{P}^{(\kappa)}$ acting on the space spanned in the κth DOF by the SPFs,

$$\hat{P}^{(\kappa)} = \sum_{j_\kappa}^{n_\kappa}\left|\varphi_{j_\kappa}^{(\kappa)}\right\rangle\left\langle\varphi_{j_\kappa}^{(\kappa)}\right| \tag{4.27}$$

$\delta\varphi_{j_\kappa}^{(\kappa)}$ can now be split into two parts,[25]

$$\delta\varphi_{j_\kappa}^{(\kappa)} = \hat{P}^{(\kappa)}\delta\varphi_{j_\kappa}^{(\kappa)} + \left(\hat{1}-\hat{P}^{(\kappa)}\right)\delta\varphi_{j_\kappa}^{(\kappa)} \tag{4.28}$$

where $\left(\hat{1}-\hat{P}^{(\kappa)}\right)$ projects onto the space orthogonal to the space spanned by the SPFs for the κth DOF. In Eqn. 4.28 the variation is therefore split, where one

part is in the space of the original SPFs (A) and the other part is in the space orthogonal to that (B). Accordingly, Eqn. 4.23 can be rewritten,

$$\underbrace{\left\langle \hat{P}^{(\kappa)}\delta\varphi_{j_\kappa}^{(\kappa)}\psi_{j_\kappa}^{(\kappa)} \middle| i\frac{\partial}{\partial t}-\hat{H}\middle|\Psi\right\rangle}_{\text{(A)}}+\underbrace{\left\langle \left(\hat{1}-\hat{P}^{(\kappa)}\right)\delta\varphi_{j_\kappa}^{(\kappa)}\psi_{j_\kappa}^{(\kappa)} \middle| i\frac{\partial}{\partial t}-\hat{H}\middle|\Psi\right\rangle}_{\text{(B)}}=0 \quad (4.29)$$

The projector acting on $\delta\varphi_{j_\kappa}^{(\kappa)}$ can be expanded in a linear combination of SPFs, as the projector $\hat{P}^{(\kappa)}$ projects any vector into the space spanned by the SPF of the κth degree of freedom,

$$\hat{P}^{(\kappa)}\delta\varphi_{j_\kappa}^{(\kappa)}=\sum_{l_\kappa} cl_\kappa\varphi_{l_\kappa}^{(\kappa)} \quad (4.30)$$

Introducing this in (A) one gets,

$$\begin{aligned}\text{(A)} &= \sum_{l_\kappa}\bar{c}_{l_\kappa}\left\langle \varphi_{l_\kappa}^{(\kappa)}\psi_{l_\kappa}^{(\kappa)}\middle| i\frac{\partial}{\partial t}-\hat{H}\middle|\Psi\right\rangle \\ &= \sum_{l_\kappa}\bar{c}_{l_\kappa}\sum_{J_{(\kappa)}} A_{J_{(\kappa:l_\kappa)}}\left\langle \Phi_{J_{(\kappa:l_\kappa)}}\middle| i\frac{\partial}{\partial t}-\hat{H}\middle|\Psi\right\rangle \end{aligned} \quad (4.31)$$

where the solution for the bracket term is already given by Eqn. 4.22, stating that for any configuration this bracket is equal to zero and thus also (A) is equal to zero. With (A) being eliminated one only needs to consider part (B). Rewriting (B) by using the fact that $\left(\hat{1}-\hat{P}^{(\kappa)}\right)$ is hermitian and inserting the time derivative of the total wave function (Eqn. 4.24) one gets,

$$\begin{aligned}0 =& i\sum_J \frac{dA_J}{dt}\left\langle \delta\varphi_{j_\kappa}^{(\kappa)}\psi_{j_\kappa}^{(\kappa)}\middle|\left(\hat{1}-\hat{P}^{(\kappa)}\right)\Phi_J\right\rangle \\ &+\sum_{\kappa'}\sum_{l_\kappa} i\left\langle \delta\varphi_{j_\kappa}^{(\kappa)}\psi_{j_\kappa}^{(\kappa)}\middle|\left(\hat{1}-\hat{P}^{(\kappa)}\right)\frac{\partial\varphi^{(\kappa')}}{\partial t}\psi_{l_{\kappa'}}^{(\kappa')}\right\rangle \\ &-\left\langle \delta\varphi_{j_\kappa}^{(\kappa)}\psi_{j_\kappa}^{(\kappa)}\middle|\left(\hat{1}-\hat{P}^{(\kappa)}\right)\hat{H}\middle|\Psi\right\rangle \end{aligned} \quad (4.32)$$

This equation can be reduced by the fact that the projection $\left(\hat{1}-\hat{P}^{(\kappa)}\right)$ of a SPF $\varphi_{j_\kappa}^{(\kappa)}$ on the orthogonal complement of the span $\left\{\varphi_{j_\kappa}^{(\kappa)}\right\}$ is always zero,[25]

$$\left(\hat{1}-\hat{P}^{(\kappa)}\right)\left|\varphi_{j_\kappa}^{(\kappa)}\right\rangle=0 \quad (4.33)$$

therefore the first term vanishes. Further, in the second term, the operator $\hat{P}^{(\kappa)}$ acts only on the κth DOF, hence the sum reduces to one term. By substituting $\Psi=\sum_{l_\kappa}\psi_{l_\kappa}^{(\kappa)}\varphi_{l_\kappa}^{(\kappa)}$ the above equation reduces to,

$$
\begin{aligned}
0 =& \sum_{l_\kappa} i \left\langle \delta\varphi_{j_\kappa}^{(\kappa)} \middle| \left(\hat{1} - \hat{P}^{(\kappa)}\right) \frac{\partial \varphi_{l_\kappa}^{(\kappa)}}{\partial t} \right\rangle \left\langle \varphi_{j_\kappa}^{(\kappa)} \middle| \varphi_{l_\kappa}^{(\kappa)} \right\rangle \\
& - \sum_{l_\kappa} \left\langle \delta\varphi_{j_\kappa}^{(\kappa)} \psi_{j_\kappa}^{(\kappa)} \middle| \left(\hat{1} - \hat{P}^{(\kappa)}\right) \hat{H} \middle| \psi_{l_\kappa}^{(\kappa)} \varphi_{l_\kappa}^{(\kappa)} \right\rangle \\
=& \sum_{l_\kappa} i \left\langle \delta\varphi_{j_\kappa}^{(\kappa)} \middle| \left(\hat{1} - \hat{P}^{(\kappa)}\right) \frac{\partial \varphi_{l_\kappa}^{(\kappa)}}{\partial t} \right\rangle \rho_{l_\kappa}^{(\kappa)} \\
& - \sum_{l_\kappa} \left\langle \delta\varphi_{j_\kappa}^{(\kappa)} \middle| \left(\hat{1} - \hat{P}^{(\kappa)}\right) \hat{H}_{jl}^{(\kappa)} \varphi_{l_\kappa}^{(\kappa)} \right\rangle \\
=& \left\langle \delta\varphi_{j_\kappa}^{(\kappa)} \middle| \sum_{l_\kappa} \left(\hat{1} - \hat{P}^{(\kappa)}\right) \left(\rho_{l_\kappa}^{(\kappa)} \frac{\partial \varphi_{l_\kappa}^{(\kappa)}}{\partial t} - \hat{H}_{jl}^{(\kappa)} \varphi_{l_\kappa}^{(\kappa)} \right) \right\rangle
\end{aligned} \tag{4.34}
$$

where we have used the above introduced definitions for the density matrix and the mean-field Hamiltonian. Furthermore, the variation $\delta\varphi_{j_\kappa}^{(\kappa)}$ is arbitrary in this scalar product, hence, the sum on the right in the above equation has to be zero, in order for the scalar product to be equal to zero,

$$
0 = \sum_{l_\kappa} \left(\hat{1} - \hat{P}^{(\kappa)}\right) \left(\rho_{l_\kappa}^{(\kappa)} \frac{\partial \varphi_{l_\kappa}^{(\kappa)}}{\partial t} - \hat{H}_{jl}^{(\kappa)} \varphi_{l_\kappa}^{(\kappa)} \right) \tag{4.35}
$$

Using again the constraint operator $\hat{g}^{(\kappa)}$,

$$
i\hat{P}^{(\kappa)} \frac{\varphi_{l_\kappa}^{(\kappa)}}{\partial t} = \hat{P}^{(\kappa)} \left| \hat{g}^{(\kappa)} \varphi_{l_\kappa}^{(\kappa)} \right\rangle \tag{4.36}
$$

and after rearranging the equation to have $\frac{\partial \varphi_{l_\kappa}^{(\kappa)}}{\partial t}$ alone on one side, one ends up with,[25]

$$
i\frac{\partial \varphi_{l_\kappa}^{(\kappa)}}{\partial t} = \sum_{l_\kappa} \left[\hat{g}^{(\kappa)} + \left(\rho_{l_\kappa}^{(\kappa)}\right)^{-1} \left(\hat{1} - \hat{P}^{(\kappa)}\right) \left(H_{jl}^{(\kappa)} - \hat{g}^{(\kappa)} \right) \right] \varphi_{l_\kappa}^{(\kappa)} \tag{4.37}
$$

Where the expression $\hat{P}^{(\kappa)} = \hat{1} - \left(\hat{1} - \hat{P}^{(\kappa)}\right)$ has been used to simplify the equation.

4.3.2 Choice of Constraints

The MCTDH EOMs have been derived without an explicit definition of the constraint operator $\hat{g}^{(\kappa)}$. Since this operator is arbitrary and does not affect the quality of the MCTDH wave function, one typically chooses $\hat{g}^{(\kappa)} = 0$ for all modes κ.[25] Rewriting Eqns. 4.25 and 4.37 using matrix notation and using the shorthand notation for the time derivatives $\left(\frac{dA_J}{dt} = \dot{A}_J, \frac{\partial \varphi_{l_\kappa}^{(\kappa)}}{\partial t} = \dot{\varphi}_{l_\kappa}^{(\kappa)} \right)$ and the Hamiltonian matrix $\underline{H} = \langle \Phi_J | \hat{H} | \Phi_L \rangle$, the equations of motion simplify to,

$$i\dot{\vec{A}} = \underline{H}\vec{A} \tag{4.38}$$

$$i\dot{\vec{\varphi}} = \left[\left(\underline{\rho}^{(\kappa)}\right)^{-1}\left(\hat{1} - \hat{P}^{(\kappa)}\right)\underline{H}^{(\kappa)}\right]\vec{\varphi}^{(\kappa)}. \tag{4.39}$$

With these one obtains unambiguous equations of motion for the coefficients and the SPFs, where the latter are coupled by mean-fields, meaning that every SPF evolves under an effective Hamiltonian, averaged over all remaining modes ($\kappa \neq \kappa'$).

4.3.3 Representation of the Single Particle Functions

Having derived the working equations for MCTDH, still nothing has been said about how the basis functions $\varphi_{j_\kappa}^{(\kappa)}$ are represented. In order to implement these equations (Eqns. 4.38 and 4.39), the single particle functions have to be represented by a finite set of basis functions. This is done by expanding the SPFs in a set of primitive, time-independent basis functions.[25] There exist several approaches to do this which have been successfully used. For example, when treating polar angles, spherical harmonic functions $Y_{lm}(\theta, \varphi)$ can be used.[76] Furthermore, one can employ a collocation scheme of the fast Fourier transform (FFT) or the mostly used discrete variable representation (DVR). The DVR can simplistically be understood as basis functions sitting locally on grid points. This is done by using a primitive basis in orthogonal polynomials and diagonalizing the position operator $\hat{q}$ in this basis. Then, a set of DVR basis functions and grid points are obtained, which can be used in the propagation.

4.3.4 Representation of the Hamiltonian

An efficient way in representing the Hamiltonian for the MCTDH method is to use a sum of products of single particle operators $\hat{h}_r^{(\kappa)}$,

$$\hat{H} = \sum_{r=1}^{m} c_r \prod_{\kappa=1}^{f} \hat{h}_r^{(\kappa)} \tag{4.40}$$

where c_r are the expansion coefficients.[25] With this one can rewrite the Hamiltonian and mean-field elements:

$$\left\langle \Phi_j \left| \hat{H} \right| \Phi_L \right\rangle = \sum_{r=1}^{m} c_r \prod_{\kappa=1}^{f} \left\langle \varphi_{j_\kappa}^{(\kappa)} \left| \hat{h}_r^{(\kappa)} \right| \varphi_{l_\kappa}^{(\kappa)} \right\rangle \tag{4.41}$$

$$\begin{aligned} H_{jl}^{(\kappa)} =& \sum_{r=1}^{m} \mathcal{H}_{r,jl}^{(\kappa)} \hat{h}_r^{(\kappa)} \\ \mathcal{H}_{r,jl}^{(\kappa)} =& c_r \sum_{J_{(\kappa)}} \bar{A}_{J_{(\kappa)}} \sum_{l_1} \left\langle \varphi_{j_1}^{(1)} \left| \hat{h}_r^{(1)} \right| \varphi_{l_1}^{(1)} \right\rangle \dots \\ & \dots \left\langle \varphi_{j_{\kappa-1}}^{(\kappa-1)} \left| \hat{h}_r^{(\kappa-1)} \right| \varphi_{l_{\kappa-1}}^{(\kappa-1)} \right\rangle \left\langle \varphi_{j_{\kappa+1}}^{(\kappa+1)} \left| \hat{h}_r^{(\kappa+1)} \right| \varphi_{l_{\kappa+1}}^{(\kappa+1)} \right\rangle \dots \\ & \dots \left\langle \varphi_{j_f}^{(f)} \left| \hat{h}_r^{(f)} \right| \varphi_{l_f}^{(f)} \right\rangle A_{L_{(\kappa)}} \end{aligned} \tag{4.42}$$

4.3.5 Scaling Properties

Based on these findings one can deduce the scaling behavior of this method. Due to the use of the efficient sum of products representation of the Hamiltonian, the effort for calculating the action of the single particle operators $\hat{h}_r^{(\kappa)}$ on the SPFs grows linearly with the number of DOFs and is proportional to $mfnN^2$. For small values of n and f this is the dominant contribution. When going to larger systems (i.e. larger n and f) the dominant contribution, however, becomes the calculation of the mean-field matrices. Their effort depends exponentially on the number of modes f and is proportional to sf^2n^{f+1}.[25] The total numerical effort is therefore,

$$\text{effort}^{MCTDH} \approx mfnN^2 + mf^2n^{f+1} \tag{4.43}$$

In comparison to the effort of the standard method the major gains in computational cost stem from the reduction of the number of configurations (c.f. n vs. N). Also important to mention are the reduced memory requirements due to this reduction.

4.3.6 Multi-Layer-MCTDH

An extension to the conventional MCTDH method has been introduced by the multi-layer-MCTDH (ML-MCTDH) method.[26,27,77,78] The ML-MCTDH wavefunction ansatz is given by a hierarchical representation. The ansatz for the ML-MCTDH wavefunction is, in principle, identical to that from MCTDH (Eqn. 4.10. The difference to the conventional MCTDH scheme is the representation of the single particle functions. The SPFs are expanded in a MCTDH-like tensor form, but in a smaller subspace with less degrees of freedom. This procedure can be repeated $(M-1)$ times such that a M-layer representation of the wavefunction is obtained. The last layer of the ML-MCTDH scheme is then similar to the con-

ventional MCTDH representation, where the SPFs are expanded in terms of the underlying primitive basis, but in a low-dimensional subspace.

The ML-MCTDH approach can reduce the memory requirements and computation time drastically by choosing an appropriate mode distribution and mode combination in the various subspaces. With the ML-MCTDH method more than 1000 DOFs are accessible and can be propagated.

4.4 Gaussian-MCTDH

To first order, a Gaussian function is a good approximation for the description of wave packet dynamics. As long as the potential is nearly harmonic and the wave packet is not too broad and stays of Gaussian form throughout the propagation (e.g. the coherent state[57,79]), the potential can be sufficiently well described by a Taylor expansion up to second order. Heller and Lee showed in a solution to the TDSE that the GWP centre coordinate and momentum (q, p) follow classical trajectories.[57,80] An extension to the Heller wave function is the use of a multi-configurational approach as in the already introduced MCTDH scheme.

In the Gaussian-MCTDH (G-MCTDH) approach some or all single particle functions $\varphi_{j_\kappa}^{(\kappa)}$ (c.f. Eqn. 4.10) are replaced by parametrized Gaussian functions $G_{j_\kappa}^{(\kappa)}$, so called Gaussian wavepackets (GWPs).[14,15,81] Here, the GWPs do not follow classical trajectories, but the time-derivatives of their parameters are obtained variationally. Compared to the traditional, fully flexible SPFs, the GWPs are less flexible, but are advantageous in an efficient treatment of a large number of modes, due to the analytical calculation of high-dimensional integrals (Gaussian moments), which is much more efficient compared to the numerical integration over large, high-dimensional DVR grids in MCTDH. Additionally, in contrast to the time-independent primitive grid representation, a GWP represents a localized basis moving in phase space. An obvious disadvantage is the non-orthogonality of the GWPs.

4.4.1 Ansatz

The wave function ansatz of the G-MCTDH method in its hybrid form[14,15] is given by

$$\Psi\left(\vec{X},t\right) = \sum_{J} A_J\left(t\right)\Phi_J\left(\vec{X},t\right) \tag{4.44}$$

$$= \sum_{j_1}^{n_1}\sum_{j_2}^{n_2}\cdots\sum_{j_f}^{n_f} A_{j_1,j_2,\ldots,j_f}\left(t\right)\left(\prod_{\kappa=1}^{p}\varphi_{j_\kappa}^{(\kappa)}\left(\vec{X}_\kappa,t\right)\right)\left(\prod_{\kappa=p+1}^{f} g_{j_\kappa}^{(\kappa)}\left(\vec{X}_\kappa,t\right)\right) \tag{4.45}$$

with $\varphi_{j_\kappa}^{(\kappa)}$ as in standard MCTDH and the multidimensional GWPs $g_{j_\kappa}^{(\kappa)}$ taking the form,

$$g_{j_\kappa}^{(\kappa)}\left(\vec{X}_\kappa,t\right) = g_{j_\kappa}^{(\kappa)}\left(\vec{\Lambda}_{j_\kappa}^{(\kappa)}\left(t\right),\vec{X}_\kappa\right)$$

$$= \exp\left[\vec{X}_\kappa^{T}\underline{a}_{j_\kappa}^{(\kappa)}\left(t\right)\vec{X}_\kappa + \left(\vec{\xi}_{j_\kappa}^{(\kappa)}\left(t\right)\right)^{T}\vec{X}_\kappa + \eta_{j_\kappa}^{(\kappa)}\left(t\right)\right] \tag{4.46}$$

The time evolution of the GWP is determined by complex, time-dependent parameters $\vec{\Lambda}_{j_\kappa}^{(\kappa)} = \left(\underline{a}_{j_\kappa}^{(\kappa)},\vec{\xi}_{j_\kappa}^{(\kappa)},\eta_{j_\kappa}^{(\kappa)}\right)$. Here, the complex, symmetric matrix $\underline{a}_{j_\kappa}^{(\kappa)}$ controls the width of $g_{j_\kappa}^{(\kappa)}$. The off-diagonal terms of $\underline{a}_{j_\kappa}^{(\kappa)}$ characterize the coupling between the degrees of freedom within a combined mode GWP. The next parameter $\vec{\xi}_{j_\kappa}^{(\kappa)}$ represents the center of the GWP in phase space with the relation $\vec{\xi}_{j_\kappa}^{(\kappa)} = -2\underline{a}_{j_\kappa}^{(\kappa)}\vec{q}_{j_\kappa}^{\kappa} + i\vec{p}_{j_\kappa}^{\kappa}$ and real parameters $\vec{q}_{j_\kappa}^{\kappa}$ and $\vec{p}_{j_\kappa}^{\kappa}$. $\vec{q}_{j_\kappa}^{\kappa}$ stands for the GWPs center in position space, whereas $\vec{q}_{j_\kappa}^{\kappa}$ represents the center in momentum space. The last parameter $\eta_{j_\kappa}^{(\kappa)}$ defines the norm and the phase of the GWP. With these parameters it is possible to transform the GWP into the typical Heller form.[57] Typically, the real part of $\eta_{j_\kappa}^{(\kappa)}$ is used to fix the norm of the GWP to $\left\|g_{j_\kappa}^{(\kappa)}\right\| = 1$ (which is possible since the complex phase parameter is ill determined from the variational equations). The imaginary part is set to zero or evolves with the classical action. This reduces the parameters which have to be determined variationally to $\vec{\Lambda}_{j_\kappa}^{(\kappa)} = \left(\underline{a}_{j_\kappa}^{(\kappa)},\vec{\xi}_{j_\kappa}^{(\kappa)}\right)$.

In practice, two variants are used: *thawed* Gaussians (TG) and *frozen* Gaussians (FG). For the TGs all above mentioned parameters are propagated while for the FGs the width is fixed. In the latter case, the width matrix can be chosen to be diagonal (resulting in a product of 1-dimensional GWPs) and therefore the GWP $g_{j_\kappa}^{(\kappa)}$ can be rewritten (Eqn. 4.47) with the parameters which are time-dependent being further reduced to $\vec{\Lambda}_{j_\kappa}^{(\kappa)} = \left(\vec{\xi}_{j_\kappa}^{(\kappa)}\right)$,

$$g_{j_\kappa}^{(\kappa)}\left(\vec{X}_\kappa,t\right)=\prod_{d}^{d_\kappa}N\left(\left(\underline{a}_{j_\kappa}^{(\kappa)}\right)_{dd},\left(\vec{\xi}_{j_\kappa}^{(\kappa)}\right)_d\right)\times\exp\left[\left(\underline{a}_{j_\kappa}^{(\kappa)}\right)_{dd}x_{\kappa,d}^2+\left(\vec{\xi}_{j_\kappa}^{(\kappa)}(t)\right)_d x_{\kappa,d}\right] \tag{4.47}$$

where $N(a,\xi)=\left(-2\mathrm{Re}(a)/\pi\right)^{1/4}\exp\left(\left(\mathrm{Re}(\xi)\right)^2/4\mathrm{Re}(a)\right)$ is the normalization factor and $x_{\kappa,d}=\left(\vec{x_\kappa}\right)_d$ is a shorthand notation. Eqn. 4.47 states that each FG corresponds to a product of one-dimensional FGs.

4.4.2 Equations of Motion

The equations of motion can again be derived by applying the Dirac-Frenkel variational principle. Here, only the final equations for the GWP-only case ($p=0$) will be presented. For details see Ref. [14, 15] or chapter 6 (c.f. 2-Layer-G-MCTDH EOMs).

In the GWP-only case the wave function Ψ is given by,

$$\Psi\left(\vec{X},t\right)=\sum_{j_1}^{n_1}\sum_{j_2}^{n_2}\cdots\sum_{j_f}^{n_f}A_{j_1,j_2,\ldots,j_f}(t)\prod_{\kappa=1}^{f}g_{j_\kappa}^{(\kappa)}\left(\vec{X}_\kappa,t\right) \tag{4.48}$$

With the single hole functions given as,

$$\psi_{j_\kappa}^{(\kappa)}=\sum_{J^{(\kappa)}}A_{J^{(\kappa:j_\kappa)}}G_{J^{(\kappa)}} \tag{4.49}$$

where $G_{J^{(\kappa)}}=\prod_{\kappa'\neq\kappa}g_{j_{\kappa'}}^{(\kappa')}$. The mean field operators are defined as,

$$\hat{H}_{jj'}^{(\kappa)}=\left\langle\psi_{j_\kappa}^{(\kappa)}\middle|\hat{H}\middle|\psi_{j'_\kappa}^{(\kappa)}\right\rangle \tag{4.50}$$

The EOMs for the coefficients $\vec{A}$ and the GWP parameters $\vec{\Lambda}$ can be obtained by applying the DF-VP and are given as,

$$i\underline{S}\dot{\vec{A}}=\left(\underline{H}^{(G)}-i\vec{\tau}\right)\vec{A} \tag{4.51}$$

$$i\underline{C}^{(\kappa)}\dot{\vec{\Lambda}}^{(\kappa)}=\vec{Y}^{(\kappa)} \tag{4.52}$$

Here, the shorthand notations for the overlap matrix $S_{JJ'}=\langle G_J\,|\,G_{J'}\rangle$, the differential overlap $\tau_{JJ'}=\left\langle G_J\middle|\frac{\partial}{\partial t}G_{J'}\right\rangle$ and the Hamiltonian matrix $H_{JJ'}^{(G)}=\left\langle G_J\middle|\hat{H}\middle|G_{J'}\right\rangle$ are used. Both, the matrices $\underline{S}$ and $\underline{\tau}$ are defined in a direct product space, e.g. $\underline{S}=\underline{S}^{(1)}\otimes\cdots\otimes\underline{S}^{(f)}$. Due to the differential overlap matrix $\underline{\tau}$, which is a function of the time-dependent GWP parameters, a dynamical correlation between the coefficients $\vec{A}$ and the GWP parameters $\vec{\Lambda}$ arises. This allows to set the phase of the

GWPs to zero as mentioned above. The matrix $\underline{C}^{(\kappa)}$ and the vector $\vec{Y}^{(\kappa)}$, which define the evolution of the GWPs, are given as,

$$C^{(\kappa)}_{j_\kappa\alpha,j'_\kappa\beta} = \left\langle \frac{\partial}{\partial\Lambda^{(\kappa)}_{j\alpha}} g^{(\kappa)}_{j_\kappa} \middle| \left(\hat{1} - \hat{P}^{(\kappa)}\right) \frac{\partial}{\partial\Lambda^{(\kappa)}_{j'\beta}} g^{(\kappa)}_{j'_\kappa} \right\rangle \tag{4.53}$$

$$Y^{(\kappa)}_{j\alpha} = \sum_{j'} \left\langle \frac{\partial}{\partial\Lambda^{(\kappa)}_{j\alpha}} g^{(\kappa)}_{j_\kappa} \middle| \left(\hat{1} - \hat{P}^{(\kappa)}\right) \hat{H}^{(\kappa)}_{jj'} g^{(\kappa)}_{j'_\kappa} \right\rangle \tag{4.54}$$

Since the GWPs form a non-orthogonal basis the definition for the projector is not identical to the conventional MCTDH propagator (c.f. Eqn.4.27) and therefore, is given by,

$$\hat{P}^{(\kappa)} = \sum_{jj'} \left| g^{(\kappa)}_{j_\kappa} \right\rangle \left(\left(\underline{S}^{(\kappa)} \right)^{-1} \right)_{jj'} \left\langle g^{(\kappa)}_{j'_\kappa} \right| \tag{4.55}$$

with the inverse of the overlap matrix between the GWPs $S^{(\kappa)}_{jj'} = \left\langle g^{(\kappa)}_{j_\kappa} \middle| g^{(\kappa)}_{j'_\kappa} \right\rangle$.

The dynamics of the GWP parameters can be seen as pseudo-classical, which for a single Gaussian function reduces to Hamilton's classical equations for the center, momentum and width of a GWP as derived by Heller.[57] This connection follows from the analogy of the quantum Lagrangian $L = \langle H \rangle - i \left\langle \Psi \middle| \frac{\partial\Psi}{\partial\lambda_\alpha} \right\rangle \dot{\lambda}_\alpha$ and the classical Lagrangian $L = H - p\dot{q}$.[13,67,82,83] When two or more Gaussian functions are used, a non-classical coupling occurs from the off-diagonal elements in the $\underline{C}$ matrix.

4.4.3 Special Case: vMCG

A special case of the G-MCTDH method is given by the variational multi-configuration Gaussian (vMCG) method. Here, all degrees of freedom are chosen to be combined in a multidimensional GWP G_j. Then, Eqn. 4.48 reduces to a sum over multidimensional GWPs,

$$\Psi\left(\vec{X}, t\right) = \sum_{j}^{n} A_j\left(t\right) G_j\left(\vec{X}, t\right) \tag{4.56}$$

By combining all degrees of freedom into one particle/GWP the equations of motion for the GWP parameters $\vec{\Lambda}$ simplify in the sense that the mean field matrices reduce to the density matrix. While the working equations for the coefficients essentially do not change, the equations for the parameters now read,

$$C_{i\alpha,j\beta} = \rho_{ij}\left(S_{ij}^{(\alpha\beta)} - \left[\underline{S}^{(\alpha 0)}\left(\underline{S}\right)^{-1}\underline{S}^{(0\beta)}\right]_{ij}\right) \tag{4.57}$$

$$Y_{i\alpha} = \sum_{l}\rho_{il}\left(H_{ij}^{(\alpha 0)} - \left[\underline{S}^{(\alpha 0)}\left(\underline{S}\right)^{-1}\underline{H}\right]_{ij}\right) \tag{4.58}$$

with the density matrix $\rho_{ij} = \bar{A}_i A_j$ and α and β referring to the derivatives of the Gaussian functions with respect to the parameters of the GWPs,

$$S_{ij}^{(\alpha\beta)} = \left\langle \frac{\partial g_i}{\partial \lambda_{i\alpha}} \middle| \frac{\partial g_j}{\partial \lambda_{j\beta}} \right\rangle \tag{4.59}$$

$$H_{ij}^{(\alpha\beta)} = \left\langle \frac{\partial g_i}{\partial \lambda_{i\alpha}} \middle| \hat{H} \middle| \frac{\partial g_j}{\partial \lambda_{j\beta}} \right\rangle \tag{4.60}$$

For α or β equal to zero no derivative is done and only the GWP remains,

$$\frac{\partial g_i}{\partial \lambda_{i\alpha}} \overset{\alpha=0}{=} g_i \tag{4.61}$$

4.4.4 Properties of the Gaussian-MCTDH Approach

The G-MCTDH approach (hybrid and all-GWP) as well as the vMCG variant are used for two types of applications. While the first approach is very suitable for system-bath type problems, where the system can be partitioned into primary and secondary modes, e.g. effective modes and environmental *bath* modes,[15,81,84,85] the vMCG variant is mainly used in combination with on-the-fly electronic structure calculations.[17,18,86] Convergence properties of these methods tend to be favorable if the modes, described by GWPs, remain near-harmonic, but in anharmonic systems a large number of GWPs may be required. E.g. this has been shown for a pyrazine benchmark system with 24 DOF near a conical intersection, showing complicated dynamics.[81]

Originally, this method was intended to use high dimensional TGs. Compared to MCTDH this seems a reasonable choice as the DOFs within a high dimensional GWP are correlated through the off-diagonal terms in the width matrix. However, this proved to be rather unstable and worked only in typical system-bath situations, where only a small number of GWPs are necessary because of almost harmonic bath modes. As a consequence, nowadays almost only FGs are used. In general, these are more numerically robust, but of course lack correlations between the combined DOFs within such a FG. Hence, a larger number of configurations is needed for the calculation to converge and capture the correlations appropriately.

The vMCG method usually does not converge well. Because of the lack of correlation between the DOF within one GWP, many configurations are needed to describe the wave packet dynamics appropriately and to conserve the results. But, due to this *unreduced* particle every GWP reflects one complete configuration, e.g. a representation of the system. Hence, vMCG is especially suitable to use in conjunction with on-the-fly electronic structure calculations. On the other hand (G-)MCTDH is typically used in combination with parametrized model Hamiltonians, where one needs to pre-compute selected cuts of the potential energy surface (PES) and do a multidimensional fit. This is not only a tedious, but also insufficient work as one might not cover the PES correctly or miss out important areas. On-the-fly dynamics (or direct dynamics) therefore bear the advantage that the PES is only calculated at points where the wave function is located. However, in order to have a sufficient accuracy, an appropriate electronic structure method has to be chosen (c.f. chapter 3). Consequently, the electronic structure calculations become the dominant computational effort.

4.4.5 Scaling Properties of G-MCTDH

For the sake of brevity only the scaling behavior of the all-GWP G-MCTDH approach is discussed. The scaling of the mixed variant, however, can easily be derived by combining both behaviors. In the following, for simplicity it is assumed that each mode has the same number of SPFs $n^{(1)} = \cdots = n^{(f)} := n$ and that every FG contains the same number of DOFs $d_1 = \cdots = d_f^{()} := d$. The scaling is derived similarly to the MCTDH method. The most expensive steps are the calculation of the mean fields $\hat{H}_{jj'}^{(\kappa)}$ and solving the system of linear equations for the GWP parameters $\dot{\vec{\Lambda}}^{(\kappa)}$. The effort for the mean fields is essentially identical to the MCTDH method. Solving the linear equations can be done in various ways. Typically this is done by inverting the $\underline{C}$ matrix. An inversion of a complex hermitian matrix scales cubically with the dimensionality and is therefore in the order $f\,(dn)^3$. The overall effort of the G-MCTDH method is then given as,[14,81]

$$\text{effort}^{G-MCTDH} = mf^2n^{f+1} + f\,(dn)^3 \tag{4.62}$$

where again a sum of products Hamiltonian (Eqn. 4.40) is assumed. As one directly sees from this term, combining many degrees of freedom into a high-dimensional GWP will be particularly disadvantageous. This is especially pronounced for the vMCG method, where all DOF are combined into one mode ($f = 1$). As a consequence only a limited number of FGs can be used and numerical convergence is difficult to achieve.

5 | Theoretical Models for Energy and Charge Transfer

Excitation energy (EET) and electron transfer (ET) processes play an important role in many areas of biology, physics and chemistry. EETs and ETs are crucial steps in many processes where isolated molecules, molecular aggregates, light harvesting complexes, photovoltaics and light emitting diodes (and their organic counterparts) are involved. For example in organic photovoltaic (OPV) systems, three elementary steps have to be considered:

1. creation of electron-hole pairs (excitons)
2. exciton transport (EETs) and dissociation (ETs) at donor-acceptor junctions
3. transport and capture of charge carriers at the electrodes.

For a better understanding of these processes, it is necessary to describe the EET and ET kinetics (section 5.1). In this work, the focus lies on the initial exciton transport and dissociation, i.e. the charge generation. To study this, several models have been developed and two of them, based on the Marcus theory,[87] are presented in the following (section 5.2). However, these models are not sufficient for the description of ultrafast non-adiabatic ETs. Therefore, in section 5.3 model Hamiltonians for the description of energy transfers are discussed, which can be used in conjunction with the methods discussed in chapters 3 and 4.

5.1 Charge and Exciton Generation

The first step in (E)ET processes is the creation of an excited state. Such an excited state may be the result of a scattering process with another molecule, a preceding EET step, or created by an optical absorption. In the latter case, a photon which is in resonance with the energy gap between the highest occupied molecular orbital (HOMO) and the lowest unoccupied molecular orbital (LUMO) is absorbed. Hence, an electron from the HOMO is promoted (excited) to the LUMO. Therefore a hole and an unpaired electron is left behind in the HOMO, illustrated by the sketch in Fig. 5.1(a). This electron-hole pair, also called exciton, is an electronically quasi-particle bound via the Coulomb attraction.

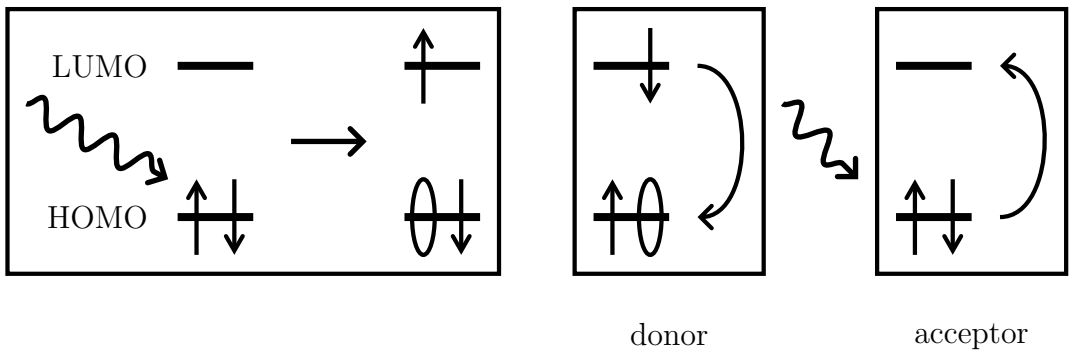

(a) photoexcitation **(b)** EET

Figure 5.1: (a) Illustration of the creation of an electron-hole pair via a photoexcitation and (b) and an excitation energy transfer process between donor and acceptor.

Applying this to a donor-acceptor molecule (or complex), an electron is excited to the LUMO of the donor $D \rightarrow D^*$, where D^* indicates the excited state of the donor. Then, the energy can be transferred to the acceptor,

$$D^*A \rightarrow DA^*$$

where the donor returns to the ground state and an electron from the acceptors HOMO is excited to the LUMO (EET, Fig. 5.1(b)). Alternatively to the EET, an electron can be transferred from the donor to the acceptor, creating a so called charge transfer (CT) state,

$$D^*A \rightarrow D^+A^-$$

After the ET event the donor is left with a hole in its HOMO and the acceptor carries an additional electron in its LUMO. As an alternative, the CT state can be formed after an initial EET, followed by a hole transfer from the acceptor to the donor,

$$DA^* \rightarrow D^+A^-$$

5.2 Electron Transfer Theories

The classical description of an electron transfer is based on the transition state theory and the Arrhenius relation. Marcus theory uses this as basis to describe the transfer of an electron from a spherical donor to a spherical acceptor molecule in solution via a classical reaction coordinate. The distortion of the donor, acceptor and the environment from their equilibrium configuration is described by two

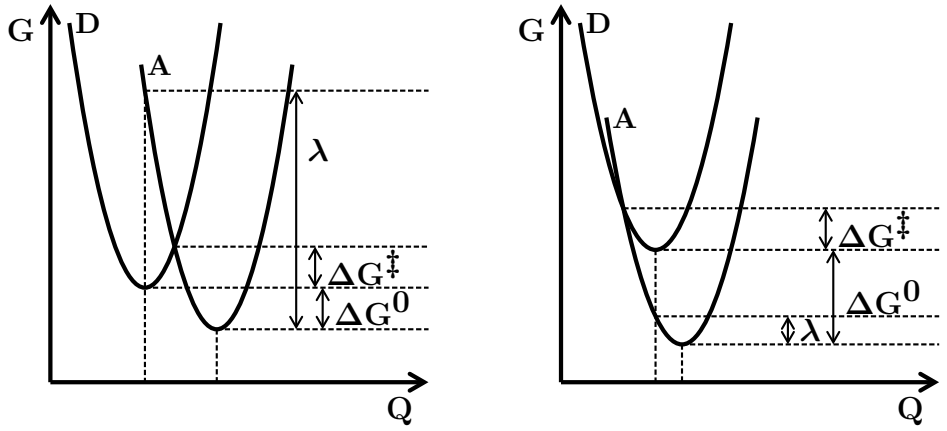

(a) normal regime **(b)** inverted regime

Figure 5.2: Illustration of the Marcus model for (a) the normal and (b) inverted regime. ΔG^0 represents the difference of the Gibbs free energy, $\Delta G^\ddagger$ is the expression for the activation energy and λ is the reorganization energy.

parabolas, which are shifted relatively to each other according to the reaction Gibbs free energy ΔG_0 (Fig. 5.2).

The transfer rate for the Marcus Theory is given as,

$$k_{ET} = \frac{2\pi}{\hbar} \frac{|V_{DA}|^2}{\sqrt{4\pi\lambda k_B T}} \exp\left(\frac{-\left(\Delta G^0 + \lambda\right)^2}{4\lambda k_B T}\right) \tag{5.1}$$

where V_{DA} represents the coupling (transfer integral) between the two donor and acceptor states, T is the temperature and k_B is the Boltzmann constant. In the case of a weak coupling, $|V_{DA}|^2$ is taken to be exponentially dependent on the distance between donor and acceptor R_{DA},

$$|V_{DA}|^2 = |V_{DA}^0|^2 \exp\left(-\beta R_{DA}\right) \tag{5.2}$$

The reaction rate is mainly dependent on two variables: the difference in Gibbs free energy ΔG^0 for the both states and the reorganisation energy λ. ΔG^0 describes the reaction energy of the transfer process, while λ gives insight into the change of the electrostatic field of the environment and the reorganization of the internal modes.

If the value of ΔG_0 is smaller than λ the transfer rate k_{ET} increases with the absolute of the reaction Gibbs free energy $|\Delta G^0|$. This behavior is typically referred to as the *normal* regime. If $|\Delta G^0|$ increases even more, becoming larger than λ, the reaction rate decreases with growing $|\Delta G^0|$. This is typically referred to as the *inverted* regime. This change in behavior is due to an increased activation energy

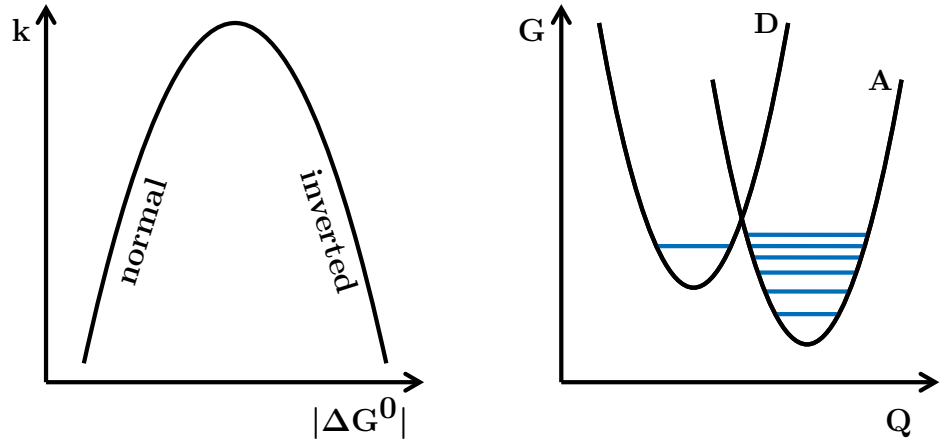

(a) k_{ET} in normal vs. inverted regime **(b)** Marcus-Levich-Jortner model

Figure 5.3: (a) Illustration of the Marcus transfer rate dependence of $|\Delta G^0|$ and (b) illustration of the Marcus-Jortner-Levich scheme.

$\Delta G^{\ddagger}$ for the transfer, as the crossing of the both state parabolas is increased in energy. In the case of $\lambda = \Delta G^0$ the reaction becomes barrierless.

Within the framework of a simplified model, only taking into account the electrostatic interaction with the solvent, λ can be approximated by the Born-Hush approach,[88]

$$\lambda = \frac{e^2}{4\pi\epsilon_0}\left(\frac{1}{2r_{\mathrm{D}^+}} + \frac{1}{2r_{\mathrm{A}^-}} - \frac{1}{R_{\mathrm{DA}}}\right)\left(\frac{1}{n^2} + \frac{1}{\epsilon}\right) \tag{5.3}$$

where ϵ is the dielectric constant and n the refraction index of the solvent, r_{D^+} and r_{A^-} are the radii of the oxidized donor and reduced acceptor and R_{DA} is the distance of the centroids of acceptor and donor. The reaction energy ΔG_0 can either be measured or calculated. For example, when the solvation after the transfer process is rapid, one can approximate ΔG_0 by,

$$\Delta G^0 = E_{ox}^{\mathrm{D/D}^+} - \left(E_{red}^{\mathrm{A/A}^+} + E_{\mathrm{D}^*}\right) - \frac{e^2}{\epsilon}\left(r_{\mathrm{D}^+} + r_{\mathrm{A}^-}\right) \tag{5.4}$$

where $E_{ox}^{\mathrm{D/D}^+}$ and $E_{red}^{\mathrm{A/A}^+}$ are the standard redox potentials of the donor and acceptor respectively, E_{D^*} is the energy of the donor excited state and ϵ is the dielectric constant of the medium.

An extension to the classical Marcus theory is given by the Marcus-Levich-Jortner theory. Here, one assumes that the low-frequency, classical reaction coordinate is coupled to high-frequency intra-molecular (quantum) modes. Since the energy of the high-frequency mode is usually much higher than the thermal energy, one

assumes, that for the initial state only the vibrational ground state is occupied. Therefore, one has a single initial, but several final vibrational states and therefore several pathways are to be considered,

$$k_{ET}^{MLJ} = \frac{2\pi}{\hbar} \frac{|V_{DA}|^2}{\sqrt{4\pi\lambda_{sol} k_B T}} \sum_{n=0}^{\infty} \frac{\left(\frac{\lambda_{mol}}{E_{vib}}\right)^n}{n!} \exp\left(-\frac{\lambda_{mol}}{E_{vib}}\right) \exp\left(-\frac{\left(\Delta G^0 + \lambda_{sol} + nE_{vib}\right)^2}{4\lambda_{sol} k_B T}\right) \tag{5.5}$$

E_{vib} represents the vibrational energy of the high-frequency vibrational mode. The manifold of the vibrational final states is included in the reaction Gibbs free energy. Here, λ is now considered to be comprised of two terms describing the reorganization energy of the solvent (λ_{sol}) and the nuclear coordinates (λ_{mol}). λ_{sol} can be approximated as before by the Born-Hush model, while λ_{mol} can be extracted from electronic structure calculations.

5.3 Model Hamiltonians for the Description of Energy and Charge Transfer Processes

For the theoretical investigation of energy and electron transfer processes, a Hamiltonian is needed to describe the physical properties of such processes. The Hamiltonian carries all information about the internal DOFs of the system, the environment and electron-phonon-couplings. The full molecular Hamiltonian would describe all physical effects and aspects explicitly. However, the computational effort for accurate methods typically rises exponentially with the number of DOFs and the full Hamiltonian cannot be used. Therefore it is necessary to focus on specific DOFs and interactions of the Hamiltonian, describing the elementary parts of the energy or electron transfer process of interest.[31]

The first step towards an accurate and efficient description is to use a system-bath-type Hamiltonian, where the Hamiltonian consists of three main parts,

$$\hat{H}_{ET} = \hat{H}_{system} + \hat{H}_{bath} + \hat{H}_{system-bath} \tag{5.6}$$

As Eqn. 5.6 shows, the Hamiltonian is split into a system Hamiltonian $\hat{H}_{system}$, a Hamiltonian representing the environment, here denoted *bath* Hamiltonian $\hat{H}_{bath}$, and the system-bath Hamiltonian $\hat{H}_{system-bath}$, which couples the system to the environment. The setup and approximation of $\hat{H}_{system}$ is crucial for a reasonable description of the investigated process on the one hand and on the other hand to

keep the computational costs sufficiently low. The system Hamiltonian is further split into an electronic and nuclear part and an interaction between those. This enables the possibility to include only the relevant DOFs and electronic states and couplings or to approximate these with simple expressions. In contrast, $\hat{H}_{bath}$ describes the environment of the system under study. Depending on the environment, the Hamiltonian has to be chosen appropriately, i.e. if the system is in solution or embedded in a high-dimensional molecular arrangement like a protein or nucleic acid, also enabling the description of dissipative and relaxation effects. Several appropriate models are available such as a Langevin description or hierarchical normal mode representations (also see the IVR Hamiltonian below). $\hat{H}_{system-bath}$ finally characterizes the coupling between the system and the environment, e.g. a linear coupling to one or a few modes of the system.

A simple system-bath Hamiltonian for the study of energy transfer dynamics of a donor-acceptor system in a dissipative environment can be written in a normal mode representation and mass-weighted coordinates as depicted in Eqn. 5.6. In a pure electronic expression the system Hamiltonian represents the excitation of molecular sites on a basis of localized molecular excitations,

$$\hat{H}_{system} = \sum_{\alpha=1}^{n_{state}} \epsilon_\alpha \left|\alpha\right\rangle \left\langle\alpha\right| + \sum_{\beta\neq\alpha}^{n_{state}} \Delta_{\alpha,\beta} \left|\alpha\right\rangle \left\langle\beta\right| \tag{5.7}$$

where ϵ_α represents the excitation energy of state $|\alpha\rangle$ and $\Delta_{\alpha,\beta}$ a constant coupling between states $|\alpha\rangle$ and $|\beta\rangle$. The bath Hamiltonian may be written as a sum of independent harmonic oscillators for each state,

$$\hat{H}_{bath} = \sum_{\alpha=1}^{n_{state}} \sum_{i=1}^{n^{(\alpha)}} \frac{1}{2} \left(\left(\hat{p}_i^{(\alpha)}\right)^2 + \left(\omega_i^{(\alpha)} \hat{q}_i^{(\alpha)}\right)^2 \right) \tag{5.8}$$

where $\omega_i^{(\alpha)}$ represents the frequency of a harmonic oscillator of the bath. The coupling between the environment and the system can be expressed with a linear coupling,

$$\hat{H}_{system-bath} = \sum_{\alpha=1}^{n_{state}} \sum_{i=1}^{n^{(\alpha)}} c_i^{(\alpha)} \hat{q}_i^{(\alpha)} \left|\alpha\right\rangle \left\langle\alpha\right| \tag{5.9}$$

where $c_i^{(\alpha)}$ controls the strength of the coupling between the states and the ith mode of the bath. Here, every state is supposed to have its own local environment. Due the coupling to the bath, the site are shifted in energy and a counter term may have to be included to correct this behaviour,

$$\hat{H}_{counter} = \sum_{\alpha=1}^{n_{state}} \sum_{i=1}^{n^{(\alpha)}} \frac{\left(c_i^{(\alpha)}\right)^2}{2\left(\omega_i^{(\alpha)}\right)^2} |\alpha\rangle \langle\alpha| \tag{5.10}$$

Another type of energy transfer Hamiltonians focuses solely on the vibrational energy redistribution. Specifically, an intra-molecular vibrational energy redistribution Hamiltonian in a normal mode representation is introduced. Such a Hamiltonian describes the relaxation of energy from an initial vibrationally excited state into other vibrational DOFs of a polyatomic molecule. Here, an anharmonic, Morse-like, potential is expanded with respect to the mass-weighted normal mode coordinates q_i. Therefore, a N-dimensional vibrational Hamiltonian is obtained,

$$\hat{H}_{IVR} = \frac{1}{2} \sum_{i}^{N} \left(\hat{p}_i^2 + \omega_i^2 \hat{q}_i^2\right) + \sum_{i,j}^{N^2} K_{i,j} q_i q_j + \sum_{i,j,k}^{N^3} K_{i,j,k} q_i q_j q_k + \ldots \tag{5.11}$$

where $K_{i,j,\ldots}$ describes the anharmonic coupling constants. By employing such a Hamiltonian it is possible to study energy transfer processes and obtain transfer rates in macro molecular arrangements. This vibrational Hamiltonian could also be used as bath Hamiltonian, if a more detailed description would be necessary due to a strong coupling to specific environmental modes.

Part II

The 2-Layer-Gaussian-MCTDH Method: Implementation and Applications

The first main project of this work is the development, implementation and first application of the novel 2-Layer Gaussian-Multiconfigurational Time-Dependent Hartree (2L-G-MCTDH) method which was developed in our group by S. Römer et al.[1] The 2L-G-MCTDH method is a new variant of the existing Gaussian-MCTDH (G-MCTDH) method and uses a hierarchical structure of the wave function, analogously to the ML-MCTDH approach.[26,27,77,78] Given that the G-MCTDH method and its vMCG variant have to overcome several bottlenecks, as mentioned in section 4.4, the goal of the 2L-G-MCTDH method is to alleviate these by combining the flexible MCTDH-like single particle functions with factorizable multi-dimensional frozen Gaussians. As a result, the expensive variational evolution of the Gaussian parameters is reduced to low-dimensional subspaces.

This part is divided into four chapters: In chapter 6 the method is introduced and the equations of motion are derived. Together with an extension to multi-state wavefunctions the improved scaling properties are discussed. Chapter 7 focuses on the implementation of the novel method and gives insights into the overall program structure, scaling properties and further details to specific algorithms. In chapter 8 the developed code is tested and approved by application to two systems. The first system is a model system for intra-molecular vibrational energy redistribution in a molecular chain. The second example describes an ultrafast charge transfer state formation in a donor-acceptor system. Lastly, in chapter 9 the results are summarized and an outlook to future developments is given.

6 | The 2L-G-MCTDH Method

The G-MCTDH and vMCG approaches encounter their limits very quickly when using frozen Gaussians (FGs) as basis functions. Therefore it is necessary to re-introduce correlations into the FG-based wavefunction ansatz. To bridge between the fully flexible combined-mode SPFs of the MCTDH method and the moving FG basis sets, a new ansatz has been proposed in [1] which employs a novel type of FG based SPFs.

In this chapter, the concept of the novel 2-Layer-Gaussian MCTDH method is introduced. The ansatz of the wavefunction is discussed and the equations of motion are derived with the help of the Dirac-Frenkel variational principle, following.[1] Against this background, the improved scaling properties are shown from theoretical estimates. Following this, an extension of the method for multi-state Hamiltonians is demonstrated.

6.1 Wave Function Ansatz

To retain the flexibility of the original MCTDH type SPFs, the wave function ansatz in the new 2L-G-MCTDH scheme is taken exactly as in the MCTDH method in the first place, i.e., the wave function is constructed as a sum over products of SPFs. In a second step, as will be discussed below, the SPFs are expanded in an FG basis. Hence, the starting point is the wave function

$$\begin{aligned}\Psi\left(\vec{X},t\right) &= \sum_{J} A_J\left(t\right)\Phi_J\left(\vec{X},t\right) \\ &= \sum_{j_1}^{n_1}\sum_{j_2}^{n_2}\cdots\sum_{j_f}^{n_f} A_{j_1,j_2,\ldots,j_f}\left(t\right)\prod_{\kappa=1}^{f}\varphi_{j_\kappa}^{(\kappa)}\left(\vec{x}_\kappa,t\right)\end{aligned} \tag{6.1}$$

where J is a multi-index with $J = j_1, j_2, \ldots, j_\kappa, \ldots, j_f$, the coefficients $A_J\left(t\right)$ are complex-valued, and the configurations $\Phi_J\left(\vec{X},t\right)$ are expanded as a product of SPFs $\varphi_{j_\kappa}^{(\kappa)}$. The $\kappa = 1, 2, \ldots, f$ describe a set of modes $\vec{X} = \left(\vec{x}_1, \vec{x}_2, \ldots, \vec{x}_f\right)$.
The SPFs are then expanded in a G-MCTDH like approach, with FGs as basis functions,

$$\varphi_j^{(\kappa)}\left(\vec{x}_\kappa,t\right) = \sum_{L_\kappa} B_{j_\kappa,L_\kappa}^{(\kappa)}\left(t\right) G_{L_\kappa}^{(\kappa)}\left(\vec{x}_\kappa,t\right) = \sum_{L_\kappa} B_{j_\kappa,L_\kappa}^{(\kappa)}\left(t\right)\prod_{\mu=1}^{f_\kappa} g_{l_{\kappa,\mu}}^{(\kappa,\mu)}\left(\vec{x}_{\kappa,\mu},t\right) \tag{6.2}$$

where $L_\kappa = l_{\kappa,1}, l_{\kappa,2}, \ldots, l_{\kappa,\mu}, \ldots, l_{\kappa,f_\kappa}$ is also a multi-index. The multi-dimensional GWPs are identical to the GWPs used in the G-MCTDH approach, but now carry a double index referring to the smaller (κ,μ)-subspace (c.f. 4.46),

$$\begin{aligned} g^{(\kappa,\mu)}_{l_{\kappa,\mu}}\left(\vec{x}_{\kappa,\mu},t\right) &= g^{(\kappa,\mu)}_{l_{\kappa,\mu}}\left(\vec{\Lambda}^{(\kappa,\mu)}_{l_{\kappa,\mu}}(t),\vec{x}_{\kappa,\mu}\right) \\ &= \exp\left[\left(\vec{x}_{\kappa,\mu}\right)^T \underline{a}^{(\kappa,\mu)}_{l_{\kappa,\mu}}(t)\,\vec{x}_{\kappa,\mu} + \left(\vec{\xi}^{(\kappa,\mu)}_{l_{\kappa,\mu}}(t)\right)^T \vec{x}_{\kappa,\mu} + \eta^{(\kappa,\mu)}_{l_{\kappa,\mu}}(t)\right] \end{aligned} \tag{6.3}$$

with the GWP parameters $\vec{\Lambda}^{(\kappa,\mu)}_{l_{\kappa,\mu}} = \left(\underline{a}^{(\kappa,\mu)}_{l_{\kappa,\mu}}, \vec{\xi}^{(\kappa,\mu)}_{l_{\kappa,\mu}}, \eta^{(\kappa,\mu)}_{l_{\kappa,\mu}}\right)$, where $\vec{\xi}^{(\kappa,\mu)}_{l_{\kappa,\mu}}$ again describes the GWP center position in phase space $\vec{\xi}^{(\kappa,\mu)}_{l_{\kappa,\mu}} = -2\underline{a}^{(\kappa,\mu)}_{l_{\kappa,\mu}}\vec{q}^{(\kappa,\mu)}_{l_{\kappa,\mu}} + i\vec{p}^{(\kappa,\mu)}_{l_{\kappa,\mu}}$. As this approach uses FGs rather than TGs, the width matrix can be chosen to be diagonal such that the multi-dimensional GWPs can be written as a product of 1-dimensional GWPs,

$$\begin{aligned} g^{(\kappa,\mu)}_{l_{\kappa,\mu}}\left(\vec{x}_{\kappa,\mu},t\right) = \prod_d^{d_{\kappa,\mu}} & N\left(\left(\underline{a}^{(\kappa,\mu)}_{l_{\kappa,\mu}}\right)_{dd}, \left(\vec{\xi}^{(\kappa,\mu)}_{l_{\kappa,\mu}}\right)_d(t)\right) \\ & \times \exp\left[\left(\underline{a}^{(\kappa,\mu)}_{l_{\kappa,\mu}}\right)_{dd} x^2_{\kappa,\mu,d} + \left(\vec{\xi}^{(\kappa,\mu)}_{l_{\kappa,\mu}}\right)_d(t)\, x_{\kappa,\mu,d} + \eta^{(\kappa,\mu)}_{l_{\kappa,\mu}}(t)\right] \end{aligned} \tag{6.4}$$

where $N(a,\xi) = \left(-2Re(a)/\pi\right)^{1/4} \exp\left(\left(Re(\xi)\right)^2 / 4Re(a)\right)$ is the same normalization factor as for the GWPs in G-MCTDH.

In other words, a two-layered G-MCTDH ansatz is constructed where the first-layer SPFs $\varphi^{(\kappa)}_{j_\kappa}$ have more flexibility than the conventional GWPs (c.f. G-MCTDH), due to the time-evolving $B^{(\kappa)}_{j_\kappa,L_\kappa}$ coefficients.[1]

Like in the standard (G-)MCTDH ansatz, the representation of the wave function in terms of the new (first-layer) SPFs (Eqn. 6.2) is unique only up to change of spanning sets. For any subspace $\mathscr{H}^{(\kappa)}$ that is in the span of a finite number of SPFs of the form of Eqn. 6.2, one can find – by adapting the coefficients $B^{(\kappa)}_{j_\kappa,L_\kappa}$ appropriately – an orthogonal basis of $\mathscr{H}^{(\kappa)}$, which is still of the form of Eqn. (6.2). Thus we are free to use the same 'gauge' freedom as in standard MCTDH and the first-layer SPFs $\varphi^{(\kappa)}_{j_\kappa}$ can be chosen to be orthonormal at all times,

$$\left\langle \varphi^{(\kappa)}_{j_\kappa} \middle| \varphi^{(\kappa)}_{l_\kappa} \right\rangle = \delta_{jl} \tag{6.5}$$

$$\hat{P}^{(\kappa)}(t)\left(i\frac{\partial}{\partial t} - \hat{g}^{(\kappa)}\right)\left|\varphi^{(\kappa)}_{j_\kappa}\right\rangle = 0 \tag{6.6}$$

For the derivation of the EOMs the constraint operator $\hat{g}^{(\kappa)}$ is chosen to be equal to zero, as typically done in MCTDH.

By the use of parametrized Gaussian functions one retains the efficient treatment of a large number of modes due to the analytic calculations of high dimensional integrals, but sacrificing some flexibility of the SPFs. As for the first layer, the representation of each SPF is not unique, which results in a free choice of $\eta_{l_{\kappa,\mu}}^{(\kappa,\mu)}$. (This is similar to G-MCTDH where the variational equations for the GWP phase parameter are undetermined.) Typically the real part $\mathrm{Re}\left(\eta_{l_{\kappa,\mu}}^{(\kappa,\mu)}\right)$ is fixed, such that the GWP $g_{l_{\kappa,\mu}}^{(\kappa,\mu)}$ is normalized at any time, while the imaginary part $\mathrm{Im}\left(\eta_{l_{\kappa,\mu}}^{(\kappa,\mu)}\right)$ is set to zero. For the FGs the only time-dependent parameters of the GWPs are the positions in phase space $\vec{\Lambda}_{l_{\kappa,\mu}}^{(\kappa,\mu)} = \left(\vec{\xi}_{l_{\kappa,\mu}}^{(\kappa,\mu)}\right)$.

6.2 Equations of Motion

In order to derive the equations of motion it is convenient to define some shorthand notations. First, we define the first- and second-layer single hole functions (SHFs),

$$\psi_{j'}^{(\kappa)} = \sum_{J^{(\kappa)}} A_{J^{(\kappa:j')}} \Phi_{J^{(k)}} \tag{6.7}$$

$$\psi_{l'}^{(\kappa,\mu)} = \sum_{j_\kappa} \left[\sum_{L^{(\mu)}} B_{j_\kappa, L^{(\mu:l')}}^{(\kappa)} G_{L^{(\mu:l')}}^{(\kappa)} \right] \psi_{j_\kappa}^{(\kappa)} \tag{6.8}$$

where $J^{(\kappa)} = j_1, \ldots, j_{\kappa-1}, j_{\kappa+1}, \ldots, j_f$ and $J^{(\kappa:j')} = j_1, \ldots, j_{\kappa-1}, j', j_{\kappa+1}, \ldots, j_f$ are reduced multi-indices and $\Phi_{J^{(\kappa)}} = \prod_{\kappa' \neq \kappa} \varphi_{j_{\kappa'}}^{(\kappa')}$ is a reduced configuration. The quantities $L^{(\mu)}$, $L^{(\mu:l')}$ and $G_{L^{(\mu:l')}}^{(\kappa)}$ are defined analogously. Second, given the definition of the SHFs, one is able to rewrite the wave function Ψ as,

$$\Psi = \sum_{j_\kappa} \varphi_{j_\kappa}^{(\kappa)} \psi_{j_\kappa}^{(\kappa)} = \sum_{l_{\kappa,\mu}} g_{l_{\kappa,\mu}}^{(\kappa,\mu)} \psi_{l_{\kappa,\mu}}^{(\kappa,\mu)} \tag{6.9}$$

The equations of motion are again derived by applying the DF-VP (Eqn. 4.3) to the wave function ansatz. The variation of the wave function $\delta\Psi$ is given by,

$$\begin{aligned}
\delta\Psi =& \sum_J \delta A_J \Phi_J + \sum_{\kappa, j_\kappa} \delta\varphi_{j_\kappa}^{(\kappa)} \psi_{j_\kappa}^{(\kappa)} \\
=& \sum_J \delta A_J \Phi_J + \sum_{\kappa, j_\kappa, L_\kappa} \delta B_{j_\kappa, L_\kappa}^{(\kappa)} G_{L_\kappa}^{(\kappa)} \psi_{j_\kappa}^{(\kappa)} + \sum_{\kappa,\mu,l_{\kappa,\mu}} \delta g_{l_{\kappa,\mu}}^{(\kappa,\mu)} \psi_{l_{\kappa,\mu}}^{(\kappa,\mu)} \\
=& \sum_J \delta A_J \Phi_J + \sum_{\kappa, j_\kappa, L_\kappa} \delta B_{j_\kappa, L_\kappa}^{(\kappa)} G_{L_\kappa}^{(\kappa)} \psi_{j_\kappa}^{(\kappa)} + \sum_{\kappa,\mu,l_{\kappa,\mu},\alpha} \delta\Lambda_{l_{\kappa,\mu},\alpha}^{(\kappa,\mu)} \left(\frac{\partial}{\partial\alpha} g_{l_{\kappa,\mu}}^{(\kappa,\mu)} \right) \psi_{l_{\kappa,\mu}}^{(\kappa,\mu)}
\end{aligned} \tag{6.10}$$

where α refers to one of the time-dependent GWP parameters $\vec{\Lambda}_{l_{\kappa,\mu}}^{(\kappa,\mu)}$. The variations of the coefficients δA_J, $\delta B_{j_\kappa, L_\kappa}^{(\kappa)}$ and the parameters $\delta\Lambda_{l_{\kappa,\mu},\alpha}^{(\kappa,\mu)}$ are independent

and therefore three independent equations are obtained from the Dirac-Frenkel variational principle,

$$0 = \left\langle \Phi_J \middle| \left(i\frac{\partial}{\partial t} - \hat{H} \right) \middle| \Psi \right\rangle \qquad \forall J \tag{6.11}$$

$$0 = \left\langle G^{(\kappa)}_{L_\kappa} \psi^{(\kappa)}_{j_\kappa} \middle| \left(i\frac{\partial}{\partial t} - \hat{H} \right) \middle| \Psi \right\rangle \qquad \forall \kappa, j_\kappa, L_\kappa \tag{6.12}$$

$$0 = \left\langle \frac{\partial}{\partial \alpha} g^{(\kappa,\mu)}_{l_{\kappa,\mu}} \psi^{(\kappa,\mu)}_{l_{\kappa,\mu}} \middle| \left(i\frac{\partial}{\partial t} - \hat{H} \right) \middle| \Psi \right\rangle \qquad \forall \kappa, \mu, l_{\kappa,\mu}, \alpha \tag{6.13}$$

6.2.1 Variation of the First-Layer Coefficients

The time derivatives of the first-layer coefficients are obtained using Eqn. 6.11 analogously to the MCTDH coefficients (c.f. Eqn. 4.22). Therefore, one obtains the same EOM (with $\hat{g}^{(\kappa)}$),

$$i\dot{A}_J = \sum_{J'} \left\langle \Phi_J \middle| \hat{H} \middle| \Phi_{J'} \right\rangle A_{J'} \tag{6.14}$$

6.2.2 Variation of the Second-Layer Coefficients

Before treating Eqn. 6.12, the orthogonal projector $\hat{P}^{(\kappa)}$ (Eqn. 4.27) is used to split off the part of $G^{(\kappa)}_{L_\kappa}$ that lies in the κth subspace that is already spanned by the first-layer SPFs $\varphi^{(\kappa)}_{j_\kappa}$,

$$G^{(\kappa)}_{L_\kappa} = \hat{P}^{(\kappa)} G^{(\kappa)}_{L_\kappa} + \left(\hat{1} - \hat{P}^{(\kappa)} \right) G^{(\kappa)}_{L_\kappa} \tag{6.15}$$

Eqn. 6.12 can then be rewritten,

$$0 = \left\langle \hat{P}^{(\kappa)} G^{(\kappa)}_{L_\kappa} \psi^{(\kappa)}_{j_\kappa} \middle| \left(i\frac{\partial}{\partial t} - \hat{H} \right) \middle| \Psi \right\rangle + \left\langle \left(\hat{1} - \hat{P}^{(\kappa)} \right) G^{(\kappa)}_{L_\kappa} \psi^{(\kappa)}_{j_\kappa} \middle| \left(i\frac{\partial}{\partial t} - \hat{H} \right) \middle| \Psi \right\rangle \tag{6.16}$$

Since $\hat{P}^{(\kappa)} G^{(\kappa)}_{L_\kappa}$ is a linear combination of first-layer SPFs $\varphi^{(\kappa)}_{j_\kappa}$ and $\psi^{(\kappa)}_{j_\kappa}$ is a linear combination of configurations $\Phi_{J^{(\kappa)}}$, the product $\hat{P}^{(\kappa)} G^{(\kappa)}_{L_\kappa} \psi^{(\kappa)}_{j_\kappa}$ is then a linear combination of the first layer configurations Φ_J (c.f. MCTDH Eqn. 4.31),

$$\hat{P}^{(\kappa)} G^{(\kappa)}_{L_\kappa} \psi^{(\kappa)}_{j_\kappa} = \sum_J c_J \Phi_J \tag{6.17}$$

Together with Eqn. 6.11 this implies that the first term in Eqn. 6.16 vanishes (i.e., the SPFs move only in the space that is not yet spanned) and reduces to,

$$
\begin{aligned}
0 =& \left\langle \left(\hat{1} - \hat{P}^{(\kappa)}\right) G^{(\kappa)}_{L_\kappa} \varphi^{(\kappa)}_{j_\kappa} \middle| \left(i\frac{\partial}{\partial t} - \hat{H} \right) \middle| \Psi \right\rangle \\
=& \left\langle G^{(\kappa)}_{L_\kappa} \varphi^{(\kappa)}_{j_\kappa} \middle| \left(\hat{1} - \hat{P}^{(\kappa)}\right) \left(i\frac{\partial}{\partial t} - \hat{H} \right) \middle| \Psi \right\rangle \\
=& \sum_{j'} i\rho^{(\kappa)}_{j_\kappa j'_\kappa} \left\langle G^{(\kappa)}_{L_\kappa} \middle| \left(\hat{1} - \hat{P}^{(\kappa)}\right) \frac{\partial}{\partial t} \varphi^{(\kappa)}_{j'_\kappa} \right\rangle \\
&+ i \left\langle \psi^{(\kappa)}_{j_\kappa} \middle| \frac{\partial}{\partial t} \psi^{(\kappa)}_{j'_\kappa} \right\rangle \left\langle G^{(\kappa)}_{L_\kappa} \middle| \left(\hat{1} - \hat{P}^{(\kappa)}\right) \varphi^{(\kappa)}_{j'_\kappa} \right\rangle \\
&- \left\langle G^{(\kappa)}_{L_\kappa} \middle| \left(\hat{1} - \hat{P}^{(\kappa)}\right) \hat{\mathcal{H}}^{(\kappa)}_{j_\kappa j'_\kappa} \middle| \varphi^{(\kappa)}_{j'_\kappa} \right\rangle
\end{aligned} \tag{6.18}
$$

where the definitions for the density matrix $\rho^{(\kappa)}_{j_\kappa j'_\kappa} = \left\langle \psi^{(\kappa)}_{j_\kappa} \middle| \psi^{(\kappa)}_{j'_\kappa} \right\rangle$ and the first-layer mean-fields $\hat{\mathcal{H}}^{(\kappa)}_{j_\kappa j'_\kappa} = \left\langle \psi^{(\kappa)}_{j_\kappa} \middle| \hat{H} \middle| \psi^{(\kappa)}_{j'_\kappa} \right\rangle$ have been used. Using $\left(\hat{1} - \hat{P}^{(\kappa)}\right) \left|\varphi^{(\kappa)}_{j'_\kappa}\right\rangle = 0$ (c.f. Eqn. 4.33) and the 'gauge' freedom to choose orthonormal SPFs one gets,

$$
\begin{aligned}
0 =& \sum_{j'_\kappa} \left\{ i\rho^{(\kappa)}_{j_\kappa j'_\kappa} \left\langle G^{(\kappa)}_{L_\kappa} \middle| \frac{\partial}{\partial t} \varphi^{(\kappa)}_{j'_\kappa} \right\rangle - \left\langle G^{(\kappa)}_{L_\kappa} \middle| \left(\hat{1} - \hat{P}^{(\kappa)}\right) \hat{\mathcal{H}}^{(\kappa)}_{j_\kappa j'_\kappa} \middle| \varphi^{(\kappa)}_{j'_\kappa} \right\rangle \right\} \\
=& \sum_{j'_\kappa L'_\kappa} \left\{ i\rho^{(\kappa)}_{j_\kappa j'_\kappa} \left[\left\langle G^{(\kappa)}_{L_\kappa} \middle| G^{(\kappa)}_{L'_\kappa} \right\rangle \frac{\partial}{\partial t} B^{(\kappa)}_{j'_\kappa L'_\kappa} + \left\langle G^{(\kappa)}_{L_\kappa} \middle| \frac{\partial}{\partial t} G^{(\kappa)}_{L'_\kappa} \right\rangle B^{(\kappa)}_{j'_\kappa L'_\kappa} \right] \right. \\
&\left. - \left\langle G^{(\kappa)}_{L_\kappa} \middle| \left(\hat{1} - \hat{P}^{(\kappa)}\right) \hat{\mathcal{H}}^{(\kappa)}_{j_\kappa j'_\kappa} \middle| G^{(\kappa)}_{L'_\kappa} \right\rangle B^{(\kappa)}_{j'_\kappa L'_\kappa} \right\}
\end{aligned} \tag{6.19}
$$

With the definition of the overlap($\tilde{S}^{(\kappa)}_{j_\kappa L_\kappa, j'_\kappa L'_\kappa}$), Hamiltonian ($\tilde{H}^{(\kappa)}_{j_\kappa L_\kappa, j'_\kappa L'_\kappa}$) and differential overlap matrix elements ($\tilde{\tau}^{(\kappa)}_{j_\kappa L_\kappa, j'_\kappa L'_\kappa}$),

$$
\tilde{S}^{(\kappa)}_{j_\kappa L_\kappa, j'_\kappa L'_\kappa} = \delta_{j_\kappa j'_\kappa} \left\langle G^{(\kappa)}_{L_\kappa} \middle| G^{(\kappa)}_{L'_\kappa} \right\rangle \tag{6.20}
$$

$$
\tilde{\tau}^{(\kappa)}_{j_\kappa L_\kappa, j'_\kappa L'_\kappa} = \delta_{j_\kappa j'_\kappa} \left\langle G^{(\kappa)}_{L_\kappa} \middle| \frac{\partial}{\partial t} G^{(\kappa)}_{L'_\kappa} \right\rangle \tag{6.21}
$$

$$
\tilde{H}^{(\kappa)}_{j_\kappa L_\kappa, j'_\kappa L'_\kappa} = \left\langle G^{(\kappa)}_{L_\kappa} \middle| \left(\hat{1} - P^{(\kappa)}\right) \left[\left(\underline{\rho}^{(\kappa)}\right)^{-1} \underline{\hat{\mathcal{H}}}^{(\kappa)} \right]_{j_\kappa j'_\kappa} G^{(\kappa)}_{L'_\kappa} \right\rangle \tag{6.22}
$$

one can rewrite the equation and obtain the EOM for the coefficients $\frac{\partial}{\partial t} B^{(\kappa)}_{j'_\kappa L'_\kappa} = \dot{B}^{(\kappa)}_{j'_\kappa L'_\kappa}$:

$$
\begin{aligned}
\sum_{j''_\kappa j'_\kappa L'_\kappa} i\rho^{(\kappa)}_{j_\kappa j'_\kappa} \tilde{S}^{(\kappa)}_{j''_\kappa L_\kappa, j'_\kappa L'_\kappa} \dot{B}^{(\kappa)}_{j'_\kappa L'_\kappa} =& \sum_{j''_\kappa j'_\kappa L'_\kappa} \rho^{(\kappa)}_{j_\kappa j'_\kappa} \left\{ \tilde{H}^{(\kappa)}_{j_\kappa L_\kappa, j'_\kappa L'_\kappa} B^{(\kappa)}_{j'_\kappa L'_\kappa} \right. \\
& \left. - i\tilde{\tau}^{(\kappa)}_{j_\kappa L_\kappa, j'_\kappa L'_\kappa} B^{(\kappa)}_{j'_\kappa L'_\kappa} \right\} \\
\sum_{j''_\kappa j'_\kappa L'_\kappa} i\tilde{S}^{(\kappa)}_{j''_\kappa L_\kappa, j'_\kappa L'_\kappa} \dot{B}^{(\kappa)}_{j'_\kappa L'_\kappa} =& \sum_{j''_\kappa j'_\kappa L'_\kappa} \left\{ \tilde{H}^{(\kappa)}_{j_\kappa L_\kappa, j'_\kappa L'_\kappa} B^{(\kappa)}_{j'_\kappa L'_\kappa} - i\tilde{\tau}^{(\kappa)}_{j_\kappa L_\kappa, j'_\kappa L'_\kappa} B^{(\kappa)}_{j'_\kappa L'_\kappa} \right\}
\end{aligned} \tag{6.23}
$$

6.2.3 Variation of the GWP Parameters

The time derivatives of the GWP parameters are obtained from Eqn. 6.13. Beforehand, one can define a non-orthogonal second-layer projector as for the first-layer,

$$\hat{P}^{(\kappa,\mu)} = \sum_{l_{\kappa,\mu} l'_{\kappa,\mu}} \left| g^{(\kappa,\mu)}_{l_{\kappa,\mu}} \right\rangle \left(\left(\underline{S}^{(\kappa,\mu)} \right)^{-1} \right)_{l_{\kappa,\mu} l'_{\kappa,\mu}} \left\langle g^{(\kappa,\mu)}_{l'_{\kappa,\mu}} \right| \tag{6.24}$$

where $\underline{S}^{(\kappa,\mu)} = \left\langle g^{(\kappa,\mu)}_{l_{\kappa,\mu}} \middle| g^{(\kappa,\mu)}_{l'_{\kappa,\mu}} \right\rangle$ is the second-layer overlap matrix. With the projector it is again possible to split off the part that lies in the (κ,μ)th subspace $\mathscr{H}^{(\kappa,\mu)}$ spanned by the second-layer SPFs $g^{(\kappa,\mu)}_{l_{\kappa,\mu}}$,

$$\frac{\partial}{\partial\alpha} g^{(\kappa,\mu)}_{l_{\kappa,\mu}} = \hat{P}^{(\kappa,\mu)} \frac{\partial}{\partial\alpha} g^{(\kappa,\mu)}_{l_{\kappa,\mu}} + \left(\hat{1} - \hat{P}^{(\kappa,\mu)} \right) \frac{\partial}{\partial\alpha} g^{(\kappa,\mu)}_{l_{\kappa,\mu}} \tag{6.25}$$

Since $\hat{P}^{(\kappa,\mu)} g^{(\kappa,\mu)}_{l_{\kappa,\mu}} \psi^{(\kappa,\mu)}_{l_{\kappa,\mu}}$ is a linear combination,

$$\hat{P}^{(\kappa,\mu)} \frac{\partial}{\partial\alpha} g^{(\kappa,\mu)}_{l_{\kappa,\mu}} \psi^{(\kappa,\mu)}_{l_{\kappa,\mu}} = \sum_{j_\kappa, L_\kappa} c_{j_\kappa, L_\kappa} G^{(\kappa)}_{L_\kappa} \psi^{(\kappa,\mu)}_{l_{\kappa,\mu}} \tag{6.26}$$

the first term of Eqn. 6.25 can be rewritten as,

$$\begin{aligned} &\left\langle \hat{P}^{(\kappa,\mu)} g^{(\kappa,\mu)}_{l_{\kappa,\mu}} \psi^{(\kappa,\mu)}_{l_{\kappa,\mu}} \middle| \left(i\frac{\partial}{\partial t} - \hat{H} \right) \middle| \Psi \right\rangle \\ &\quad = \sum_{j_\kappa, L_\kappa} \bar{c}_{j_\kappa, L_\kappa} \left\langle G^{(\kappa)}_{L_\kappa} \psi^{(\kappa,\mu)}_{l_{\kappa,\mu}} \middle| \left(i\frac{\partial}{\partial t} - \hat{H} \right) \middle| \Psi \right\rangle = 0 \end{aligned} \tag{6.27}$$

Together with Eqn. 6.12 the first term of Eqn. 6.13 vanishes and Eqn. 6.13 reduces to,

$$0 = \left\langle \frac{\partial}{\partial\alpha} g^{(\kappa,\mu)}_{l_{\kappa,\mu}} \psi^{(\kappa,\mu)}_{l_{\kappa,\mu}} \middle| \left(\hat{1} - \hat{P}^{(\kappa,\mu)} \right) \left(i\frac{\partial}{\partial t} - \hat{H} \right) \middle| \Psi \right\rangle \tag{6.28}$$

With the help of Eqn. 6.9 one is able to rewrite this equation and by using the definitions for the second-layer density matrix $\rho^{(\kappa,\mu)}_{l_{\kappa,\mu} l'_{\kappa,\mu}} = \left\langle \psi^{(\kappa,\mu)}_{l_{\kappa,\mu}} \middle| \psi^{(\kappa,\mu)}_{l'_{\kappa,\mu}} \right\rangle$ and second-layer mean-fields matrix elements $\hat{\mathcal{H}}^{(\kappa,\mu)}_{l_{\kappa,\mu} l'_{\kappa,\mu}} = \left\langle \psi^{(\kappa,\mu)}_{l_{\kappa,\mu}} \middle| \hat{H} \middle| \psi^{(\kappa,\mu)}_{l'_{\kappa,\mu}} \right\rangle$ one obtains the EOM for the GWP parameters,

$$\begin{aligned} 0 = &\sum_{l'_{\kappa,\mu}} \left\{ i\rho^{(\kappa,\mu)}_{l_{\kappa,\mu} l'_{\kappa,\mu}} \left\langle \frac{\partial}{\partial\alpha} g^{(\kappa,\mu)}_{l_{\kappa,\mu}} \middle| \left(\hat{1} - \hat{P}^{(\kappa,\mu)} \right) \frac{\partial}{\partial t} g^{(\kappa,\mu)}_{l'_{\kappa,\mu}} \right\rangle \right. \\ &\left. - \left\langle \frac{\partial}{\partial\alpha} g^{(\kappa,\mu)}_{l_{\kappa,\mu}} \middle| \left(\hat{1} - \hat{P}^{(\kappa,\mu)} \right) \hat{\mathcal{H}}^{(\kappa,\mu)}_{l_{\kappa,\mu} l'_{\kappa,\mu}} \middle| g^{(\kappa,\mu)}_{l'_{\kappa,\mu}} \right\rangle \right\} \end{aligned} \tag{6.29}$$

$$= \sum_{l'_{\kappa,\mu},\beta} i\rho^{(\kappa,\mu)}_{l_{\kappa,\mu} l'_{\kappa,\mu}} \left\langle \frac{\partial}{\partial\alpha} g^{(\kappa,\mu)}_{l_{\kappa,\mu}} \middle| \left(\hat{1} - \hat{P}^{(\kappa,\mu)} \right) \frac{\partial}{\partial\beta} g^{(\kappa,\mu)}_{l'_{\kappa,\mu}} \right\rangle \frac{\partial}{\partial t} \Lambda^{(\kappa,\mu)}_{l'_{\kappa,\mu},\beta} \tag{6.30}$$

$$- \sum_{l'_{\kappa,\mu}} \left\langle \frac{\partial}{\partial\alpha} g^{(\kappa,\mu)}_{l_{\kappa,\mu}} \middle| \left(\hat{1} - \hat{P}^{(\kappa,\mu)} \right) \hat{\mathcal{H}}^{(\kappa,\mu)}_{l_{\kappa,\mu} l'_{\kappa,\mu}} \middle| g^{(\kappa,\mu)}_{l'_{\kappa,\mu}} \right\rangle \tag{6.31}$$

With the definitions for the $\underline{C}$ matrix and $\vec{Y}$ vector,

$$C^{(\kappa,\mu)}_{l_{\kappa,\mu}\alpha,l'_{\kappa,\mu}\beta} = \rho^{(\kappa,\mu)}_{l_{\kappa,\mu}l'_{\kappa,\mu}} \left\langle \frac{\partial}{\partial\alpha} g^{(\kappa,\mu)}_{l_{\kappa,\mu}} \middle| \left(\hat{1} - \hat{P}^{(\kappa,\mu)}\right) \frac{\partial}{\partial\beta} g^{(\kappa,\mu)}_{l'_{\kappa,\mu}} \right\rangle \tag{6.32}$$

$$Y^{(\kappa,\mu)}_{l_{\kappa,\mu}\alpha} = \sum_{l'_{\kappa,\mu}} \left\langle \frac{\partial}{\partial\alpha} g^{(\kappa,\mu)}_{l_{\kappa,\mu}} \middle| \left(\hat{1} - \hat{P}^{(\kappa,\mu)}\right) \hat{\mathcal{H}}^{(\kappa,\mu)}_{l_{\kappa,\mu}l'_{\kappa,\mu}} g^{(\kappa,\mu)}_{l'_{\kappa,\mu}} \right\rangle \tag{6.33}$$

one obtains the variational EOMs for the GWP parameters in matrix notation,

$$i\underline{C}^{(\kappa,\mu)}\dot{\vec{\Lambda}}^{(\kappa,\mu)} = \vec{Y}^{(\kappa,\mu)} \tag{6.34}$$

6.3 Summary of Equation of Motions

To recapitulate, the equations of motion are presented in matrix notation:

$$i\dot{\vec{A}} = \underline{H}^{(\Phi)}\vec{A} \tag{6.35}$$

$$i\underline{\tilde{S}}^{(\kappa)}\dot{\vec{B}}^{(\kappa)} = \left[\underline{\tilde{H}}^{(\kappa)} - i\underline{\tilde{\tau}}^{(\kappa)}\right]\vec{B}^{(\kappa)} \tag{6.36}$$

$$i\underline{C}^{(\kappa,\mu)}\dot{\vec{\Lambda}}^{(\kappa,\mu)} = \vec{Y}^{(\kappa,\mu)} \tag{6.37}$$

The dynamical equations combine a standard MCTDH-like equation for the first-layer coefficients $\vec{A}$, a G-MCTDH-like equations for the second-layer coefficients $\vec{B}^{(\kappa)}$ and the GWP parameters $\vec{\Lambda}^{(\kappa,\mu)}$. Due to the hierarchical two-layer structure the equation for the GWP parameters is restricted to the lower (κ,μ)th subspace (c.f. κth subspace in G-MCTDH) and therefore leading to a significant reduction of the numerical effort for inversion of the $\underline{C}^{(\kappa,\mu)}$ matrix.

6.4 Scaling Properties

The scaling behavior is again analyzed by counting the multiplications for the evaluation of the EOMs. For the scaling analysis the same assumptions are made as for G-MCTDH: f_1 shall be the number of first-layer modes ($\kappa = 1, \cdots, f_1$). Each first-layer mode κ is split into the same number of second-layer modes $f^{(1)} = \cdots = f^{(f_1)} =: f_2$. We further assume that the length of all basis sets is $n^{(1)} = \cdots = n^{(f_1)} =: n_1$ in the first-layer and $n^{(1,1)} = \cdots = n^{(f_1,f_2)} =: n_2$ in the second-layer is equal for all modes and that all second-layer SPFs have the same number $d_{1,1} = \cdots = d_{f_1,f_2} = d_2$ of degrees of freedom.

The numerically most expensive steps turn out to be the calculation of the first- and second-layer mean-fields ($\hat{\mathcal{H}}^{(\kappa)}_{j_\kappa j'_{\kappa,\mu}}$ and $\hat{\mathcal{H}}^{(\kappa,\mu)}_{l_{\kappa,\mu}l'_{\kappa,\mu}}$) and solving the system of linear equations for $\dot{\vec{\Lambda}}^{(\kappa,\mu)}$ (particularly the $\underline{C}$ matrix inversion). Similar to G-MCTDH

and MCTDH the Hamiltonian is expanded as a sum of products (c.f. Eqn. 4.40), both in the first and the second layer:

$$\hat{H} = \sum_{t=1}^{m_1} a_t \prod_{\kappa=1}^{f_1} \hat{h}_t^{(\kappa)} \left(\vec{x}_\kappa\right) \tag{6.38}$$

$$\hat{h}_t^{(\kappa)} \left(\vec{x}_\kappa\right) = \sum_{u=1}^{m_2} b_{t,u}^{\kappa} \prod_{\mu=1}^{f_2} \hat{h}_{t,u}^{(\kappa,\mu)} \left(\vec{x}_{\kappa,\mu}\right) \tag{6.39}$$

The second-layer Hamiltonian operators are further expanded to get the one-dimensional operators acting on a DOF,

$$\hat{h}_{t,u}^{(\kappa,\mu)} \left(\vec{x}_{\kappa,\mu}\right) = \sum_{v=1}^{m_3} \prod_{d=1}^{d_2} \hat{h}_{t,u,v}^{(\kappa,\mu,d)} \left(x_{\kappa,\mu,d}\right) \tag{6.40}$$

By counting the number of multiplications needed to evaluate these function one gets the overall scaling of the 2-Layer-Gaussian-MCTDH method,[1]

$$\text{effort}^{\text{2L-G-MCTDH}} \sim m_1 f_1^2 n_1^{f_1+1} + m_1 m_2 f_1 f_2 n_1 n_2^{f_2+1} \left(f_2 + n_1\right) + f_1 f_2 \left(d_2 n_2\right)^3 \tag{6.41}$$

The first term represents the scaling for the first-layer mean-fields and is equivalent to G-MCTDH, the second term describes the scaling of the second-layer mean-fields and the last term stands for the effort for the $\underline{C}$ matrix inversion. For the mean-fields only correlated terms contribute (uncorrelated terms fall back to the corresponding density matrices) and need to be considered. As a side note it should be mentioned that solving the equation for $\dot{\vec{B}}^{(\kappa)}$ is only slightly less expensive ($\sim m_1 m_2 f_1 f_2 n_1 n_2^{f_2}$ multiplications) than the calculation of the second layer mean-fields.

As already mentioned the scaling for the first-layer mean-fields is similar to that for the mean-fields of G-MCTDH. However, since the first-layer SPFs of the two-layer approach are designed to be more flexible than the G-MCTDH GWPs, one can expect that fewer basis functions (n_1) are needed. Therefore the calculation becomes (assuming the same number of Hamiltonian terms $m_1 = m$) indeed less expensive.

By comparing the scaling of G-MCTDH (c.f Eqn. 4.62) to the two-layer variant (Eqn. 6.41) one can directly see a big improvement resulting from the last term whose scaling is reduced from $\left(\tilde{dn}\right)^3 \rightarrow \left(d_2 n_2\right)^3$, since the $\underline{C}$ matrix inversion is now carried out in the lower-dimensional second-layer subspaces. Nevertheless one

has to find a balance between the gain and the additional effort for the second-layer mean-field calculation (second term of Eqn. 6.41).

6.4.1 Scaling Properties: Examples

Here, two examples are presented that convey a better understanding of the improved scaling behavior of the two-layer method. In particular, the effort of vMCG and 2L-G-MCTDH is compared, such that we consider specifically $f = f_1 = 1$ and consequently $m = m_1$.

The first example is based on a reduced 4-DOF vibronic coupling model for the electronically excited states of the pyrazine molecule, where the dynamics around the S_2 — S_1 conical intersection is studied.[81] As reported in Ref.,[81] a large number of 200 GWPs was necessary to achieve a sufficiently converged vMCG result. Therefore, the relative effort, with $d = 4$ and $n = 200$, can be approximated as $n^2 + (dn)^3 = 512.0 \times 10^6$. MCTDH calculations for the same system were carried out with ~ 10 SPFs; the effort of these reference calculations will be taken as a lower-limit estimate for the 2L-G-MCTDH effort calculation.

To be on the safe side, a rather conservative guess of $n_1 = 20$ SPFs is taken in our two-layer calculations. Two cases with different mode combination schemes are considered:

1. four 1-dimensional second-layer modes ($f_2 = 4, d_2 = 1, m_2 = 14$)
2. two 2-dimensional second-layer modes ($f_2 = 2, d_2 = 2, m_2 = 8$)

Here, the first case is less favorable due to the more costly second-layer mean-field calculation. For the first case we assume $n_2 = 5$ GWPs per second-layer mode, resulting in overall $n_2^{f_2} = 5^4 = 625$ second-layer GWP configurations (to be compared with 200 GWPs for vMCG). Based on this, the numerical effort, from Eqn. 6.41, of 84.0×10^6 is calculated. This is around 16% of the effort one estimates for vMCG, even though the latter employed less configurations.

An even better scaling is achieved for the second case with two 2-dimensional second-layer modes. Assuming $n_2 = 15$ second-layer GWP configurations per second-layer mode (resulting in $n_2^{f_2} = 15^2 = 225$ in total) one obtains a relative effort of 23.8×10^6, which is about 5% of the corresponding vMCG effort. The doubly logarithmic plot in Fig. 6.1(a) illustrates the behavior of the numerical

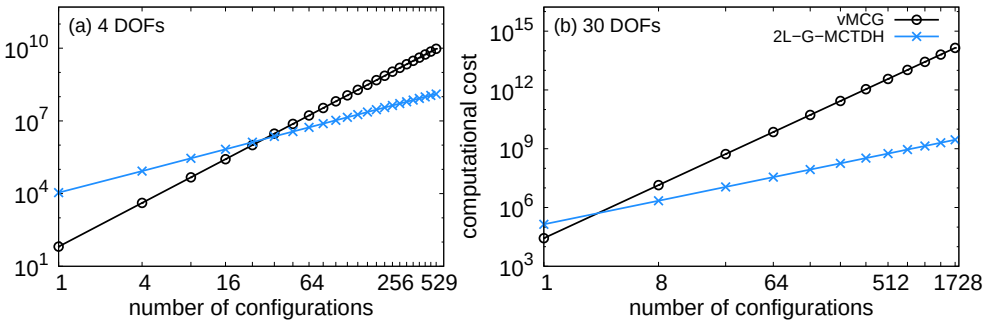

Figure 6.1: Comparison of of the estimated scaling behavior of 2-Layer-G-MCTDH vs. vMCG. with increasing number of configurations. n_{conf} refers to $n_{\text{conf}} = n$ for vMCG and $n_{\text{conf}} = n_2^{f_2}$ for 2L-G-MCTDH. (a) 4 DOFs with $f_1 = 1, m_1 = 1, n_1 = 20, f_2 = 2, m_2 = 8$ and $d_2 = 2$ for 2L-G-MCTDH. (b) 30 DOFs with $f_1 = 1, m_1 = 1, n_1 = 20, f_2 = 3, m_2 = 100$ and $d_2 = 10$ for 2L-G-MCTDH. For details on the numerical effort see chapter 4.4.5 (vMCG) and chapter 6.4 (2L-G-MCTDH).

effort with increasing number of configurations compared to vMCG with the same parameter set ($f_2 = 2, d_2 = 2, m_2 = 8$). Already around 30 configurations ($n_2^{f_2}$, not n_2!) a turn over is seen, indicating that 2L-G-MCTDH is more favorable than vMCG.

The second example is an extension of the previous model to estimate the scaling for more DOFs. Typically, vMCG is used with up to 30 DOF. For this dimensionality up to 50 Gaussian basis functions are practicable,[89] but the results are presumably not yet converged (noting that for the small 4-DOF pyrazine system, 200 GWPs were necessary for a near-converged result). For vMCG the relative effort is then 3.375×10^9, already one order of magnitude higher than for the 4-DOF example. With 2L-G-MCTDH, using again $n_1 = 20$ first-layer SPFs, where each SPF contains three 10-dimensional second-layer modes ($f_2 = 3, d_2$ and assuming $m_2 = 100$), a comparable numerical effort is reached for 12 GWP functions per second-layer mode. This results in $n_2^{f_2} = 12^3 = 1728$ second-layer GWP configurations, which is a significantly larger number than for vMCG. This is again illustrated in Fig. 6.1(b). One can see that the turn-over point is noticeably shifted towards a lower total number of configurations. Hence, the 2-Layer-Gaussian approach becomes more and more favorable with a growing number of DOFs.

6.5 Multi-State 2-Layer-Gaussian-MCTDH

So far the method has only been described for single-surface systems. To be able to study non-adiabatic dynamics, the representation of the Hamiltonian and the wave function ansatz have to be extended in order to describe a multi-state wave function and the equations of motion need to be reformulated.

2L-G-MCTDH uses a sum-of-products representation of the Hamiltonian (see Eqn. 6.38). By expanding the Hamiltonian in a set of electronic states one can rewrite the Hamiltonian,

$$\hat{H} = \sum_{s}^{n_s} \sum_{s'}^{n_s} |s\rangle \, \hat{H}^{(ss')} \, \langle s'| \tag{6.42}$$

where n_s is the number of electronic states.[25] Each component of the Hamiltonian corresponds to a combination of two electronic states ($s = s'$ or $s \neq s'$) and is then further expanded in a sum of products of one-particle Hamiltonians as in Eqns. 6.38, 6.39 and 6.40. Finally, each term carries two additional indices (s, s').

There are several options of how to choose the multi-state wave function ansatz. The simplest approach is the so-called single-set formulation,[90,91] where the electronic states are treated as an additional mode like the other DOFs. The number of single particle functions for such an electronic mode is then equal to the number of electronic states (Eqn. 6.43). In this approach the configurations Φ_J describe the wave packet on all electronic states such that usually more configurations are needed in order to converge the calculation,

$$\begin{aligned} \Psi\left(\vec{X}, t\right) &= \sum_{J} \sum_{s}^{n_s} A_J^{(s)}(t) \, \Phi_J\left(\vec{X}, t\right) |s\rangle \\ &= \sum_{j_1}^{n_1} \sum_{j_2}^{n_2} \cdots \sum_{j_f}^{n_f} \sum_{s}^{n_s} A_{j_1, j_2, \ldots, j_f}^{(s)}(t) \prod_{\kappa=1}^{f} \varphi_{j_\kappa}^{(\kappa)}\left(\vec{x}_\kappa, t\right) |s\rangle \end{aligned} \tag{6.43}$$

This represents a time-independent approach for the electronic particle and is used within this work for the 2-L-G-MCTDH. Another approach for the single-set variant – which is not employed in this work – uses time-dependent electronic SPFs,

$$\Psi\left(\vec{X}, t\right) = \sum_{j_1}^{n_1} \sum_{j_2}^{n_2} \cdots \sum_{j_f}^{n_f} \sum_{j_s}^{N} A_{j_1, j_2, \ldots, j_f, j_s}(t) \prod_{\kappa=1}^{f} \varphi_{j_\kappa}^{(\kappa)}\left(\vec{x}_\kappa, t\right) \left|\varphi_{j_s}^{(el)}(t)\right\rangle \tag{6.44}$$

with an arbitrary number of N electronic SPFs of type $\left|\varphi_s^{(el)}\right\rangle = \sum_s^{n_s} c_s^{j_s}(t) \, |s\rangle$.

The alternative approach is the so-called multi-set formulation.[92,93] Here, the SPFs are restricted to belong to a specific electronic state ($\rightarrow \varphi_{j_\kappa}^{(\kappa,s)}$). Hence, the B-coefficients and the GWPs are also state-specific. In this approach the wave function is written as a linear combination of state-specific wave functions,

$$\begin{aligned}\Psi\left(\vec{X},t\right) &= \sum_{s}^{n_s} \Psi^{(s)} \left|s\right\rangle \\ &= \sum_{J} \sum_{s}^{n_s} A_J^{(s)}\left(t\right) \Phi_J^{(s)}\left(\vec{X},t\right) \left|s\right\rangle \\ &= \sum_{j_1}^{n_1} \sum_{j_2}^{n_2} \cdots \sum_{j_f}^{n_f} \sum_{s}^{n_s} A_{j_1,j_2,\ldots,j_f}^{(s)}\left(t\right) \prod_{\kappa=1}^{f} \varphi_{j_\kappa}^{(\kappa,s)}\left(\vec{x}_\kappa,t\right) \left|s\right\rangle \end{aligned} \tag{6.45}$$

with,

$$\varphi_{j_\kappa}^{(\kappa,s)}\left(\vec{x}_\kappa,t\right) = \sum_{L_\kappa} B_{L_\kappa}^{(\kappa,s)}\left(t\right) G_{L_\kappa}^{(\kappa,s)}\left(\vec{x}_{\kappa,\mu},t\right) \tag{6.46}$$

In addition to these two standard approaches one can think of a new scheme explicitly tailored to the two-layer approach, where the single- and multi-set approach are combined. This approach will be called "hybrid-set" in the following. Here, the first-layer SPFs are still state-specific, in the sense that the B coefficients are restricted to one electronic state. However, the GWPs are "shared" by all electronic states. Therefore, the $\varphi_{j_\kappa}^{(\kappa,s)}$ now read as follows:

$$\varphi_{j_\kappa}^{(\kappa,s)}\left(\vec{x}_\kappa,t\right) = \sum_{L_\kappa} B_{L_\kappa}^{(\kappa,s)}\left(t\right) G_{L_\kappa}^{(\kappa)}\left(\vec{x}_{\kappa,\mu},t\right) \tag{6.47}$$

In the following, equations of motion for these three approaches will be presented. The derivation follows the same steps as outlined in chapter 6.2.

6.5.1 Single-Set 2L-G-MCTDH

First, the EOMs for the single-set variant are presented. As compared to the single-state EOMs, the equation for the A coefficients now carries the indices for the electronic states,

$$i\dot{\vec{A}}^{(s)} = \underline{H}^{(\Phi,ss')}\vec{A}^{(s')} \tag{6.48}$$

where the Hamiltonian matrix elements are defined as

$$\hat{H}_{JL}^{(\Phi,ss')} = \left\langle \Phi_J \middle| \hat{H}^{(ss')} \middle| \Phi_L \right\rangle \tag{6.49}$$

Likewise, the new density matrices are state-specific; these are derived from state-specific single hole functions,

$$\rho^{(\kappa,s)}_{j_\kappa,j'_\kappa} = \left\langle \psi^{(\kappa,s)}_{j_\kappa} \middle| \psi^{(\kappa,s)}_{j'_\kappa} \right\rangle \tag{6.50}$$

$$\rho^{(\kappa,\mu,s)}_{l_{\kappa,\mu}l'_{\kappa,\mu}} = \left\langle \psi^{(\kappa,\mu,s)}_{l_{\kappa,\mu}} \middle| \psi^{(\kappa,\mu,s)}_{l'_{\kappa,\mu}} \right\rangle \tag{6.51}$$

where the SHFs are given by,

$$\psi^{(\kappa,s)}_{j'} = \sum_{J^{(\kappa)}} A^{(s)}_{J^{(\kappa:j')}} \Phi_{J^{(\kappa)}} \tag{6.52}$$

$$\psi^{(\kappa,\mu,s)}_{l'} = \sum_{j_\kappa} \left[\sum_{L^{(\mu)}} B^{(\kappa)}_{j_\kappa,L^{(\mu:l')}} G^{(\kappa)}_{L^{(\mu:l')}} \right] \psi^{(\kappa,s)}_{j_\kappa} \tag{6.53}$$

Since the SPFs are not exclusive to one state, the projectors do not change.

With these definitions, the equation for the B coefficients is then written as,

$$i\underline{\tilde{S}}^{(\kappa)} \dot{\vec{B}}^{(\kappa)} = \left[\sum_{s}^{n_s} \sum_{s'}^{n_s} \underline{\tilde{H}}^{(\kappa,ss')} - i\underline{\tilde{\tau}}^{(\kappa)} \right] \vec{B}^{(\kappa)} \tag{6.54}$$

with,

$$\tilde{H}^{(\kappa,ss')}_{j_\kappa L_\kappa, j'_\kappa L'_\kappa} = \left\langle G^{(\kappa)}_{L_\kappa} \middle| \left(\hat{1} - P^{(\kappa)}\right) \left[\left(\underline{\rho}^{(\kappa,s)}\right)^{-1} \underline{\hat{\mathcal{H}}}^{(\kappa,ss')} \right]_{j_\kappa j'_\kappa} G^{(\kappa)}_{L'_\kappa} \right\rangle \tag{6.55}$$

Similarly to the changes for the A coefficients, one obtains additional sums over the electronic states and therefore state-specific mean-fields. The formula for the GWP parameters looks identical at first sight,

$$i\underline{C}^{(\kappa,\mu)} \dot{\vec{\Lambda}}^{(\kappa,\mu)} = \vec{Y}^{(\kappa,\mu)} \tag{6.56}$$

but the definitions of the $\underline{C}$ matrix and the $\vec{Y}$ vector are again changed by additional sums over the electronic states:

$$C^{(\kappa,\mu)}_{l_{\kappa,\mu}\alpha, l'_{\kappa,\mu}\beta} = \left[\sum_{s}^{n_s} \rho^{(\kappa,\mu,s)}_{l_{\kappa,\mu}l'_{\kappa,\mu}} \right] \left\langle \frac{\partial}{\partial\alpha} g^{(\kappa,\mu)}_{l_{\kappa,\mu}} \middle| \left(\hat{1} - \hat{P}^{(\kappa,\mu)}\right) \frac{\partial}{\partial\beta} g^{(\kappa,\mu)}_{l'_{\kappa,\mu}} \right\rangle \tag{6.57}$$

$$Y^{(\kappa,\mu)}_{l_{\kappa,\mu}\alpha} = \sum_{s}^{n_s} \sum_{s'}^{n_s} \sum_{l'_{\kappa,\mu}} \left\langle \frac{\partial}{\partial\alpha} g^{(\kappa,\mu)}_{l_{\kappa,\mu}} \middle| \left(\hat{1} - \hat{P}^{(\kappa,\mu)}\right) \hat{\mathcal{H}}^{(\kappa,\mu,ss')}_{l_{\kappa,\mu}l'_{\kappa,\mu}} g^{(\kappa,\mu)}_{l'_{\kappa,\mu}} \right\rangle \tag{6.58}$$

6.5.2 Hybrid-Set 2L-G-MCTDH

For the hybrid-set approach the definitions for the density matrices are unchanged, but the single-hole functions are redefined as follows:

$$\psi_{j'}^{(\kappa,s)} = \sum_{J^{(\kappa)}} A^{(s)}_{J^{(\kappa:j')}} \Phi^{(s)}_{J^{(\kappa)}} \tag{6.59}$$

$$\psi_{l'}^{(\kappa,\mu,s)} = \sum_{j_\kappa} \left[\sum_{L^{(\mu)}} B^{(\kappa,s)}_{j_\kappa, L^{(\mu:l')}} G^{(\kappa)}_{L^{(\mu:l')}} \right] \psi_{j_\kappa}^{(\kappa,s)} \tag{6.60}$$

Additionally the first-layer projector,

$$\hat{P}^{(\kappa,s)} = \sum_{j_\kappa} \left| \varphi_{j_\kappa}^{(\kappa,s)} \right\rangle \left\langle \varphi_{j_\kappa}^{(\kappa,s)} \right| \tag{6.61}$$

is now defined to be state specific.

The EOMs for the hybrid-set case show that the equations for the GWP parameters are the same as for the single-set case. While the equation for the A coefficients only differs by state specific configurations in the Hamiltonian matrix ($\hat{H}_{JL}^{(\Phi,ss')} = \left\langle \Phi_J^{(s)} \middle| \hat{H}^{(ss')} \middle| \Phi_L^{(s')} \right\rangle$), the EOM for the B coefficients is now given by,

$$i\underline{\tilde{S}}^{(\kappa)} \dot{\vec{B}}^{(\kappa,s)} = \sum_{s'}^{n_s} \left[\underline{\tilde{H}}^{(\kappa,ss')} - i\underline{\tilde{\tau}}^{(\kappa)} \right] \vec{B}^{(\kappa,s')} \tag{6.62}$$

where

$$\tilde{H}^{(\kappa,ss')}_{j_\kappa L_\kappa, j'_\kappa L'_\kappa} = \left\langle G^{(\kappa)}_{L_\kappa} \middle| \left(\hat{1} - P^{(\kappa,s)} \right) \left[\left(\underline{\rho}^{(\kappa,s)} \right)^{-1} \underline{\hat{\mathcal{H}}}^{(\kappa,ss')} \right]_{j_\kappa j'_\kappa} G^{(\kappa)}_{L'_\kappa} \right\rangle \tag{6.63}$$

such that only the definition of the projector is changed.

6.5.3 Multi-Set 2L-G-MCTDH

Lastly, the multi-set approach is presented. Since the GWPs are now also state-specific, one needs to rewrite the second-layer single-hole functions,

$$\psi_{l'}^{(\kappa,\mu,s)} = \sum_{j_\kappa} \left[\sum_{L^{(\mu)}} B^{(\kappa,s)}_{j_\kappa, L^{(\mu:l')}} G^{(\kappa,s)}_{L^{(\mu:l')}} \right] \psi_{j_\kappa}^{(\kappa,s)} \tag{6.64}$$

Furthermore, the second-layer projector,

$$\hat{P}^{(\kappa,\mu,s)} = \sum_{l_{\kappa,\mu}} \sum_{l'_{\kappa,\mu}} \left| g_{l_{\kappa,\mu}}^{(\kappa,\mu,s)} \right\rangle \left(\underline{S}^{(\kappa,\mu,s)} \right)^{-1} \left\langle g_{l'_{\kappa,\mu}}^{(\kappa,\mu,s)} \right| \tag{6.65}$$

becomes state specific as well. In fact, all EOMs change by making the GWPs state specific. In particular, the equations for the A and B coefficients exhibit additional

state indices. (These equations are not presented here since they represent a straightforward extension to the single-state form.) The equations for the GWP parameters read as follows,

$$i\underline{C}^{(\kappa,\mu,s)}\dot{\vec{\Lambda}}^{(\kappa,\mu,s)} = \vec{Y}^{(\kappa,\mu)} \tag{6.66}$$

with the definitions for $\underline{C}^{(\kappa,\mu,s)}$ and $\vec{Y}^{(\kappa,\mu,s)}$ vector, where essentially only one sum over the electronic states is still present,

$$C^{(\kappa,\mu,s)}_{l_{\kappa,\mu}\alpha,l'_{\kappa,\mu}\beta} = \rho^{(\kappa,\mu,s)}_{l_{\kappa,\mu}l'_{\kappa,\mu}} \left\langle \frac{\partial}{\partial\alpha} g^{(\kappa,\mu,s)}_{l_{\kappa,\mu}} \middle| \left(\hat{1} - \hat{P}^{(\kappa,\mu)}\right) \frac{\partial}{\partial\beta} g^{(\kappa,\mu,s)}_{l'_{\kappa,\mu}} \right\rangle \tag{6.67}$$

$$Y^{(\kappa,\mu,d)}_{l_{\kappa,\mu}\alpha} = \sum_{s'}^{n_s} \sum_{l'_{\kappa,\mu}} \left\langle \frac{\partial}{\partial\alpha} g^{(\kappa,\mu,s)}_{l_{\kappa,\mu}} \middle| \left(\hat{1} - \hat{P}^{(\kappa,\mu)}\right) \hat{\mathcal{H}}^{(\kappa,\mu,ss')}_{l_{\kappa,\mu}l'_{\kappa,\mu}} g^{(\kappa,\mu,s')}_{l'_{\kappa,\mu}} \right\rangle \tag{6.68}$$

6.5.4 Comparison of Single-Set, Multi-Set, and Hybrid-Set Approaches

All of the three presented approaches have their advantages and disadvantages. The single-set approach is the computationally cheapest approach, but one might need more SPFs as compared to the multi-set in order to achieve convergence. Especially in non-adiabatic dynamics situations where the potential energy surfaces are very similar for the different electronic states – e.g., nearly parallel – single-set can be useful. In other cases, the multi-set approach is the preferred variant. The hybrid approach builds a bridge between these two approaches by making the first-layer SPFs state specific and therefore more flexible. Nevertheless, the GWPs are still state independent and one might need to many of them. Again, the features of the dynamics on coupled electronic states will determine which approach is best adapted.

7 | The 2L-G-MCTDH Method: Implementation Details

A central part of this work is the implementation of the 2L-G-MCTDH method. The implementation was initiated by Matthias Ruckenbauer (post-doctoral fellow in our group from 2011-2013) and further extended within this work. Fortran90 was chosen as programming language as it is designed to be easily readable and create high-performance codes, especially for scientific computations. In this chapter details about the implementation of the code are presented. First, the overall structure of the program is illustrated, second, the setup of the wave function is demonstrated, and third, an efficient algorithm for the evaluation of matrix-vector products is demonstrated; this algorithm is adapted to the wave function in tensor form and a sum-over-products (SOP) form of the Hamiltonian and is used extensively in the program. Finally, additional remarks are made with regard to the implementation of some selected equations.

7.1 Program Structure

The program is structured in a modular way, where each module focuses on a specific task or part of the program. The modules of the program are listed in Tab. 7.1. In general, the modules are inter-dependent. This dependency is reflected in this list such that modules generally depend on those listed above.

The program flow follows the natural flow of a time propagation. After reading the input and operator files, the wave function is created, along with some auxiliary arrays that store the derivatives of the wave function, the arrays that store the Hamilton operator, and arrays to store the first- and second-layer Hamiltonian and mean-field matrices. After initializing the wave function – which is usually done by reading it from a file – the time propagation starts with the integration loop. In each integration step, the derivatives are computed and the wave function is propagated for the chosen timestep. After checking if the wave function should be written to file and/or the propagation is finished, the whole process is repeated or the calculation is finalized. Fig. 7.1 illustrates the program flow in a simplified manner.

Table 7.1: Module structure of the program.

module	description
`sysparam`	handles type definitions for real and integer variables
`timingmod`	organizes the timing measurements for subroutines and the total program
`global`	handles definitions, e.g. conversion factors and globally available parameters
`psi`	definition of the wave function, auxiliary functions for easier access on specific elements
`invert`	includes the routines that drive the inversion of the program
`storagemod`	contains definitions and initialization routines for storage arrays, e.g. Gaussian moment pre-factors
`gaussmod`	comprises routines that handle GWP related operations like the calculation of Gaussian moments (overlap and pre-factors)
`hamilton`	includes anything related to the Hamilton operator
`derivatives`	contains the routines necessary to calculate the time-derivative of the wave function
`writing`	handles all output regarding the wave function, properties and expectation values
`integrators`	handles the integration of the wave function (presently two integrators are implemented: Adams-Bashforth-Moulten[94] and 4th order Runge-Kutte[95,96])
`propagator`	driver for the propagation
`inputmod`	organizes reading of the input and operator file
`init_wf`	handles the initialization of the wave function (read from file or setting a random initial condition)
`main`	main program, follows the same process as the flow chart in Fig. 7.1

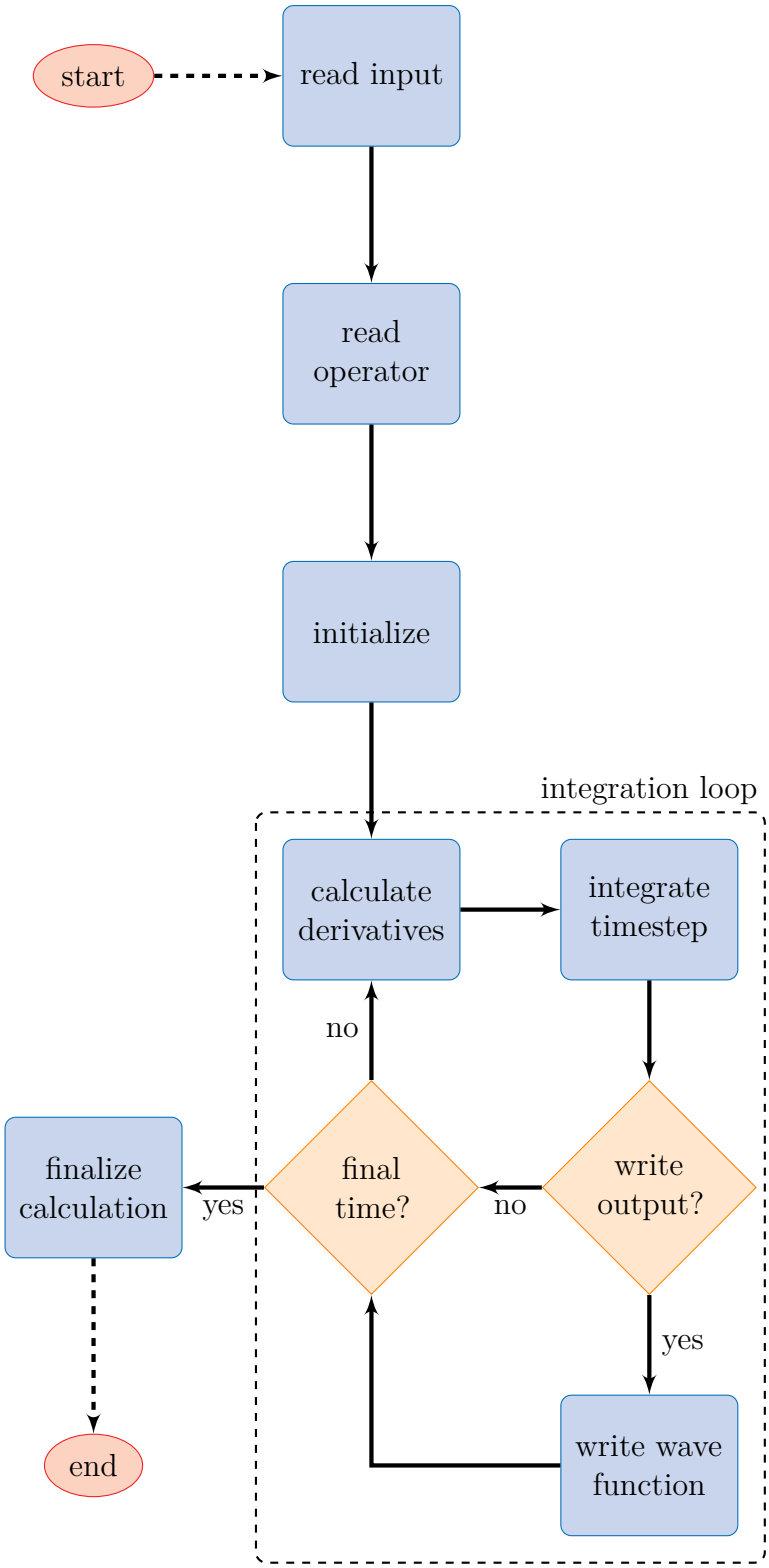

Figure 7.1: Flowchart illustrating the overall composition of the program.

7.2 Memory Layout

7.2.1 Memory Layout of the Wave Function

The structure of the wave function is organized within several arrays. The number of first-layer modes f is stored in a variable with the same name `f`. The number of second-layer modes for each κ-mode is stored in the array `f_kappa`. Each second-layer mode can be composed of individual degrees of freedom and their number for each κ, μ-mode is stored in `mudim`. The number of first- and second-layer SPFs are stored in the arrays `n_kappa` and `n_kappamu`, respectively.

The coefficients and GWP parameters are stored in separate arrays. The A and B coefficients are uniquely defined with a multi-index $J = j_1, j_2, \ldots, j_f$ in case of the first-layer coefficients A, and $L_\kappa = l_1, l_2, \ldots, l_{f_\kappa}$ for the second-layer coefficients B. The coefficients are both stored in individual one-dimensional arrays. For the A coefficients, the array index is equivalent to the multi-index $J(i)$, i.e., $A(i) = A(J(i))$. Here, $n_{Aconfig} = \prod_\kappa^f n_\kappa$ gives the total number of first-layer configurations and therefore the length of the A coefficient array. The sequence of configurations is organized such that the sub-indices j_κ are incremented from left to right resulting in,

$$
\begin{array}{lcccccccc}
J(1) & = & 1_1, & 1_2, & \ldots, & 1_\kappa, & \ldots, & 1_f \\
J(2) & = & 2_1, & 1_2, & \ldots, & & & 1_f \\
\vdots & & & & & & \vdots & \\
J(n_1) & = & n_1, & 1_2, & \ldots, & & & 1_f \\
J(n_1+1) & = & 1_1, & 2_2, & \ldots, & 1_\kappa, & \ldots, & 1_f \\
J(n_1+2) & = & 2_1, & 2_2, & \ldots, & & & 1_f \\
\vdots & & & & & & \vdots & \\
J(n_{Aconfig}) & = & n_1, & n_2, & \ldots, & & & n_f
\end{array}
$$

for the order of the A coefficient array `avector`. The array for the B coefficients `bvector` is organized in a similar way in blocks with increasing κ. Each κ block is further organized in smaller sub-blocks with increasing j_κ. These κ, j_κ blocks then have a similar structure as the A coefficients, containing the $B^{(\kappa)}_{j_\kappa, L_\kappa}$ with an increasing number of the $L_\kappa(i)$ index.

Within the program FGs are used throughout. Hence, the GWPs are stored as one-dimensional GWPs in the two-dimensional array `gaussians`, containing the three parameters $\vec{\Lambda}^{(\kappa,\mu)}_{l_{\kappa,\mu}} = \left(\underline{a}^{(\kappa,\mu)}_{l_{\kappa,\mu}}, \vec{\xi}^{(\kappa,\mu)}_{l_{\kappa,\mu}}, \eta^{(\kappa,\mu)}_{l_{\kappa,\mu}}\right)$ to describe the GWP. The total

$$\text{gaussians} = \begin{pmatrix} a_{l_{\kappa,\mu}=1}^{(\kappa=1,\mu=1,d=1)} & \xi_1^{(1,1,1)} & \eta_1^{(1,1,1)} \\ a_1^{(1,1,2)} & \xi_1^{(1,1,2)} & \eta_1^{(1,1,2)} \\ \vdots & \vdots & \vdots \\ a_1^{\left(1,1,d_{1,1}\right)} & \xi_1^{\left(1,1,d_{1,1}\right)} & \eta_1^{\left(1,1,d_{1,1}\right)} \\ a_2^{(1,1,1)} & \xi_2^{(1,1,1)} & \eta_2^{(1,1,1)} \\ \vdots & \vdots & \vdots \\ a_{n_{1,1}}^{(1,1,1)} & \xi_{n_{1,1}}^{(1,1,1)} & \eta_{n_{1,1}}^{(1,1,1)} \\ a_1^{(1,2,1)} & \xi_1^{(1,2,1)} & \eta_1^{(1,2,1)} \\ \vdots & \vdots & \vdots \\ a_1^{\left(1,f_1,1\right)} & \xi_1^{\left(1,f_1,1\right)} & \eta_1^{\left(1,f_1,1\right)} \\ a_1^{(2,1,1)} & \xi_1^{(2,1,1)} & \eta_1^{(2,1,1)} \\ \vdots & \vdots & \vdots \\ a_{n_{f,f_f}}^{\left(f,f_f,d_{f,f_f}\right)} & \xi_{n_{f,f_f}}^{\left(f,f_f,d_{f,f_f}\right)} & \eta_{n_{f,f_f}}^{\left(f,f_f,d_{f,f_f}\right)} \end{pmatrix}$$

Figure 7.2: Memory setup of the `gaussians` array

dimension of the `gaussians`-array is $n_{primGauss} \times 3$, where $n_{primGauss}$ is the total number of one-dimensional GWPs. A one-dimensional GWP $g_{l_{\kappa,\mu}}^{(\kappa,\mu,d)}$ is described by four indices $\left\{\kappa, \mu, l_{\kappa,\mu}, d\right\}$. κ and μ define the mapping to the first- and second-layer modes, d is the primitive dimension (the DOF) of the GWP and $l_{\kappa,\mu}$ is the number of the second-layer configuration the GWP belongs to. The array is then built in several blocks, all divided into smaller sub-blocks. The GWPs are stored in blocks with increasing κ, where each κ block is divided into smaller blocks with increasing μ. The (κ, μ) blocks are further subdivided in blocks with increasing $l_{\kappa,\mu}$, each defining a multi-dimensional GWP which is stored with increasing d. An illustration of this ordering scheme is given in Fig. 7.2,

It should be noted that the width parameter a of the GWP is related to the standard deviation of a Gaussian distribution by,

$$a = \frac{1}{2\sqrt{\sigma}}. \tag{7.1}$$

Due to this relation, the width of the GWPs is inversely proportional to a, thus the width is reduced with increasing a.

7.2.2 Memory Layout of the Hamiltonian

The sum-of-products (SOP) Hamiltonian (Eqns. 6.38, 6.39 and 6.40) is organized within several variables and arrays as explained below. The number of first-layer operator elements is given by the variable `me`. The coefficients for these operator elements a_t are stored in the array `ae`.

The numbers of summands for the second-layer Hamilton operators for each κ subspace are stored in the array `me_rek`. The coefficients for the second-layer Hamilton operators are stored in array `be`. On the level of the second-layer operators the code distinguishes between (Cartesian) kinetic energy elements ($\hat{T}$) and potential terms ($\hat{V}$). The array `op_reksemu` stores the information which type of operator belongs to this operator element. In this context a "0" identifies a potential term (built-up of monomials of type $\hat{x}^n$), while "1" calls the kinetic energy calculation. Presently, only Hamiltonians in the form of monomials and polynomials are implemented. An extension of the code to other (user-defined) functions is easily possible, since the necessary local harmonic approximation – which is required to express the Hamiltonian matrix elements in Gaussian moments – has already been generalized to third order.

Finally, the elements defining the one-dimensional elements are stored in the arrays `me_reksemu` and `op_primdim`. `me_reksemu` stores the number of summands included in this operator element and `op_primdim` holds the information about the one-dimensional operator elements of the monomial order.

7.3 Implementation Details

7.3.1 Gaussian Moments

One of the key advantages of using parametrized GWPs as basis functions is the availability of analytic expressions for integrals of type

$$\langle g \,|\, x^n \,|\, g' \rangle = \int_{-\infty}^{\infty} \bar{g}\,(x)\, x^n g'\,(x)\, dx \tag{7.2}$$

i.e., so-called Gaussian moments. Any Gaussian moment of this form can be rearranged to give the zeroth-order moment (i.e., the overlap of the GWPs) multiplied with a prefactor. The zeroth-order moment of a one-dimensional GWP is given as follows, using the definition of the GWPs as introduced above,

$$\begin{aligned}
\langle g \,|\, g' \rangle =& \int_{-\infty}^{\infty} \exp\left(\bar{a}x^2 + \bar{\xi}x + \bar{\eta}\right) \exp\left(a'x^2 + \xi'x + \eta'\right) dx \\
=& \exp\left(\bar{\eta} + \eta'\right) \int_{-\infty}^{\infty} \exp\left(\left(\bar{a} + a'\right) x^2 + \left(\bar{\xi} + xi'\right) x\right) dx \\
=& \exp\left(q\right) \int_{-\infty}^{\infty} \exp\left(-ox^2 + px\right) dx \\
=& \exp\left(q + \frac{p^2}{4o}\right) \frac{1}{\sqrt{o}} \int_{-\infty}^{\infty} \exp\left(-y^2\right) dy \\
=& \exp\left(q + \frac{p^2}{4o}\right) \frac{1}{\sqrt{o}} \sqrt{\frac{\pi}{o}} \\
=& \exp\left(\bar{\eta} + \eta' - \frac{\left(\bar{\xi} + \xi'\right)^2}{4\left(\bar{a} + a'\right)}\right) \sqrt{-\frac{\pi}{\bar{a} + a'}}
\end{aligned} \tag{7.3}$$

where $-o = \bar{a} + a'$,$p = \bar{\xi} + \xi'$, $q = \bar{\eta} + \eta'$ and $y = \sqrt{o}\left(x - \frac{p}{2o}\right)$.
An arbitrary Gaussian moment is then expressed by,

$$\langle g \,|\, x^n \,|\, g' \rangle = \langle g \,|\, g' \rangle \cdot \sum_{j=0}^{m=\lfloor \frac{n}{2} \rfloor} \left[\begin{pmatrix} n \\ 2j \end{pmatrix} \left(\frac{p}{2}\right)^{(n-2j)} o^{(j-n)} \prod_{k=1}^{j} \frac{2j - 2k + 1}{2} \right] \tag{7.4}$$

where $m = \lfloor \frac{n}{2} \rfloor = \frac{n}{2}$ if n is even and $m = \lfloor \frac{n}{2} \rfloor = \frac{n-1}{2}$ if n is odd. The second term then corresponds to the pre-factor.

The function `gmoment_factor` computes Gaussian moments of arbitrary order. In the following equations, where Gaussian moments appear, the shorthand notation $\mathrm{M}^{(\kappa,\mu,d)}_{l_{\kappa,\mu} l''_{\kappa,\mu}}(n)$ will be used for the pre-factor.

7.3.2 Kinetic Energy Operator

The kinetic energy operator is given as a sum over the single κ-modes,

$$\hat{T} = \sum_{\kappa} \hat{T}^{(\kappa)} \tag{7.5}$$

with,

$$\hat{T}^{(\kappa)} = \sum_{\mu}^{f_\kappa} \hat{T}^{(\kappa,\mu)} \tag{7.6}$$

Further, as the μ-modes can be multi-dimensional,

$$\hat{T}^{(\kappa,\mu)} = \sum_{d}^{dim_{\kappa,\mu}} \hat{T}^{(\kappa,\mu,d)} \tag{7.7}$$

The standard Cartesian form for the latter (one-dimensional) operator is,

$$\hat{T}^{(\kappa,\mu,d)} = -\frac{1}{2m_{\kappa,\mu,d}}\frac{\partial^2}{\partial {x_{\kappa,\mu,d}}^2} \tag{7.8}$$

One matrix element of the first-layer kinetic Hamiltonian is then given by,

$$\begin{aligned}\left\langle \Phi_J \left| \hat{T} \right| \Phi_{J'} \right\rangle &= \sum_\kappa \left\langle \Phi_J \left| \hat{T}^{(\kappa)} \right| \Phi_{J'} \right\rangle \\ &= \sum_\kappa \left\langle \varphi^{(\kappa)}_{j_\kappa} \left| \hat{T}^{(\kappa)} \right| \varphi^{(\kappa)}_{j'_\kappa} \right\rangle \cdot \underbrace{\prod_{\lambda\neq\kappa} \left\langle \varphi^{(\lambda)}_{j_\lambda} \left| \varphi^{(\lambda)}_{j'_\lambda} \right\rangle}_{\begin{cases} =1 \text{ if } j_\lambda = j'_\lambda \ \forall\lambda \\ =0 \text{ otherwise}\end{cases}}\end{aligned} \tag{7.9}$$

with,

$$\begin{aligned}\left\langle \varphi^{(\kappa)}_{j_\kappa} \left| \hat{T}^{(\kappa)} \right| \varphi^{(\kappa)}_{j'_\kappa} \right\rangle &= \sum_{L_\kappa} \left\{ \bar{B}^{(\kappa)}_{j_\kappa,L_\kappa} \left(\sum_{L'_\kappa} \left(\sum_\mu^{f_\kappa} \left\langle \prod_\nu^{f_\kappa} g^{(\kappa,\nu)}_{l_{\kappa,\nu}} \left| \hat{T}^{(\kappa,\mu)} \right| \prod_{\nu'}^{f_\kappa} g^{(\kappa,\nu')}_{l'_{\kappa,\nu'}} \right\rangle \right) B^{(\kappa)}_{j'_\kappa,L'_\kappa} \right) \right\} \\ &= \sum_{L_\kappa} \left\{ \bar{B}^{(\kappa)}_{j_\kappa,L_\kappa} \cdot \left(\sum_{L'_\kappa} \left(\sum_\mu^{f_\kappa} \left\langle g^{(\kappa,\mu)}_{l_{\kappa,\mu}} \left| \hat{T}^{(\kappa,\mu)} \right| g^{(\kappa,\mu)}_{l'_{\kappa,\mu}} \right\rangle \cdot \right.\right.\right. \\ &\quad \left.\left.\left. \cdot \prod_{\nu\neq\mu}^{f_\kappa} \left\langle g^{(\kappa,\nu)}_{l_{\kappa,\nu}} \left| g^{(\kappa,\nu)}_{l'_{\kappa,\nu}} \right\rangle \right) B^{(\kappa)}_{j'_\kappa,L'_\kappa} \right) \right\}\end{aligned}$$

and, when expanding into the sub-dimensions of the μ/ν-modes:

$$\begin{aligned}&= \sum_{L_\kappa} \left\{ \bar{B}^{(\kappa)}_{j_\kappa,L_\kappa} \left(\sum_{L'_\kappa} \sum_\mu^{f_\kappa} \left(\sum_d^{dim_{\kappa,\mu}} \left(\prod_{d'}^{dim_{\kappa,\mu}} \left\langle g^{(\kappa,\mu,d')}_{l_{\kappa,\mu,d'}} \left| \hat{T}^{(\kappa,\mu,d)} \right| g^{(\kappa,\mu,d')}_{l'_{\kappa,\mu,d'}} \right\rangle \right) \cdot \right.\right.\right. \\ &\quad \left.\left.\left. \cdot \prod_{\nu\neq\mu}^{f_\kappa} \left\langle g^{(\kappa,\nu)}_{l_{\kappa,\nu}} \left| g^{(\kappa,\nu)}_{l'_{\kappa,\nu}} \right\rangle \right) B^{(\kappa)}_{j'_\kappa,L'_\kappa} \right) \right\} \\ &= \sum_{L_\kappa} \left\{ \bar{B}^{(\kappa)}_{j_\kappa,L_\kappa} \left(\sum_{L'_\kappa} \sum_\mu^{f_\kappa} \left(\sum_d^{dim_{\kappa,\mu}} \left(\left\langle g^{(\kappa,\mu,d)}_{l_{\kappa,\mu,d}} \left| \hat{T}^{(\kappa,\mu,d)} \right| g^{(\kappa,\mu,d)}_{l'_{\kappa,\mu,d}} \right\rangle \cdot \right.\right.\right.\right. \\ &\quad \left.\left.\left.\left. \cdot \prod_{d'\neq d}^{dim_{\kappa,\mu}} \left\langle g^{(\kappa,\mu,d')}_{l_{\kappa,\mu,d'}} \left| g^{(\kappa,\mu,d')}_{l'_{\kappa,\mu,d'}} \right\rangle \right) \cdot \prod_{\nu\neq\mu}^{f_\kappa} \left\langle g^{(\kappa,\nu)}_{l_{\kappa,\nu}} \left| g^{(\kappa,\nu)}_{l'_{\kappa,\nu}} \right\rangle \right) B^{(\kappa)}_{j'_\kappa,L'_\kappa} \right) \right\} \\ &= \sum_{L_\kappa} \left\{ \bar{B}^{(\kappa)}_{j_\kappa,L_\kappa} \left(\sum_{L'_\kappa} \sum_\mu^{f_\kappa} \left(\sum_d^{dim_{\kappa,\mu}} \left(\mathrm{FuncT}^{(\kappa,\mu,d)}_{l_{\kappa,\mu},l'_{\kappa,\mu}} \cdot \left\langle g^{(\kappa,\mu,d)}_{l_{\kappa,\mu,d}} \left| g^{(\kappa,\mu,d)}_{l'_{\kappa,\mu,d}} \right\rangle \cdot \right.\right.\right.\right. \\ &\quad \left.\left.\left.\left. \cdot \prod_{d'\neq d}^{dim_{\kappa,\mu}} \left\langle g^{(\kappa,\mu,d')}_{l_{\kappa,\mu,d'}} \left| g^{(\kappa,\mu,d')}_{l'_{\kappa,\mu,d'}} \right\rangle \right) \cdot \prod_{\nu\neq\mu}^{f_\kappa} \left\langle g^{(\kappa,\nu)}_{l_{\kappa,\nu}} \left| g^{(\kappa,\nu)}_{l'_{\kappa,\nu}} \right\rangle \right) B^{(\kappa)}_{j'_\kappa,L'_\kappa} \right) \right\} \\ &= \sum_{L_\kappa} \left\{ \bar{B}^{(\kappa)}_{j_\kappa,L_\kappa} \left(\sum_{L'_\kappa} \sum_\mu^{f_\kappa} \left(\sum_d^{dim_{\kappa,\mu}} \left(\mathrm{FuncT}^{(\kappa,\mu,d)}_{l_{\kappa,\mu},l'_{\kappa,\mu}} \cdot \prod_{d'}^{dim_{\kappa,\mu}} \left\langle g^{(\kappa,\mu,d')}_{l_{\kappa,\mu,d'}} \left| g^{(\kappa,\mu,d')}_{l'_{\kappa,\mu,d'}} \right\rangle \right) \cdot \right.\right.\right. \\ &\quad \left.\left.\left. \cdot \prod_{\nu\neq\mu}^{f_\kappa} \left\langle g^{(\kappa,\nu)}_{l_{\kappa,\nu}} \left| g^{(\kappa,\nu)}_{l'_{\kappa,\nu}} \right\rangle \right) B^{(\kappa)}_{j'_\kappa,L'_\kappa} \right) \right\}\end{aligned} \tag{7.10}$$

$\mathrm{FuncT}^{(\kappa,\mu,d)}_{l_{\kappa,\mu},l'_{\kappa,\mu}}$ represents a function that computes the factor to be multiplied to the overlap of two GWPs to get the kinetic energy element between them for a given set of κ, μ, d and $l_{\kappa,\mu}, l'_{\kappa,\mu}$ indices, i.e.,

$$\left\langle g^{(\kappa,\mu,d)}_{l_{\kappa,\mu,d}} \middle| \hat{T}^{(\kappa,\mu,d)} \middle| g^{(\kappa,\mu,d)}_{l'_{\kappa,\mu,d}} \right\rangle = \mathrm{FuncT}^{(\kappa,\mu,d)}_{l_{\kappa,\mu},l'_{\kappa,\mu}} \left\langle g^{(\kappa,\mu,d)}_{l_{\kappa,\mu,d}} \middle| g^{(\kappa,\mu,d)}_{l'_{\kappa,\mu,d}} \right\rangle \tag{7.11}$$

7.3.3 Potential Energy Operator

The potential is given as,

$$\hat{V}\left(\vec{x}\right) = \sum_{t=1}^{m} a_t \prod_{\kappa}^{f} \hat{v}_t^{(\kappa)}\left(\vec{x}_\kappa\right) \tag{7.12}$$

with,

$$\hat{v}_t^{(\kappa)}\left(\vec{x}_\kappa\right) = \sum_{u=1}^{m_\kappa} b_{t,u}^{(\kappa)} \prod_{\mu}^{f_\kappa} \hat{v}_{t,u}^{(\kappa,\mu)}\left(\vec{x}_{\kappa,\mu}\right) \tag{7.13}$$

where,

$$\hat{v}_{t,u}^{(\kappa,\mu)} = \sum_{v}^{m_{\kappa,\mu}} \prod_{d}^{dim_{\kappa,\mu}} v_{t,u,v}^{(\kappa,\mu,d)}\left(x_{\kappa,\mu,d}\right) \tag{7.14}$$

The $v_{t,u}^{(\kappa,\mu)}$ are arbitrary functions in the degrees of freedom of the κ,μ-mode and $v_{t,u,v}^{(\kappa,\mu,d)}$ are the corresponding one-dimensional expressions in the individual DOFs. One matrix element of the first-layer potential energy operator is then,

$$\begin{aligned}\left\langle \Phi_J \middle| \hat{V} \middle| \Phi_{J'} \right\rangle &= \sum_{t}^{m} a_t \prod_{\kappa}^{f} \left\langle \Phi_J \middle| \hat{v}_t^{\kappa} \middle| \Phi_{J'} \right\rangle \\ &= \sum_{t}^{m} a_t \prod_{\kappa}^{f} \left\langle \varphi_{j_\kappa}^{(\kappa)} \middle| \hat{v}_t^{(\kappa)} \middle| \varphi_{j'_\kappa}^{(\kappa)} \right\rangle \end{aligned} \tag{7.15}$$

with,

$$\left\langle \varphi_{j_\kappa}^{(\kappa)} \middle| \hat{v}_t^{(\kappa)} \middle| \varphi_{j'_\kappa}^{(\kappa)} \right\rangle = \sum_{L_\kappa} \bar{B}^{(\kappa)}_{j_\kappa,L_\kappa} \left(\sum_{L'_\kappa} \left(\sum_{u=1}^{m_\kappa} b_{t,u}^{(\kappa)} \prod_{\mu}^{f_\kappa} \left\langle g^{(\kappa,\mu)}_{l_{\kappa,\mu}} \middle| \hat{v}^{(\kappa,\mu)}_{t,u} \middle| g^{(\kappa,\mu)}_{l'_{\kappa,\mu}} \right\rangle \right) B^{(\kappa)}_{j'_\kappa,L'_\kappa} \right) \tag{7.16}$$

If $\hat{v}_{t,u}^{(\kappa,\mu)}$ corresponds to a monomial expression, the integral $\left\langle g^{(\kappa,\mu)}_{l_{\kappa,\mu}} \middle| \hat{v}^{(\kappa,\mu)}_{t,u} \middle| g^{(\kappa,\mu)}_{l'_{\kappa,\mu}} \right\rangle$ can be rewritten in terms of Gaussian moments using the above defined pre-factor $\mathrm{M}^{(\kappa,\mu,d)}_{l_{\kappa,\mu}l"_{\kappa,\mu}}(n)$,

$$\left\langle g^{(\kappa,\mu)}_{l_{\kappa,\mu}} \middle| \hat{v}^{(\kappa,\mu)}_{t,u} \middle| g^{(\kappa,\mu)}_{l'_{\kappa,\mu}} \right\rangle = \sum_{v}^{m_{\kappa,\mu}} \prod_{d}^{dim_{\kappa,\mu}} \left\langle g^{(\kappa,\mu,d')}_{l_{\kappa,\mu,d}} \middle| v^{(\kappa,\mu,d)}_{t,u,v} \middle| g^{(\kappa,\mu,d)}_{l'_{\kappa,\mu}d} \right\rangle$$

$$= \sum_{v}^{m_{\kappa,\mu}} \prod_{d}^{dim_{\kappa,\mu}} \mathrm{M}^{(\kappa,\mu,d)}_{l_{\kappa,\mu} l"_{\kappa,\mu}}(n) \left\langle g^{(\kappa,\mu,d')}_{l_{\kappa,\mu,d}} \middle| g^{(\kappa,\mu,d)}_{l'_{\kappa,\mu} d} \right\rangle \tag{7.17}$$

where n corresponds to the exponent of the corresponding monomial, e.g. $v^{(\kappa,\mu,d)}_{t,u,v} = x^2_{\kappa\, mu,d} \rightarrow n = 2$.

7.3.3.1 Local Harmonic Approximation

If the potential terms $\hat{v}^{(\kappa,\mu)}_{t,u}$ are not represented by monomial terms, the Local Harmonic Approximation (LHA) can be used to describe the potential. For the LHA the potential of one (combined) μ-mode is then expanded in a power series around the center, $\vec{q}_{\kappa,\mu}(t)$, of the multidimensional GWP:

$$\hat{v}^{(\kappa,\mu)}_{t,u} = v_{\kappa,\mu} + \vec{v}'_{\kappa,\mu}\left(\vec{x}_{\kappa,\mu} - \vec{q}_{\kappa,\mu}\right) + \frac{1}{2}\left(\vec{x}_{\kappa,\mu} - \vec{q}_{\kappa,\mu}\right) \underline{v}''_{\kappa,\mu}\left(\vec{x}_{\kappa,\mu} - \vec{q}_{\kappa,\mu}\right) \tag{7.18}$$

where the local potential energy $v\left(\vec{q}_{\kappa,\mu}\right)$ is written as $v_{\kappa,\mu}$, $v'_i\left(\vec{q}_{\kappa,\mu}\right) = v'_{\kappa,\mu,i} = \frac{\partial v_{\kappa,\mu}}{\partial x_i}$ represents the vector of first derivatives in the sub-dimensions of (κ,μ), and $v''_{i,j}\left(\vec{q}_{\kappa,\mu}\right) = v''_{\kappa,\mu,i,j} = \frac{\partial^2 v_{\kappa,\mu}}{\partial x_i \partial x_j}$ the matrix of second derivatives in these dimensions. The integral of equation (7.16) is thus expanded as follows,

$$\begin{aligned}
&\left\langle g^{(\kappa,\mu)}_{l_{\kappa,\mu}} \middle| \hat{v}^{(\kappa,\mu)}_{t,u} \middle| g^{(\kappa,\mu)}_{l'_{\kappa,\mu}} \right\rangle_{LHA} = \\
=&v_{\kappa,\mu} \left\langle g^{(\kappa,\mu)}_{l_{\kappa,\mu}} \middle| g^{(\kappa,\mu)}_{l'_{\kappa,\mu}} \right\rangle + \left\langle g^{(\kappa,\mu)}_{l_{\kappa,\mu}} \middle| v'_{\kappa,\mu}\left(\vec{x}_{\kappa,\mu} - \vec{q}_{\kappa,\mu}\right) \right\rangle \\
&+ \frac{1}{2}\left\langle g^{(\kappa,\mu)}_{l_{\kappa,\mu}} \middle| \left(\vec{x}_{\kappa,\mu} - \vec{q}_{\kappa,\mu}\right) \underline{v}''_{\kappa,\mu}\left(\vec{x}_{\kappa,\mu} - \vec{q}_{\kappa,\mu}\right) \right\rangle \\
=&\left\langle g^{(\kappa,\mu)}_{l_{\kappa,\mu}} \middle| g^{(\kappa,\mu)}_{l'_{\kappa,\mu}} \right\rangle \left(v_{\kappa,\mu} + \sum_{d}^{dim_{\kappa,\mu}} \left(v'_{\kappa,\mu,d}\left(M^{(\kappa,\mu,d)}_{L_\kappa L'_\kappa}(1) - q_{\kappa,\mu,d} \right) \right.\right. \\
&+\frac{1}{2} v''_{\kappa,\mu,d,d}\left(M^{(\kappa,\mu,d)}_{L_\kappa L'_\kappa}(2) - 2 M^{(\kappa,\mu,d)}_{L_\kappa L'_\kappa}(1)\, q_{\kappa,\mu,d} + q_{\kappa,\mu,d} \right) \\
&\left.\left. + \sum_{d' \neq d}^{dim_{\kappa,\mu}} \left(\frac{1}{2} v''_{\kappa,\mu,d,d'}\left(\vec{q}_{\kappa,\mu}\right)\left(M^{(\kappa,\mu,d)}_{L_\kappa L'_\kappa}(1) - q_{\kappa,\mu,d} \right)\left(M^{(\kappa,\mu,d')}_{L_\kappa L'_\kappa}(1) - q_{\kappa,\mu,d'} \right) \right) \right) \right)
\end{aligned} \tag{7.19}$$

7.3.4 Expansion of Matrix-Vector Products in a Multi-Sum Structure

The most time-consuming steps in the propagation scheme result from high-dimensional matrix-vector products that are present in both layers. An efficient scheme that is adapted to the SOP form of the Hamiltonian and the tensor form of the wavefunction is given by the evaluation of "multi-sums" as detailed below. For a standard matrix-vector product, this leads to an advantageous $N^{(d+1)}$ scaling

(where N is the number of grid points and d is the number of DOFs), as discussed, e.g., in [97].

In the 2L-G-MCTDH scheme, such matrix-vector multiplications appear in many equations, including the calculation of mean-fields, the EOMs for the A and B coefficients, etc. This chapter aims to describe the implemented "multi-sum" algorithm which attempts to avoid multiple calculations of the same integrals. The gain in efficiency, however, goes along with increased memory consumption. Therefore, in the following algorithm two auxiliary arrays `array` and `array2` are used.

An example for such multi-sums is given in Eqn. 7.16. Expanding this equation into the individual sums, and using again the general expression for the Hamilton operator, gives,

$$\begin{aligned}
&\sum_{L_\kappa} \bar{B}^{(\kappa)}_{j_\kappa,L_\kappa} \left(\sum_{L'_\kappa} \left(\sum_{u=1}^{m_\kappa} b^{(\kappa)}_{t,u} \prod_{\mu}^{f_\kappa} \left\langle g^{(\kappa,\mu)}_{l_{\kappa,\mu}} \middle| \hat{h}^{(\kappa,\mu)}_{t,u} \middle| g^{(\kappa,\mu)}_{l'_{\kappa,\mu}} \right\rangle \right) B^{(\kappa)}_{j'_\kappa,L'_\kappa} \right) = \\
&= \sum_{u=1}^{m_\kappa} \sum_{L_\kappa} \left(\bar{B}^{(\kappa)}_{j_\kappa,L_\kappa} \sum_{l'_{\kappa,1}}^{n_{\kappa,1}} \left\langle g^{(\kappa,1)}_{l_{\kappa,1}} \middle| \hat{h}^{(\kappa,1)}_{t,u} \middle| g^{(\kappa,1)}_{l'_{\kappa,1}} \right\rangle \sum_{l'_{\kappa,2}}^{n_{\kappa,2}} \left\langle g^{(\kappa,2)}_{l_{\kappa,2}} \middle| \hat{h}^{(\kappa,2)}_{t,u} \middle| g^{(\kappa,2)}_{l'_{\kappa,2}} \right\rangle \cdots \right. \\
&\left. \cdots \sum_{l'_{\kappa,\mu}}^{n_{\kappa,\mu}} \left\langle g^{(\kappa,\mu)}_{l_{\kappa,\mu}} \middle| \hat{h}^{(\kappa,\mu)}_{t,u} \middle| g^{(\kappa,\mu)}_{l'_{\kappa,\mu}} \right\rangle \cdots \sum_{l'_{\kappa,f_\kappa}}^{n_{\kappa,f_\kappa}} \left\langle g^{(\kappa,f_\kappa)}_{l_{\kappa,f_\kappa}} \middle| \hat{h}^{(\kappa,f_\kappa)}_{t,u} \middle| g^{(\kappa,f_\kappa)}_{l'_{\kappa,f_\kappa}} \right\rangle B^{(\kappa)}_{j'_\kappa,L'_\kappa} \right)
\end{aligned} \tag{7.20}$$

where the integrals $\left\langle g^{(\kappa,\mu)}_{l_{\kappa,\mu}} \middle| \hat{h}^{(\kappa,\mu)}_{t,u} \middle| g^{(\kappa,\mu)}_{l'_{\kappa,\mu}} \right\rangle$ are calculated by the function `funcH`.

The calculation starts with the last κ, f_κ-mode, going from the highest to the lowest second-layer mode. Therefore the bracket $\left\langle g^{(\kappa,f_\kappa)}_{\kappa,l_{f_\kappa}} \middle| \hat{h}^{(\kappa,f_\kappa)}_{t,u} \middle| g^{(\kappa,f_\kappa)}_{\kappa,l'_{\kappa,f_\kappa}} \right\rangle$ is calculated for all l_{κ,f_κ} and l_{κ,f'_κ} and distributed in an $n^{(\kappa)}_{conf} \times n_{\kappa,f_\kappa}$ array (auxiliary `array1`). The l_{κ,f_κ} hereby determines the row and each integral with the right-hand-side l'_{κ,f_κ} is written to $n^{(\kappa)}_{conf}/n_{\kappa,f_\kappa}$ columns in the same order as l'_{κ,f_κ} appears in the multi-index L'_κ. Then the right hand side B coefficients $B^{(\kappa)}_{j'_\kappa,L'_\kappa}$ are multiplied component-wise to each column of `array1`. This is illustrated in the upper part of Fig. 7.3. `array1` is then copied to `array2` and `array1` is used with dimension $\frac{n^{(\kappa)}_{conf}}{n_{\kappa,f_\kappa}} \times n_{\kappa,f_\kappa} n_{\kappa,f_\kappa-1}$.

Then `array1` is again constructed in a similar way with the $l_{\kappa,f_\kappa-1}$,$l'_{\kappa,f_\kappa-1}$-brackets. Each $l_{\kappa,f_\kappa-1}$ contributes to n_{κ,f_κ} columns (every $n_{\kappa,f_\kappa-1}$ column) and each $l'_{\kappa,f_\kappa-1}$ is written to $\frac{n^{(\kappa)}_{conf}}{n_{\kappa,f_\kappa} n_{\kappa,f_\kappa-1}}$ columns (again, according to their appearance in L'_κ).

From `array2` every $\sum_{l'_{\kappa,f_\kappa}}$ is built (see lower part of Fig. 7.3) and multiplied to the according cells in `array1`. This means that each l_{κ,f_κ}-row is repeated n_{κ,f_κ} times.

Then `array2` is reshaped to the same dimension as `array1` and `array1` copied to `array2`. `array1` is again reshaped by dividing the old width and multiplying the old height by $n_{\kappa,f_\kappa-2}$. The cells are calculated in the same fashion as above and distributed among `array1`. The $\sum_{l'_{\kappa,f_\kappa-1}}$ sums are built and multiplied to the according cells. This scheme is repeated for all remaining μ-modes. In the last step after $\mu = 1$ the sums over $l_{\kappa,1}$ for the last `array2` (with dimensions $n_{\kappa,1} \times n^{(\kappa)}_{conf}$) are built and multiplied with the left-hand-side B coefficients.

This scheme is used in variations wherever similar kinds of multi-sums appear, e.g., in the derivatives for the A and B coefficients, the first- and second-layer mean-fields, the density matrices, etc.

Although the implemented algorithm uses two 1-dimensional auxiliary arrays for the multi-sum calculation, it is easier to understand for two 2-dimensional arrays changing their shape between the different rounds, as explained above. In order to avoid permanent creation and destruction of these arrays, they are allocated once at the beginning. For a two-dimensional array as it is used in the algorithm, this array would need to be of length $n^{(\kappa)}_{conf} \times n^{(\kappa)}_{conf}$. This can get extremely large for a large number of configurations such that the available memory is exceeded. Therefore, in the program the two indices are combined into one index to save memory. This way the length of the arrays used in the above example can be reduced to $n^{(\kappa)}_{conf} \times \mathtt{max}\left(n_{\kappa,f}\right)$. These arrays are used in different dimensions for the first- and second-layer multi-sums throughout the algorithm, resulting in 4 permanent arrays (`work_beta1` and `work_beta2` for the first-layer, `work_gamma1` and `gamma2` for the second-layer) with lengths $n_{Aconfig} \times \mathtt{max}\left(n_\kappa\right)$ for the `work_beta` arrays and $n^{(\kappa)}_{conf} \times \mathtt{max}\left(n_{\kappa,f}\right)$ for the `work_gamma` arrays.

7.3.5 Technical Details

Important steps in the calculation of the EOMs are the inversion of the first-layer density matrix $\underline{\rho}^{(\kappa)}$, the inversion of the $\underline{C}$ matrix and inversion of the overlap matrix. A well-known problem is the occurrence of singularities in these matrices. Even in standard MCTDH, the initial density matrix $\underline{\rho}^{(\kappa)}$ is highly singular since only few configurations – or only a single configuration – are initially populated. When using Gaussian basis functions, the occurrence of such singularities

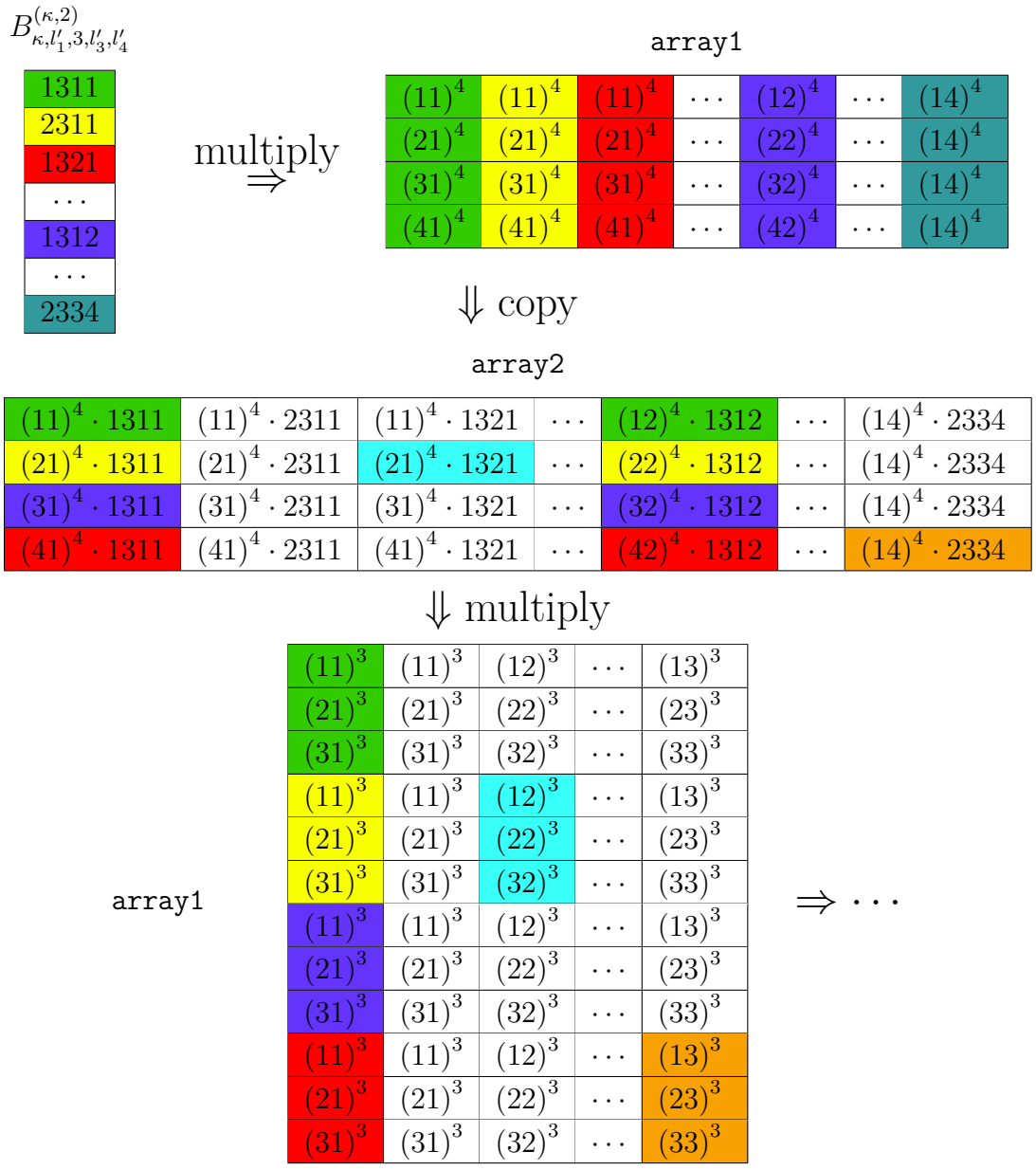

Figure 7.3: Illustration of the first steps in the multi-sums algorithm. For illustration, the wave function is built for a second-layer Hamiltonian matrix element f_κ=4, μ = 2, l_2=2, l'_2=3, n_1=2, n_2=4, n_3=3, n_4=4. Furthermore, the shorthand notation $\langle g_x^{(\kappa,z)}|\hat{h}_{t,u}^{(\kappa,z)}|g_y^{(\kappa,z)}\rangle \equiv (xy)^z$ is used for the Hamiltonian elements. For the B coefficients the shorthand notation $B^{(\kappa,2)}_{\kappa,a_1,b_2,c_3,d_4} \equiv abcd$ is used. In the first round `array1` is constructed and distributed according to L'_κ (see text for details) and in a second step the right-hand-side B coefficients are multiplied onto the according elements on `array1` and copied to `array2`. Here, the colors indicate the cells each B coefficient is multiplied to. The second round follows the same procedure, after constructing `array1` the sums over $\sum_{l'_{\kappa,f_\kappa}}$ are built and again multiplied on `array1` and copied to `array2`. In `array2` the colors show cells that are summed up. They are then multiplied to the corresponding cells in `array1`. This procedure is then repeated for the remaining μ-modes.

is aggravated due to linear dependencies within the non-orthogonal GWP basis, which typically appear when a large overlap of two or more GWPs is observed. Furthermore, as in the case of standard MCTDH, the standard initial conditions where one coefficient is set to 1.0 and all others to 0.0 causes the first-layer density matrix to be singular at the beginning of the propagation. Since these matrices all need to be inverted during the evaluation of the EOMs, these singularities have to be "smoothed out" numerically as they prohibit a regular inversion. The standard way of handling such singularities is to regularize the relevant matrices, which is here done by adjusting all eigenvalues below a pre-defined threshold value $d_{threshold}$ as follows,

$$E_{EV} = E_{EV} + d_{threshold} \times \exp\left(-\frac{E_{EV}}{d_{threshold}}\right) \tag{7.21}$$

Typical values for $d_{threshold}$ are in the range of 10^{-6} to 10^{-8}. This regularization scheme is entirely analogous to the standard MCTDH code.

Another technical detail concerns the orthogonalization of the first-layer SPFs $\varphi_{j_\kappa}^{(\kappa)}$. This is done by employing the Gram-Schmidt orthogonalization[98–100] scheme once at time $t = 0$, before propagating the wave function. In this context, one has to be aware that only the first SPF is left unchanged and the others change accordingly.

7.3.6 Additional Remarks on Selected Equations

In this chapter some special remarks are made regarding the equations of motion for the B coefficients and the GWP parameters. Here, the first- and second-layer projectors were introduced in the derivation. In order to implement these formulas in the Fortran90 code these projectors have to be expressed explicitly. Therefore, the explicit formulas are presented here.

First, the expression for the $\underline{C}$ matrix and the $\vec{Y}$ vector are shown. As starting point Eqn. 6.32 is used,

$$C^{(\kappa,\mu)}_{l_{\kappa,\mu}d,l'_{\kappa,\mu}d'} = \rho^{(\kappa,\mu)}_{l_{\kappa,\mu}l'_{\kappa,\mu}} \left\langle \frac{\partial}{\partial \xi^{(\kappa,\mu,d)}_{l_{\kappa,\mu}}} g^{(\kappa,\mu)}_{l_{\kappa,\mu}} \middle| \left(\hat{1} - \hat{P}^{(\kappa,\mu)}\right) \frac{\partial}{\partial \xi^{(\kappa,\mu,d')}_{l'_{\kappa,\mu}}} g^{(\kappa,\mu)}_{l'_{\kappa,\mu}} \right\rangle$$
$$= \rho^{(\kappa,\mu)}_{l_{\kappa,\mu}l'_{\kappa,\mu}} \left(\left\langle \frac{\partial}{\partial \xi^{(\kappa,\mu,d)}_{l_{\kappa,\mu}}} g^{(\kappa,\mu)}_{l_{\kappa,\mu}} \middle| \frac{\partial}{\partial \xi^{(\kappa,\mu,d')}_{l'_{\kappa,\mu}}} g^{(\kappa,\mu)}_{l'_{\kappa,\mu}} \right\rangle \right.$$

$$-\sum_{P_\kappa}\sum_{P'_\kappa}\left\langle \frac{\partial}{\partial\xi^{(\kappa,\mu,d)}_{l^{(\kappa,\mu)}_{\kappa,\mu}}} g^{(\kappa,\mu)}_{l^{(\kappa,\mu)}_{\kappa,\mu}} \middle| g^{(\kappa,\mu)}_{p_{\kappa,\mu}} \right\rangle \left(\left(\underline{S}^{(\kappa,\mu)}\right)^{-1} \right)_{p_{\kappa,\mu},p'_{\kappa,\mu}} \left\langle g^{(\kappa,\mu)}_{p'_{\kappa,\mu}} \middle| \frac{\partial}{\partial\xi^{(\kappa,\mu,d')}_{l'^{(\kappa,\mu)}_{\kappa,\mu}}} g^{(\kappa,\mu)}_{l'^{(\kappa,\mu)}_{\kappa,\mu}} \right\rangle \right) \tag{7.22}$$

where P_κ and P'_κ are multi-indices like L_κ and L'_κ. The same is done for the $\vec{Y}$ vector. Additionally, the Hamiltonian is expanded explicitly in the product form. Starting from Eqn. 6.33,

$$\begin{aligned}
Y^{(\kappa,\mu)}_{l^{(\kappa,\mu)}_{\kappa,\mu},d} =& \sum_{l'^{(\kappa,\mu)}_{\kappa,\mu}} \left\langle \frac{\partial}{\partial\xi^{(\kappa,\mu,d)}_{l^{(\kappa,\mu)}_{\kappa,\mu}}} g^{(\kappa,\mu)}_{l^{(\kappa,\mu)}_{\kappa,\mu}} \middle| \left(\hat{1}-\hat{P}^{(\kappa,\mu)}\right) \hat{\mathcal{H}}^{(\kappa,\mu)}_{l^{(\kappa,\mu)}_{\kappa,\mu} l'^{(\kappa,\mu)}_{\kappa,\mu}} g^{(\kappa,\mu)}_{l'^{(\kappa,\mu)}_{\kappa,\mu}} \right\rangle \\
=& \sum_{l'^{(\kappa,\mu)}_{\kappa,\mu}} \Bigg\{ \sum_t a_t \sum_u b^{(\kappa)}_{t,u} \left(\underline{\mathcal{H}}^{(\kappa,\mu)}_{t,u}\right)_{l^{(\kappa,\mu)}_{\kappa,\mu} l'^{(\kappa,\mu)}_{\kappa,\mu}} \Bigg(\left\langle g^{(\kappa,\mu)}_{l^{(\kappa,\mu)}_{\kappa,\mu}} \middle| x^{(\kappa,\mu,d)} \hat{h}^{(\kappa,\mu)}_{t,u} \middle| g^{(\kappa,\mu)}_{l'^{(\kappa,\mu)}_{\kappa,\mu}} \right\rangle - \\
& - \sum_{P_\kappa}\sum_{P'_\kappa} \left\langle \frac{\partial}{\partial\xi^{(\kappa,\mu,d)}_{l^{(\kappa,\mu)}_{\kappa,\mu}}} g^{(\kappa,\mu)}_{l^{(\kappa,\mu)}_{\kappa,\mu}} \middle| g^{(\kappa,\mu)}_{p_{\kappa,\mu}} \right\rangle \left(\left(\underline{S}^{(\kappa,\mu)}\right)^{-1} \right)_{p_{\kappa,\mu},p'_{\kappa,\mu}} \cdot \\
& \cdot \left\langle g^{(\kappa,\mu)}_{p'_{\kappa,\mu}} \middle| \hat{h}^{(\kappa,\mu)}_{t,u} \middle| \frac{\partial}{\partial\xi^{(\kappa,\mu,d')}_{l'^{(\kappa,\mu)}_{\kappa,\mu}}} g^{(\kappa,\mu)}_{l'^{(\kappa,\mu)}_{\kappa,\mu}} \right\rangle \Bigg) \Bigg\}
\end{aligned} \tag{7.23}$$

where $\underline{\mathcal{H}}^{(\kappa,\mu)}_{t,u}$ denotes the first-layer mean-field matrix.

Finally, the expression for the B coefficients (Eqn. 6.36) is rewritten:

$$i\dot{\vec{B}}^{(\kappa)} = \left[\left(\underline{\tilde{S}}^{(\kappa)}\right)^{-1} \underline{\tilde{H}}^{(\kappa)} - i \left(\underline{\tilde{S}}^{(\kappa)}\right)^{-1} \underline{\tilde{\tau}}^{(\kappa)} \right] \vec{B}^{(\kappa)} \tag{7.24}$$

This expression is split into two components,

$$\left[\left(\underline{\tilde{S}}^{(\kappa)}\right)^{-1} \underline{\tilde{H}}^{(\kappa)} \vec{B}^{(\kappa)} \right] \tag{7.25}$$

and,

$$-\left[i \left(\underline{\tilde{S}}^{(\kappa)}\right)^{-1} \underline{\tilde{\tau}}^{(\kappa)} \vec{B}^{(\kappa)} \right] \tag{7.26}$$

These two components are considered individually in the following.

Expanding Eqn 7.26 is straightforward as no projector is involved in this term. The Gaussian moments are expressed, as introduced above, as the prefactor multiplied with the zeroth order overlap,

$$\left[\left(\underline{\tilde{S}}^{(\kappa)}\right)^{-1} \underline{\tilde{\tau}}^{(\kappa)} \vec{B}^{(\kappa)} \right]_{j_\kappa, L_\kappa} =$$

$$= \sum_{\mu} \sum_{l'_{\kappa,\mu}} \sum_{l''_{\kappa,\mu}} \left(\underline{S}^{(\kappa,\mu)}\right)^{-1}_{l_{\kappa,\mu} l''_{\kappa,\mu}} S^{(\kappa,\mu)}_{l''_{\kappa,\mu} l'_{\kappa,\mu}} \left(\sum_{d} M^{(\kappa,\mu,d)}_{l''_{\kappa,\mu} l'_{\kappa,\mu}} (1)\, \dot{\xi}^{(\kappa,\mu,d)}_{l'_{\kappa,\mu}} - \dot{\eta}^{(\kappa,\mu,d)}_{l'_{\kappa,\mu}} \right) B^{(\kappa)}_{j_\kappa, L_\kappa^{\left(\mu: l'_{\kappa,\mu}\right)}} \tag{7.27}$$

Here, the differential overlap matrix $\underline{\tilde{\tau}}^{(\kappa)}$ is further expanded in the derivatives of the GWP parameters. The first half is expanded similarly to the $\vec{Y}$ vector and the second half is given as,

$$\begin{aligned}
&\left[\left(\underline{\tilde{S}}^{(\kappa)}\right)^{-1} \underline{\tilde{H}}^{(\kappa)} \vec{B}^{(\kappa)} \right]_{j_\kappa, L_\kappa} = \\
&= \sum_{t} a_t \sum_{j'_\kappa} \left(\underline{\rho}^{(\kappa)}\right)^{-1}_{j_\kappa j'_\kappa} \sum_{j''_\kappa} \left(\underline{\mathcal{H}}^{(\kappa)}\right)_{j'_\kappa j''_\kappa} \cdot \\
&\cdot \left(\sum_{L'_\kappa} \left(\prod_{\mu} \left(\underline{S}^{(\kappa,\mu)}\right)^{-1}_{l_{\kappa,\mu} l''_{\kappa,\mu}} \sum_{u} b^{(\kappa)}_{t,u} \sum_{L''_\kappa} \prod_{\mu} \left\langle g^{(\kappa,\mu)}_{l'_{\kappa,\mu}} \middle| \hat{h}^{(\kappa,\mu)}_{t,u} \middle| g^{(\kappa,\mu)}_{l''_{\kappa,\mu}} \right\rangle B^{(\kappa)}_{j''_\kappa, L''_\kappa} \right) - \right. \\
&\left. - \sum_{P} \left\langle \varphi^{(\kappa)}_{p_\kappa} \middle| \hat{h}^{(\kappa)}_{t} \middle| \varphi^{(\kappa)}_{j''_\kappa} \right\rangle B^{(\kappa)}_{p_\kappa, L_\kappa} \right)
\end{aligned} \tag{7.28}$$

where $P = p_1, \ldots, p_f$ is a first-layer index like J.

All other formulas introduced in the derivation of the equations of motion can be straightforwardly expressed, similarly to the second half of the derivatives for the B coefficients and are therefore not further mentioned here.

7.3.7 Auxiliary Programs

The implementation described above applies to the main program, which is responsible for the propagation of the wave function with a given Hamilton operator. There, all DOF expectation values and variances, trajectories of the GWPs and properties of the wave function, e.g. norm and autocorrelation function, are written to files. Two further auxiliary programs were developed, using the same modules as in the main program, in order to simplify the creation of input files and the analysis of the propagation (i.e., computation of expectation values, plotting one-dimensional projections of the wave function, etc.).

The auxiliary program for the creation of the input files for the main program uses a similar, but not identical, input structure as the MCTDH package.[101] If only the Cartesian kinetic energy operator and potentials consisting of monomial operator elements are used, then a typical MCTDH operator file can be expected to work without any changes. The inputfile however uses a different notation, adapted to the main program.

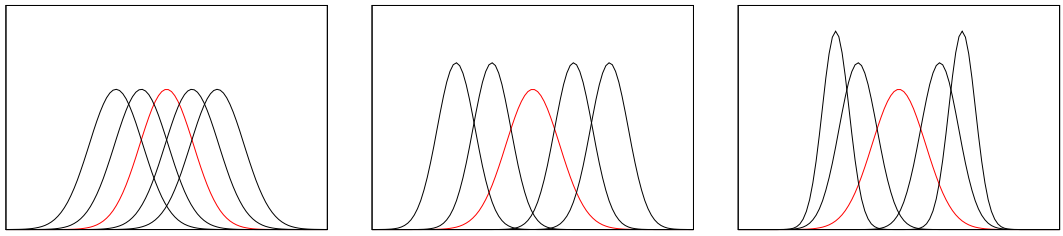

(a) `shell-q` **(b)** `shell-q-half` **(c)** `shell-q-half-nn`

Figure 7.4: Overview of employed initial GWP positions.

Within this program, various possibilities to place the initial, unoccupied GWPs have been implemented. The most relevant examples are presented here. The standard option is the `shell-q` option. Here, the GWPs are placed next to each other with a specified overlap (in the input-file), creating a 1-dimensional shell around the occupied GWP (Fig. 7.4(a)). Another option is offered by the `shell-q-half` keyword. Here, only the initial occupied GWP takes the initially specified width (typically the coherent state width of the corresponding harmonic oscillator of the potential). The width of neighboring GWPs is reduced by multiplying the initial width by a factor of 2: $a_{new} = 2a_0$ (see Fig. 7.4(b)). Additionally the option `shell-q-half-nn` is available. Here, all next-neighbor GWP that are added have a reduced width by a factor of 2 (Fig. 7.4(c)).

These options can be useful to avoid the appearance of singularities in the overlap matrix, due to a large overlap between two or more GWPs. The influence of the choice among the presented variants on the propagation is investigated in section 8 for a 3-site system.

The "analysis" program can be used to analyze the propagation. Several options are available for this purpose:

- calculate expectation values of an arbitrary operator (following the rules mentioned above)
- create plots of one- and two-dimensional projections of the wave function onto desired DOFs
- calculate the cross-correlation function
- calculate first- and second-layer natural populations
- create restart files.

7.4 Scaling Observations

In this section, the scaling behavior of the most time consuming part of the code will be reviewed: the calculation of the mean-fields. Additionally, the scaling behavior of the total computation time is presented.

The scaling behavior of the code has been analyzed using the system from chapter 8.1. Two sets of compositions were chosen for the scaling analysis:

- $f_1 = 5$, $f_2 = 2$ and $d_2 = 2$ (system 1)
- $f_1 = 4$, $f_2 = 4$ and $d_2 = 2$ (system 2)

All first-layer modes were assigned the same number of combined modes and the second-layer modes consisted of two DOFs.

The scaling was analyzed as a function of either the first-layer or second-layer configurations, i.e., n_1 and n_2 respectively. The numbers of configurations per mode were chosen to be 3, 5, 7 and 9, both for first layer and second layer, taken individually. Therefore, for each analysis four parameters could be obtained, showing the behavior for smaller and larger numbers of configurations.

First, the second-layer scaling is analyzed. Here, the focus lies on the total scaling and the second-layer mean-fields. The theoretical scaling for system 1 should

Table 7.2: Observed numerical scaling behavior for the total and second-layer computation time. Two different compositions of the modes were investigated. Depicted are the exponents x^n representing the scaling. System 1 consists of $f_1 = 5$ first-layer and $f_2 = 2$ second-layer modes, while system 2 is build of $f_1 = 4$ first-layer and $f_2 = 4$ second-layer modes. In both cases the second-layer modes were combined modes with two dimensions. The scaling was observed for four different numbers of first-layer configurations between 3 to 9. The theoretical scaling should be $\approx x^3$ for system 1 and $\approx x^5$ for system 2.

	system 1		system 2	
n_1	total	second-layer mean-fields	total	second-layer mean-fields
3	3.6	3.6	5.0	5.6
5	3.5	3.7	5.4	5.5
7	3.6	3.8	5.3	5.6
9	3.9	3.7	5.2	5.4

be proportional to $n_2^{f_2+1} \approx n_2^3$, for both the total and second-layer scaling. For system 2, the scaling should be $\approx n_2^5$. Tab. 7.2 shows the numerical scaling of the program and the second-layer mean-fields as a function of the number of second-layer configurations for different first-layer configurations. The scaling is in a good agreement with the theoretical scaling, revealing only a small overhead. It turns out that the total scaling of system 2 is slightly below the second-layer mean-field scaling. A possible reason for this is that in the total scaling, the less expensive parts are included whose effect is reduced as more configurations are considered.

A similar result is obtained for the first-layer scaling of system 1 in Tab. 7.3. The theoretical scaling for this system – both for total and mean-field scaling – should be $\sim n_1^{f_1+1} \approx n_2^6$. The observed scaling is only slightly higher, showing a small overhead for the calculation. System 2 shows the expected scaling behavior of the first-layer mean-field calculation. However, the total scaling of system 2 shows a different performance and scales almost linearly with the number of first-layer configurations. The reason is that the calculation of the second-layer mean-field matrices is still the most expensive part, exceeding the computation time of the first-layer mean-fields. Tab. 7.4 illustrates this behavior. Although the contribution for the calculation of the first-layer mean-fields grows with more SPFs, the second-layer mean-fields still take almost 50 % of the total computation time. Therefore an almost linear behavior is observed for the first-layer scaling with more second-layer configurations n_2. This was not observed for the second-layer scaling in system

Table 7.3: Observed numerical scaling behavior for the total and first-layer computation time. Two different compositions of the modes were investigated. Depicted are the exponents x^n representing the scaling. System 1 consists of $f_1 = 5$ first-layer and $f_2 = 2$ second-layer modes, while system 2 is build of $f_1 = 4$ first-layer and $f_2 = 4$ second-layer modes. In both cases the second-layer modes were combined modes with two dimensions. The scaling was observed for four different numbers of first-layer configurations between 3 to 9. The theoretical scaling should be $\approx x^6$ for system 1 and $\approx x^5$ for system 2.

	system 1		system 2	
n_2	total	first-layer mean-fields	total	first-layer mean-fields
3	6.3	6.5	3.6	5.2
5	6.2	6.5	1.5	5.2
7	6.2	6.5	1.2	5.2
9	5.7	6.6	1.0	5.2

1, although there were only 2 second-layer modes. This is, however, in agreement with the theoretical scaling (Eqn. 6.41), as the calculation of the second-layer mean-fields is more expensive for the same number of SPFs and modes, due to the non-orthogonal second-layer SPFs.

Table 7.4: Observed numerical scaling for system 2 ($f_1 = 4, f_2 = 4$ and $d_2 = 2$). The percentage of the total computation time is shown for the first- and second-layer mean-fields with increasing n_1; $n_2 = 5$ for all variants.

n_1	first-layer mean-fields [%]	second-layer mean-fields [%]
3	0.31	50.83
5	1.74	50.29
7	5.90	48.28
9	14.61	42.26

8 | The 2L-G-MCTDH Method: Applications

This chapter presents the application of the 2L-G-MCTDH method to two model systems, using the code which was presented in the preceding chapters. In particular, (i) site-to-site vibrational energy transfer in a molecular chain, as an example of intra-molecular vibrational redistribution (IVR), and (ii) charge transfer in a donor-acceptor system, as an example of high-dimensional non-adiabatic dynamics, are studied. Both model systems can be extended to a variable number of modes, permitting to analyze the scaling behavior of the 2L-G-MCTDH method. The results were compared with reference calculations obtained with either the MCTDH method or the ML-MCTDH method.

For the IVR Hamiltonian adapted from Schade and Hamm,[102] a detailed analysis of the 2L-G-MCTDH set-up will be presented for a small system with 15 DOFs, followed by the application of the method to analogous systems with 35 and 90 DOFs. This is followed by the presentation of the ultra-fast non-adiabatic charge transfer dynamics for a series of different bath-mode realizations ranging from 20 to 100 DOFs for the 2L-G-MCTDH method for coupled electronic states, using the single-set approach described in the preceding chapter.

8.1 Vibrational Energy Transfer in a Molecular Chain

8.1.1 Model Hamiltonian

The first application concerns a Hamiltonian describing site-to-site vibrational energy transfer in a molecular chain. This Hamiltonian is adapted from Schade and Hamm[102] and is a suitable model to test the 2L-G-MCTDH implementation for a single-surface problem involving a variable number of coupled vibrational degrees of freedom. This model was originally designed to mimic energy transport in proteins.[102]

As illustrated in Fig. 8.1, the model system is built up from a variable number of sites i ($i = 1, \ldots, n$) which are coupled to each other *via* so-called transporting

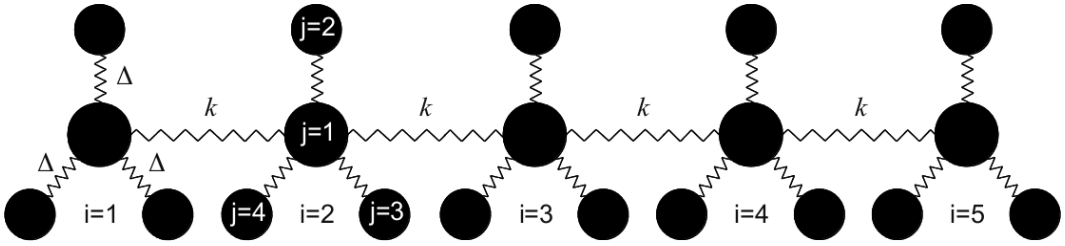

Figure 8.1: Representation of the Schade-Hamm Hamiltonian[102] for a $n = 5$ site system with $m = 4$ modes per site

modes $q_{i,j}$ that exhibit nearest-neighbor bi-linear couplings. Further, each site contains additional modes $q_{i,j}$, $1 < j \leq m$. These $(m-1)$ higher-frequency modes are locally coupled to the central transporting mode *via* the cubic coupling Δ which induces Fermi resonances and, hence, gives rise to efficient vibrational redistribution.

The analytic expression for the mass- and frequency weighted Hamiltonian in atomic units is given as,

$$\hat{H} = \frac{1}{2}\sum_{i=1}^{n}\sum_{j=1}^{m}\omega_{i,j}\left(\hat{p}_{i,j}^2 + \hat{q}_{i,j}^2\right) - \sum_{i=1}^{n-1} k\hat{q}_{i,1}\hat{q}_{i+1,1} + \Delta\sum_{i=1}^{n}\sum_{j=2}^{m}\hat{q}_{i,1}^2\hat{q}_{i,j} \tag{8.1}$$

where $\omega_{i,j}$ is the frequency of the corresponding mode. As explained above, $j = 1$ always corresponds to a transporting mode and $j > 1$ corresponds to a higher-frequency mode. The transporting modes were chosen to be resonant, i.e., equal frequencies are assumed for all transporting modes $\omega_{1,1} = \omega_{2,1} = \omega_{3,1} = \cdots$. Furthermore, as already mentioned, the high-frequency modes communicate with the transporting mode *via* Fermi resonances, i.e., resonance conditions such that $\omega_{i,k} = 2\omega_{i,k'}$ inducing rapid on-site energy redistribution. Hence, the frequencies at a given site i are doubled with increasing ordering number $\left\{\omega_{i,1}, \omega_{i,2}, \omega_{i,3}, \cdots\right\} = \left\{\omega_{i,1}, 2\omega_{i,1}, 4\omega_{i,1}, \cdots\right\}$.

Fig. 8.2 shows a 3D representation of two-dimensional cuts along the potential, i.e., the near-harmonic potential along the two transporting modes $q_{1,1}$ and $q_{2,1}$ (8.2(a)) and the anharmonic potential along a transporting mode $q_{1,1}$ and the local mode $q_{1,2}$ (8.2(b)). The model Hamiltonian (Eqn. 8.1) generates a potential in the subspace of a given transporting mode and a coupled site-local mode that is bonding only in a restricted, shallow region. The non-bonding character depends on the strength of the anharmonicity given by the coupling parameter Δ.

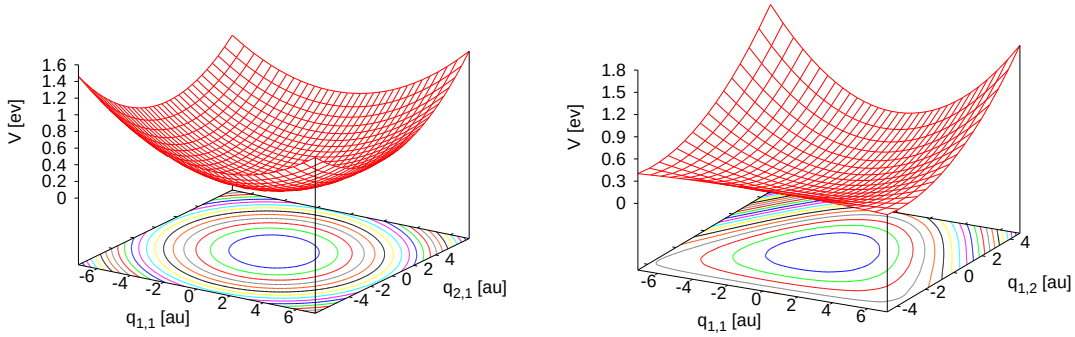

(a) PES along $q_{1,1}$ and $q_{2,1}$ **(b)** PES along $q_{1,1}$ and $q_{1,2}$

Figure 8.2: 3D representation of the potential energy surfaces (PES) along the transporting and high-frequency modes.

By choosing the coupling parameters k and Δ appropriately, the site-local IVR can be switched on and off. By increasing the coupling Δ relative to k, the IVR efficiency is increased. In the calculations presented below, the coupling between the sites has been set to $k = 0.15$ and the intra-site coupling was either chosen to be very small $\Delta = 0.01$ or rather high $\Delta = 0.10$.

Higher intra-site coupling values lead to problems in the propagation – both for (ML-)MCTDH and 2L-G-MCTDH – due to the non-bonding part of the potential, resulting in a reflection at the grid ends in the (ML-)MCTDH calculations and *escaping* GWPs for the 2L-G-MCTDH method, (i.e., the GWPs move downhill in the non-bonding potential region).

8.1.2 Initial Condition

The initial condition in all of the following calculations is set up such that all high-frequency modes are initialized with $q_{i,2:m} = p_{i,2:m} = 0.0$. All transporting modes except for the first are also set to $q_{2:n,1} = p_{2:n,1} = 0.0$. The transporting mode on site 1, however, is displaced. This is done by shifting the initial GWP to have a (virtual) overlap of 0.8 with a virtual GWP located at $q_{1,1} = 0.0$. The initial momentum is set to zero. The initial condition for the first transporting mode is therefore $q_{1,1} = 0.944$ and $p_{1,1} = 0.0$. The width of the initially populated wave packet in all modes was set to the coherent-state width of the corresponding harmonic oscillator $\left(a = \frac{m\omega}{2}\right)$.[79] Therefore, the width is set to $a = 0.5$, since the Hamiltonian is set up in mass- and frequency-weighted coordinates. For 2L-G-MCTDH, the initial condition was defined by populating only one Gaussian

basis function of the transporting mode. The unoccupied GWPs are arranged as described in section 7.3 using an overlap of 0.8 with the next-neighbor GWPs.

8.1.3 3-Site System: Method Evaluation

The 3-site system is a minimal realization that was chosen to check the implementation, verify whether the method shows correct convergence properties, and assess how mode combination and the choice of the initially unoccupied GWPs affect the calculation. To evaluate and answer these questions, several calculations have been performed.

The 3 sites all contain 5 modes per site, adding up to a total of 15 degrees of freedom. In the following calculations, each site corresponds to one first-layer particle, ensuring a symmetrical and equal description of all sites. The 5 modes within a site are split into a variable number of second-layer particles. While the central transporting mode is always set to be an uncombined second-layer mode, three variations of combination schemes for the four high-frequency modes are tested. Fig. 8.3 illustrates these variants. The simplest and most flexible approach is to use a single second-layer mode for each high-frequency mode ("4x1 scheme"). The opposite limit is to put all four modes into one distinct second-layer particle ("1x4 scheme"). The third scheme is a compromise between the two previous approaches, where two 2-dimensional second-layer modes are constructed ("2x2 scheme"). This setup is especially useful in the case of strong coupling ($\Delta = 0.1$).

All three first-layer modes use the same number of SPFs n_κ and all second-layer modes are also set up symmetrically, such that in all three first-layer modes the same number of second-layer SPFs $n_{\kappa,\mu}$ are used.

In order to investigate the convergence behavior for the first-layer and second-layer configurations, either the number of second-layer configurations or first-layer configurations is fixed, respectively. For all three basis set-ups presented above (i.e., `shell-q`, `shell-q-half` and `shell-q-half-nn`), the convergence behavior is analyzed.

8.1.3.1 MCTDH vs. ML-MCTDH

The different combination schemes are compared within a MCTDH or ML-MCTDH setup, which are used as reference calculations. In particular, the ML-MCTDH

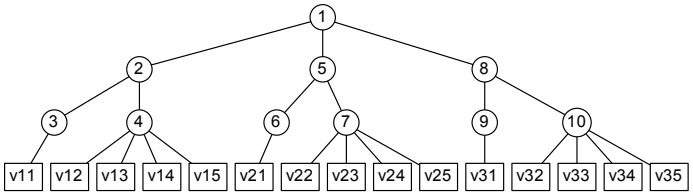

(a) Mode Combination scheme 1: All high-frequency modes combined into one second-layer particle (1x4).

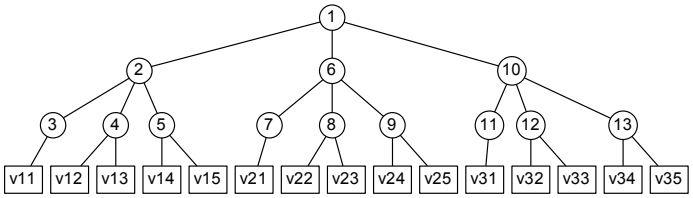

(b) Mode Combination scheme 2: Two high-frequency modes combined into one second-layer particle (2x2).

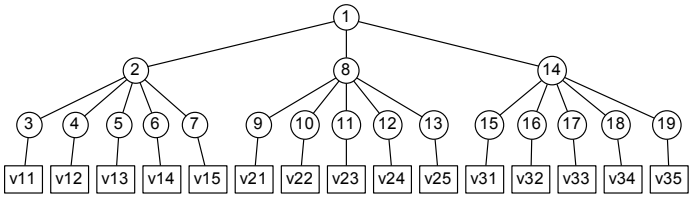

(c) Mode Combination scheme 3: All high-frequency modes are separated into individual particles (4x1).

Figure 8.3: Mode Combination schemes for the 3 site system. (a) 1x4 scheme, (b) 2x2 scheme and (c) 4x1 scheme.

method is used with the same combination schemes as described above for the 2L-G-MCTDH. By contrast, the mode combination schemes presented above cannot be used directly with the MCTDH method and needs to be adapted. Therefore, each second-layer particle is treated as a MCTDH mode. This means that for the 1x4 splitting, $f = 6$ modes are used and for the 2x2 splitting $f = 9$ are used. The 4x1 scheme ($f = 12$) is unfeasible for the MCTDH method due to the exponential scaling of the numerical effort.

The ML-MCTDH calculations are performed with $n_\kappa = n_{\kappa,\mu} = 5$ first-layer and second-layer SPFs for both transporting and high-frequency modes. Since the MCTDH calculations are computationally quite expensive for this setup, they use

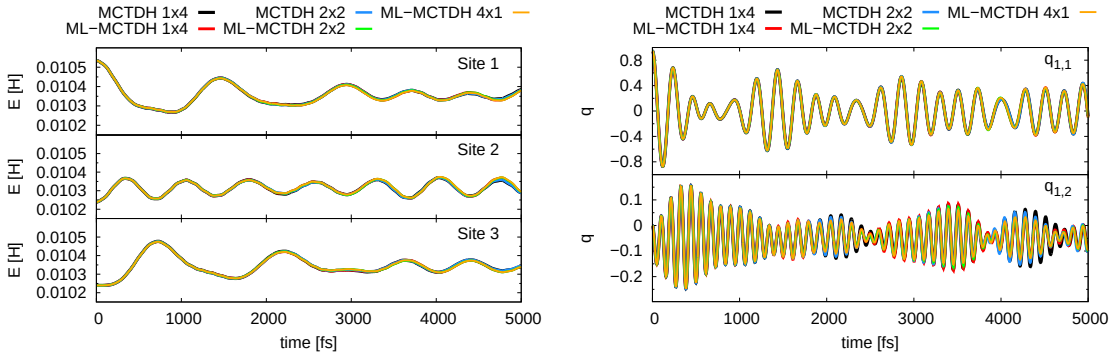

(a) site energies **(b)** modes $q_{1,1}$ and $q_{1,2}$

Figure 8.4: Comparison of (a) the site energies and (b) position of modes $q_{1,1}$ and $q_{1,2}$ calculated with MCTDH and ML-MCTDH for different mode combinations.

$n_\kappa\left(q_{:,1}\right) = 5$ SPFs for the transporting and $n_\kappa\left(q_{:,2:m}\right) = 3$ SPFs for the high-frequency modes.

First, the energy flow through the chain is compared and analyzed. Fig. 8.4(a) shows the different results. In general, the results show that the energy is distributed among the three sites along the chain. While the energy for site 2 is almost continuously oscillating, sites 1 and 3 show a delay in the oscillations due to the transport along the chain. The comparison shows that the three combination schemes have no visible influence. Only differences between MCTDH and ML-MCTDH are visible.

Furthermore, the expectation values of the modes are compared directly. For illustration purposes, the expectation values for the modes $q_{1,1}$ and $q_{1,2}$ are shown in Fig. 8.4(b) for the different setups. As expected, the trend is similar to that of the energy distribution. For mode $q_{1,1}$, MCTDH and ML-MCTDH only differ slightly and mode combination does not have a significant influence. Mode $q_{1,2}$ shows a similar behavior. The calculations show only slightly deviations in the amplitudes, but all quantitative features are visible. This is also valid for the other high-frequency modes that are not shown. Since the MCTDH and ML-MCTDH results are nearly identical and show the same behavior, only the ML-MCTDH calculations are used to compare to the 2L-G-MCTDH results.

For the comparison of the 2L-G-MCTDH results to the reference calculations, the same combination scheme is used throughout.

8.1.3.2 1x4 Combination Scheme

First, the first-layer convergence properties of the 1x4 scheme are analyzed in combination with the `shell-q` basis. For this purpose, the number of second-layer SPFs has been fixed to $n_{\kappa,\mu} = 5$ for each mode. One can see in Fig. 8.5(a) for the modes $q_{1,1}$ (transporting mode on site 1) and $q_{1,2}$ (first high-frequency mode on site 1) that the results do converge with an increasing number of first-layer SPFs. This can be seen especially for the $q_{1,2}$-mode in Fig. 8.5(a). Furthermore, the results show a very good agreement to ML-MCTDH over the time period of 2000 fs. To reproduce the ML-MCTDH results, 7 SPFs are needed (at least for $q_{1,2}$), and 5 SPFs already show the same features, even over a duration of 5000 fs.

Second, the second-layer convergence properties are analyzed for the same setup. The same calculations as before are performed with an increasing number of second-layer $n_{\kappa,\mu}$ SPFs for a fixed number of $n_\kappa = 5$ first-layer SPFs per mode. Again, a clear improvement with increasing number of second-layer configurations is visible. As can be seen in Fig. 8.5(b), 3 second-layer configurations do not suffice as mode $q_{1,1}$ is not described correctly, since the amplitude is slightly smaller. The same holds true for mode $q_{1,2}$.

Fig. 8.5(b) also shows a problem arising from the GWP basis. Although five GWPs are sufficient to accurately describe the dynamics of the modes up to 5000 fs, using more GWPs can lead to numerical instabilities due to singularities arising from a large overlap of two (or more) GWPs. As a consequence, the timesteps of the adaptive integrator drop down and do not recover, so that the calculations are eventually stopped.

Due to these problems, no more than 5 SPFs per first- and second-layer mode can be used for the combination of the `shell-q` basis setup and the 1x4 combination scheme. But, as shown in Fig. 8.6, this is sufficient to achieve an almost perfect agreement with the reference results. Fig. 8.6 shows the energy redistribution among the sites for $n_\kappa = n_{\kappa,\mu} = 3$ and $n_\kappa = n_{\kappa,\mu} = 5$. While for 3 SPFs the results strongly differ from the reference, 5 SPFs show a very good agreement up to the depicted 5000 fs.

Next, the `shell-q-half` initial setup is analyzed. Therefore the same expectation values are compared. This setup should reduce the problems arising from singularities caused by a large overlap of the GWPs.

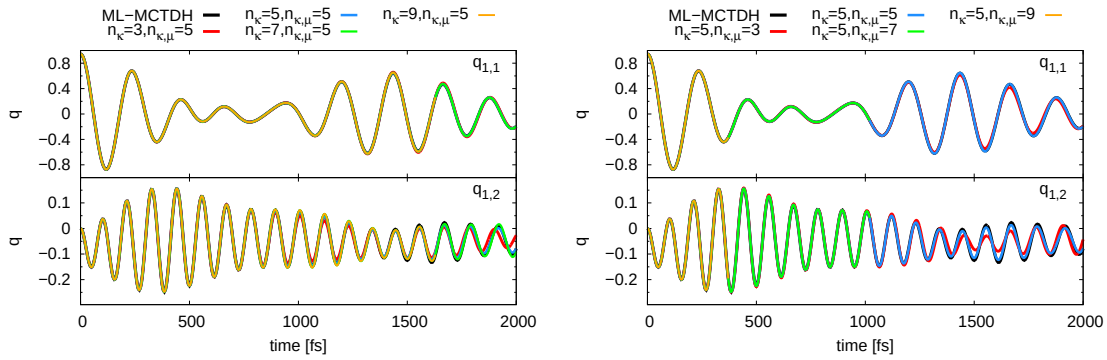

(a) first-layer convergence **(b)** second-layer convergence

Figure 8.5: First and second layer convergence for modes $q_{1,1}$ and $q_{1,2}$ with 2L-G-MCTDH (colored lines) compared to ML-MCTDH(black lines). (a) $n_{\kappa,\mu} = 5$ for the first-layer convergence and (b) $n_\kappa = 5$ for the second-layer convergence. The mode combination scheme 1x4 in conjunction with the `shell-q` basis is used.

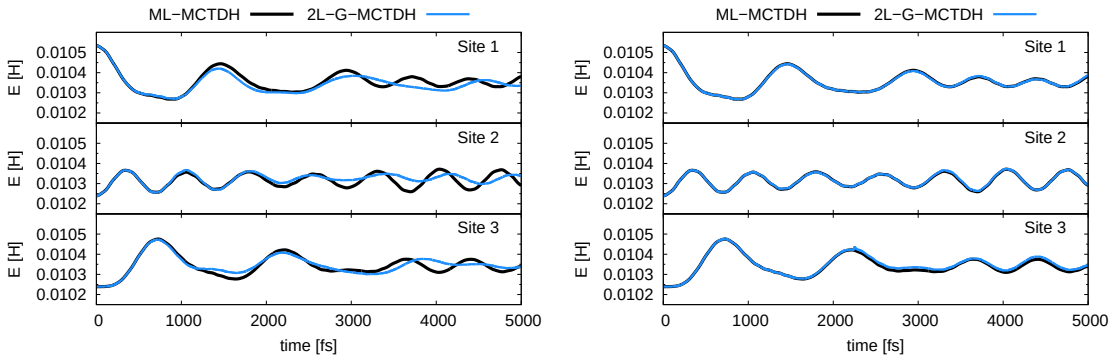

(a) $n_\kappa = 3$, $n_{\kappa,\mu} = 3$ **(b)** $n_\kappa = 5$, $n_{\kappa,\mu} = 5$

Figure 8.6: Comparison of ML-MCTDH (black) and 2L-G-MCTDH (blue) for the energy redistribution along the 3 sites over 5000 fs. The results for (a) $n_\kappa = 3$, $n_{\kappa,\mu} = 3$ and (b) $n_\kappa = 5$, $n_{\kappa,\mu} = 5$ are shown. The mode combination scheme 1x4 in conjunction with the `shell-q` basis is used.

Again, first the convergence behavior with the number of first-layer SPFs is considered. The number of second-layer configurations is again fixed to $n_{\kappa,\mu} = 5$. The results for mode $q_{1,1}$ (Fig. 8.7(a)) show that the result does not change with the addition of more first-layer SPFs. Three first-layer SPFs seem to be sufficient, but the second-layer basis might be too restrictive and therefore prohibits a better description.

However, mode $q_{1,2}$ ($n_\kappa = 3$, Fig 8.7(a)) seems to be strongly dependent on the number of second-layer SPFs. The results do not seem to be converged with 5 second-layer SPFs. As Fig. 8.7(a) shows, 7 second-layer SPFs are also not sufficient to cover all features correctly (i.e., the small rise in amplitude at ∼1600 fs for $q_{1,2}$),

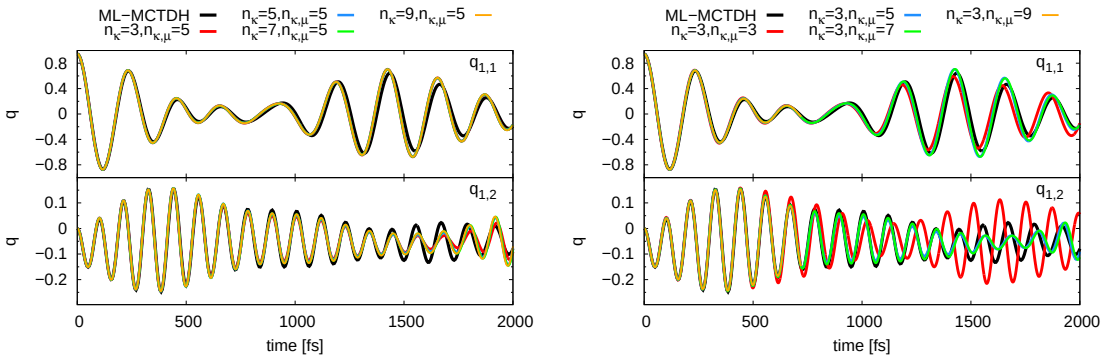

(a) first-layer convergence **(b)** second-layer convergence

Figure 8.7: First and second layer convergence for modes $q_{1,1}$ and $q_{1,2}$ with 2L-G-MCTDH (colored lines) compared to ML-MCTDH(black lines). (a) $n_{\kappa,\mu} = 5$ for the first-layer convergence and (b) $n_\kappa = 3$ for the second-layer convergence. The mode combination scheme 1x4 in conjunction with the `shell-q-half` basis is used.

but the calculation almost shows the same result as for $n_{\kappa,\mu} = 5$, and therefore indicates a good convergence behavior. Unfortunately, with 9 second-layer SPFs, numerical problems due to singularities arise and an extension of the basis is not possible.

The convergence with the number of second-layer SPFs is analyzed for a rather small number of first-layer SPF $n_\kappa = 3$, because a larger number of n_κ are again found to cause severe problems due to singularities. Fig. 8.7(b) shows an almost converged result for $n_{\kappa,\mu} = 5$, which is hardly improved by using $n_{\kappa,\mu} = 7$ SPFs. While the description of $q_{1,1}$ is in quite good agreement for $n_\kappa = 5$ or more, the comparison for $q_{1,2}$ to the reference again reveals problems, as the small rise in amplitude at $\sim$1600 fs is again not reproduced correctly.

Consequently, these results, as compared to the `shell-q` basis setup, are not quite as good, due to the insufficient description of the modes by the `shell-q-half` basis setup. However, the plot for the energy redistribution (Fig. 8.8) shows that the overall performance until 5000 fs is showing all features for $n_\kappa = n_{\kappa,\mu} = 5$, but is slightly worse than `shell-q`.

The last basis setup that is investigated is the `shell-q-half-nn` setup. Here, the problem of singularities should be almost eliminated, as only two GWPs with the same width are present in each DOF. However, this means that presumably more SPFs are needed for a correct description. Also the convergence behavior might be

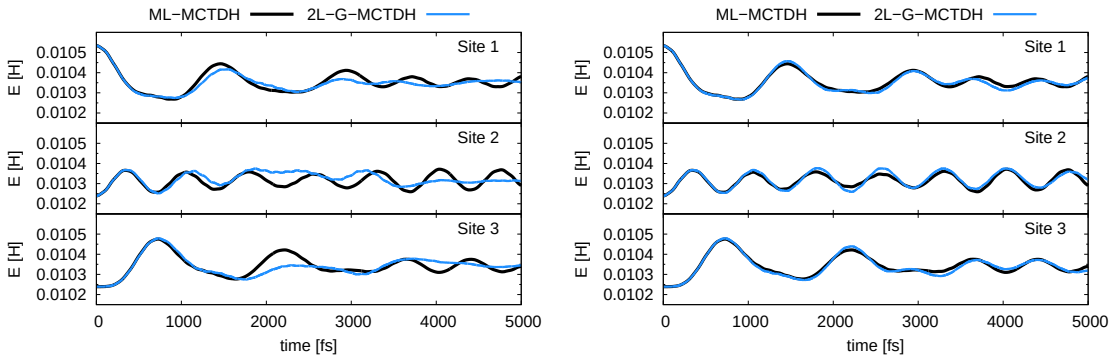

(a) $n_\kappa = 3$, $n_{\kappa,\mu} = 3$ **(b)** $n_\kappa = 5$, $n_{\kappa,\mu} = 5$

Figure 8.8: Comparison of ML-MCTDH (black) and 2L-G-MCTDH (blue) for the energy redistribution along the 3 sites over 5000 fs. The results for (a) $n_\kappa = 3$, $n_{\kappa,\mu} = 3$ and (b) $n_\kappa = 5$, $n_{\kappa,\mu} = 5$ are shown. The mode combination scheme 1x4 in conjunction with the `shell-q-half` basis is used.

worse, as the added GWPs are getting increasingly narrow. Note that this setup is equal to `shell-q-half` for $n_{\kappa,\mu} = 3$.

Fig. 8.9(a) shows the first layer convergence for modes $q_{1,1}$ and $q_{1,2}$. One can see that for mode $q_{1,1}$, the results do not improve much with more SPFs. Indeed, $n_\kappa = 5$ appears to be sufficient. Furthermore, a slightly faster oscillation frequency is observed, possibly due to the narrower GWPs compared to `shell-q` and `shell-q-half`. Mode $q_{1,2}$, however, does not show a convergence behavior up to 9 first-layer SPFs. The description is again limited by the second-layer configurations as for the `shell-q-half` setup. Up to 1000 fs the results are almost identical but then begin to diverge. For mode $q_{1,2}$, the small increase in amplitude at 1600 fs is again not described correctly by this basis setup. A positive side note is that absolutely no numerical problems occurred during the propagation. The integration is stable throughout all propagations.

Fig. 8.9(b) shows the second-layer convergence. For mode $q_{1,1}$, one sees that 5 second-layer SPFs are enough to reach convergence. Again, for mode $q_{1,2}$ this is not the case. Up to about 1200 fs the results are almost identical for all number of SPFs except for $n_{\kappa,\mu} = 3$. By increasing $n_{\kappa,\mu}$, the time at which the results begin to diverge is increased by almost 500 fs. Furthermore, the small increase in amplitude is again not captured with this basis setup.

Since no problems occurred with an increasing number of SPFs, the results for up to 9 first and second-layer SPFs can be presented. The lower limit in this case is

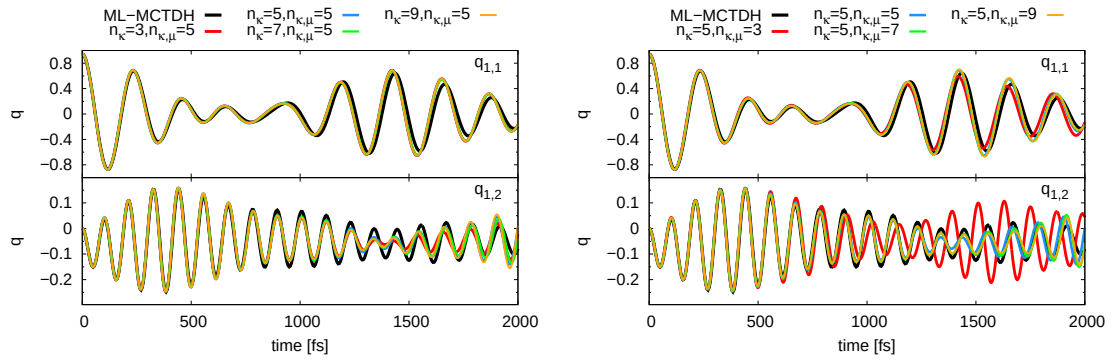

(a) first-layer convergence **(b)** second-layer convergence

Figure 8.9: First and second layer convergence for modes $q_{1,1}$ and $q_{1,2}$ with 2L-G-MCTDH (colored lines) compared to ML-MCTDH(black lines). (a) $n_{\kappa,\mu} = 5$ for the first-layer convergence and (b) $n_\kappa = 3$ for the second-layer convergence. The mode combination scheme 1x4 in conjunction with the `shell-q-half-nn` basis is used.

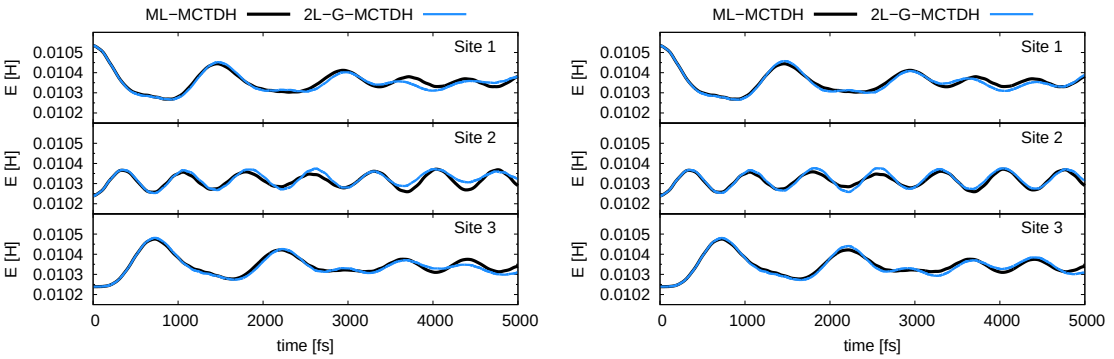

(a) $n_\kappa = 5$, $n_{\kappa,\mu} = 5$ **(b)** $n_\kappa = 9$, $n_{\kappa,\mu} = 9$

Figure 8.10: Comparison of ML-MCTDH (black) and 2L-G-MCTDH (blue) for the energy redistribution along the 3 sites over 5000 fs. The results for (a) $n_\kappa = 5$, $n_{\kappa,\mu} = 5$ and (b) $n_\kappa = 9$, $n_{\kappa,\mu} = 9$ are shown. The mode combination scheme 1x4 in conjunction with the `shell-q-half-nn` basis is used.

represented by the calculation with $n_\kappa = n_{\kappa,\mu} = 5$ as 3 SPFs give the same result as for `shell-q-half`. As can be seen in Fig. 8.10 the results with $n_\kappa = n_{\kappa,\mu} = 9$ are in good agreement to (ML-)MCTDH. The overall behavior is well described with this basis setup. 5 first- and second-layer SPFs are not sufficient, especially at the end around 4000 fs.

8.1.3.3 2x2 Combination Scheme

In this setup, the 4 high-frequency modes are split among two multi-dimensional GWPs. Thus, there are 3 multi-dimensional GWPs per first-layer SPF, where one SPF contains the transporting mode and two combined particles carry 2 high-

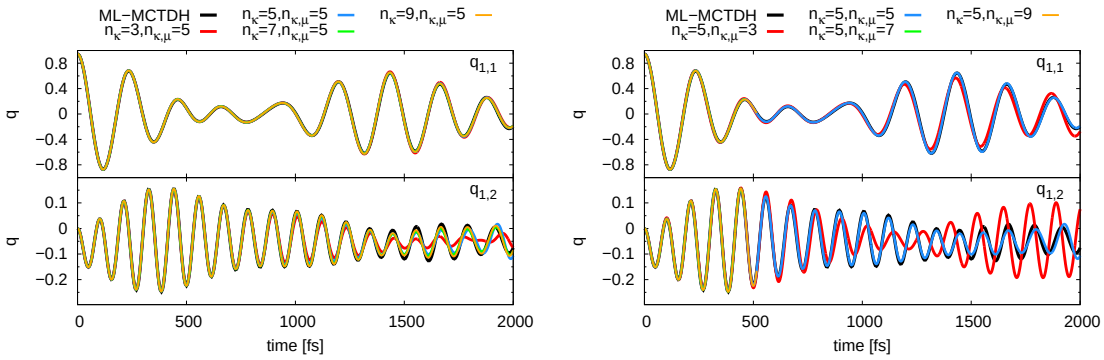

(a) first-layer convergence **(b)** second-layer convergence

Figure 8.11: First and second layer convergence for modes $q_{1,1}$ and $q_{1,2}$ with 2L-G-MCTDH (colored lines) compared to ML-MCTDH(black lines). (a) $n_{\kappa,\mu} = 5$ for the first-layer convergence and (b) $n_\kappa = 5$ for the second-layer convergence. The mode combination scheme 2x2 in conjunction with the `shell-q-half` basis is used.

frequency modes each. This scheme should cause the modes to be more flexible and the same number of SPFs should show better results.

Similarly to the 1x4 combination scheme, the results for the different basis setups are analyzed. However, the results with the `shell-q` basis show a very problematic behavior due to singularities and cause the time-steps of the propagation to be very small ($< 10^{-6}$ fs). Hence, only the calculations with the two other setups are presented.

Fig 8.11(a) shows the results for modes $q_{1,1}$ and $q_{1,2}$ for a fixed number of $n_{\kappa,\mu} = 5$ second-layer SPFs with basis setup `shell-q-half`. For mode $q_{1,1}$ $n_\kappa = 3$ SPFs are already sufficient. Yet, for $q_{1,2}$ at least $n_\kappa = 5$ SPFs are needed to get a near-converged result. More SPFs only add small corrections to the amplitude. As expected, the results show a better consistency with the ML-MCTDH results compared to the 1x4 scheme as the small rise in amplitude at 1600 fs is captured correctly in these calculations.

Turning to the results for a fixed number of second-layer configurations, $n_\kappa = 5$ shows the same problems as for the 1x4 scheme. Calculations with more than $n_{\kappa,\mu} \geq 7$ exhibit problems due to singularities. Results for mode $q_{1,1}$ (Fig. 8.11(b)) show a very good agreement with the reference for $n_{\kappa,\mu} = 5$. The result for $q_{1,2}$ is however limited by the first-layer SPFs, as already seen in Fig. 8.11(a), where $n_\kappa = 9$ SPFs shows a good agreement.

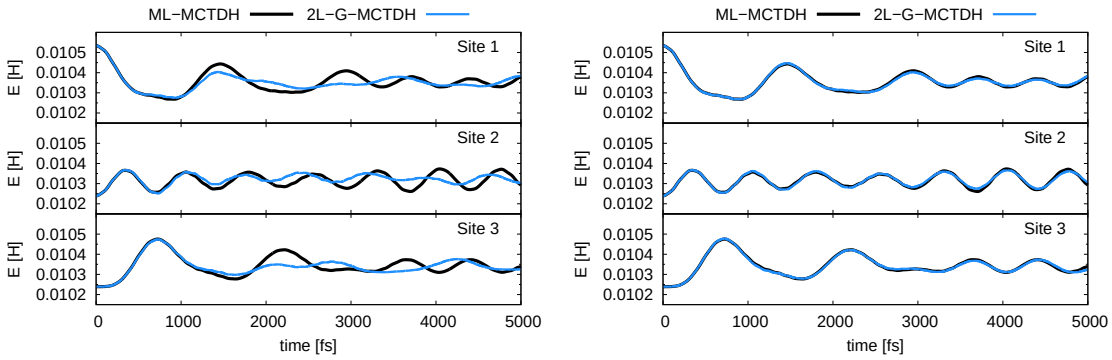

(a) $n_\kappa = 3$, $n_{\kappa,\mu} = 3$ **(b)** $n_\kappa = 5$, $n_{\kappa,\mu} = 5$

Figure 8.12: Comparison of ML-MCTDH (black) and 2L-G-MCTDH (blue) for the energy redistribution along the 3 sites over 5000 fs. The results for (a) $n_\kappa = 3$, $n_{\kappa,\mu} = 3$ and (b) $n_\kappa = 5$, $n_{\kappa,\mu} = 5$ are shown. The mode combination scheme 2x2 in conjunction with the `shell-q-half` basis is used.

Therefore, the energy re-distribution along the sites is also shown with $n_\kappa = 9$ SPFs. As above the results with 5 first- and second-layer SPFs are in good agreement to the reference calculations (Fig. 8.12). The use of 9 first-layer SPFs only gives negligible improvement. Hence $n_\kappa = 5$ is enough to capture the correct behavior.

The basis setup `shell-q-half-nn` again shows no problems during the propagations and no singularities or problematic time-step drops. The results also show a very good convergence behavior with the number of first-layer SPFs n_κ (Fig. 8.13(a)). While mode $q_{1,1}$ shows already a good agreement for $n_\kappa = 3$, mode $q_{1,2}$ shows convergence with increasing first-layer SPFs. However, the results differ slightly from the reference. The frequency shift, that was observed for the 1x4 scheme, is not present in these results (at least for $n_\kappa \geq 7$).

Similarly to the previous results with a fixed number of first-layer configurations ($n_\kappa = 5$), $n_{\kappa,\mu} = 5$ SPFs are at least needed to obtain a nearly converged result for mode $q_{1,1}$ (Fig. 8.13(b)). Mode $q_{1,2}$ is again restricted by the first-layer configurations as $n_\kappa = 9$ SPFs are needed for a nearly perfect agreement.

As for the 1x4 combination scheme, the results of the energy re-distribution among the site chain are depicted for 5 and 9 first- and second-layer SPFs. While 5 SPFs are not sufficient, 9 SPFs give a very good agreement compared to the reference calculations. This again shows the excellent convergence behavior of the method for the present system.

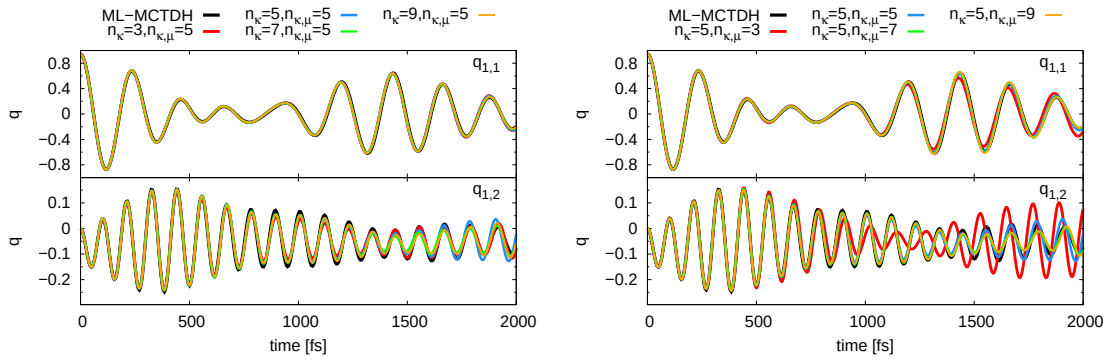

(a) first-layer convergence **(b)** second-layer convergence

Figure 8.13: First and second layer convergence for modes $q_{1,1}$ and $q_{1,2}$ with 2L-G-MCTDH (colored lines) compared to ML-MCTDH(black lines). (a) $n_{\kappa,\mu} = 5$ for the first-layer convergence and (b) $n_\kappa = 5$ for the second-layer convergence. The mode combination scheme 2x2 in conjunction with the `shell-q-half-nn` basis is used.

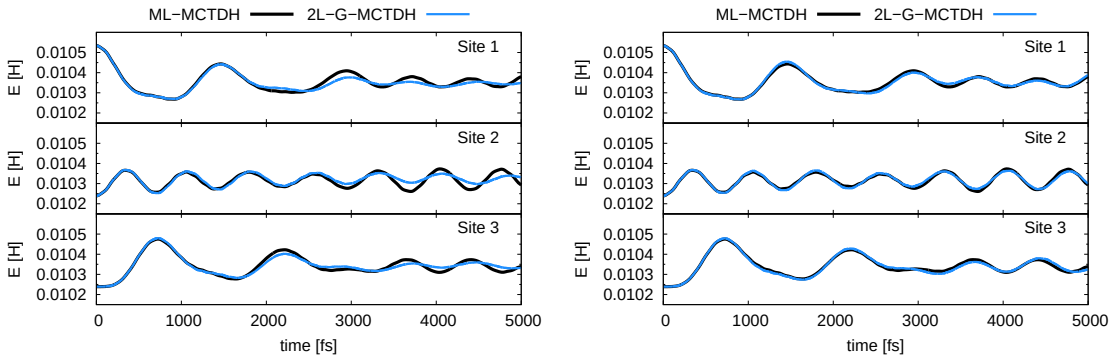

(a) $n_\kappa = 5$, $n_{\kappa,\mu} = 5$ **(b)** $n_\kappa = 9$, $n_{\kappa,\mu} = 9$

Figure 8.14: Comparison of ML-MCTDH (black) and 2L-G-MCTDH (blue) for the energy redistribution along the 3 sites over 5000 fs. The results for (a) $n_\kappa = 5$, $n_{\kappa,\mu} = 5$ and (b) $n_\kappa = 9$, $n_{\kappa,\mu} = 9$ are shown. The mode combination scheme 2x2 in conjunction with the `shell-q-half-nn` basis is used.

8.1.3.4 4x1 Combination Scheme

The 4x1 combination scheme revealed severe numerical problems. With none of the three tested basis setups – not even the `shell-q-half-nn` setup – was it possible to use more than 3 second-layer configurations. Hence, the calculations for the `shell-q-half-nn` setup are identical to the `shell-q-half` setup. Furthermore, no calculation reached a reasonable propagation time due to singularities for the `shell-q` setup.

Since only with $n_{\kappa,\mu} = 3$ second-layer SPFs, we could reach more than a few femtoseconds, the results do not show good agreement to the reference calculations. In the previous combination schemes, at least 5 SPFs were necessary for near-

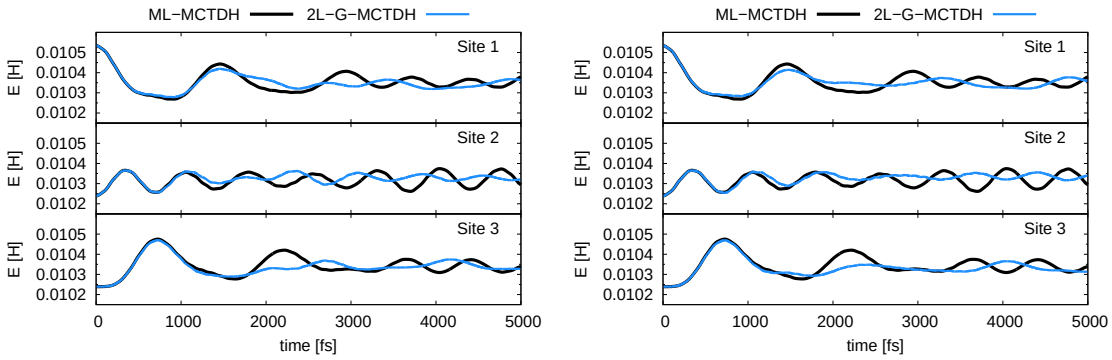

(a) $n_\kappa = 3$, $n_{\kappa,\mu} = 3$ **(b)** $n_\kappa = 9$, $n_{\kappa,\mu} = 3$

Figure 8.15: Comparison of ML-MCTDH (black) and 2L-G-MCTDH (blue) for the energy redistribution along the 3 sites over 5000 fs. The results for (a) $n_\kappa = 3$, $n_{\kappa,\mu} = 3$ and (b) $n_\kappa = 9$, $n_{\kappa,\mu} = 3$ are shown. The mode combination scheme 4x1 in conjunction with the `shell-q-half` basis is used.

converged results. Here, the situation is different, as one can see for the energy distribution (Fig. 8.15). Even $n_\kappa = 9$ first-layer SPFs are not able to make up for the inaccurate description by the second-layer modes.

8.1.3.5 Conclusion

The results presented above show that the 2L-G-MCTDH method in general performs well and shows good convergence properties. Nevertheless the choice of mode combination and the setup of the unoccupied GWPs is crucial, regarding numerical stability and reliability of the results.

The 1x4 combination scheme is the least flexible of the investigated schemes. Here, the best result is obtained with the `shell-q` basis setup. However, because of numerical issues caused by singularities due to the large overlap of (at least) two GWPs, no more than 5 second-layer SPFs could be used for the calculations. Curiously, the problem also appeared for too many first-layer SPFs with only 5 second-layer SPFs. The reason for this is not yet understood, but a possible reason might be the less flexible second-layer SPFs, as all high-frequency modes are combined together in one second-layer mode. As more second-layer SPFs are not feasible, it is not directly possible to confirm this assumption. The same problem occurred for the `shell-q-half` basis setup with this mode combination. However for 5 first- and second-layer SPFs the results are in a good agreement to the reference. Using the basis `shell-q-half-nn` eliminates all these problems and also demonstrates the very good convergence properties by increasing the number

of GWPs. But, the results show quite a remarkable difference to the reference calculations, because of the bad description of the high-frequency modes.

By using the 2x2 combination scheme, significantly improved results are obtained. Both `shell-q-half` and `shell-q-half-nn` show a nearly perfect agreement to the reference calculations. While for `shell-q-half`, 5 first and second-layer SPFs are sufficient (more SPFs again caused numerical problems), for `shell-q-half-nn` at least 9 first and second-layer SPFs are needed.

Finally, the most flexible combination scheme, i.e., the 1x4 scheme, caused severe numerical problems. While for `shell-q`, no calculation reached a reasonable propagation time, `shell-q-half` as well as `shell-q-half-nn` are only stable with 3 first and second-layer SPFs and are therefore equivalent. However, these are not sufficient to get a reasonable agreement.

If possible, the `shell-q` and `shell-q-half` basis setup should be employed in order to use less numbers of configurations. To avoid numerical instabilities, one should check another mode combination scheme or try a different setup (width and position in phase space) of the unoccupied GWPs.

8.1.4 5-Site System (35 DOFs)

In this section, the results for a 5-site system comprising a total of 35 DOFs are discussed. The 35 DOFs distribute equally among the 5 sites, where each site is attributed one first-layer mode. Each site consists of 7 modes, i.e., 1 transporting mode and 6 high-frequency modes. The transporting modes $q_{:,1}$ are again set up in an individual second-layer mode, separated from the high-frequency modes. Combining the 6 high-frequency modes in one particle would require many SPFs, which would probably be problematic regarding the numerical stability. Therefore, always three high-frequency modes are combined, as a compromise of the above mentioned 1x4 and 2x2 combination schemes or, using the same naming convention, constructing a 2x3 combination scheme. As basis setup `shell-q-half` is chosen, since it gave a reasonable result for small numbers of SPFs for the 3 site system and was quite stable.

As reference, a ML-MCTDH calculation is employed, using the same mode setup. The system parameters are chosen identical to the 3 site system: $k = 0.15$ and $\Delta = 0.10$. For the ML-MCTDH calculation again 5 SPFs for the first- and second-

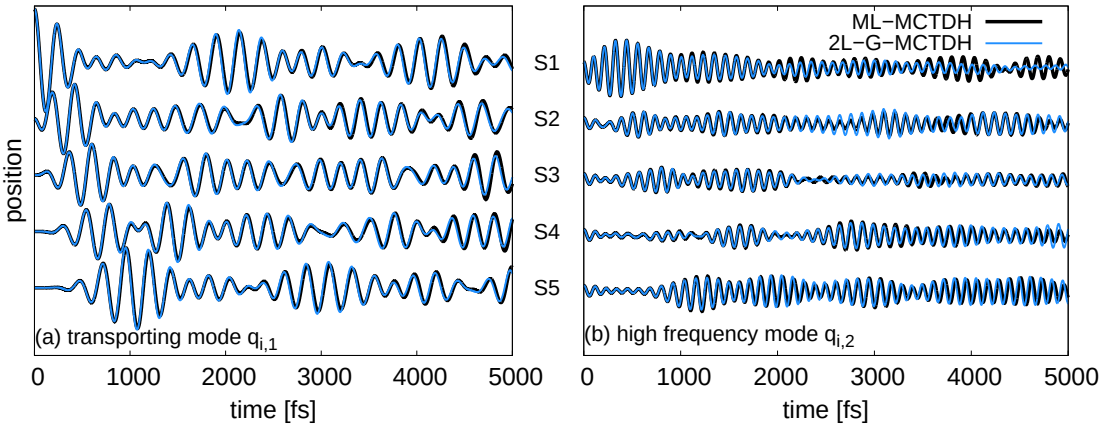

Figure 8.16: Comparison of ML-MCTDH (black) and 2L-G-MCTDH (blue) for (a) the transporting modes and (b) the first 5 high-frequency-modes of the 5 sites for 5000 fs.

layer modes are used. The calculations for 2L-G-MCTDH are presented with the same number of SPFs.

Fig. 8.16 shows the results for a period of 5000 fs. Since all modes are in resonance with each other, one sees an efficient energy transfer between the sites. The excess energy that is initially localized at site 1 takes about 1100 fs to move from site 1 to site 5. Therefore, a back and forth transfer takes about 2200 fs. The results are in a good agreement to the ML-MCTDH calculation. Over the complete time period, a similar behavior for all 5 transporting modes is observed. The high-frequency mode $q_{1,2}$ shows a slight deviation from the reference. This is especially visible in the amplitude of the oscillations. Furthermore, a slight shift of the frequency of the oscillations for this mode is observed. The other high-frequency modes show a better agreement.

The site energies and the energy transfer along the sites depicted in Fig. 8.17 confirm the good agreement to the reference calculations. A slightly faster energy transfer is observed, especially seen for site 1 at around 4200 fs. For comparison, the result with only 3 SPFs is plotted, underlining the good convergence behavior of the method. Until ∼2000 fs, corresponding to the time range of one energy transfer cycle, the results are comparable, but then exhibit a more oscillatory behavior as the correlations are not captured correctly any more and an equilibrium state seems to be reached more rapidly.

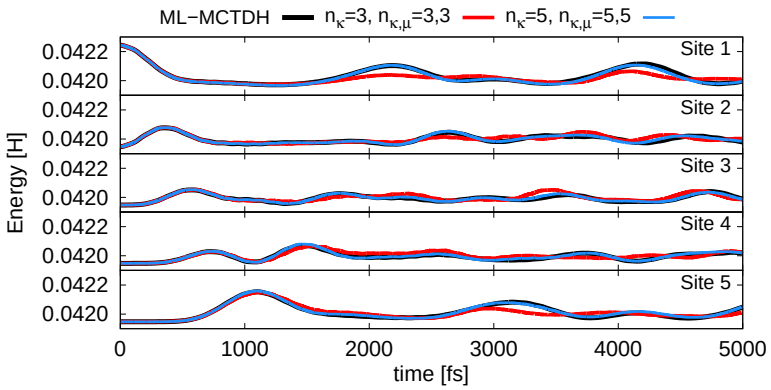

Figure 8.17: Comparison of ML-MCTDH (black) and 2L-G-MCTDH (red: $n_\kappa = 3$,$n_{\kappa,\mu} = 3$ and blue: $n_\kappa = 5$, $n_{\kappa,\mu} = 5$) for the site energies of the 5 sites for 5000 fs.

8.1.5 18-Site System (90 DOFs)

The last system that is studied for this Hamiltonian is a rather large example with 18 sites, comprising 90 degrees of freedom. Each site consists of 5 modes, i.e., 1 transporting mode and 4 high-frequency modes. After explaining the mode partitioning, the results of the 2L-G-MCTDH code and the ML-MCTDH package are compared. Here, two intra-site coupling parameters $\Delta = 0.01$ and $\Delta = 0.1$ are compared; for the inter-site coupling the same value $k = 0.15$ as before is taken.

8.1.5.1 System Partitioning

For this system, the mode combination is crucial for the description. For both the ML-MCTDH and 2L-G-MCTDH methods, it is not possible to follow the same approach as for the 5-site system. In the latter, one site corresponds to one first-layer particle. Here, this would result in 18 first-layer modes, which is unfeasible due to the exponential scaling behavior. Therefore, several sites have to be combined into one first-layer particle. Various partitioning schemes (Tab. 8.1) have been employed and compared to each other.

Scheme 1 represents the natural follow-up of the previously used partitioning schemes. Similar to the 1x4 combination scheme for the 3 site system, the transporting modes have a specific second-layer mode and the four high-frequency modes are combined into one mode. In this scheme, three sites are combined, but DOFs from different sites are not combined in the same second-layer particle. Therefore, $f = 6$ first-layer modes with $f_\kappa = 6$ second-layer modes are obtained. This is expected to be the computationally most expensive, but also most flexible scheme.

The second scheme is a small variation of the first one. Instead of having a specific second-layer mode for themselves, several transporting modes are combined. Due to the reduction of second-layer modes per first-layer mode, up to four sites can be combined in one first-layer mode. Therefore, $f = 5$ first-layer modes are obtained, where two comprise only three sites. Each first-layer mode consists of up-to $f_\kappa = 5$ second-layer modes.

The first two schemes have only up to 4 DOFs combined into one second-layer particle. For a 2L-MCTDH setup, this is feasible, but a higher-dimensional mode combination is not possible due to the exponential rise of the numerical effort and memory requirements of the grid representation. Especially the transporting modes need around 30 grid points per mode, resulting in a large number of 30^4 grid points for scheme 2. Therefore, the following schemes 3 and 4 are not applicable with a 2L-MCTDH setup. However, for the GWP setup more modes can be combined; a possible drawback is, however, that more SPFs might be required in turn.

Hence, scheme 3 increases the mode combination of scheme 2. Furthermore the second-layer modes are now not restricted to only contain high-frequency modes of one site. Here, the high-frequency modes with the same frequency $q_{:,j}$ are combined together. As they are uncoupled to each other, this should reduce the number of SPFs required for these second-layer modes, as the FGs are not directly coupled due to the diagonal width matrix. Six DOFs are combined, giving a total number of 15 second-layer modes, that are distributed among $f = 5$ first-layer modes ($\rightarrow f_\kappa = 3$). Here, packets of $q_{i:i+5,1}$, $q_{i:i+5,3}$ and $q_{i:i+5,5}$ for 5 sites are combined in the first three first-layer modes and the modes $q_{i:i+5,2}$ and $q_{i:i+5,4}$ are combined in the remaining two first-layer particles.

The fourth and last scheme combines even more DOFs in a second-layer mode. By combining 9 DOFs, the number of first-layer modes can be reduced to three. The particles, containing the modes $q_{i:i+9,2}$ and $q_{i:i+9,4}$ are combined into one first-layer particle, such that $f_\kappa = 4$ second-layer modes are used. The other first-layer modes contain $f_\kappa = 3$ second-layer modes. This should be the computationally least flexible, but also the computationally least expensive (for 2L-G-MCTDH) approach. For more details, the reader is referred to Tab. 8.1.

Furthermore, an additional 5-Layer partitioning scheme (denoted as scheme 5L, not depicted in Tab. 8.1) is used exclusively for the ML-MCTDH calculations,

since the 2-layer approach did not yield converged results within reasonable times with ML-MCTDH. The scheme is illustrated in Fig. 8.18. The multi-layer tree is split in two halves, such that the first nine sites are depicted in the first half (Fig. 8.18(a)) and the remaining nine in the second half (Fig. 8.18(b)).

8.1.5.2 Small Intra-Site Coupling – $\Delta = 0.01$

First, the results for the small intra-site coupling $\Delta = 0.01$ are presented. The ML-MCTDH result is taken to be converged. Both for ML-MCTDH and 2L-G-MCTDH, $n_\kappa = n_{\kappa,\mu} = 3$ SPFs together with partitioning scheme 1 are employed. ML-MCTDH gives the same results for schemes 1, 2 and 5L, all being converged. For this setup, the 2L-G-MCTDH results are in perfect agreement with ML-MCTDH. This can be seen for the transporting modes and for the site energies in Fig. 8.19. The plot shows the sequential transfer of energy to site 18 and back to site 1. The energy is transported along the chain almost without any disturbance, due to the small intra-site coupling. It takes around 6600 fs to complete a full transfer cycle.

8.1.5.3 Large Intra-Site Coupling – $\Delta = 0.1$

The results for a larger intra-site coupling of $\Delta = 0.1$ are here summarized for the 2L-G-MCTDH method as compared with ML-MCTDH reference results. To start with, schemes 1, 2 and 5L are discussed for the ML-MCTDH method, followed by schemes 1 to 4 for the 2L-G-MCTDH method.

First, the results for the ML-MCTDH calculations are compared for the partitioning schemes 1 and 2, as well as scheme 5L. The calculations with scheme 1 use 3 SPFs for all first and second-layer modes, as more configurations were not feasible. These calculations do not represent a fully converged result. The same holds true for the results with scheme 2. Here, due to a higher-dimensional mode combination of the transporting modes, 5 SPFs per first- and second-layer mode could be used. By contrast, the results obtained with the 5-layer setup (scheme 5L) represent converged results. For the transporting modes $q_{:,1}$, the difference is rather small. Scheme 2 shows a negligibly slower oscillation frequency and slightly smaller amplitudes, whereas scheme 1 presents a slightly faster osclillation with larger amplitudes (Fig. 8.20(a)). However, the differences are more pronounced for the energy distribution along the sites. The amount of energy reaching the last site – but also the sites in the middle of the chain – is higher for schemes 2 and 5L than for scheme 1. Furthermore, the calculation with scheme 5L also shows a slightly slower energy transfer by about 200 fs back to site 1, as one can see at

Table 8.1: Overview of the partitioning schemes used for the 18 site system.

	$f\,(f_\kappa)$	μ_d
scheme 1	1(6)	[v11],[v12,v13,v14,v15],[v21],[v22,v23,v24,v25],[v31],[v32,v33,v34,v35]
	2(6)	[v41],[v42,v43,v44,v45],[v51],[v52,v53,v54,v55],[v61],[v62,v63,v64,v65]
	3(6)	[v71],[v72,v73,v74,v75],[v81],[v82,v83,v84,v85],[v91],[v92,v93,v94,v95]
	4(6)	[v101],[v102,v103,v104,v105],[v111],[v112,v113,v114,v115],[v121],[v122,v123,v124,v125]
	5(6)	[v131],[v132,v133,v134,v135],[v141],[v142,v143,v144,v145],[v151],[v152,v153,v154,v155]
	6(6)	[v161],[v162,v163,v164,v165],[v171],[v172,v173,v174,v175],[v181],[v182,v183,v184,v185]
scheme 2	1(5)	[v11,v21,v31,v41],[v12,v13,v14,v15],[v22,v23,v24,v25],[v32,v33,v34,v35],[v42,v43,v44,v45]
	2(5)	[v51,v61,v71,v81],[v52,v53,v54,v55],[v62,v63,v64,v65],[v72,v73,v74,v75],[v82,v83,v84,v85]
	3(5)	[v91,v101,v111,v121],[v92,v93,v94,v95],[v102,v103,v104,v105],[v112,v113,v114,v115],[v122,v123,v124,v125]
	4(5)	[v131,v141,v151],[v132,v133,v134,v135],[v142,v143,v144,v145],[v152,v153,v154,v155]
	5(5)	[v161,v171,v181],[v162,v163,v164,v165],[v172,v173,v174,v175],[v182,v183,v184,v185]
scheme 3	1(3)	[v11,v21,v31,v41,v51,v61],[v13,v23,v33,v43,v53,v63],[v15,v25,v35,v45,v55,v65]
	2(3)	[v71,v81,v91,v101,v111,v121],[v73,v83,v93,v103,v113,v123],[v75,v85,v95,v105,v115,v125]
	3(3)	[v131,v141,v151,v161,v171,v181],[v13,v23,v33,v43,v53,v63],[v73,v83,v93,v103,v113,v123]
	4(3)	[v12,v22,v32,v42,v52,v62],[v72,v82,v92,v102,v112,v122],[v132,v142,v152.v162.v172,v182]
	5(3)	[v14,v24,v34,v44,v54,v64],[v74,v84,v94,v104,v114,v124],[v134,v144,v154.v164.v174,v184]
scheme 4	1(3)	[v11,v21,$\cdots$,v81,v91],[v13,v23,$\cdots$,v83,v93],[v15,v25,$\cdots$,v85,v95]
	2(3)	[v101,v111,$\cdots$,v171,v181],[v103,v113,$\cdots$,v173,v183],[v105,v115,$\cdots$,v175,v185]
	3(4)	[v12,v22,$\cdots$,v82,v92],[v102,v112,$\cdots$,v172,v182],[v14,v24,$\cdots$,v84,v94],[v104,v114,$\cdots$,v174,v184]

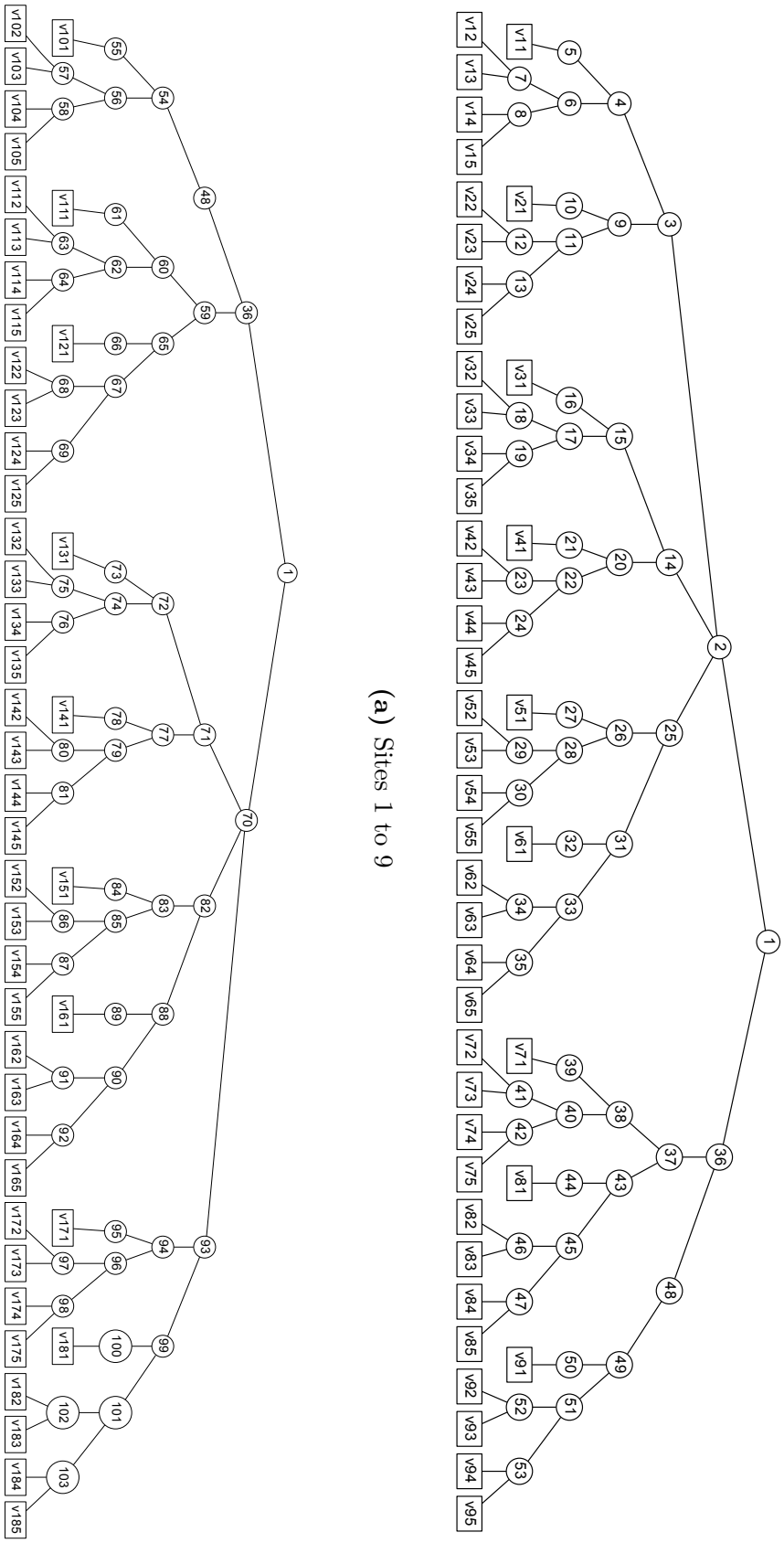

(a) Sites 1 to 9

(b) Sites 10 to 18

Figure 8.18: Illustration of the 5-layer (5L) tree structure used for the 18 site system.

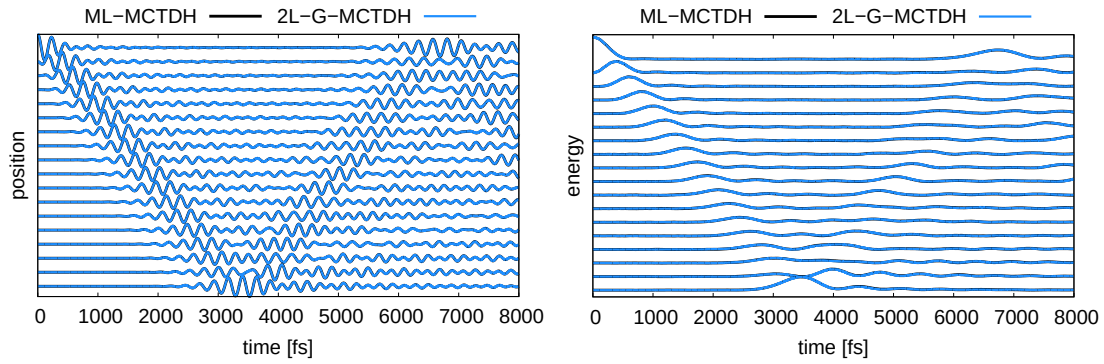

(a) $q_{:,1}$ mode positions **(b)** site energies

Figure 8.19: Comparison of ML-MCTDH (black, 2 layers) and 2L-G-MCTDH (blue) for (a) the $q_{:,1}$ modes and (b) the site energies for the 18 site system (site number increasing from top to bottom). ML-MCTDH and 2L-G-MCTDH employ the same mode partitioning and the same number of configurations ($n_\kappa = 3$, $n_{\kappa,\mu} = 3$). The intra-site coupling is small with $\Delta = 0.01$.

Table 8.2: Overview of the numbers of first- and second-layer SPFs for the 18 site system. The ordering of the modes is identical to Tab. 8.1. The square brackets denote first- or second-layer modes. n_{conf}^{gauss} is the total number of GWP configurations.

scheme	n_κ	$n_{\kappa,\mu}$	n_{conf}^{gauss}
1	[3,3,3,3,3,3]	[3,3,3,3,3,3],[3,3,3,3,3,3],[3,3,3,3,3,3] [3,3,3,3,3,3],[3,3,3,3,3,3],[3,3,3,3,3,3]	13 122
2	[5,5,5,5,5]	[5,5,5,5,5],[5,5,5,5,5],[5,5,5,5,5] [5,5,5,5,5],[5,5,5,5,5]	53 125
3	[7,7,7,7,7]	[5,5,3],[5,5,3],[5,5,3],[5,5,5],[5,5,5]	3325
4	[7,7,7]	[7,7,7],[7,7,7],[5,5,5,5]	9177

∼6500 fs. Overall, the energy *profile* with scheme 1 is more shallow such that the energy transfer is described to be less effective than for the other two partitioning schemes. The behavior of schemes 2 and 5L is nevertheless similar, and will be used as a point of comparison for the calculations reported below.

Second, the results obtained with the 2L-G-MCTDH method are compared for the different schemes, and to the ML-MCTDH reference results. The number of first-layer and second-layer SPFs that are employed for the various schemes, are depicted in Tab. 8.2. These correspond to the largest number of configurations that can be employed to achieve a numerically stable propagation. As a general observation, one should note that more second-layer SPFs can be used if more DOFs are combined into a given second-layer mode.

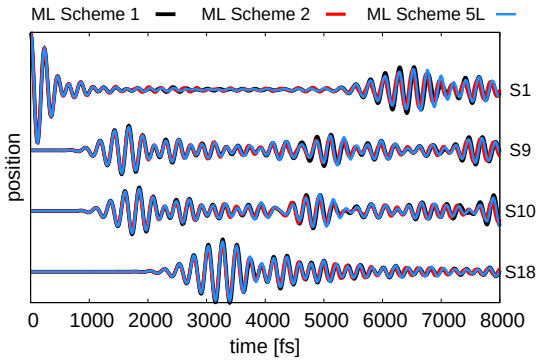

(a) positions for $q_{1,1}$, $q_{9,1}$, $q_{10,1}$ and $q_{18,1}$

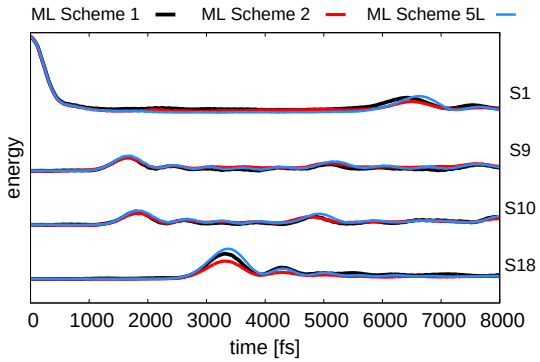

(b) site energies of sites 1, 9, 10 and 18

Figure 8.20: Comparison of 2 layer ML-MCTDH (black and red) and 5 layer ML-MCTDH (blue) for (a) the $q_{:,1}$ mode and (b) the site energies for sites 1, 9, 10 and 18 of the 18 site system. For the 2-layer ML-MCTDH results schemes 1 (black) and scheme num2 (red) are depicted. The 5-layer calculation employs the scheme 5L. The intra-site coupling is small with $\Delta = 0.1$.

Similarly to the ML-MCTDH results, the differences for the center modes $q_{:,1}$ are very small. The energy transfer shows more pronounced differences between the schemes, depicted in Fig. 8.21(a). While schemes 3 and 4 show a very similar redistribution among the sites, schemes 1 and 2 show a different behavior for site 1 as more energy is transferred compared to the other schemes, showing a better agreement with the ML-MCTDH results. For scheme 2, the first site retains more energy over the complete propagation time after the initial energy transfer. However, the amount of energy received by site 18 is equal for all four schemes with 2L-G-MCTDH. It is very similar to the 2L-MCTDH calculation with scheme 1, and therefore smaller than for the 5L-MCTDH calculation. Furthermore, the local energy of sites 2 to 17 is described rather well by all 2L-G-MCTDH calculations and is in agreement with the ML-MCTDH results.

The good description of the energy flow can be attributed to the fact that the transporting modes are not combined in scheme 1; these modes are therefore more flexible as compared with a combined description. This is especially pronounced when comparing to scheme 2. Here, for the 2L-G-MCTDH results, the energy loss is remarkably smaller for site 1 and the energy transfer to the high-frequency modes is overemphasized as can be seen in Fig. 8.21(b). The energy located in the high-frequency modes of site 1 ($q_{1,2:5}$) is transferred back more rapidly for scheme 1, which is in better agreement to the reference calculations. In general, the overall energy transferred to the high-frequency modes seems to be overestimated by the 2L-G-MCTDH calculations.

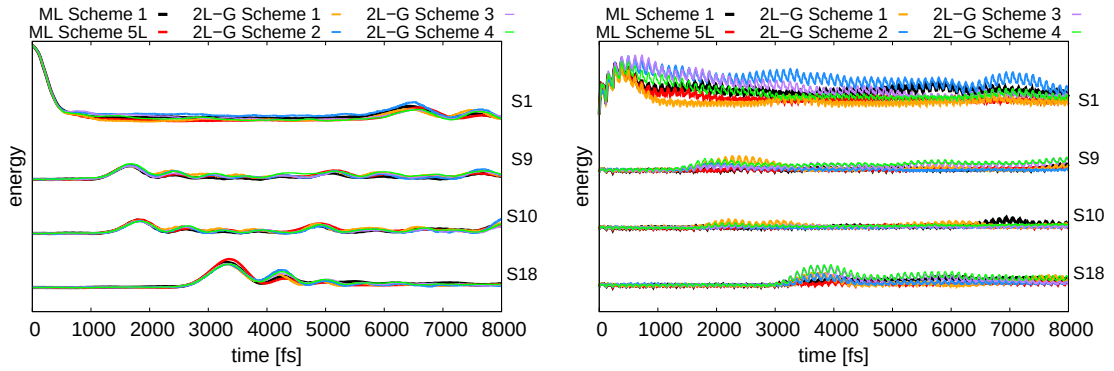

(a) site energies including the center modes **(b)** site energies excluding the center modes

Figure 8.21: Comparison of the site energies (a) including the energy of the transporting modes and (b) excluding the energy of the transporting mode. The ML-MCTDH results with schemes 1 and 5L and the four partitioning schemes in combination with 2L-G-MCTDH are shown. Depicted are sites 1, 9, 10 and 18.

Scheme 4 represents the opposite of scheme 1 regarding mode combination. Scheme 4 has the highest mode combination employed. As a result, more SPFs can be employed. Furthermore, it shows some improvements compared to scheme 3 due to the combination of uncoupled modes having a similar behavior. Although the results show a good agreement, especially for the energy transfer and the center modes, the description of the high-frequency modes is worse than the results with scheme 1 or ML-MCTDH.

The best agreement for the 2L-G-MCTDH method is achieved with mode combination scheme 1. In this scheme mode combination is reduced to a minimum. Therefore the modes are more flexible and no (direct) mode couplings between modes in the same second-layer particle exist. As a consequence, less configurations need to be used to achieve a near-converged result. A full comparison for all sites regarding the mode positions of the transporting modes and the site energies is shown in Fig. 8.22. In comparison to the small intra-site coupling $\Delta = 0.01$ the energy transfer along the sites is reduced, as one can deduce from the smaller amount of energy received from site 18. The results for the mode positions exhibit a small deviation of the oscillation frequency for all transporting modes. However, the energy transfer along the site-chain is in a good agreement, showing only minor deviations mainly for sites 17 and 18.

Overall, the 2L-G-MCTDH method shows a good agreement to the reference calculations for this kind of system. By employing a higher-dimensional mode combination, even larger numbers of degrees of freedom are accessible. A redesigned

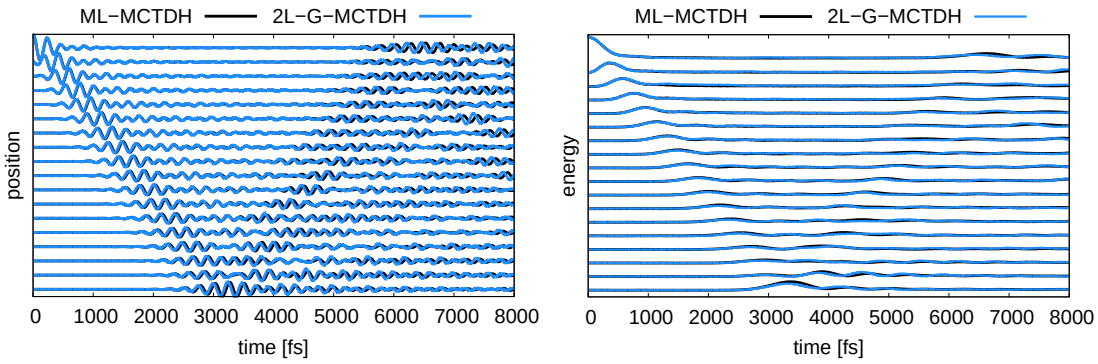

(a) $q_{:,1}$ mode positions **(b)** site energies

Figure 8.22: Comparison of ML-MCTDH (black, scheme 5L) and 2L-G-MCTDH (blue, scheme 1) for (a) the $q_{:,1}$ modes and (b) the site energies for the 18 site system (site number increasing from top to bottom). The intra-site coupling is $\Delta = 0.1$.

mode combination scheme may be used for this purpose, following the concept of scheme 4.

8.2 Non-Adiabatic Charge Transfer Dynamics

The second system to which the 2L-G-MCTDH method has been applied, is a donor-acceptor system composed of an oligothiophene (OT_4) donor moiety and a fullerene (C_{60}) acceptor moiety, as depicted in Fig. 8.23. This system is a minimal model for the charge transfer in a paradigm system of organic photovoltaics, i.e., a so-called bulk heterojunction composed of poly-3-hexylthiophene (P3HT) and phenyl-C_{61} butyric acid methyl ester (PCBM) components.[103–108] The P3HT-PCBM system exhibits an ultrafast charge transfer, on a time scale of ∼50 fs to 200 fs.[104,105,109,110] In a previous study in our group, by Tamura et al.,[84,85] a Linear Vibronic Coupling (LVC) electron-phonon Hamiltonian has been parametrized for this system. To this end, electronic structure calculations using long-range-corrected density functional theory and an *ab initio* based diabatization procedure were performed.[84] Furthermore, the LVC was combined with an *ab initio* generated spectral density of the phonon modes of the system. Here, geometry displacements for all normal modes were used to obtain vibronic couplings. The results presented here are obtained considering the original data and procedures presented in Ref. [84, 85].

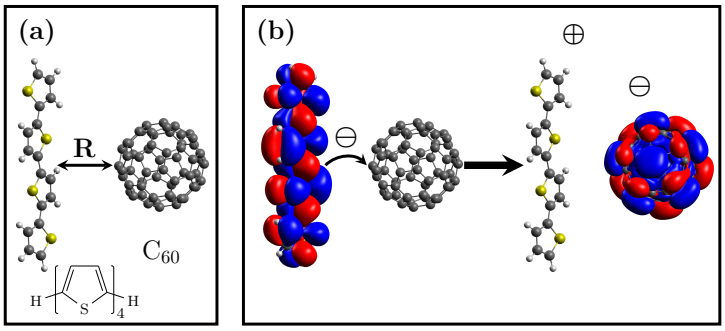

Figure 8.23: (a) OT_4/C_{60} interface model system, where the five- or six-membered ring of C_{60} and the π-conjugate plane of OT_4 are arranged in parallel. (b) Scheme of the electron transfer with the LUMOs of OT_4 and C_{60}.

8.2.1 Hamiltonian

The abovementioned LVC model describes the coupling of an excitonic donor state (OT_4^*-C_{60}), denoted XT, to a charge separated state (OT_4^+-C_{60}^-), denoted CT.

The Hamiltonian takes the general form,

$$\hat{H} = \hat{H}_0 + \hat{H}_R + \hat{H}_B \tag{8.2}$$

where $\hat{H}_0$ refers to the electronic part, $\hat{H}_R$ is the part depending on the inter-fragment distance coordinate R and $\hat{H}_B$ represents the collection of the intra-molecular "bath" modes.[85] The individual parts are given as follows,

$$\hat{H}_0 = -\Delta_{\text{XT-CT}} \left|\text{CT}\right\rangle \left\langle\text{CT}\right| + \gamma \left(\left|\text{XT}\right\rangle \left\langle\text{CT}\right| + \left|\text{CT}\right\rangle \left\langle\text{XT}\right|\right) \tag{8.3}$$

$$\begin{aligned}\hat{H}_R = &\frac{\omega_R}{2}\left(\hat{R}^2 + \hat{P}^2\right) + \kappa_R \hat{R} \left|\text{CT}\right\rangle \left\langle\text{CT}\right| \\ &+ \gamma_R \hat{R} \left(\left|\text{XT}\right\rangle \left\langle\text{CT}\right| + \left|\text{CT}\right\rangle \left\langle\text{XT}\right|\right)\end{aligned} \tag{8.4}$$

$$\hat{H}_B = \sum_{i=1}^{N_0} \frac{\omega_i}{2}\left(\hat{x}_i^2 + \hat{p}_i^2\right) + \sum_{i=1}^{N_0} \kappa_i \hat{x}_i \left|\text{CT}\right\rangle \left\langle\text{CT}\right| + \sum_{i=1}^{N_0} \frac{\kappa_i^2}{2\omega_i} \tag{8.5}$$

The Hamiltonian uses mass- and frequency-weighted coordinates. The diagonal coupling parameter κ_R and the vibronic couplings κ_i reflect the displacement of the CT equilibrium geometry from the XT reference geometry. The bath Hamiltonian (Eqn. 8.5) represents the intra-fragment modes, which are diagonally coupled to the CT state. The last term of Eqn. 8.5 corresponds to the CT reorganization energy $\lambda = \sum_{i=1}^{N_0} \frac{\kappa_i^2}{2\omega_i}$.

The electron-phonon-couplings κ_i were determined by projecting the displacement between the XT and the CT minima onto the CT normal mode coordinates (Fig.

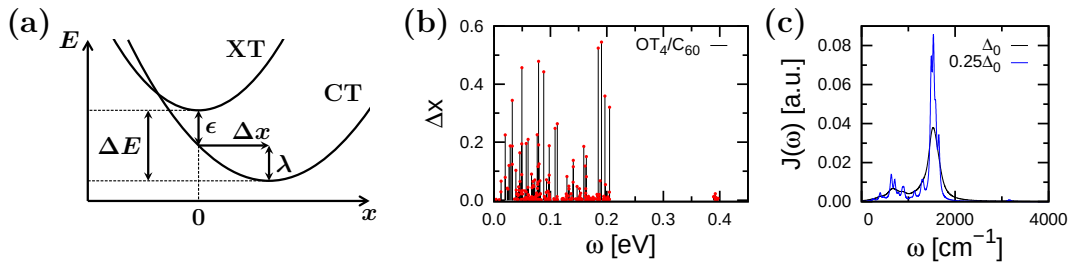

Figure 8.24: (a) Schematic illustration of the XT/CT potential crossing. (b) Phonon-induced shifts Δx for the vibrational normal modes of the OT_4^+ and C_{60}^- fragments. (c) Broadend spectral densities, based upon a convolution of the original data shown in (b).

8.24(a)). The normal mode analysis yields $N_0 = 246$ normal modes in total for both separate fragments.[85]

The discrete distribution of the electron-phonon couplings, depicted in Fig. 8.24(b), has been used to construct a smooth spectral density $J(\omega)$ function, representing a continuous density of modes that gives a better description of the high-dimensional polymer system. A Lorentzian envelope function (Eqn. 8.6) was used to convolute the discrete spectrum,

$$\begin{aligned} J(\omega) =& \frac{\pi}{2} \sum_{i=1}^{N_0} \kappa_i^2 \delta(\omega - \omega_i) \\ =& \frac{\pi}{2} \sum_{i=1}^{N_0} \frac{\kappa_i^2}{\pi} \frac{\Delta}{(\omega - \omega_i)^2 + \Delta^2} \end{aligned} \tag{8.6}$$

where the parameter Δ specifies the Lorentzian width. As a reference value, the width Δ_0 is used that was determined from the root mean square of the frequency spacings of the original, discrete couplings. Fig. 8.24(c) illustrates the continuous spectral density for two different choices of the width Δ. The calculations presented below are performed with a Lorentzian width of $\Delta = 0.25\Delta_0$.

The continuous spectral density can then be re-discretized with an arbitrary number of N bath modes for an equidistant sampling interval $\Delta\omega$,[111]

$$\begin{aligned} J(\omega) =& \frac{\pi}{2} \sum_{i=1}^{N} \kappa_i^2 \delta(\omega - \omega_i) \\ \kappa_i =& \left(\frac{2}{\pi} J(\omega) \Delta\omega \right)^{\frac{1}{2}} \end{aligned} \tag{8.7}$$

Using this re-discretization scheme, several setups of variable dimensionality were generated, as described in the next section.

Table 8.3: Frequency spacings and Poincaré recurrence times for the different bath mode realizations.

# bath modes	$\Delta\omega$ [cm^{-1}]	τ_p[fs]
19	154.3	216
39	74.8	446
59	49.4	675
79	36.8	906
99	29.4	1135

8.2.2 Series of Re-Discretizations

Following the re-discretization procedure explained above, several realizations of the Hamiltonian were obtained for different numbers of bath modes, as listed in Tab. 8.3. These finite-dimensional realizations have different Poincaré recurrence times $\tau_p = \frac{2\pi}{\Delta\omega}$. For times smaller than τ_p, though, the dynamics is effectively irreversible for all realizations. Therefore the different simulations are compared for a simulation time that is less than the shortest Poincaré time ($\tau_p = 216\,\text{fs}$). The calculations reported below show a propagation time of about 180 fs.

The re-discretization is done for the frequency range from $0\,\text{cm}^{-1}$ to $2920\,\text{cm}^{-1}$, since the small peak at around $3500\,\text{cm}^{-1}$ plays no important role. As a side effect, the Poincaré recurrence time is increased since the width of the frequency window decreases.

The total number of DOFs is given by the number of bath modes plus the inter-fragment distance coordinate R. The calculations are again performed with the MCTDH-package[101] and the 2L-Gaussian code presented above. MCDTH (20 modes) and ML-MCTDH (40, 60, 80 and 100 modes) calculations serve as references. The initial condition for all calculations corresponds to a wave packet which is centered at the reference XT state minimum potential, i.e., all modes are initialized at $q_i = p_i = 0.0$.

8.2.3 Results and Discussion

Fig. 8.25 shows the results for the different setups. In each panel, the upper trace shows the XT state population, and the lower traces correspond to the real and imaginary parts of the electronic coherence,

$$\begin{aligned}\rho_{\mathrm{XT,CT}}(t) &= \mathrm{Tr}\left\{|\mathrm{XT}\rangle\langle\mathrm{CT}|\,\hat{\rho}(t)\right\} \\ &= \mathrm{Tr}\left\{|\mathrm{XT}\rangle\langle\mathrm{CT}|\,|\psi(t)\rangle\langle\psi(t)|\right\}\end{aligned} \tag{8.8}$$

where the pure-state density operator $\hat{\rho}(t) = |\psi(t)\rangle\langle\psi(t)|$ is defined by the wave-function that is propagated in the full dimensionality of the system. The imaginary part of the electronic coherence (Eqn. 8.8) $\mathrm{Im}\left(\rho_{\mathrm{XT,CT}}\right)$ determines the state-to-state population flux.[85]

As can be inferred from Fig. 8.25, the photogenerated XT state decays rapidly within 10 fs, followed by pronounced oscillatory features in the first 50 fs to 100 fs. Furthermore, the initial XT state does not deplete completely and keeps a residual population of $P_{XT} \sim 0.1$ even beyond the interval of 180 fs that is shown here.

The initial oscillatory behavior of the XT population is mirrored in the oscillations of the electronic coherence. This indicates that electronic coherence is at the origin of the oscillatory population observed in the initial 50 fs time. After this time, the electronic coherence dephases due to the coupling to the vibrations. Note that the imaginary part of the electronic coherence decays to zero. The real part, however, persists and indicates a stationary coherent superposition of the XT and CT states.

In accordance with the construction scheme described above, all re-discretizations – with 20, 40, 60, 80 and 100 modes – show the same results and can be taken to be converged. In the following, we give details of the numerical setup.

Tab. 8.4 shows the mode partitioning used for the various realizations. Although all modes are only indirectly coupled through the electronic subsystem, it turned out that mode combination is crucial for the 2-Layer-Gaussian setup. Interestingly, mode combination according to the frequency ordering of the bath modes seems to result in an unstable propagation. A possible reason for this is that modes which have a strong electron-phonon coupling are combined within a particle and therefore cause numerical issues. However, the partitionings presented in Tab. 8.4 result in more stable propagations. All calculations shown here employ the single-set setup; the results of the hybrid-set and multi-set setups will be briefly addressed below.

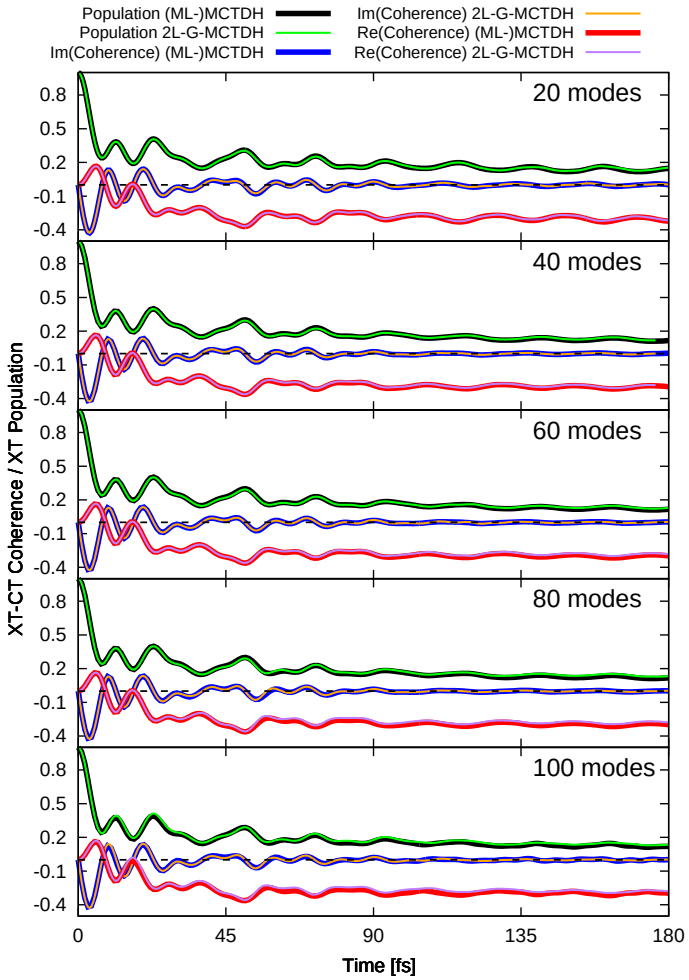

Figure 8.25: Comparison of the results of the non-adiabatic charge transfer for different numbers of bath modes plus inter-fragment distance coordinate (20, 40, 60, 80 and 100). Also, the 2L-G-MCTDH calculations are compared to the reference (ML-)MCTDH calculations.

The reference calculations are performed for the 20 mode system with MCTDH and with 40 to 100 modes with the ML-MCTDH method. The ML-MCTDH calculations are not restricted to a 2-layer setup and therefore, up to 6 layers can be used. The reference calculations are numerically converged.

For all different bath mode representations, the 2L-Gaussian-MCTDH method shows very good – in fact, almost perfect – agreement with the reference calculation. Even for the calculation with 100 modes, the initial decay of the XT state and the electronic coherence are depicted correctly. The correct description of the real part of the electronic coherence results in the correct characterization of the final superposition of the XT and CT states. Also, the admixture of the XT state with $P_{XT} \sim 0.1$ is captured.

Table 8.4: Mode partitioning for the various rediscretizations of the spectral density for OT_4/C_{60}.

# Modes	$f\left(f_{\kappa,\mu}\right)$	μ_d
20	1(1)	[b1,b5,b9,b13,b17]
	2(1)	[b2,b6,b10,b14,b18]
	3(1)	[b3,b7,b11,b15,b19]
	4(1)	[b4,b8,b12,b16]
	5(1)	[R]
40	1(3)	[b1,b6,b11,b16],[b21,b26,b31],[b36,b2,b7]
	2(3)	[b12,b17,b22,b27],[b32,b37,b3],[b8,b13,b18]
	3(3)	[b23,b28,b33,b38],[b4,b9,b14],[b19,b24,b29]
	4(3)	[b34,b39,b5],[b10,b15,b20],[b25,b30,b35]
	5(1)	[R]
60	1(4)	[b1,b10,b20,b30],[b40,b50,b11,b21] [b31,b41,b51,b2],[b12,b22,b32,b42]
	2(4)	[b52,b3,b13,b23],[b33,b43,b53,b4] [b14,b24,b34,b44],[b54,b5,b15,b25]
	3(4)	[b35,b45,b55,b6],[b16,b26,b36,b46] [b56,b7,b17,b27],[b37,b47,b57,b8]
	4(4)	[b18,b28,b38,b48],[b58,b9,b19,b29],[b39,b49,b59]
	5(1)	[R]
80	1(4)	[b1,b10,b20,b30],[b40,b50,b60,b70] [b11,b21,b31,b41],[b51,b61,b71,b2]
	2(4)	[b12,b22,b32,b42],[b52,b62,b72,b3] [b13,b23,b33,b43],[b53,b63,b73,b4]
	3(4)	[b14,b24,b34,b44],[b54,b64,b74,b5] [b15,b25,b35,b45],[b55,b65,b75,b6]
	4(4)	[b16,b26,b36,b46],[b56,b66,b76,b7] [b17,b27,b37,b47],[b57,b67,b77,b8]
	5(4)	[b18,b28,b38,b48],[b58,b68,b78,b9] [b19,b29,b39,b49],[b59,b69,b79]
	6(1)	[R]
100	1(4)	[b1,b10,b20,b30,b40],[b50,b60,b70,b80,b90] [b11,b21,b31,b41,b51],[b61,b71,b81,b91,b2]
	2(4)	[b12,b22,b32,b42,b52],[b62,b72,b82,b92,b3] [b13,b23,b33,b43,b53],[b63,b73,b83,b93,b4]
	3(4)	[b14,b24,b34,b44,b54],[b64,b74,b84,b94,b5] [b15,b25,b35,b45,b55],[b65,b75,b85,b95,b6]
	4(4)	[b16,b26,b36,b46,b56],[b66,b76,b86,b96,b7] [b17,b27,b37,b47,b57],[b67,b77,b87,b97,b8]
	5(4)	[b18,b28,b38,b48,b58],[b68,b78,b88,b98,b9] [b19,b29,b39,b49,b59],[b69,b79,b89,b99]
	6(1)	[R]

Table 8.5: Overview of the number of first- and second-layer SPF for the various re-discretizations of the spectral density for OT_4/C_{60}.

# modes	n_κ	$n_{\kappa,\mu}$	n_{conf}^{gauss}
20	[8,8,8,8,10]	[8],[8],[8],[8],[10]	356
40	[8,8,8,8,8]	[7,6,6],[7,6,6],[7,6,6],[7,6,6],[8]	7840
60	[7,7,8,7,9]	[5,5,5,5],[5,5,5,5],[5,5,5,5],[5,5],[10]	14 540
80	[5,5,5,5,5,8]	[4,4,4,4],[4,4,4,4],[4,4,4,4],[4,4,4,4],[4,4,4,4],[8]	6464
100	[6,6,5,5,5,7]	[5,5,5,4],[5,4,5,4],[5,4,5,4],[5,4,5,4],[5,4,3,3],[8]	10 356

The LVC model Hamiltonian is of course a favorable system for the 2L-G-MCTDH method as it comprises only displaced harmonic oscillators and a linearly dependent XT-CT coupling.

Tab. 8.5 illustrates the number of first- and second-layer SPFs. The numbers represent the calculations for which a stable propagation is possible. The calculation for 20 modes represents a converged result, the others are nearly-converged. Also, it is notable that the results most strongly depend on the number of first-layer SPFs, as the A-coefficients describe the electronic degree of freedom. The number of second-layer SPFs – corresponding to the number of GWPs – mainly describe the vibrational coupling and are responsible for the correct admixture of the XT state at the end. This can be seen by comparing the results for 20 and 100 modes. For the 20-mode calculation, the highest number of second-layer GWPs can be employed (under stable propagation conditions) and the behavior at the end of the propagation – here, 100 fs to 180 fs – is in perfect agreement. For 100 modes, where the calculation represents near-converged results, the agreement is still very good and shows all features correctly, but the population of the XT state is slightly higher than for the reference.

But, one should keep in mind that the reference uses a 6-layer setup for the wave function description. Therefore, Fig. 8.26 shows an additional comparison with a 2-layer setup for ML-MCTDH. There one can see that the result obtained with 2L-G-MCTDH is in fact in better agreement with the 5-layer reference calculation, underlining the suitability of GWPs for a system-bath Hamiltonian.

Lastly, good convergence properties are observed for the 100-mode example. Fig. 8.27 illustrates the convergence behavior for the first 70 fs of the XT state population with a series of basis sets of increasing size (here denoted *minimal*, *small*, *medium*, *large*, see Tab. 8.6). With an increasing basis set size, the method con-

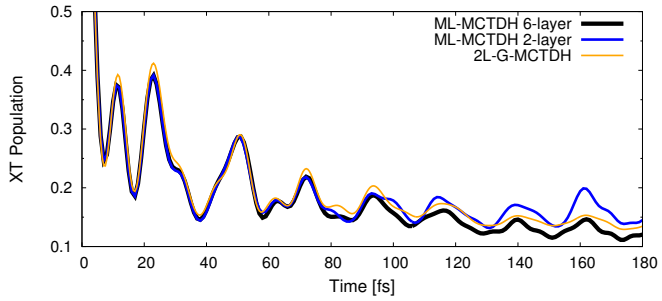

Figure 8.26: Comparison of the 6-layer ML-MCTDH (black) reference calculation to a 2-layer ML-MCTDH (blue) and the 2L-G-MCTDH (orange) calculations.

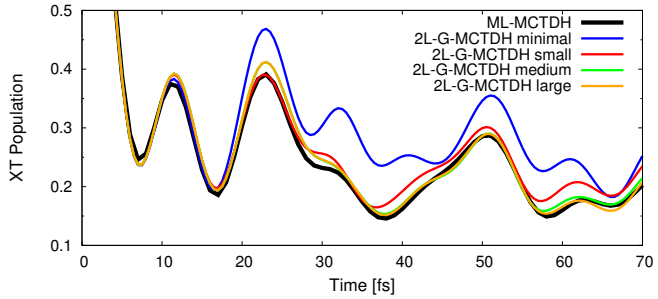

Figure 8.27: Convergence behavior for the 99 mode re-discretization of the spectral density for OT_4/C_{60}. The reference ML-MCTDH calculation is depicted in black and the various 2L-G-MCTDH results in color.

verges progressively to the correct results. For the first 50 fs, the basis-sets *medium* and *large* give the same results showing an almost converged result. Tab. 8.6 shows the number of SPFs for the four different realizations. However, the *large* basis again exhibits problems arising from singularities due to too high overlaps of the GWPs.

8.2.3.1 Remarks on Single-Set, Hybrid-Set and Multi-Set

All results presented above have been obtained using the single-set approach. However, calculations with the hybrid-set and multi-set approaches have also been performed for the present system. Here, we briefly comment on the performance of these variants.

First, the performance of the hybrid-set approach is very close to the single-set approach. In principle, one would expect some additional advantage of the hybrid-set approach, i.e., one would expect to achieve a qualitatively similar result to the single-set approach with a *lower* number of first-layer configurations. However, in order to obtain a comparable result as for the single-set scheme, a similar number of first-layer SPFs had to be employed for the hybrid approach, too.

Table 8.6: Number of first- and second-layer SPFs for different basis compositions for the 99 mode discretization used in Fig. 8.27.

Basis	n_κ	$n_{\kappa,\mu}$	n_{conf}^{gauss}
minimum	[3,3,3,3,3,3]	[2,2,2,2],[2,2,2,2],[2,2,2,2],[2,2,2,2],[2,2,2,2],[3]	249
small	[4,4,4,4,4,7]	[3,3,3,3],[3,3,3,3],[3,3,3,3],[3,3,3,3],[3,3,3,3],[7]	1669
medium	[6,6,5,5,5,7]	[5,5,5,4],[5,4,5,4],[5,4,5,4],[5,4,5,4],[5,4,3,3],[8]	10 356
large	[7,7,8,8,7,8]	[5,5,5,5],[6,5,6,5],[5,5,6,5],[7,5,6,6],[6,5,3,5],[9]	29 977

A possible reason for this might be the peculiarities of the investigated model system: In this system the coupling of the distance mode R and the harmonic oscillator bath is purely vibronic, as they are not coupled directly. The description of the electronic subsystem in the present implementation is completely shifted into the first-layer coefficients A. Therefore, the number of first-layer coefficients stays identical when expanding the single-set approach into the hybrid approach. As a consequence, the description of the electronic coherence and hence the quality of the results is very similar for equal numbers of first-layer SPFs.

Lastly, the multi-set approach did not yield results of comparable quality as obtained with the single-set and hybrid-set approaches. Furthermore, an oscillation in the total energy of the system is observed. The reason for these problems is still unclear and under further investigation. A potential bug in the code cannot be ruled out.

9 | The 2L-G-MCTDH Method: Conclusion and Outlook

To summarize, the novel 2-Layer-Gaussian-MCTDH method has been presented, and its implementation into a Fortran90 code has been described in detail. This method combines the flexible single-particle functions (SPFs) used in MCTDH with a time-evolving GWP basis set of frozen Gaussian (FG) type in a two-layer wavefunction ansatz. FG basis set have proven to be numerically more robust than thawed Gaussians, but as a consequence lack flexibility, especially compared to conventional SPFs. Therefore, the original G-MCTDH approach that uses high-dimensional, factorizable FGs, encounters convergence problems when moving towards higher dimensions. Even though the FG basis functions are uncorrelated, their propagation is expensive due to an unfavorable cubic scaling ($\sim (dn)^3$) with the number of DOFs (d) and the number of configurations (number of basis functions n). This is especially emphasized in the vMCG method, where all DOFs are combined into a single multi-dimensional particle.

In the present two-layer approach, the orthogonal first-layer SPFs are represented by a linear combination of non-orthogonal multi-dimensional GWPs and therefore accommodate correlations like conventional multi-dimensional MCTDH combined modes.[1] Furthermore, the second-layer FGs now evolve in low-dimensional subspaces, which require a less expensive propagation. The additional effort resulting from the calculation of the first- and second-layer mean-fields then needs to be balanced against these advantages. By a suitable mode partitioning and combination, significant improvements regarding the scaling properties, compared to G-MCTDH (vMCG) can be achieved.

In the framework of this thesis, the method has been extended to multi-state, non-adiabatic systems. Three formulations of multi-state wavefunctions have been implemented: On the one hand, the single-set and multi-set approaches as known from MCTDH[25] and, on the other hand, a hybrid approach which mixes the single-set and multi-set forms. Specifically, in the single-set approach, the electronic states are represented by an additional first-layer particle, whereas the multi-set approach employs a sum of state-specific wavefunctions. In the third, hybrid, approach, the

first-layer particles are state specific, similar to the multi-set approach, but the multi-dimensional GWPs in the second layer are shared between the states.

In this work, a first implementation of the method has been presented, including details regarding the memory layout of the wavefunction and the efficient treatment of the tensor form of the wavefunction which leads to a multi-sum structure of all matrix-vector products. The multiple calculation of products of integrals is thus avoided. Furthermore, the scaling properties of the code have been analysed, especially with respect to the first- and second-layer mean-fields which represent the most expensive elements of the method. The scaling properties have been found to be in good agreement with the theoretical prediction.

The method has been successfully applied to two types of model systems. The first Hamiltonian describes intra-molecular vibrational energy redistribution (IVR) in a site-based model system, while the second Hamiltonian describes ultrafast charge separation in a donor-acceptor system. Propagation times were typically in the range of 2 ps for the IVR dynamics, and within 50 fs to 200 fs for the charge transfer system where various rediscretizations of the spectral density, with variable Poincaré recurrence times, were treated. For these systems, excellent convergence properties as compared with ML-MCTDH benchmark calculations were found. These results also show that the mode partitioning within the first layer and the mode combination in the second layer play an important role for the quality of the results.

However, the method suffers from similar problems as the original G-MCTDH (vMCG) method, where singularities of the overlap matrix and the $\underline{C}$ matrix arise from too large overlaps between GWPs and therefore linear dependencies within the non-orthogonal GWP basis. Especially the choice of the initially unoccupied Gaussian basis functions shows a large influence on the numerical stability and the results of the method. In particular, many GWPs with the same width tend to exhibit singularities. This is particularly pronounced for small numbers of combined DOFs in one second-layer GWP mode. In contrast, more configurations can generally be used within higher dimensional combined modes. This problem can be alleviated by choosing unoccupied GWPs which feature different widths for the GWPs. By this choice, the GWPs do not develop a near-unity overlap, and the singularities are reduced. However, more configurations may be required to achieve a good agreement to the reference calculations.

Regarding the comparison between the three types of multi-state approaches (single-set, multi-set, hybrid), the single-set method has been shown to be in good agreement for the second system. Similar results were obtain for the hybrid approach, showing no improvement by needing less first-layer configurations as compared to single-set. However, this is probably related to the investigated system. The convergence properties of the multi-set approach are somewhat different within the current implementation.

Overall, these results can be considered to be promising. Importantly, the method can be easily combined with the existing ML-MCTDH approach (as implemented in the Heidelberg-MCTDH[112] and Quantics packages[113]), since only the final layer needs to be replaced with GWPs.[1] All upper layers – and specifically the first layer in the 2L-G-MCTDH scheme – are equivalent to the upper layers of the ML-MCTDH method. By replacing the final layer with the factorizable, multi-dimensional GWPs, the efficient, analytical Gaussian integrals can be combined with the flexible, multi-layer treatment. As a result, a very large number of DOFs become accessible. In addition, within our in-house code, multi-core parallelization can be introduced, such that up to 1000 DOFs can be calculated even within our 2-layer scheme. For this purpose, the algorithm treating the multi-sum structure will need to be revisited.

As the GWPs provide a semi-classical trajectory-like picture via the GWP positions and momenta, the method can be combined with on-the-fly electronic structure calculations, similar to the Direct Dynamics-vMCG (DD-vMCG) method.[17,18] As the on-the-fly electronic structure calculations – including the gradient and Hessian calculation – are the limiting factor in the propagation of the wavefunction, the challenge in this context is to reduce the number of configurations where electronic structure calculations are performed. Therefore, one needs to develop a sampling and interpolation scheme which matches the large number of 2L-GMCTDH configurations with the much smaller set of geometries where electronic structure calculations are carried out. For this purpose, one might adopt a database approach as used for the DD-vMCG method[17] together with neural network based PES fitting schemes.[114]

Part III

Electronic Structure and Quantum Dynamical Characterization of Novel Donor-Acceptor Systems

10 | Molecular Design of Novel Donor-Acceptor Systems

This project focuses on two generations of a novel type of covalently bound bisthiophene-perylene diimide type donor-acceptor materials, which were synthesized and spectroscopically characterized in the groups of S. Méry and S. Haacke at Strasbourg University. In the framework of a joint DFG/ANR project on "Molecular Level Approaches to Photosensitive Nanostructured Materials: A Combined Theoretical and Experimental Study of Ultrafast Energy and Charge Transfer", our group has investigated these systems by employing state-of-the-art electronic structure and high-level quantum dynamical methods.

As mentioned above, two generations of the relevant materials have been investigated, which differ both in their chemical composition and nanoscale morphology. The first-generation system consists of DAD triad combinations that are organized in smectic liquid crystalline (LC) films, while the second-generation system exhibits DA dyads or DAD triads with a different ordering in lamellar mesophases. In both cases, a highly organized nanomorphology is generated by design. Since the first-generation system was found to be comparatively inefficient, a central aim has been the optimal engineering of the second-generation system at a molecular level.

This project part summarizes results obtained for the first-generation system together with M. Polkehn from our group (section 10.1), and then focuses mainly on the second-generation systems in solution. Different variants of these systems are introduced, the experimental observations are summarized (section 10.2.1), and quantum chemical results (section 10.2.3) are discussed. Finally, an analysis of the charge separation and charge recombination kinetics with the Marcus-Levich-Jortner rate theory (section 10.2) is presented.

The dynamics observed in the two generations of donor-acceptor systems under study span several orders of magnitude. In the first-generation system, the initial charge separation is ultrafast, on a time scale of less than 100 fs, while recombination occurs on a scale of tens of picoseconds and triplet formation is observed on a nanosecond time scale. To investigate the initial, ultrafast dynamics, we undertook

a dynamical study using the ML-MCTDH method is closely related to the study of the oligothiophene-fullerene model system addressed in the previous chapter. In the second-generation system, by contrast, charge separation is much slower, in the range of tens to hundreds of picoseconds. Therefore, the focus of the present study gradually shifted from quantum dynamical investigations to kinetic studies in the course of the investigations.

10.1 First Generation Donor-Acceptor Material in Solution and Liquid Crystalline Film

In this section, the results of spectroscopic and theoretical studies on the first-generation bisthiophene-perylene system (Fig. 10.1(a)) are presented[115–119] The spectroscopic results for the system in solution and in a liquid crystalline (LC) film are briefly summarized, together with the electronic structure results for this system in solution (section 10.1.1). This is followed by the results of high-dimensional quantum dynamics for a model system of the LC film (section 10.1.2).

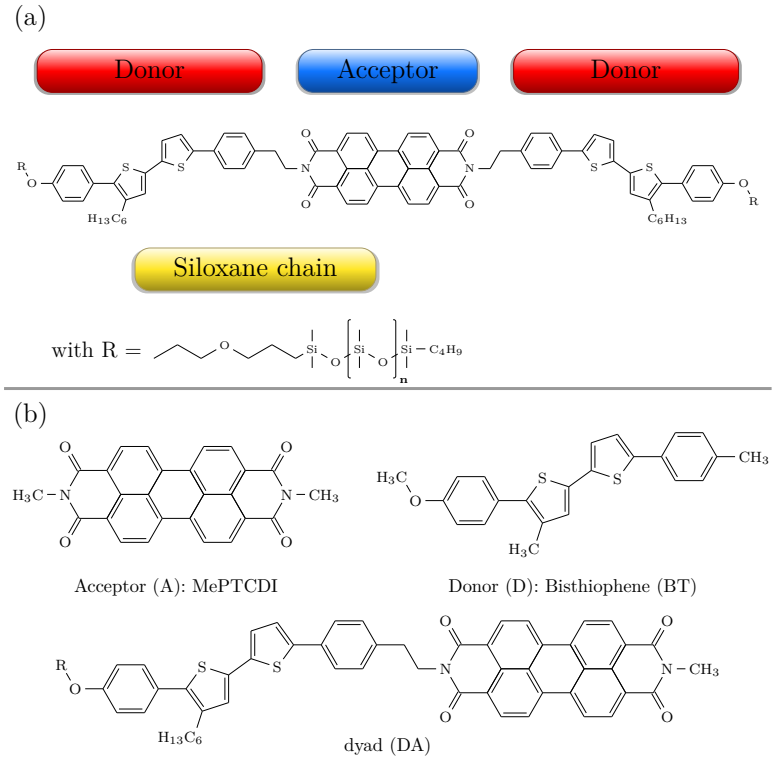

Figure 10.1: (a) Sketch of the molecular structure of the DAD compound. (b) For the theoretical description the triad has been reduced to a DA dyad, which is justified by the localized character of the excitations. The siloxane groups (R) and the hexyl-groups are reduced to methyl-groups. The dyad (DA) is therefore build of the acceptor moiety (A), *N,N*-dimethylperylene-3,4,9,10-dicarboximide (MePTCDI), and the donor moiety (D), 5-(4-methoxyphenyl)-4-methy-5'-4-methylphenyl)-2,2'-bithiophene (BT).

10.1.1 Spectroscopic and Quantum Chemical Characterization of the First Generation DAD

The first generation of the donor-acceptor material, a donor-acceptor-donor triad (see Fig. 10.1(a)), was spectroscopically characterized in the group of S. Haacke at Strasbourg University,[115–117] both in solution and in a LC film. The steady-state absorption and emission spectra in chloroform show a broad absorption band of the donor molecule around 300 nm to 425 nm, whereas the acceptor shows a three-peak absorption at 460 nm, 490 nm and 525 nm (indicating a vibrational progression). The acceptor band exhibits a spectral overlap with the emission of the donor moiety. The absorption spectrum of the DAD triad is given by the sum of the absorption spectra of the individual molecular moieties. The emission spectrum does not show the expected emission band of the donor moiety, suggesting that excitation energy transfer takes place. The absorption spectrum of the film shows essentially the same features, but the overall spectrum is red-shifted by ∼0.1 eV and the acceptor absorption is significantly weaker. In addition, a low-energy shoulder at 400 nm is present. These features indicate the presence of an inter-molecular, excitonic coupling between neighboring DAD molecules. The red-shift can be interpreted as an effect of J-aggregate formation, as will be further discussed below.

The pump-probe experiments exhibit a remarkably different photochemistry in solution and in the LC film. In solution, an ultrafast excitation energy transfer (EET) from the donor to the acceptor moiety is followed by charge separation on a timescale of about 2.7 ps, EET is found to be absent in the LC film. Instead, an ultrafast charge transfer (CT) state formation is found (Fig. 10.2). Additionally, a recombination time of ∼50 ps is observed, as well as triplet formation on a longer time scale (>1 ns). These factors severely limit the transient photocurrent and therefore the applicability as a photovoltaic device.

On the theory side, we have aimed to understand these widely different properties of the excitations in solution and the LC film in detail. The electronic structure results that were initially obtained in our group by by J. Wenzel et al.[119] illustrate that the electronic transitions in solution can be understood in terms of well-separated excitations of the D and A moieties (denoted as D1 and A1), together with a principal intra-molecular CT state (Fig. 10.3). To reduce the computational cost, the electronic structure calculations were done only for the DA dyad species (see Fig. 10.1(b)). This does not conflict with the experimental

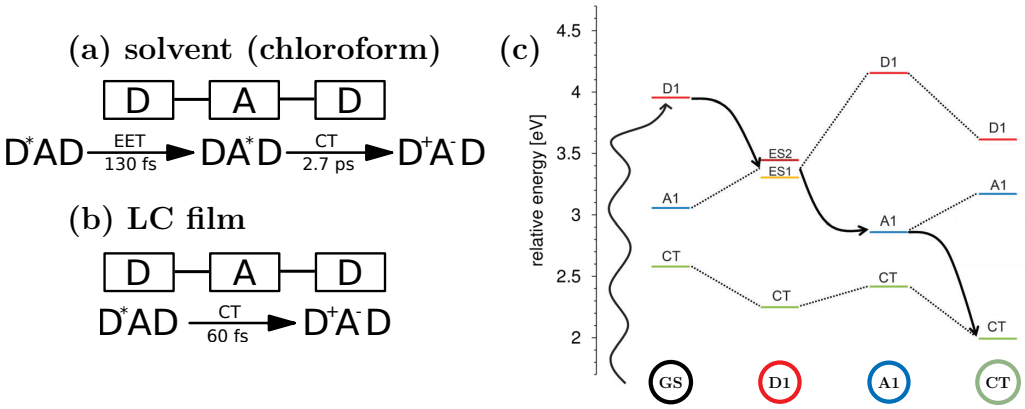

Figure 10.2: Left Panel: Schematic illustration of the kinetic pathways of the first-generation DAD triad system in (a) solution and (b) LC phase. The time scales for the EET and CT steps have been obtained from pump-probe spectroscopy.[115,116] Right Panel: (c) Proposed photoreaction mechanism of the DAD system by selective excitation of the D1 state. The energies of the three principal excited states are shown for four different geometries, which have been obtained by ground and excited state geometry optimizations, performed in the gas phase. Energies are given for the system in chloroform solution, calculated with COSMO.[119–121]

results, since the presence of two donor moieties only increases the photoabsorption cross-section. Furthermore, the siloxane and alkyl-chains are shortened to methyl groups to further reduce the computation time. The spectroscopic properties of the DA dyad are expected to be essentially unchanged. By performing excited state optimizations, the experimental kinetic pathway in chloroform (c.f. Figs. 10.2(a) and 10.2(c)) was confirmed. The calculations have been performed at the TDDFT level with a self-adapted functional, which was benchmarked against the high-level CC2 method with the triple-zeta basis set TZVP.[122] The solvent contributions were taken into account with the conductor-like screening model (COSMO)[120,121] and the solvent equilibrated to the ground state.

10.1.2 Charge Separation in Liquid Crystalline 1st Generation Donor-Acceptor Material

As shown in section 10.1.1, the charge transfer formation time scales change drastically between solution and the smectic LC film. While the formation is rather slow in solution (few tens of picoseconds), an ultrafast charge transfer is observed in LC film. To understand this change, a combined electronic structure and quantum dynamical analysis that is tailored to the nanoscale order of the LC phase is performed.[123]

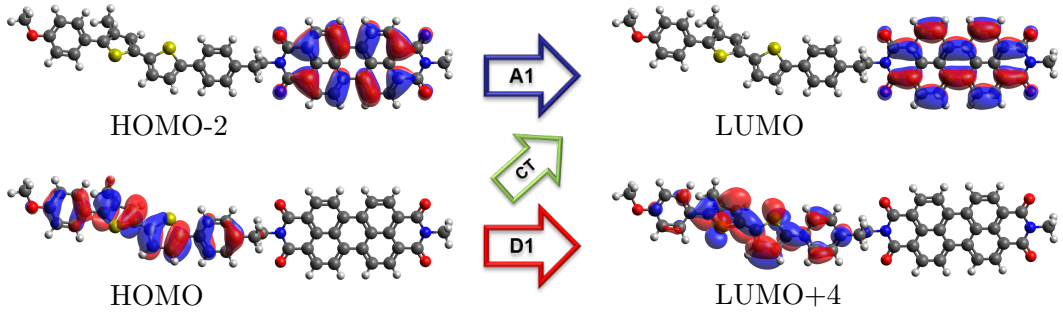

Figure 10.3: Vertical electronic transitions in the DA system, including local excitations of the donor moiety (D1) and acceptor moiety (A1), along with a D→A charge transfer transition. Calculations were carried out at the TDDFT level with suitable benchmarks using the CC2 approach.

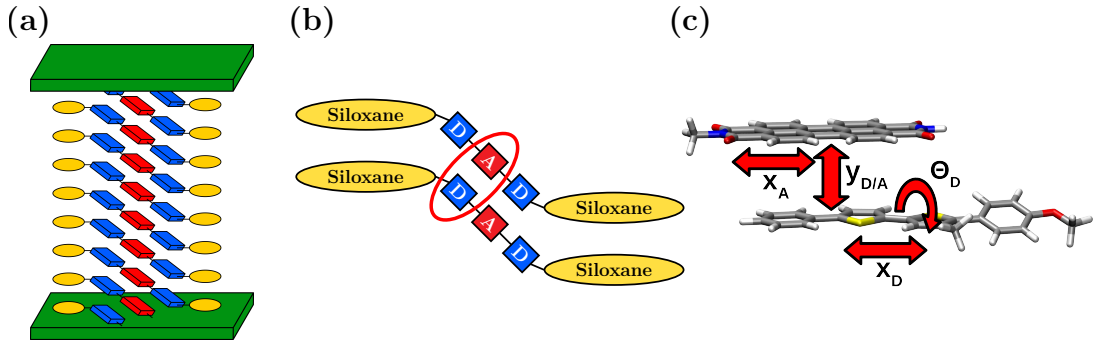

Figure 10.4: (a)Schematic representation of the smectic LC phase stabilized by the stacking of the siloxane side chains including the 70° tilt angle between the molecular planes. (b) Fragment taken from the supra-molecular assembly in the smectic LC phase. (c) Molecular structure of a stacked D-A pair corresponding to the LC phase geometry, with the most relevant nuclear modes.

Fig. 10.4 illustrates the stacked DA model structure taken from the X-ray structure of the LC film.[117] The molecular packing within the LC phase shows that the DAD molecules are not stacked directly above each other, i.e., they do not form an H-aggregate. Instead they are shifted due to a large tilt angle of ∼70° between the molecular plane and the normal plane of the crystal. As a consequence, the donor and acceptor moieties are shifted on top of each other. Therefore, inter-molecular π-stacking of monomers of the same type does not occur, but is observed between donor-acceptor pairs of neighboring, parallel segments. Furthermore, an initially delocalized exciton, that is extended across several donor units, creates a J-aggregate, rather than a H-aggregate[31,124] as one would expect for vertically stacked donor-acceptor monomers. This leads to the idea that inter-molecular DA interactions could effectively compete with intra-molecular EET and CT processes.

To investigate and clarify the elementary processes in the smectic LC phase, electronic structure calculations for selected fragments are combined with high dimensional quantum dynamics using a vibronic Hamiltonian in a generalized electron-hole (*e-h*) representation.[22,125] An *e-h* pair is represented by $|\nu_e \mu_h\rangle \equiv |\nu\mu\rangle$, where the electron is located at site $\nu_e = \nu$ and the hole is located at site $\mu_h = \mu$. A localized *e-h* pair $|\nu\nu\rangle$ corresponds to Frenkel excitonic (XT) configuration on the donor or acceptor moieties: $\left|D_i^{XT}\right\rangle = |\nu = i, \mu = i\rangle$ (where $i = 1, \ldots, N_D$) and $\left|A_j^{XT}\right\rangle = |\nu = j, \mu = i\rangle$ (where $j = 1, \ldots, N_A$). Consequently, a non-local *e-h* pair ($|\nu\mu\rangle$, with $\nu \neq \mu$ ($\nu = 0, \mu = 1, \ldots, N$)) represents a charge-separated (CS) state ($\left|D_i^+ A_j^-\right\rangle = |\nu_i \mu_j\rangle$). To simplify matters, the short-hand notation CS(n) is used to identify the subsets of CS configurations with an electron-hole separation of $i - j \equiv n$.

In the electron-hole representation, the Hamiltonian takes the form,

$$\hat{H} = \hat{H}_{\text{el}} + \hat{H}_{\text{e-ph}} \tag{10.1}$$

$$= \underbrace{\hat{H}_{\text{on-site}} + \hat{H}_{\text{coupl}}}_{\hat{H}_{\text{el}}} + \hat{H}_{\text{e-ph}} \tag{10.2}$$

where $\hat{H}$ is written as the combination of an electronic part ($\hat{H}_{\text{el}}$) and a phonon part including electron-phonon interactions ($\hat{H}_{\text{e-ph}}$). The electronic part, $\hat{H}_{\text{el}}$, includes the on-site energies ($\hat{H}_{\text{on-site}}$) and the intra- and inter-molecular electronic couplings ($\hat{H}_{\text{coupl}}$). $\hat{H}_{\text{e-ph}}$ represents the phonon (vibrational) Hamiltonian including the electron-phonon (e-ph) coupling. To be more specific, the on-site energies are defined as,

$$\begin{aligned}\hat{H}_{\text{on-site}} =& \epsilon_D \sum_{i=1}^{N_D} \left|D_i^{XT}\right\rangle \left\langle D_i^{XT}\right| + \epsilon_A \sum_{i=1}^{N_A} \left|A_i^{XT}\right\rangle \left\langle A_i^{XT}\right| \\ &+ \sum_{i=1}^{N_D} \sum_{j=1}^{N_A} \epsilon_{D_i^+ A_j^-} \left|D_i^+ A_j^-\right\rangle \left\langle D_i^+ A_j^-\right|\end{aligned} \tag{10.3}$$

where the on-site energies of the excitonic donor (ϵ_D) or acceptor (ϵ_A) states are taken to be equal for all fragments. $\epsilon_{D_i^+ A_j^-}$ represents the energies of the CS states and are defined by an effective Coulomb barrier, as shown in Fig. 10.5. The on-site energies ϵ_D, ϵ_A and $\epsilon_{D_i^+ A_j^-}$ for Frenkel states and nearest-neighbor electron-hole states (i.e., *e-h* distance $|i - j| \leq 1$) have been determined by ADC(2) calculations for a stacked DA dimer fragment at the Franck-Condon geometry as shown in Fig. 10.4(c). The on-site energies for the charge separated states with large electron hole distances $|i - j| > 1$, on the other hand, rely on complementary TDDFT

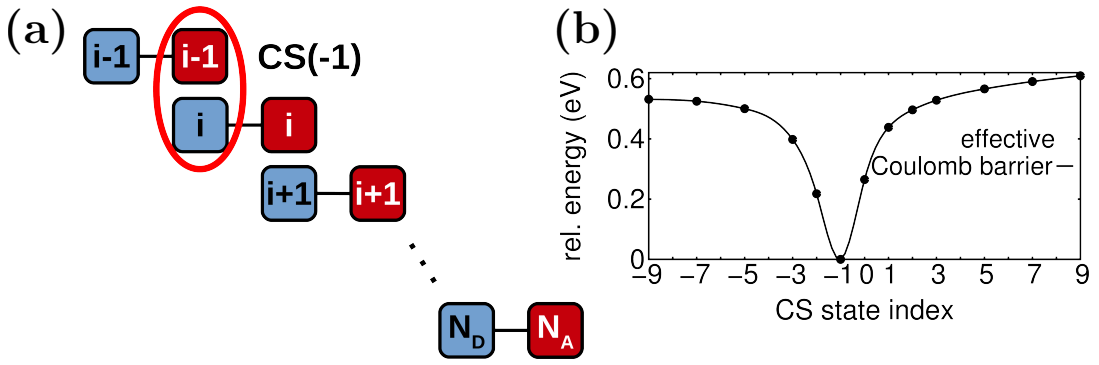

Figure 10.5: (a) Schematic representation of the LC stack consisting of N_D donor and N_A acceptor molecules. The highlighted CS(-1) configuration is the state to which the initial charge separation occurs, according to the electronic structure calculations. (b) Coulomb barrier obtained from electronic structure calculations, calculated with ωB97XD/SVP as implemented in the Gaussian09 software package[126].

calculations for larger fragments that are used to determine the Coulomb barrier. The energies of the Coulomb barrier, $\epsilon_{D_i^+ A_j^-}$ (see Fig. 10.5) have been calculated by using only two monomers (one donor and one acceptor), representative of a CS configuration, whereas the other sites are replaced by point charges. Furthermore, an external field of $50\,\mathrm{V\,\mu m^{-1}}$ has been applied in the calculations.

The electronic coupling part of the Hamiltonian is given as follows,

$$\begin{aligned}\hat{H}_{\text{coupl}} =& J_D \sum_{i=1}^{N_D}\sum_{j=1}^{N_D}\left(\left|D_i^{XT}\right\rangle\left\langle D_j^{XT}\right| + \text{h.c.}\right) + J_A \sum_{i=1}^{N_A}\sum_{j=1}^{N_A}\left(\left|A_i^{XT}\right\rangle\left\langle A_j^{XT}\right| + \text{h.c.}\right) \\ &+ J_{DA}\sum_{i=1}^{N_D}\sum_{j=1}^{N_A}\left(\left|D_i^{XT}\right\rangle\left\langle A_j^{XT}\right| + \text{h.c.}\right) \\ &+ \kappa_D \sum_{i=1}^{N_D}\sum_{j=1}^{N_A}\left(\left|D_i^{XT}\right\rangle\left\langle D_i^{+}A_j^{-}\right| + \text{h.c.}\right) + \kappa_A \sum_{i=1}^{N_A}\sum_{j=1}^{N_D}\left(\left|A_i^{XT}\right\rangle\left\langle D_j^{+}A_i^{-}\right| + \text{h.c.}\right) \\ &+ t_e \sum_{i=1}^{N_D}\sum_{j=2}^{N_A-1}\left(\left|D_i^{+}A_j^{-}\right\rangle\left\langle D_i^{+}A_{j\pm1}^{-}\right| + \text{h.c.}\right) \\ &+ t_h \sum_{i=2}^{N_D-1}\sum_{j=1}^{N_A}\left(\left|D_i^{+}A_j^{-}\right\rangle\left\langle D_{i\pm1}^{+}A_j^{-}\right| + \text{h.c.}\right) \end{aligned} \tag{10.4}$$

and describes the various types of intra- and inter-molecular couplings, i.e. the excitonic couplings between donor and acceptor moieties (J_D,J_A,J_{DA}), charge transfer couplings between excitonic states and intra-molecular CT states or charge-separated stacked donor/acceptor pairs (κ_D,κ_A) and transfer integrals for electron and hole transfers (t_e,t_h) that determine the transient conductivity of the separated

charge carriers. The pairwise (ij) interactions are restricted to nearest-neighbor couplings in our current analysis.

Lastly, the electron-phonon coupling Hamiltonian reads as,

$$\begin{aligned}\hat{H}_{\text{e-ph}} =& \hat{T}_{\text{ph}}\left(\left\{\xi^{D}\right\},\left\{\xi^{A}\right\},\left\{\xi^{DA}\right\}\right) \\ &+\sum_{i}\hat{V}_{D}^{XT}\left(\left\{\xi^{D}\right\},\left\{\xi^{DA}\right\}\right)\left|D_{i}^{XT}\right\rangle\left\langle D_{i}^{XT}\right| \\ &+\sum_{i}\hat{V}_{A}^{XT}\left(\left\{\xi^{A}\right\},\left\{\xi^{DA}\right\}\right)\left|A_{i}^{XT}\right\rangle\left\langle A_{i}^{XT}\right| \\ &+\sum_{i}\sum_{j}\hat{V}_{DA}\left(\left\{\xi^{D}\right\},\left\{\xi^{A}\right\},\left\{\xi^{DA}\right\}\right)\left|D_{i}^{+}A_{j}^{-}\right\rangle\left\langle D_{i}^{+}A_{j}^{-}\right| \end{aligned} \tag{10.5}$$

where the kinetic energy operator $\hat{T}_{\text{ph}}$ is chosen to be electronically diagonal in order to fulfill the requirement of a diabatic Hamiltonian. The potential energy terms $\hat{V}$ represent selected PES cuts of the system that were fitted by an analytic procedure. The relevant modes are chosen and identified by an analysis of the Frank-Condon gradients. As shown in Fig. 10.4(c), these modes represent high-frequency bond-length alternations (BLA) modes on the donor and acceptor, as well as a low frequency torsional degree of freedom located only on the donor moiety.[119] Furthermore, an inter-molecular mode specific to the LC phase, representing the modulation of the distance between two layers of DA chains is taken into account.

The efficiency of the various competing transfer pathways depends on the magnitude of the respective couplings and on the resonance offsets determined by $\hat{H}_{\text{on-site}}$. A detailed analysis[123] shows that (i) the excitonic coupling is sizable (J_D =−0.1 eV) and will lead to initial delocalization at the lower band edge of the donor J-aggregate, (ii) the intra-chain charge transfer coupling (κ_D^{intra} =0.002 eV) is much weaker than the inter-molecular charge transfer coupling (κ_D^{inter} =0.025 eV), (iii) the transfer integrals for electron (t_e =0.0005 eV) and hole (t_h =0.0013 eV) transport are small.

The results of the high dimensional quantum dynamical simulations are summarized in Fig. 10.6 and show a rapid decay of the excitonic donor population and complementary rise of the CS state population on an initial time scale of ∼50 fs. Cumulative populations are shown, i.e., $P_D^{XT} = \sum_i P_{D_i}^{XT}$ and $P_{\text{CS}(n)} = \sum_{i,j} P_{D_i^+A_j^-}$ (for $i - j = n$). Strikingly, practically all population accumulates in the CS($n = -1$) states. This is due to (i) the unfavorable energetics of the CS($n \neq -1$) states resulting from the Coulomb barrier (c.f. Fig. 10.5), and (ii) the small transfer inte-

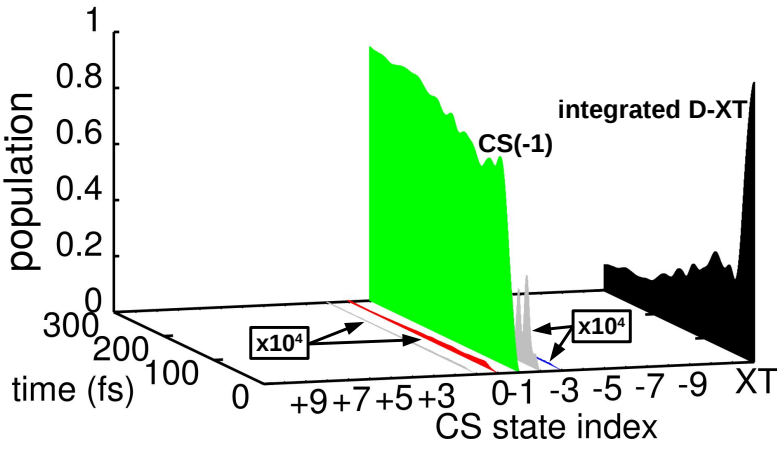

Figure 10.6: Full quantum dynamical evolution for the coupled excitonic donor and CS manifolds (156 states, 48 modes) obtained from Multi-Layer Multi-Configuration Time-Dependent Hartree (ML-MCTDH) calculations. Spatially resolved populatiions of the different CS states. The ultrafast excitonic decay of the integrated D-XT populations matches the rise of the initial CS(-1) state, while the other CS($\pm n$) states are almost not populated due to a high Coulomb barrier and small transfer integrals.[123]

grals (t_e, t_h), precluding a rapid formation of a photocurrent. After ∼250 fs, the charge transfer is essentially complete and a quasi-stationary state of the CS(-1) populations is reached.

The observed time scales are in excellent agreement with the CT formation time deduced from experiment for the LC film (i.e. ∼60 fs),[116] along with the observation that recombination rather than photocurrent formation apparently dominates in the first-generation LC material.

10.2 Chemical Design of Second-Generation Donor-Acceptor Systems

As summarized in the preceding section, the first generation of the bisthiophene-PDI type donor-acceptor triads exhibited two different pathways for the formation of a charge transfer state in solution and in a smectic LC film. While for the isolated molecules a 120 fs resonant energy transfer from the donor to the acceptor, the formation of a CT state within 2.5 ps is observed. The CT state showed a fast recombination time of 50 ps and a partially formation of the donor triplet state. Within the LC film the CT state is formed much more rapidly in 0.4 ps, in absence of the resonance energy transfer. Furthermore, a slightly longer recombination

time of 1.2 ns was observed. Due to these relatively short lifetimes, an efficient charge separation is not possible.

In view of these findings, the groups of S. Méry and S. Haacke at Strasbourg University set out to design a second-generation material that exhibits both changes in the chemical composition and in the nanoscale morphology. In the present section, we focus on the chemical design aspects and analyze a series of systems whose donor moieties are systematically modified. Based upon this analysis, we attempt to rationalize the appearance of long-lived charge transfer states, indicating slow recombination rates in the second-generation systems.

The second generation of oligomers (Fig. 10.7) was synthesized with the aim of increasing the intra-molecular CT lifetime to over 1 ns, indicating that the recombination rate is reduced accordingly. At the same time, the almost 100 % CT formation efficiency should be conserved. These new DA systems consist of several building blocks which have different effects on the DA electronic coupling and intra-molecular reorganization of the CT state formation and lifetime. While the acceptor remains unchanged as compared with the first generation, the donor is modified and is now composed of a bisthiophene-fluorene group with a variable number of donor units, D_n (from $n = 0$ to 3). The donor and acceptor moieties are linked via a short and flexible ethylene group. Furthermore, between the linker and the donor a spacer block can be chosen from two variants: The first variant exhibits a high electron affinity, while the second one exhibits a lower electron affinity, denoted δ_+ and δ. The δ group is composed of the sequence thiophene-phenyl-thiophene-phenyl, whereas the δ_+ is built up of the sequence thiophene-benzothiadiazole-thiophene-phenyl. As an optional addition, an amine group ($\delta\_$), acting as an electron donating group, can be attached to the end of the donor block.

The electron-deficient benzothiadizole group is a well known low-band-gap co-polymer and can act as acceptor for the near-by bisthiophene units.[127–129] For better solubility and mesophase formation, along with the good stacking properties of the PDIs, alkyl chains are attached to the fluorene-moieties in the donor-blocks. Although dyads (D-A) and triads (D-A-D or A-D-A) were produced, this work focuses solely on the dyad systems.

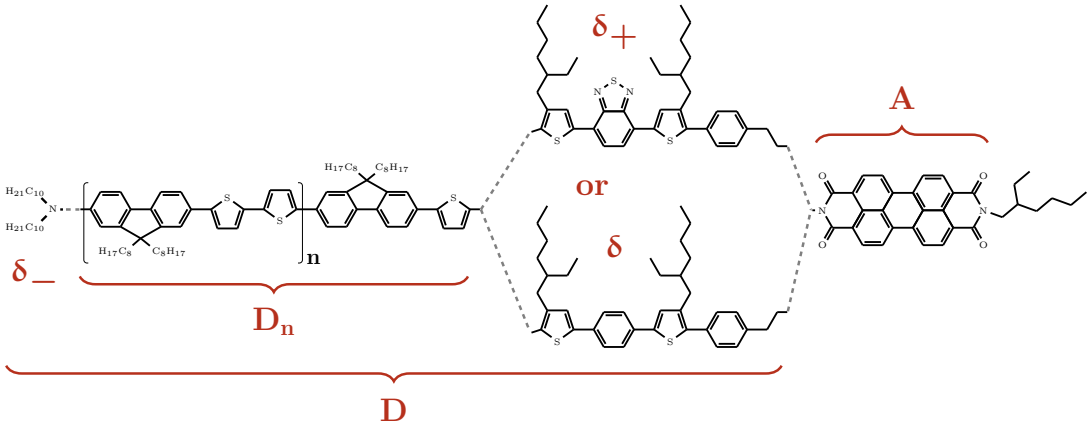

Figure 10.7: Illustration of the variable molecular structure of the second generation systems. One molecular unit always consists of the acceptor block (A), the donor block (D_n) of variable length and the linker block (δor δ_+. Additionally, a terminal amine group (δ_-) can be added.

10.2.1 Experimental Results in Solution

In the following, the spectroscopic observations are presented, followed by the characterization of the systems with high-level electronic structure methods and TDDFT.

The electronic structure analysis is done first for the individual donor species, followed by the complete donor-acceptor dyad. The acceptor is untouched and was characterized thoroughly for the first generation; therefore the results are only briefly summarized. For further analysis the DFT functionals are benchmarked against *ab initio* results, such that the photochemical pathways and the influence of various building blocks can be discussed. A combined analysis of the charge separation and recombination times is presented at the end of this chapter using Marcus-Jortner-Levich theory.

10.2.1.1 Steady-State Properties

First, the absorption spectra of the individual molecules ($D_1\delta$ and $D_1\delta_+$) as well the total system ($D_1\delta A$ and $D_1\delta_+A$) were analyzed.[130] Whereas the $D_1\delta$ donor molecule shows only one peak (408 nm), the spectra of the $D_1\delta_+$ moiety exhibit two peaks(424 nm and 510 nm). The peaks resemble the spectra of the individual molecular units (D_n and δ_+), where the lower excited states at 510 nm is located on the δ_+ moiety. The peaks of $D_1\delta_+$ are red-shifted by 12 nm and 30 nm, respectively, as compared to the single molecular units, indicating the presence of an electronic coupling between D_1 and δ_+. This is further emphasized since only one fluorescence

peak, which corresponds to the δ_+ group and is red-shifted by 49 nm, is visible in the emission spectra for $D_1\delta_+$.

The acceptor spectrum is the same as for the first generation as it is the same molecular unit. Linking $D_1\delta_+$ and the acceptor together introduces no further spectral shift for both moieties. This suggests a negligible electronic coupling between those two moieties. It should be noted that the emission spectrum of $D_1\delta$ overlaps with the absorption spectrum of A. This is not the case for $D_1\delta_+$. From this one might suggest that excitation energy transfer from $D_1\delta$ to A occurs, while EET is not expected to appear for $D_1\delta_+$.

10.2.1.2 Photodynamics in $CHCl_3$

The pump-probe experiments exposed two different pathways for the δ and δ_+ variants depicted in Fig. 10.8.

The δ variant shows a similar, but overall slower, behavior than the first generation DAD triad. With a time constant of 1.2 ps, EET from the donor to the acceptor occurs and is followed by CT formation with a time constant of 14 ps. On long time scales, the CT state recombines and the ground state is recovered. The time constant for charge recombination can be deduced from the CT lifetime of ∼500 ps.

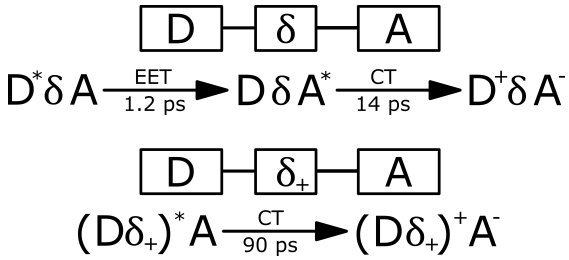

Figure 10.8: Schematic illustration of $D_1\delta A$ and $D_1\delta_+ A$ species and the relevant EET and CT transfer steps from time-resolved spectroscopy.[130] The measured time scales refer to solution phase measurements with chloroform solvent.

The δ_+ variant, however, leads to a different picture. Upon exciting the donor and forming the excited state on the $D_1\delta_+$ moiety, no EET is observed to the acceptor. Instead, the CT state is formed directly with a time constant of 90 ps. This fits to the observation that the red shifted peak in the emission spectrum of $D_1\delta_+$ does not overlap with the absorption band of the PDI. The time constant for the recombination is observed to be ∼480 ps and is in a similar time range as $D_1\delta A$.

10.2.1.3 Molecular Design of Long-Lived CT States: Effect of Donor Length and δ_on the Photodynamics

As mentioned before, the donor length is now made variable by concatenating n donor units (D_n), and adding a δ_ group. Our experimental collaborators[130] measured several variants with increasing donor length (up to $n = 3$) with and without the δ_ group.

The formation and recombination time constants for the investigated variants are shown in Tab. 10.1. As can be seen, the δ_+ group does not have a significant influence on the recombination kinetics. Hence, the influence of the δ_ group is only shown for δ_D_nδA as the effect is comparable for both species. Upon adding the δ_ group, the biggest influence is seen for the D_1 moiety. While the formation time stays almost the same, recombination times are significantly increased by a factor of 2.5 for molecules including δ_+ (0.48 ns for $D_1\delta_+A$ versus 1.2 ns for δ_$D_1\delta_+$A) and even a factor of 4.5 for molecules containing the δ group (0.51 ns for D_1δA versus 2.3 ns for δ_D_1δA).

A possible reason is the larger spatial separation between the charges by stabilizing the positive charge farther away from the acceptor to the other end of the molecule.

This could also explain the observations for the recombination times when varying the donor length. While the formation time is not changed for δ_D_nδA, the recombination time has a maximum for $n = 1$. For $n = 2$ the spatial extent of the donor might already be too large, such that the influence of δ_ gets less significant. For $D_n\delta_+$A the donor length has no impact on the kinetics. The formation time (∼100 fs) and recombination time (∼450 fs) remain almost identical.

Table 10.1: Charge Transfer state formation and recombination time constants for $D_n\delta_+$A and δ_D_nδA

	$D_n\delta_+$A		δ_D_nδA	
n	Formation (ps)	Recomb. (ps)	Formation (ps)	Recomb. (ns)
0	90	410	20	0.4
1	90	480	14	2.3
2	150	440	14	1.1
3	140	430		

Table 10.2: Charge Transfer state formation and recombination time constants dependence on the solvent.

Solvent dielectric constant ϵ		Toluene $\epsilon = 2.38\,(3.5^a)$	TCE $\epsilon = 3.42$	Chloroform $\epsilon = 4.81$
$D_1\delta A$	Formation (ns)	0.026	0.014	0.014
	Recombination (ns)	5.70	4.0	0.50
$\delta\_D_1\delta A$	Formation (ns)	0.030	0.019	0.014
	Recombination (ns)	6.7	6.0	2.3
$D_1\delta_+A$	Formation (ns)	0.26	0.15	0.090
	Recombination (ns)	6.2	2.8	0.48
$\delta\_D_1\delta_+A$	Formation (ns)			0.12
	Recombination (ns)			1.2

[a] An effective dielectric constant of 3.5 is found in the literature for toluene, to account for the effect of its strong electric quadrupole moment.[131]

10.2.1.4 Effect of the Solvent

Furthermore, the influence of the solvent polarity on the time constants of charge separation and charge generation is investigated. The results for three different solvents (chloroform, toluene and trichloroethylene (TCE)) are compared. As Tab. 10.2 shows, the CT states of all molecules are stabilized, i.e., their lifetime is increased. Furthermore, the stabilizing effect of the $\delta\_$ group is reduced for toluene and TCE, as it is observed for chloroform. A reason for this might be the experimental limitations. The pump-probe experiments of the Strasbourg group do not inform about time scales beyond 6 ns. Hence, a precise determination was not possible and would require measurements over longer time spans.[130] The formation times are almost unaffected by the solvent polarity and only increase slightly.

10.2.2 Computational Details

The second generation systems represent very large molecular species. Therefore, the application of high-level *ab initio* methods like CC2 is only possible to a limited extent. Hence, TDDFT is the method of choice and a suitable DFT functional is used after validation against the CC2 benchmark results. For the ground state optimizations of the single donor molecules, the RI-SCS-MP(2) method is used, while for the complete dyad molecules the B3LYP[51] functional is chosen due to the increased computational effort.

Since the formation of the CT state is of significant importance for this work, long range corrected DFT functionals as implementented in Gaussian09D[126] are employed to account for the electron-transfer self-interaction error (see chapter 3.3). Mainly the ωb97XD[56] and CAM-B3LYP[55] functionals are used.

The employed basis sets comprise the reparametrized Ahlrich basis sets def2-SVP and def2-TZVP.[132]

Some calculations incorporate solvent effects that are included using the conductor-like screening model (COSMO).[120,121] Calculations are performed using a solvent cavity equilibrated to the ground state charge distribution.

The analysis of the CT formation and recombination kinetics with the Marcus-Jortner-Levich method uses the distance of electron and hole density centroids. The distances are calculated employing the method implemented in the MultiWfn-package[133] incorporating the corresponding orbital transitions by using the expansion coefficients as weights based on excited state calculations.

The quantum chemical calculations are performed mostly with the Gaussian09 package.[126] Excited state calculations with the high-level *ab initio* methods RI-CC2 and RI-ADC(2) are done with the Turbomole 6.4 package.[134] Furthermore, this package is used for the ground state geometry optimizations. Finally, the COSMO calculations are performed with the Orca 3.0 package.[135] In this package, with hybrid-functionals the excitation energies can only be calculated with the Tamm-Dancoff-approximation (TDA)[136] and are not directly comparable to the Gaussian09 results.

10.2.3 Quantum Chemical Characterization of the Donor and the Donor-Acceptor Dyad

This section presents the results of the electronic structure calculations – of the ground state and the excited states – for various building blocks of the donor-acceptor system. First, the results for the single donor units $D_0\delta$ and $D_0\delta_+$ are presented, and second, the results for the PDI acceptor that were previously obtained in our group by J. Wenzel et al.[118,119] are briefly summarized. Second, the donor-acceptor dyad is characterized for both δ- and δ_+-variants.

In view of the fact that the systems under study are computationally expensive, a benchmark and the initial analysis is presented for the shorter D_0 donor block, even though the main interest from the experimental side is in the D_1 species. It is therefore important to note that the first absorption peak at 424 nm in the spectrum for $D_0\delta_+$ is strongly blue shifted by ∼60 nm (from 424 nm to 365 nm, compared to the longer donors.

10.2.3.1 Ground-State Geometry – $D_0\delta$

The torsions of bisthiophene systems have a large influence and are possible channels for EET and CT processes within the dyad.[137,138] The ground state structure of $D_0\delta$ is optimized with the RI-SCS-MP(2) method in combination with the def2-TZVP basis set and is shown in Fig. 10.9. All torsional angles between the rings in the system differ from 180° due to steric effects (c.f. Fig. 10.9 and Tab. 10.3). While for the phenyl **A** the methyl group of the thiophene ring **B** leads to a repulsion and therefore a twist in the torsion $\boldsymbol{\alpha}$, the other ring torsions are distorted due to repulsion of the sulfur atoms.

The central C-C bond length between the two thiophene rings (**D** and **E**) is 1.45 Å, which is between the lengths of a typical C=C double bond (1.34 Å) and a C-C single bond (1.55 Å),[139] and indicates a delocalized π-system. The fluorene unit exhibits a nearly completely planar structure for the rings, with bond lengths between that of typical single C-C bonds and double C=C bonds, again indicating a delocalized π-system.

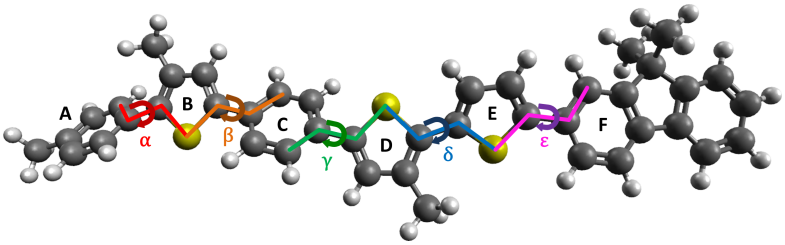

Figure 10.9: Ground state structure of $D_0\delta$ for RI-SCS-MP(2)/def2-TZVP. Rings are denoted with **A** to **F** and torsions between the rings are named from $\boldsymbol{\alpha}$ to $\boldsymbol{\epsilon}$. The fluorene unit is taken as one moiety.

The comparison to the B3LYP/def2-TZVP structure demonstrates a typical problem of DFT. The torsional barriers in delocalized π-system are usually overestimated and therefore the structure is flattened.[140,141] This is documented by the values of the torsional angles in Tab. 10.3 in the 4th column. The C-C bond

Table 10.3: Structural parameters of $D_0\delta$ and $D_0\delta_+$ for RI-SCS-MP(2)/def2-TZVP. The values are also compared to B3LYP/def2-TZVP.

Parameter	RI-SCS-MP(2)/def2-TZVP [°]		B3LYP/def2-TZVP [°]	
	$D_0\delta$	$D_0\delta_+$	$D_0\delta$	$D_0\delta_+$
$\boldsymbol{\alpha}$ (C-C-C-S)	225.5	225.3	223.0	221.7
$\boldsymbol{\beta}$ (S-C-C-C)	209.0	198.7	198.3	190.6
$\boldsymbol{\gamma}$ (C-C-C-S)	208.1	197.2	201.3	189.7
$\boldsymbol{\delta}$ (S-C-C-S)	216.6	214.5	205.2	202.3
$\boldsymbol{\epsilon}$ (S-C-C-C)	211.1	211.0	203.3	203.3

length yields 1.45 Å and is represented very good with respect to the RI-SCS-MP(2) results.

10.2.3.2 Ground-State Geometry – $D_0\delta_+$

The ground state structure for $D_0\delta_+$ is obtained again with RI-SCS-MP(2)/def2-TZVP and shown in Fig. 10.10. Similarly to $D_0\delta$, the molecular unit is not planar due to steric effects. While most of the geometrical properties are comparable to $D_0\delta$, the torsional angles $\boldsymbol{\beta}$ and $\boldsymbol{\gamma}$ are flattened by 10° compared to $D_0\delta$ (see Tab. 10.3). Further, the C-C bond between **B**-**C** and **C**-**D** is slightly shortened (∼0.01 Å), indicating a slightly increased double bond character of these bonds. Due to the electron-deficient benzothiadiazole bridge the π-system adjusts in order to account for the electron deficiency to get an improved delocalization.

The comparison to B3LYP/def2-TZVP exhibits the same behavior, resulting in a planarized molecular geometry with respect to the MP(2) geometry.

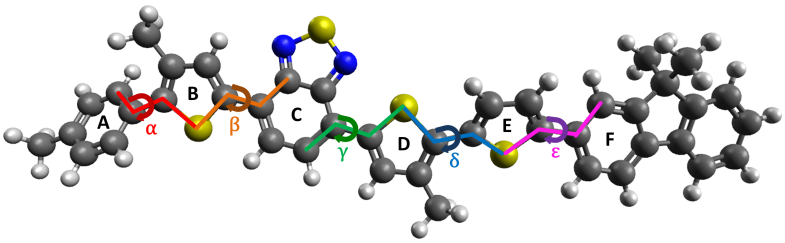

Figure 10.10: Ground state structure of $D_0\delta_+$ for RI-SCS-MP(2)/def2-TZVP. Rings are denoted with **A** to **F** and torsions between the rings are named from $\boldsymbol{\alpha}$ to $\boldsymbol{\epsilon}$. The fluorene unit is taken as one moiety.

10.2.3.3 Excited State properties – $D_0\delta$

Excited state calculations are performed with RI-CC2/def2-TZVP in vacuum, using the RI-SCS-MP(2) geometries.

Tab. 10.4 presents the first five vertical excited singlet states. Only the first excitation shows a significant oscillator strength. Hence, this state corresponds to the bright donor state that is excited in the absorption experiments. The excitation is mainly characterized by a HOMO-LUMO transition depicted in Fig. 10.11. Direct comparison to experimental data is not possible, as the absorption data is not available for $D_0\delta$. However, a very rough approximation can be made as the longer $D_1\delta$ unit shows one peak at 408 nm. The first peak in the absorption spectrum of $D_0\delta_+A$ is strongly blue shifted compared to $D_1\delta_+A$ by ∼60 nm. The estimated peak position at 348 nm (∼3.56 eV) is very close to the calculated result, indicating a good agreement to the experiment. Unfortunately, accurate calculations with RI-CC2/def2-TZVP were not feasible for $D_1\delta$.

Table 10.4: First five excited states of $D_0\delta$ calculated by CC2/def2-TZVP. Together with the energy and the oscillator strength, the two highest MO contributions and the character of the excitation are shown.

State	Excitation Energy [eV]	f_{osc}	MO contributions		Character
1	3.437	2.66	H→L	(87.1%)	$\pi \rightarrow \pi^*$
			H-1→L+1	(6.7%)	
2	3.985	0.05	H→L+1	(57.4%)	$\pi \rightarrow \pi^*$
			H-1→L	(30.4%)	
3	4.234	0.11	H-1→L	(36.8%)	$\pi \rightarrow \pi^*$
			H→L+1	(16.6%)	
4	4.284	0.01	H→L+3	(25.1%)	$\pi \rightarrow \pi^*$
			H→L+2	(12.1%)	
5	4.344	0.02	H→L+4	(45.9%)	$\pi \rightarrow \pi^*$
			H-1→L+4	(9.9%)	

10.2.3.4 Excited State properties – $D_0\delta_+$

The vertical excitations for $D_0\delta_+$ are presented in Tab. 10.5. An additional bright state is observed experimentally due to the replacement of the phenyl group by the benzothiadiazole group. This is reproduced by the RI-CC2/def2-TZVP results. The first excited state with an excitation energy of 2.61 eV shows again mainly a HOMO-LUMO excitation together with an oscillator strength of 1.24. The third

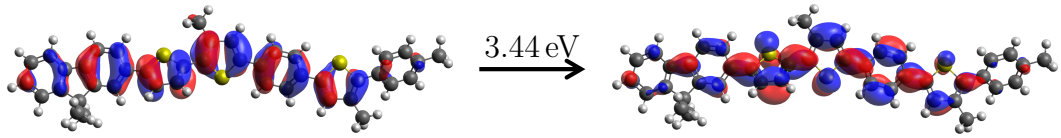

HOMO **LUMO**

Figure 10.11: Illustration of the bright donor $D_0\delta$ excitation. The excitation is mainly composed of a HOMO→LUMO transition.

excited state with an excitation energy of 3.60 eV and an oscillator strength of 1.45 is mainly composed of an HOMO-LUMO+1 excitation and corresponds to the second bright state. The transitions are depicted in Fig. 10.12. The second bright state corresponds to the donor excitation as for the bright excitation of $D_0\delta$, while the first bright state is mainly located on the δ_+ unit.

Experimentally, both states are separated by ∼0.97 eV (again, roughly approximated by a manual shift of ∼60 eV (86 nm)), showing a very good agreement to the CC2 results with an energy difference of 1.0 eV. The absolute values of the excitation energies are slightly higher (∼0.2 eV) compared to the experiment.

Table 10.5: First five excited states of $D_0\delta_+$ calculated by CC2/def2-TZVP. Together with the energy and the oscillator strength, the two highest MO contributions and the character of the excitation are shown. The first bright excitation is highlighted in orange and the second bright state in red.

State	Excitation Energy [eV]	f_{osc}	MO contributions		Character
1	2.609	1.24	H→L	(89.3%)	$\pi \rightarrow \pi^*$
			H-1→L	(5.2%)	$\pi \rightarrow \pi^*$
2	3.379	0.05	H-1→L	(65.6%)	
			H-2→L	(17.4%)	
3	3.604	1.45	H →L+1	(74.6%)	$\pi \rightarrow \pi^*$
			H→L+2	(4.7%)	
4	4.018	0.05	H→L+2	(53.7%)	$\pi \rightarrow \pi^*$
			H-1→L+1	(7.8%)	
5	4.118	0.06	H-5→L	(17.7%)	$\pi \rightarrow \pi^*$
			H-9→L	(17.3%)	

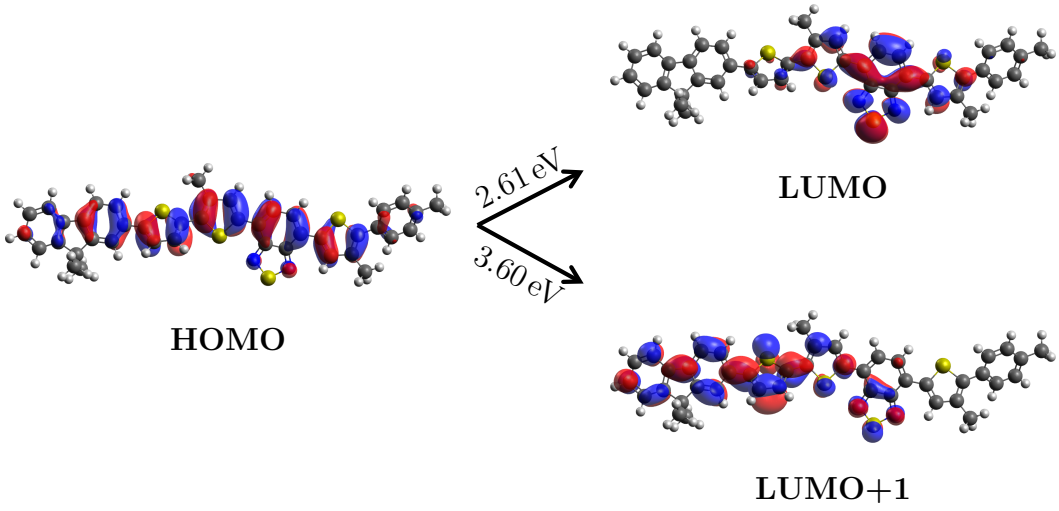

Figure 10.12: Illustration of the bright donor $D_0\delta_+$ excitation. The first excitation (2.61 eV) is mainly composed of a HOMO→LUMO transition and the second excitation (3.60 eV) is mainly composed of a HOMO→LUMO+1 transition.

10.2.3.5 Properties of PDI

In the second generation materials, the same acceptor unit is used as in the first generation species. Therefore, the relevant quantum chemical results, gained from the first generation, are briefly recapitulated.[119] Among the large number of theoretical investigations on individual perylenediimide compounds,[142–148] our focus lies on the properties of PDI as an acceptor. The results detailed in the following were obtained using the RI-CC2 method with the TZVP basis set.[119]

Tab. 10.6 presents the first five excited states of the PDI moiety. The energetically lowest excited state with an excitation energy of 2.62 eV corresponds to a HOMO-LUMO (π-π^*) transition with a noteworthy oscillator strength of 0.8. As the next higher lying excited states have practically no oscillator strength, this state resembles the experimentally observed bright state (in chloroform at about 2.4 eV).[115,116] While the second excited state is a dark π-π^* transition, the third and fourth excited states correspond to dark n-π^* transitions with a substantial CT character.

Excited state geometry optimizations in the first excited state showed bond length alternations for the C-C bonds of the perylene ring systems. This is directly linked to the HOMO-LUMO transition. Bonds with a binding character in the HOMO (and a non-binding character in the LUMO) are elongated, while bonds with a binding character in the LUMO are shortened. Therefore, these BLA coordinates

Table 10.6: First five excited states of PDI for CC2/TZVP.

State	Excitation Energy [eV]	f_{osc}	MO coefficients		Character
S_1	2.62	0.797	H → L	(0.982)	$\pi \rightarrow \pi^*$
S_2	3.49	0.000	H-1 → L	(0.810)	$\pi \rightarrow \pi^*$
			H → L+3	(-0.481)	
S_3	3.49	0.000	H-7 → L	(0.681)	$n \rightarrow \pi^*$
			H-8 → L	(0.564)	
S_4	3.50	0.000	H-8 → L	(-0.702)	$n \rightarrow \pi^*$
			H-7 → L	(0.570)	
S_5	3.72	0.000	H-4 → L	(0.856)	$\pi \rightarrow \pi^*$
			H → L+2	(-0.378)	

are expected to be the relevant relaxation modes for the CT and EET processes in the DA(D) system.

10.2.3.6 Ground-State Geometries of $D_0\delta A$ and $D_0\delta_+ A$

The ground-state geometries for $D_0\delta A$ and $D_0\delta_+ A$ could not be optimized with RI-SCS-MP(2)/def2-TZVP in a reasonable time and are therefore optimized using DFT with the hybrid-functional B3LYP and the def2-TZVP basis set.

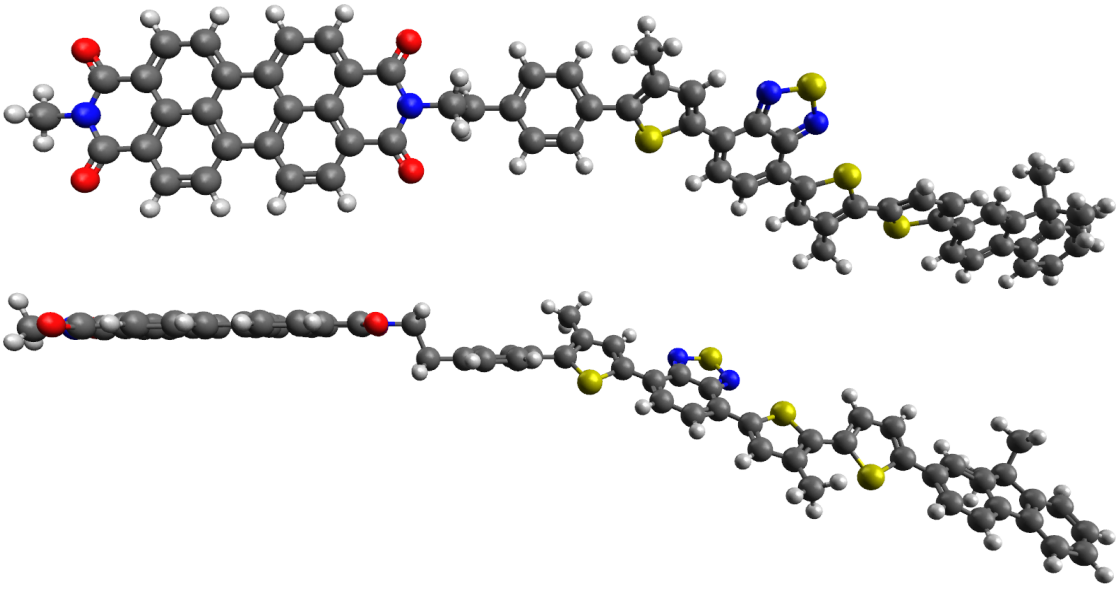

Figure 10.13: Ground state geometry of $D_0\delta_+ A$ optimized with B3YLP/def2-TZVP. Donor and acceptor are found to be in a co-planar arrangement. Views are from above and the side of the acceptor.

The acceptor is attached to the $D_0\delta$ and $D_0\delta_+$ via an ethylene bridge to the δ_+-side of the donor moiety. It was found that a linear arrangement of donor and acceptor

for both donor variants is optimal as depicted for $D_0\delta_+A$ in Fig. 10.13. The two angles **Θ** and **Φ**, as defined in Fig. 10.14, describe the ethylene bridge region, which connects the donor and acceptor moieties. These angles and the other above introduced structural parameters are presented in Tab. 10.7.

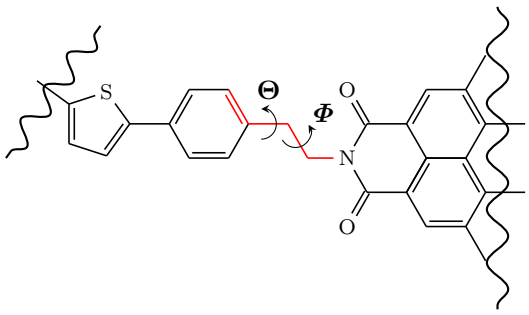

Figure 10.14: Excerpt of the ethyl bridge region of the DA dyad molecule. The dihedral angle d(C-C-C-C) = d(**Θ**) and d(C-C-C-N) = d(**Φ**) are highlighted in red.

The angles for **Θ** and **Φ** show that the phenyl-group of the donor unit is essentially co-planar to the acceptor unit and is attached co-linearly in both variants. The torsional parameters $\boldsymbol{\alpha}$ to $\boldsymbol{\epsilon}$ as introduced in section 10.2.3.1 are very similar for $D_0\delta_+A$ compared to $D_0\delta_+$ and therefore the geometries are again described to be too flat. However, for $D_0\delta A$ the B3LYP structure tends to be less flattened being closer to the RI-SCS-MP(2) structure of $D_0\delta$. The length of the C-C bond connecting the two neighboring thiophene rings with 1.45 Å is equivalent to the individual donor moieties. Since the geometries provide a good agreement in the bond lengths of the system and a reasonable agreement for the torsional angles, the study of the excited states is done on the basis of the B3LYP geometries.

Table 10.7: Structural parameters of $D_0\delta A$ and $D_0\delta_+A$ for B3LYP/def2-TZVP.

Parameter	B3LYP/def2-TZVP [°]	
	$D_0\delta A$	$D_0\delta_+A$
$\boldsymbol{\alpha}$ (C-C-C-S)	225.5	222.3
$\boldsymbol{\beta}$ (S-C-C-C)	203.4	191.1
$\boldsymbol{\gamma}$ (C-C-C-S)	204.4	189.5
$\boldsymbol{\delta}$ (S-C-C-S)	213.1	202.7
$\boldsymbol{\epsilon}$ (S-C-C-C)	207.5	203.5
Θ (C-C-C-C)	103.1	90.2
Φ (C-C-C-N)	181.7	181.3

10.2.3.7 Excited State properties of $D_0\delta A$

The vertical excited states are calculated using the B3LYP/def2-TZVP geometries. As reference method the RI-CC2 method in conjunction with the relatively small basis set def2-SVP is chosen, since a larger basis set could not be applied. For the single donor units $D_0\delta$ and $D_0\delta_+$ the calculations with this smaller basis set yield comparable results regarding the relative excitation energies and orbital contributions of the relevant states. However, the excitation energies are shifted to higher energies by about ∼0.2 eV.

First, the $D_0\delta A$ system is characterized. Tab. 10.8 presents the first five vertical excitations calculated with RI-CC2/def2-SVP in vacuum. Three relevant transitions can be identified and are marked with a corresponding color. The local acceptor excitation (AS_1) is colored in blue (2.80 eV), the local donor excitation (DS_1 in red (3.60 eV) and the corresponding charge transfer state (CT) is depicted in green (3.21 eV). Higher lying excitations correspond to local excitations ($n \rightarrow \pi^*$,$\pi \rightarrow \pi^*$) or further charge transfer states. The excitation energy of the acceptor state is equivalent to the one of the previous study shown in section 10.2.3.5. The local excitations correspond to the local excitations, indicating a clear separation of the two sub systems as shown by the experimental absorption spectra.

Table 10.8: First five excited states of $D_0\delta A$ calculated with CC2/def2-SVP. Together with the energy and the oscillator strength are the two highest MO contributions and the character of the excitation shown. The relevant excitations are colored accordingly to Fig. 10.15

State	Excitation Energy [eV]	f_{osc}	MO contributions		Character
1	2.803	1.03	H-2→L	(96.7%)	$\pi \rightarrow \pi^*$
2	3.210	0.00	H→L	(82.2%)	$\pi \rightarrow \pi^*$
			H-1→L	(15.3%)	
3	3.603	2.91	H →L+1	(86.6%)	$\pi \rightarrow \pi^*$
			H-1→L+5	(7.4%)	
4	3.657	0.00	H-13→L	(63.8%)	$\pi \rightarrow \pi^*$
			H-2→L+4	(23.8%)	
5	3.700	0.00	H-22→L	(73.2%)	$n \rightarrow \pi^*$
			H-22→L+2	(23.8%)	

In Fig. 10.15 the transitions are depicted with the corresponding molecular orbitals. They show that the acceptor and donor excitation are indeed local excitations, as they have been found for the single molecular units.

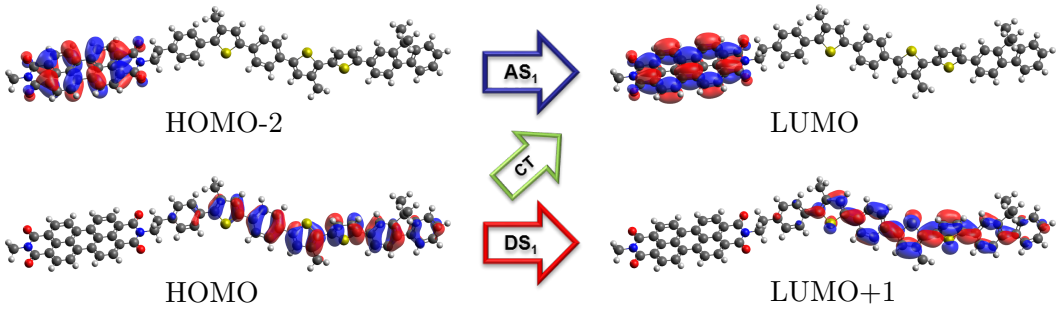

Figure 10.15: Illustration of the $D_0\delta A$ excitations. The local acceptor excitation AS_1 in blue is composed of a HOMO-2→LUMO transition, the donor excitation DS_1 in red is mainly composed of a HOMO→LUMO+1 transition. Therefore, the CT excitation in green is composed of a HOMO→LUMO transition.

The absorption experiments showed two bright absorptions, one for the $D_0\delta$ unit (3.04 eV) and one (2.36 eV) for the acceptor. The calculated values are both too high in energy by about 0.35 eV (possibly due to the small basis set). However, the relative energy difference of 0.68 eV is nearly reproduced with 0.8 eV. The CT state is described to be energetically between the two bright states.

10.2.3.8 Excited State properties of $D_0\delta_+A$

The excited states for $D_0\delta_+A$ are calculated again with RI-CC2/def2-SVP. The first ten vertical excitations are presented in Tab. 10.9. There, four relevant excitations can be identified, resembling the local excitations on the acceptor unit (AS_1 with 2.81 eV, in blue), the two local excitations on the $D_0\delta_+$ unit (DS_1 with 2.75 eV in orange and DS_2 with 3.77 eV in red) and the charge transfer state (CT_1 with 2.99 eV in green). The excitations on the $D_0\delta_+$ unit correspond to the excitations on the single moiety, but are slightly energetically higher compared to the RI-CC2/def2-TZVP results. But, the relative energy difference of these two states is nearly identical with 1.02 eV versus the experimental 0.99 eV.

The excitation energy for the acceptor is identical to the one for $D_0\delta A$, indicating again a negligible excitonic coupling between both moieties for the ground state structure. The MO contributions, on the other hand, show a negligible mixing of the MO contributions between DS_1 und AS_1. Furthermore, the calculations show a significant change in the oscillator strength for DS_1 and AS_1: DS_1 gains oscillator strength while AS_1 loses it. However, RI-ADC(2)/def2-SVP calculations predict the AS_1 state to be lower in energy than the DS_1 state and therefore gaining the oscillator strength in this case. This might be an effect of the too small basis, which

Table 10.9: First ten excited states of $D_0\delta_+A$ calculated by CC2/def2-SVP. Together with the energy and the oscillator strength are the two highest MO contributions and the character of the excitation shown. The relevant excitations are colored accordingly to Fig. 10.16

State	Excitation Energy [eV]	f_{osc}	MO contributions		Character	location
1 (DS_1)	2.748	2.46	H→L+1	(74.0%)	$\pi \rightarrow \pi^*$	D→D
			H-2→L	(16.3%)		
2 (AS_1)	2.811	0.22	H-2→L	(79.7%)	$\pi \rightarrow \pi^*$	A→A
			H→L+1	(15.9%)		
3 (CT_1)	2.986	0.00	H →L	(90.3%)	$\pi \rightarrow \pi^*$	D→A
			H-1→L	(7.9%)		
4	3.554	0.01	H-1→L	(69.0%)	$\pi \rightarrow \pi^*$	D→A
			H-13→L	(16.0%)		A→A
5	3.645	0.00	H-1→L	(40.0%)	$\pi \rightarrow \pi^*$	D→A
			H-13→L	(26.7%)		A→A
6	3.667	0.00	H-13→L	(43.0%)	$\pi \rightarrow \pi^*$	A→A
			H-1→L	(26.4%)		D→A
7	3.699	0.00	H-23→L	(71.6%)	$n \rightarrow \pi^*$	A→A
			H-23→L+2	(10.8%)		
8	3.706	0.00	H-22→L	(71.3%)	$n \rightarrow \pi^*$	A→A
			H-22→L+2	(11.1%)		
9 (DS_2)	3.774	1.25	H→L+4	(80.4%)	$\pi \rightarrow \pi^*$	D→D
			H-3→L+1	(3.4%)		
10	3.899	0.02	H-14→L	(62.6%)	$\pi \rightarrow \pi^*$	A→A
			H-2→L+7	(14.1%)		

predicts both states to be too close in energy and therefore a mixing of the orbital contributions is seen. Therefore, in this molecular arrangement donor and acceptor form a J-aggregate as the energetically lowest state gains in intensity. Also, the calculated absolute excitation energies are too high compared to the experiments, but the relative energies again fit to the absorption experiments.

10.2.3.9 DFT Benchmark

Further investigation of the DA system involves geometry optimizations of excited states. This is not achievable on modern computer clusters in a reasonable amount of time for high-level *ab inito* methods. Hence, a method that is capable – at least to a certain degree – to reproduce the results of the reference method needs to be employed. In this work, the working approach is TDDFT and the reference method was chosen to be RI-CC2/def2-SVP and the aim of this method benchmark is to reproduce the relative energy differences of the relevant vertical excitations.

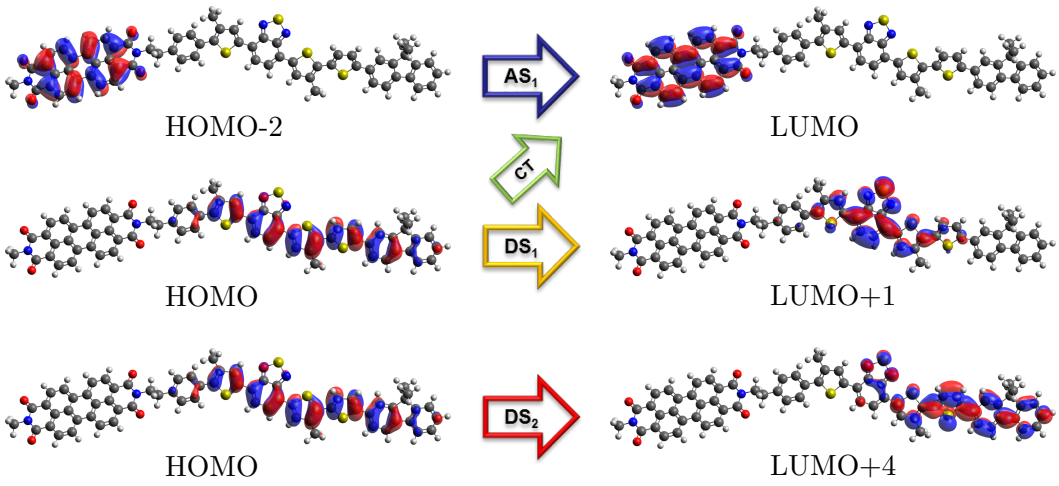

Figure 10.16: Illustration of the $D_0\delta_+A$ excitations. The local acceptor excitation AS_1 in blue is mainly composed of a HOMO-2→LUMO transition, the donor excitation DS_1 in orange is mainly composed of a HOMO→LUMO+1 transition and the DS_2 excitation in red is mainly composed of a HOMO→LUMO+4 transition. Therefore, the CT excitation in green is composed of a HOMO→LUMO transition.

Fig. 10.17 gives an overview over the results for the relevant states for the tested functionals. Additionally, the CIS and the RI-ADC(2)/def2-SVP results are plotted. If not stated differently the basis set def2-TZVP is used.

The local transitions are described rather well by most of the DFT functionals and by CIS – at least for the relative energy differences. However, the tested functionals and CIS do not show the same mixing of the AS_1 and DS_1 MO contributions, as their energy levels are more separated. A mixing of the DS_1 and DS_2 states is not found. B3LYP and CIS stick out by describing all states too low (B3LYP) or too high (CIS) in energy, while the other functionals describe them to be in roughly the same energy range.

As expected, the description of the CT state is problematic for DFT due to the ET-SI error (see section 3.3.2). This can be corrected to some extent by including more HF exchange. The functional B3LYP and the CIS method in a sense represent the two limits of HF exchange in this benchmark, with 20 % and 100 % HF-exchange. Therefore, the CT state description is shifted to very low (B3LYP) or very high (CIS) energies and the right balance needs to be found. Increasing the HF exchange from 20 % (B3LYP) to 50 % (BHLYP) shifts the CT state in the range of the DS_1 state and the local excitations in the same energy range as for the reference. But the CT state is still lower than the AS_1 state. The

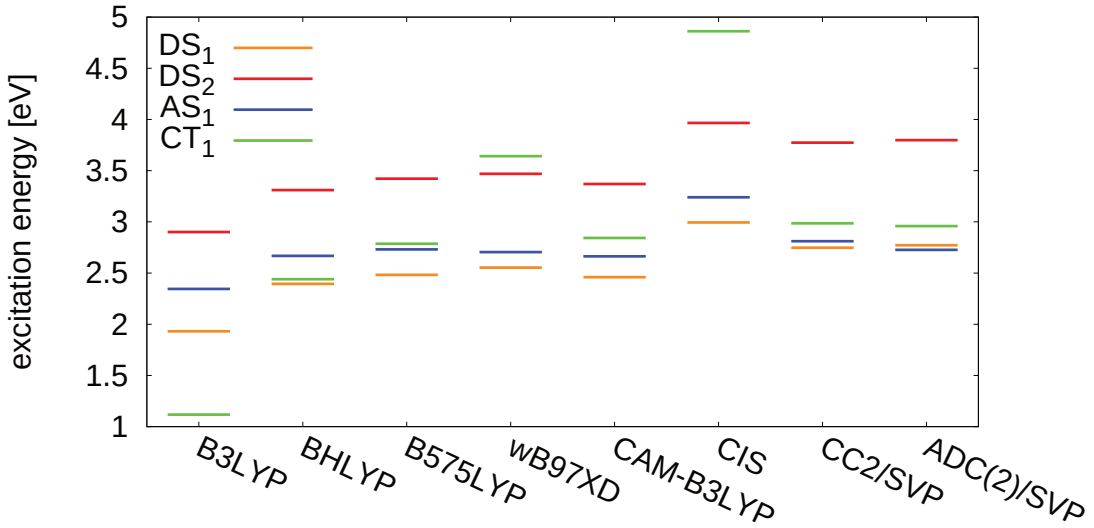

Figure 10.17: Comparison of the excitation energies for $D_0\delta_+A$ with various methods for the four relevant excited states.

specially adjusted functional B575LYP by J. Wenzel et al.[119] as it was used for the description of the first generation system with 57.5 %[119] HF exchange shifts the CT state slightly above the acceptor state. However, the energy difference between AS_1 and DS_1 is described to be too large.

A slightly better description is found for ωB97XD and CAM-B3LYP. These two functionals are also hybrid functionals incorporating HF-exchange as the other functionals, but additionally include a long-range correction to account for the ET-SI error. ωB97XD additionally includes the second empirical dispersion correction from Grimme.[52] While ωB97XD describes the energy difference between DS_1 and AS_1 to be slightly less than CAM-B3LYP, the CT state is calculated to be even higher than the DS_2 state. However, CAM-B3LYP sets the CT state similar to the reference calculations between AS_1 and DS_2. CAM-B3LYP and ωB97XD are examined further.

Tab. 10.10 presents an overview of the first vertically excited states for $D_0\delta_+A$ with the ωB97XD and CAM-B3LYP functionals. Both functionals predict the four relevant states to be the first four excited states. The relative energy difference between DS_1 and DS_2 is calculated to be equal for these, while the AS_1 state is separated a bit further from the DS_1 state for ωB97XD. And, as already mentioned above, the CT state is described differently by these two functionals. Since the orbital contributions get quite complicated, only the location of the excitation is given to keep the table as simple as possible.

Table 10.10: Results for $D_0\delta_+A$ for DFT functionals ωB97XD/def2-TZVP (a) and CAM-B3LYP/def2-TZVP (b). Only the location of the excitation and not the MO contributions are given.

(a) ωB97XD/def2-TZVP

State	E_x [eV]	f_{osc}	location
1	2.55	1.84	D→D
2	2.70	0.58	A→A
3	3.47	0.58	D→D
4	3.62	0.00	D→A
5	3.78	0.00	A→A
6	3.84	0.70	D→D
7	3.96	0.00	A→A
8	4.00	0.06	A→A
9	4.09	0.00	A→A
10	4.12	0.00	A→A

(b) CAM-B3LYP/def2-TZVP

State	E_x [eV]	f_{osc}	location
1	2.46	1.69	D→D
2	2.66	0.66	A→A
3	2.84	0.00	D→A
4	3.37	0.48	D→D
5	3.51	0.00	D→A
6	3.62	0.45	D→D
7	3.74	0.00	A→A
8	3.92	0.00	A→A
9	3.98	0.05	A→A
10	4.06	0.12	D→D

Furthermore, both functionals show a problem regarding the second donor state. An additional bright donor state, comparable to DS_2, appears with similar MO contributions. As only 10 states could be calculated for the CC2 reference (due to the large computational effort), it is not clear if this state is an artifact of the DFT calculations – it appears for all tested functionals separated by 0.3 eV to 0.5 eV to DS_1 – or is really present. In the following calculations, the lowest of these two bright states is always taken as the DS_2 state.

Based on these results, the CAM-B3LYP functional is chosen for the calculation of the excitation energies on the optimized excited state geometries. The optimizations themselves are done with the ωB987XD functional to account for empiric dispersion correction.

10.2.3.10 Mechanism of the Charge Separation

In order to study and confirm the proposed mechanism of the charge separation for the two donor variants, state specific excited state geometry optimizations are performed for the molecules $D_0\delta A$ and $D_0\delta_+A$. The optimizations are done again in vacuum. However, the relative state energies for the relevant state specific optimized geometries do not give a reasonable agreement with the experimentally observed photochemical pathway. To be more specific, for the $D_0\delta_+A$ variant, experimentally the DS_1 state is a precursor to the CT state, but the results in vacuum show that from the DS_1 state, no further state – except for the ground state

– is accessible. Therefore, using the excited state optimized structures, the excited state calculations are done with an implicit solvent description of chloroform by the COSMO method employing a solvent cavity equilibrated to the ground state charge distribution. Since the ORCA 3.0 package is only capable of employing the TDA[136] for hybrid functionals, the energies slightly differ from previously presented results in the DFT benchmark.

From the calculations in chloroform, the following photochemical scenario can be deduced. Note, though, that the following presented sketches give no information about actual state crossings.

Upon photo-excitation of the donor-moiety in $D_1\delta A$, the excitation energy is transferred via EET from the donor-unit to the acceptor unit. This is followed by the formation of the charge transfer state, before the charges recombine.

This transfer pathway is compatible with the calculated energetics for the δ-substituted system $D_0\delta A$ in Fig. 10.18(a). From the calculated energetics one can deduce that excitonic mixing between the AS_1 and DS_1 states occurs near the optimized geometry of the DS_1 state and two excitonic coupled states (ES_1 and ES_2) are obtained. After relaxation into the AS_1 state, the CT_1 state is formed. The ES_1 state shows a mixture of approximately 60 % DS_1 transition and 40 % AS_1 transition, whereas the mixing for ES_2 is interchanged. The pathway is very similar to that of the first generation system found in chloroform. The transfer rates are ignored for now, as the presented electronic structure energetics cannot give further insights into the dynamics.

A first analysis regarding the influence of the chemical design on the photophysics was done by comparing the results of $D_1\delta_+A$ with $D_1\delta A$. The fluorescence spectrum is strongly red shifted for $D_1\delta_+$ compared to $D_1\delta$ resulting in a lacking overlap with the absorption spectrum of the acceptor. As a consequence a direct charge transfer state is observed after initial excitation of the donor unit.

In full agreement with the reaction scenario derived from the experiments, the DS_2 is initially excited, followed by a subsequent transfer to the DS_1 state. From there the CT_1 state is formed directly. Due to the fast subsequent transfer from the DS_2 to the DS_1 state, no excitonic coupled states for the donor and the acceptor

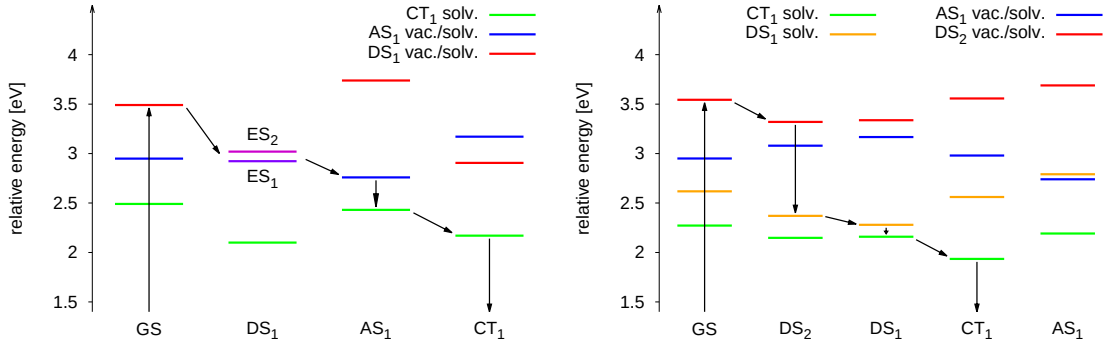

(a) $D_0\delta A$ **(b)** $D_0\delta_+ A$

Figure 10.18: Illustration of possible photochemical pathways for the $D_0\delta A$ and $D_0\delta_+ A$ species, obtained from geometry optimizations for the respective electronic states. Relative energies are reported for a series of equilibrium structures for the respective state, shown along the x axis (GS refers to the ground state equilibrium structure). All energies refer to chloroform solvent. (a) Excitonic coupling between the DS_1 and AS_1 states (ES_1 and ES_2) is observed at the DS_1 equilibrated geometry. (b) In the relaxed AS_1 structure a excitonic coupled state is found, but not reached upon excitation of the DS_1 state.

are found during the pathway. However, the optimized geometry for AS_1 reveals excitonic coupled states for DS_1 and AS_1 but is not reached.

10.2.3.11 Influence of δ_- and the Length of the Donor Moieties

As the pump-probe experiments reported in section 10.2.1 have shown, the addition of the δ_- group only influences the charge recombination times. Hence, the quantum chemical results for the excitations of the relevant excited states for eight variants of the dyad system are compared to each other to investigate the influence of the δ_- group. Variants with two donor lengths taking the values $n = 0, 1$ combined either with the δ or the δ_+ group and optionally extended with the δ_- group, resulting in eight ($2 \times 2 \times 2$) possible combinations.

The calculations are done at the ground-state optimized structure and include an implicit solvent description by the COSMO method, using a solvent cavity equilibrated to the ground state charge distribution. In Fig 10.19 both the results for vacuum and the solvated molecules are included. As mentioned above, the ORCA 3.0 package is only capable of employing the TDA for hybrid functionals, hence, the energies presented there differ slightly from previously presented results in the DFT benchmark. The results in vacuum presented in the Fig. 10.19 are obtained with the setup excluding solvent effects.

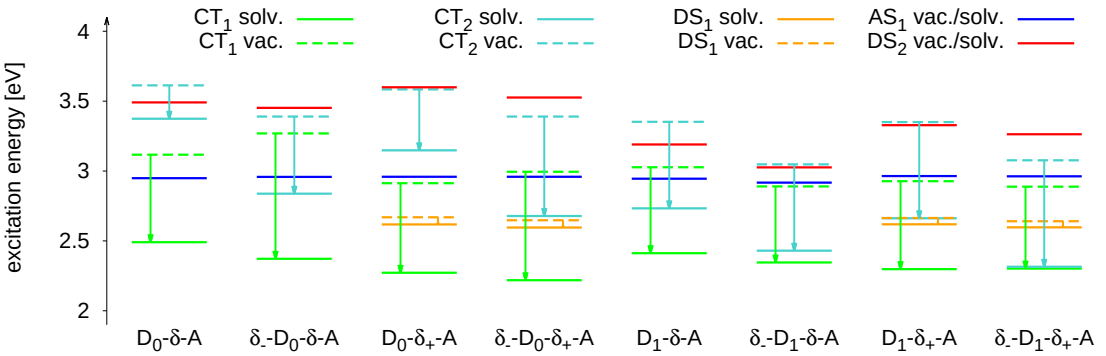

Figure 10.19: Excitation energies in vacuum and chloroform, obtained using the COSMO solvent model in conjunction with TD-DFT using the CAM-B3LYP functional. For each of the five relevant electronic states and all dyad species indicated along the abscissa, vacuum (vac) energies are indicated along with the corresponding shifted energies for the solvated species (solv.) immersed in a solvent cavity equilibrated to the ground state charge distribution. Note that the shift is negligible for AS_1 and DS_2 (<0.1 eV) such that a single entry is given for these states.

In a simplified manner one can say that the acceptor is slightly shifted higher in energy due to the TDA. This means that the DS_2 and AS_1 states are falsely described to be closer in energy. Note that the energy differences compared to the experimental results below represent the full TDDFT results in vacuum.

Fig. 10.19 presents the vertical excitation energies for the relevant excitations for the eight variants. The first aspect to notice is that an additional CT_2 state appears in the relevant energy range. This is essentially the case for the D_1 and δ_- variants, where the CT_2 state is lowered in energy. In the case of $\delta\_D_1\delta A$ and $\delta\_D_1\delta_+A$, the state even gets very close to the CT_1 state in the calculations including a solvent. Therefore, this state could play a role in the CT recombination: e.g. a superposition of CT_1 and CT_2 could stabilize the CT state. In the other variants the role of the CT_2 state is negligible.

Since the orbital contributions for some excitations are more complicated, the corresponding electron-hole densities are presented for the variant $\delta\_D_1\delta_+A$ in Fig. 10.20. The lowest local excitation AS_1 and DS_1 are equivalent to the excitations for $D_0\delta_+A$ shown in Fig. 10.16. For $D_1\delta_+A$ the DS_1 and AS_1 states show a relative energy difference of 0.5 eV. This is close to the experimental value of ∼0.56 eV. The experimental value for $\delta\_D_1\delta_+A$ is not available, but the calculations suggest an even smaller energy gap of 0.4 eV between these two state. The densities for the DS_2 excitation, however, differ. While for the $D_0\delta_+A$ variant the hole is spread almost over the complete $D_0\delta_+$ moiety, here, the hole density is only located on the

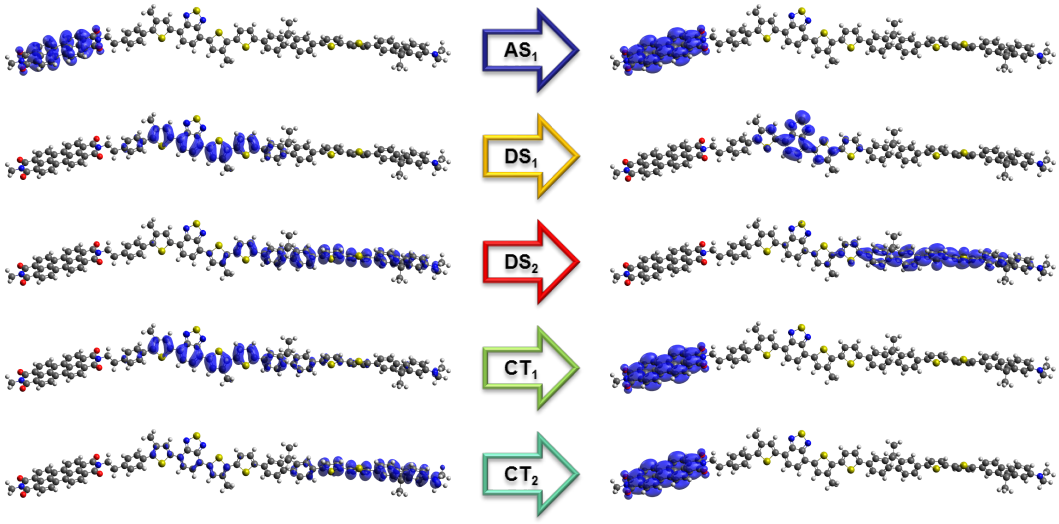

Figure 10.20: Illustration of the electron (right panel) and hole (left) densities for the five corresponding states shown in Fig. 10.19. The densities have been computed using a method which corresponds to the orbital transitions of the excitation using the amplitudes as weights as it is implemented in the MultiWfn-package[133] using the vacuum calculations as a basis.

D_1 unit. Consequently the excitations show a somewhat *local* character – although the $D_1\delta_+$ unit exhibits a delocalized π-system. The two charge transfer states CT_1 and CT_2 correspond to these two donor states. The hole-density for CT_1 is therefore equivalent to the hole density for DS_1 and analogously for CT_2 and DS_2.

The effect of the δ_-group is to pull the positive charge – i.e., the hole – spatially further apart from the negative charge, the electron, on the acceptor. Therefore the electron-hole distance R_{CC} is analyzed for the CT states. Since the electron and hole are delocalized over a certain range over the donor and acceptor, the distance is calculated using centroids of the electron and hole densities. As a measure of the electron and hole densities, several *ansaetze*, like Mulliken[149,150] or ESP charges[151,152] can be used.

In this work, the centroids of the above calculated electron and hole densities are chosen to be the measure of choice. Tab. 10.11 presents the calculated distances for the electron and hole densities, together with the radii (RMSD) of the densities, which are also calculated by the MultiWfn-package. The results show that the donor length and the δ_-group both increase the distance R_{CC}. The effect, however, is bigger for the δ_-group, resulting in an increase of at least 3.0 Å and a maximum increase of 6.0 Å for (δ_)$D_1\delta$A.

Table 10.11: For the various combinations of donor/acceptor moieties, (i) electron-hole centroid distance R_{CC}, in the lowest energy CT_1 state, along with (ii) radii of electron (r^-) and hole (r^+) densities are shown.

Structure	Distance R_{CC} [nm]	r^+ [nm]	r^- [nm]
$D_0\delta A$	2.0	0.6	0.4
$D_1\delta A$	2.3	0.8	0.4
$D_0\delta_+ A$	2.0	0.6	0.4
$D_1\delta_+ A$	2.2	0.7	0.4
$\delta\_D_0\delta A$	2.3	0.7	0.4
$\delta\_D_1\delta A$	2.9	1.0	0.4
$\delta\_D_0\delta_+ A$	2.3	0.7	0.4
$\delta\_D_1\delta_+ A$	2.5	0.9	0.4

The increase of the electron-hole distance can be completely related to the spatially more delocalized densities of the hole. The radii of the densities grow proportional to the increase of the distance, or in other words the density is pulled towards the δ_- group. In the case of the longer donor units the effect is smaller for the δ_+-variant and the spatial stretch is reduced. The electron density on the acceptor is completely unchanged by the δ_- group as the radii of the densities show, underlining the separation of the systems by the ethylene bridge.

Furthermore, the CT_2 state shows a very large increase of R_{CC} of about 20 Å with respect to the CT_1 state. At this point the role of the CT_2 state is still unclear and further analysis towards this is presented in the next section.

The spectroscopic picture of the photochemical process for $\delta\_D_0\delta_+A$ is equivalent to the one presented for $D_0\delta_+A$. This fits to the experimental results, where mainly the recombination time is effected by the addition of the δ_- unit. The main change in the electronic structure results is that the CT_2 state is lowered in energy compared to $D_0\delta_+A$, but is still too high in energy to play a more important role in the charge separation.

10.2.4 Analysis of the Charge Formation and Charge Recombination times.

The experimental and quantum chemical results can be summarized in five points: (i) The δ-variants exhibits an ultrafast (<1.0 ps) energy transfer to the acceptor, followed by the CT formation on a ∼10 ps time scale. The results are comparable to those of the first generation system. The QC results are in line and show three

relevant states being important for the photochemical process and agree to the experimental results

(ii) The δ_+-variants on the other hand does not have an initial energy transfer to the acceptor, but shows a significantly slower electron transfer in ∼100 ps directly from the donor unit. In contrast to the δ-variants, here, QC results indicate four relevant states which are involved in the photochemical process and are able to describe the results.

(iii) For both spacer molecules (δ or δ_+) the CT lifetimes are increased up to a 5-fold upon adding the terminal amine group δ_-. An optimal donor length of $n = 1$ is found accordingly in chloroform and possibly other solvents, but the experimental results are limited to lifetimes around 3 ns and cannot be measured accurately.

(iv) Electronic structure modeling gives evidence for a stabilizing effect of the CT_2 state by the δ_--group. This CT state is characterized by a much larger charge separation. Due the solvent influence both CT states may become nearly degenerate, in particular for $n = 1$, such that an effectively larger charge separation is suggested for variants incorporating δ_-D_1.

(v) As pointed out in section 10.1.1, solvent polarity (from chloroform to toluene) slows down the CT state recombination by up to one order of magnitude. CT formation is affected to a lesser extend by a factor of 2 or 3 at most.

10.2.4.1 Marcus-Jortner-Levich-Analysis

For a more detailed analysis of the observed influence of the molecular structure and solvent polarity on the charge transfer state formation and recombination times, the Marcus-Jortner-Levich (MLJ) theory for electron transfer (as introduced in section 5.2) is used. In contrast to the *classical* Marcus theory, this modified version is not restricted to the high-temperature regime and allows the inclusion of internal vibrations. Eqn. 10.6 recalls the MLJ formula presented above,

$$k_{ET}^{MLJ} = \frac{2\pi}{\hbar} \frac{|V_{DA}|^2}{\sqrt{4\pi\lambda_{sol}k_BT}} \sum_{n=0}^{\infty} \frac{\left(\frac{\lambda_{mol}}{E_{vib}}\right)^n}{n!} \exp\left(-\frac{\lambda_{mol}}{E_{vib}}\right) \cdot \cdot \exp\left(-\frac{\left(\Delta G^0 + \lambda_{sol} + nE_{vib}\right)^2}{4\lambda_{sol}k_BT}\right) \tag{10.6}$$

where V_{DA} is the electronic coupling (transfer integral) between the donor and acceptor states, T is the temperature and k_B is the Boltzmann constant. λ_{mol} represents the intra-molecular reorganization energy and is computed via the geometry optimizations in the relevant states presented above. E_{vib} represents the energy of an effective, high-frequency vibrational mode and is set to $1500\,\mathrm{cm}^{-1}$ ($0.186\,\mathrm{eV}$) corresponding to a characteristic C=C bond stretching. λ_{sol} is the solvent reorganization energy and is estimated by the Born-Hush approach[88] for the different solvents:

$$\lambda = \frac{e^2}{4\pi\epsilon_0}\left(\frac{1}{2r_{\mathrm{D}^+}} + \frac{1}{2r_{\mathrm{A}^-}} - \frac{1}{R_{\mathrm{DA}}}\right)\left(\frac{1}{n^2} + \frac{1}{\epsilon}\right), \tag{10.7}$$

Here, n represents the refractive index and ϵ the dielectric constant of the solvent. The values for R_{CC}, r^+ and r^- are taken from Tab. 10.11.

The Gibbs free energies for the charge separation (ΔG^0_{CS}) and charge recombination (ΔG^0_{CR}) are calculated with the help of continuum dielectric theory,[153]

$$\begin{aligned}\Delta G^0_{CS} = &\left[E_{ox}(D) - E_{red}(A)\right] - \frac{e^2}{4\pi\epsilon_0\epsilon R_{CC}} \\ &+ \frac{e^2}{8\pi\epsilon_0}\left(\frac{1}{r^+} + \frac{1}{r^-}\frac{1}{\epsilon_{ref}} - \frac{1}{\epsilon}\right) - E_{00}\end{aligned} \tag{10.8}$$

$$\begin{aligned}\Delta G^0_{CR} = &-\left[E_{ox}(D) - E_{red}(A)\right] - \frac{e^2}{4\pi\epsilon_0\epsilon R_{CC}} \\ &+ \frac{e^2}{8\pi\epsilon_0}\left(\frac{1}{r^+} + \frac{1}{r^-}\frac{1}{\epsilon_{ref}} - \frac{1}{\epsilon}\right)\end{aligned} \tag{10.9}$$

where E_{ox} and E_{red} are the experimentally determined oxidation and reduction potential energies. $\epsilon_{ref} = 8.93$ is the dielectric constant of dichloromethane,[154] in which the potentials were measured.[130] E_{00} refers to the energy of the excited state from which the charge transfer state is formed. In the case of the δ-variant, the CT state is formed from the acceptor state A* and in the case of the δ_+-variant it is formed from $(\mathrm{D}_n\delta_+)^*$ (also see above).

Tabs. 10.12 and 10.13 summarize all further parameters appearing in Eqns. 10.6 to 10.9 for various solvents and molecules, along with the computed solvent reorganizations and Gibbs free energies.

The first aspect to note is that the charge recombination takes place in the so-called Marcus inverted regime as $-\Delta G^0_{CR} > \lambda_{CR} = \lambda_{mol} + \lambda_{sol}$. While the CT formation in $\delta\_\mathrm{D}_n\delta_+\mathrm{A}$ and $\mathrm{D}_n\delta_+\mathrm{A}$ takes place in the normal Marcus regime, for $\delta\_\mathrm{D}_n\delta\mathrm{A}$

Table 10.12: First part of the parameters for the MLJ model. E_{red} and E_{ox} are the reduction and oxidation potential energies determined experimentally.[130] E_{00} is the lowest excited state, from which the CT states are formed. λ_{mol} is the computed reorganization energy for charge separation and recombination.

Parameter	$D_1\delta A$	$D_1\delta_+ A$	$\delta\_D_1\delta_+ A$
E_{red} (eV)	−0.40	−0.40	−0.40
E_{ox} (eV)	0.80	0.89	0.81
E_{red} (eV)	2.32	1.92	1.92
λ_{mol}^{CS} (eV)	0.33	0.30	0.28
λ_{mol}^{CR} (eV)	0.57	0.68	0.69

and $D_n\delta A$ it is in the (nearly) optimal Marcus regime with a difference of $-\Delta G_{CS}^0$ and λ_{CS} being less than 0.06 meV. From this one can conclude that a change in solvent polarity should have a stronger influence on the charge recombination than on the charge formation times. This fits very well to the observed results (see Tab. 10.2) as the solvent influence is indeed significantly stronger for the charge recombination. As the refractive index is nearly identical for all three solvents, one can infer that the main solvent influence comes from the dielectric constant.

Furthermore, using the experimentally observed electron transfer rates for k, one can exploit Eqn. 10.6 to calculate an approximate electronic coupling. The results predict a residual solvent dependence of the electronic coupling V_{DA}, which may be expected due to e.g. solvent-induced electrostatic interaction shielding.[155,156]However, the accuracy of the model is uncertain, as the approximation made for λ_{sol} is very crude and would require an accurate description like explicit molecular-based (rather than an implicit continuum-based) modeling of the solvent.[157]

The computed electronic coupling energies V_{DA} are rather small, in the range of 0.3 meV to 2.0 meV, in accordance with electronic couplings for similar dyad compounds like the first generation system[28,123] and electronic couplings obtained by a similar approach for different large organic donor and acceptor compounds.[131] Interestingly, the faster charge separation in the δ variants appears to be a result of a 2 to 3-fold stronger "hole" coupling between A^* and the CT state, compared to $(D_1\delta_+)^*$ and the CT state.[28,123]

Regarding the molecular design it is very interesting to compare the results for $D\delta A/\delta\_D_1\delta A$ and $D_1\delta_+ A/\delta\_D_1\delta_+ A$ in chloroform. As seen in Tab. 10.2 the addition of $\delta\_$ to $D_1\delta_+ A$ leads to a nearly 3-fold increase in the CT state lifetime.

Table 10.13: Second part of the parameters for the MLJ model.Estimated solvent reorganization energies λ_{sol} and Gibbs free energies using Eqns. 10.7 to 10.9 for charge separation ΔG^0_{CS} and charge recombination ΔG^0_{CR}.

Molecule	Parameter	Toluene	TCE	Chloroform
	ϵ	3.5	3.42	4.89
	n	1.496	1.477	1.446
$D_1\delta A$	λ_{sol} (eV)	0.333	0.344	0.568
	$-\Delta G^0_{CS}$ (eV)	0.739	0.725	0.907
	$\lambda_{CS} = \lambda_{mol} + \lambda_{sol}$ (eV)	0.663	0.674	0.898
	$-\Delta G^0_{CR}$ (eV)	1.580	1.594	1.412
	$\lambda_{CR} = \lambda_{mol} + \lambda_{sol}$ (eV)	0.903	0.914	1.138
$D_1\delta_+A$	λ_{sol} (eV)	0.349	0.360	0.595
	$-\Delta G^0_{CS}$ (eV)	0.323	0.309	0.500
	$\lambda_{CS} = \lambda_{mol} + \lambda_{sol}$ (eV)	0.649	0.660	0.895
	$-\Delta G^0_{CR}$ (eV)	1.594	1.609	1.418
	$\lambda_{CR} = \lambda_{mol} + \lambda_{sol}$ (eV)	1.029	1.040	1.275
$\delta\_D_1\delta_+A$	λ_{sol} (eV)			0.554
	$-\Delta G^0_{CS}$ (eV)			0.585
	$\lambda_{CS} = \lambda_{mol} + \lambda_{sol}$ (eV)			0.834
	$-\Delta G^0_{CR}$ (eV)			1.333
	$\lambda_{CR} = \lambda_{mol} + \lambda_{sol}$ (eV)			1.244

Using Eqn. 10.9 this can be related to a reduction by a factor of 1.7 in the approximated electron coupling V_{DA} (Tab. 10.14).

As the electronic couplings in these systems tend to be rather weak, $|V_{DA}|^2$ can be taken taken to be exponentially dependent on the distance between electron and hole (R_{CC}):[158]

$$|V_{DA}|^2 = |V^0_{DA}|^2 \exp\left(-\beta R_{CC}\right) \tag{10.10}$$

Typical values for the decay length scale β have been reported to be in the range of $\beta \sim 0.3\,\text{Å}^{-1}$ to $0.7\,\text{Å}^{-1}$ for electron transfer trough covalent bonds or involving carrier tunneling in organic molecules.[158–161]

As shown in Tab. 10.11 the electronic structure results predict that the addition of the $\delta\_$ group to $D_1\delta A$ increases the electron-hole distance by 3 Å in the CT_1 state. For the CT_2 state the increase results in as much as 18 Å. Using the 1.75-fold decrease of V_{DA}, this would correspond in a rather small β value of $0.34\,\text{Å}^{-1}$ for CT_1 and an unrealistic, even smaller value of $0.06\,\text{Å}^{-1}$ for CT_2. Therefore one can

Table 10.14: Electronic couplings for charge recombination and formation, calculated via Eqn. 10.6 by using the experimental rates in Tab. 10.2.

V (meV)		Toluene	TCE	Chloroform
$D_1\delta A$	Formation	1.783	2.385	2.392
	Recombination	0.313	0.376	0.535
$D_1\delta_+A$	Formation	0.682	0.975	1.381
	Recombination	0.236	0.343	0.495
$\delta\_D_1\delta_+A$	Formation			0.886
	Recombination			0.306

conclude that the experimental observed CT state is essentially of CT_1 character, which is possibly slightly mixed with a CT_2 character due to the near-degeneracy with the CT_2 state for $\delta\_D_1\delta_+A$.

10.3 Conclusion and Outlook

This part of the thesis has focused on two generations of novel class of covalently bound bisthiophene-perylene diimide donor-acceptor systems that have been designed and spectroscopically investigated by our collaboration partners at Strasbourg University. In view of the lack of efficiency of the first generation material (see section 10.1.1), a second-generation material has been developed, whose photochemical properties have been thoroughly characterized by electronic structure methods and kinetic analysis. The combined experimental and theoretical results lead to a plausible picture of the photochemical pathway, along with estimated rates for charge separation and charge recombination.

The first generation material exhibits a two-step charge transfer formation in solution, via (i) excitation energy transfer by excitonically coupled donor and acceptor states from the donor to the acceptor, followed by (ii) charge separation between the covalently bound donor and acceptor moieties.[115,116] Quantum chemical results employing an implicit solvent description confirmed this photochemical pathway involving basically three relevant states.[119]

For the self-assembled phase in a liquid crystalline (LC) film, the system showed an ultrafast ($\sim$60 fs) charge transfer formation directly after initial excitation. Electronic structure analysis and high-dimensional quantum dynamical studies lead to the conclusion that the ultrafast charge transfer formation is the consequence of the generation of an inter-molecular charge separated (CS) state. This charge sepa-

rated state, whose generation is favored by a tilt angle of 70° between the molecular planes, proves to be very stable compared to longer-range charge separated states, resulting from a Coulomb barrier and small transfer integrals. A quasi-stationary state of the local CS(-1) state is therefore reached, precluding a rapid formation of a photocurrent.[28,123] A comparatively short recombination time of ∼50 ps, as well as triplet formation on longer time scales (>1 ns), are observed. The applicability of the material in a photovoltaic device is therefore severely limited.

To circumvent local trapping and recombination while keeping the high charge generation efficiency, a second generation material was designed. The concept was to to increase the CT lifetime, i.e., reduce recombination. To this end, a first investigation was carried out in solution phase, by a joint spectroscopic and theoretical analysis. For the systems investigated here, the CT lifetime could indeed be increased up to 10-fold as compared to the first generation. Overall, the kinetic is comparatively slow, of the order of tens to hundreds of picoseconds.

Analysis with the aid of the Marcus-Jortner-Levich (MJL) formula proved the small electronic couplings to be the main reason for relatively slow CT recombination times and therefore a long lifetime. Previous experiments on a family of similar compounds, where donor and acceptor moieties are connected by an alkyl spacer of increasing length, support this conclusion.[162] Here, an additional amine (δ_)-group is shown to further reduce the electronic coupling and thus further enlarge the CT lifetime by a factor of 2 to 5 for an optimal donor length of ($n = 1$). Most likely this is given by an increase of the electron-hole distance in the charge transfer state. Electronic structure calculations show a slight increase for the lower-lying CT_1 state and a possible mixing with a different CT_2 state, showing a much larger electron-hole separation. However, the MLJ analysis does not confirm this. Interestingly, changing the donor length for variants without the terminal δ_ does not influence the charge separation or recombination kinetics, which is in agreement with other reports.[163]

Furthermore, the influence of the solvent polarity on the CT lifetime proves that the interaction with the environment is of key importance. Together with the observation for the previous generation materials, one may expect that in a self-assembled film of these compounds the inter-molecular interaction may strongly modify the conclusions drawn here. This suggests that tailoring the intrinsic

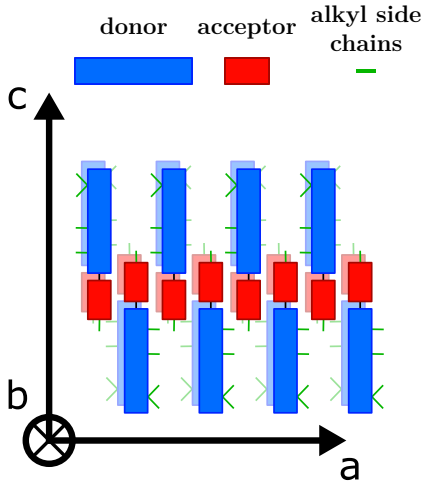

Figure 10.21: Illustration of the zipper-like molecular packing of $D_0\delta_+A$ dyads. Acceptor molecules are π-stacked along the b axis and donor molecules are flipped. The molecules are not laying perfectly on top of each other, but are slightly shifted.

building blocks should only be seen as one of the relevant building blocks in the design process of optimizing the CT lifetime in functional films.

Recently, as detailed in Ref. [164, 165], it was shown by electron diffraction and X-ray scattering methods that the second generation materials form highly ordered lamellar mesophases that feature well-defined donor and acceptor domains, where the acceptors are interlaced such that a zipper-like structure is formed.[165,166]

As illustrated in Figs. 10.21 and 10.22, the DA system is arranged in an alternating stacking pattern. While the acceptors are in close contact with each other in two dimensions (along a and b), the donors can only interact along the stacking direction (b axis) due to the alternating pattern caused by the hexyl-side chains.

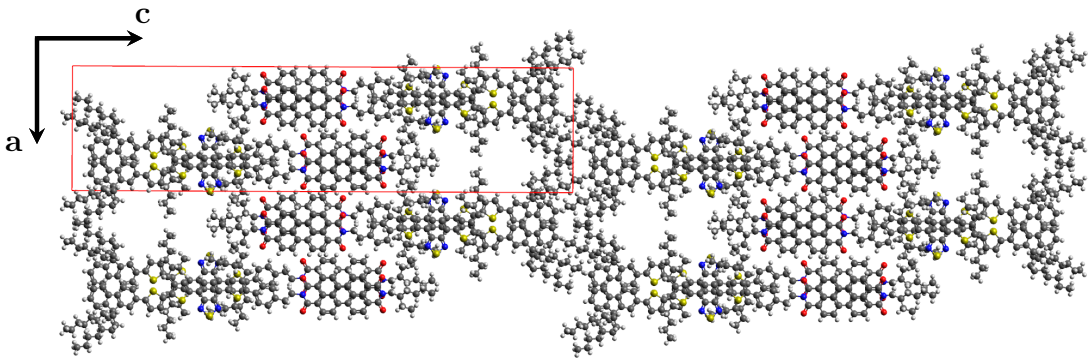

Figure 10.22: Full atomistic representation of the $D_0\delta_+A$ dyads in LC film with highlighted unit cell.

Thus, the acceptor molecules are π-stacked on top of each other, creating possible "quantum wells" for charge carrier transport. The analysis of the photochemical properties of these mesoscopic phases, as done for the first generation system, is currently ongoing.

In particular, based on the spectroscopic and electronic structure results and the MLJ analysis presented above, a theoretical analysis of the charge transport properties, focusing on electron and hole mobilities, is currently performed by Kinetic Monte Carlo simulations.[167,168]

11 | Conclusion and Outlook

This thesis presents methodological developments and applications in the area of high-dimensional quantum dynamics. The focus is placed upon multi-configurational methods, and applications to transfer phenomena in large systems, notably excitation energy transfer, electron transfer, and intra-molecular vibrational redistribution in molecular aggregates. On the application side, investigations combining electronic structure methods, high-dimensional quantum dynamics and parametrized model Hamiltonians are employed. Since the relevant elementary processes are often ultra-fast, this approach creates a unique tool for the real-time description and thorough understanding of these elementary steps.

In the first part, the implementation of the novel 2L-G-MCTDH method, proposed in Ref. [1], has been has been presented. This method remedies the lack of flexibility of existing GWP-based multi-configurational methods such as G-MCTDH and its vMCG variant. The key novelty in the method is the hierarchical construction of the wavefunction, similar to the multi-layer (ML)-MCTDH method. In fact, a combination of the method with the existing ML-MCTDH scheme is straightforward, as the first-layer of the 2L-G-MCTDH approach is chosen to be orthogonal.

Within the present implementation of the 2L-G-MCTDH method, excellent convergence properties and an improved scaling behavior have been demonstrated. However, numerical problems such as instabilities due to singularities, as a result of linear dependencies within the non-orthogonal GWP basis, remain to some extent. The method has been successfully applied to two model systems, showing very good agreement with reference calculations by the multi-layer (ML)-MCTDH method for up to 100 DOFs. The first system is a model of site-to-site vibrational energy flow in the presence of intra-site vibrational energy redistribution. The second system relates to a model for electron transfer at an oligothiophene-fullerene heterojunction of relevance to organic photovoltaics.

The second part addresses two generations of a novel donor-acceptor system for organic photovoltaic applications, which was designed by our partner groups (S. Méry, S. Haacke) at Strasbourg University. These systems rely on self-assembled block co-oligomer DA dyads and triads, which have been computationally investigated in

the present thesis. We have been able to show that the first generation variant (i) exhibits a highly efficient inter-chain ET process in a liquid-crystalline film, which is preferred over intra-molecular charge transfer, (ii) despite the highly efficient initial charge transfer, the material shows inefficient long-range charge separation due to large recombination rates and small transfer integrals. As a consequence, the first-generation material proves unsuitable for photovoltaics applications. To obtain a full understanding of the elementary steps, high-dimensional quantum dynamics simulations have been carried out using the ML-MCTDH method, in collaboration with Matthias Polkehn.

The present work has mainly focused on the second generation material, where both the nanomorphology and the chemical design have been modified. The goal is an increase the lifetime of the primary charge separated state (CT state), indicating reduced recombination. To this end, the second generation material is composed of a donor unit of variable length and additional electron withdrawing and donating groups. A rather slow electron transfer in the range of a tens to hundred picoseconds is observed, with an extended lifetime of the CT state. A kinetic analysis using the Marcus-Jortner-Levich rate theory is employed, revealing small electronic couplings for both charge separation and recombination processes. The addition of an amine group strongly increases the lifetime, due to an increase of the distance between the electron and hole density centroids. Therefore, a reduction of the recombination losses is expected. Indeed, this type of system proves to be a promising candidate for practical applications.

To conclude, this thesis has demonstrated (i) a major new development in the design of Gaussian-based multi-configurational methods, by the 2L-GMCTDH scheme and (ii) a combined electronic structure and high-dimensional quantum dynamics investigation of EET, ET and IVR processes. In the absence of numerically exact methods for high-dimensional molecular systems, the right choice of methods is crucial for a comprehensive study of the relevant processes, and approximations need to be introduced. In this context, the multi-configurational techniques that have been applied and implemented in this thesis play an important role. Moreover, the new hierarchical GWP based techniques bring a significant advantage since they can be used both in the context of model Hamiltonians (as shown in this thesis) and in the context of efficient and accurate on-the-fly quantum dynamics in many dimensions. Further developments in this direction are currently in progress.

Bibliography

[1] S. Römer, M. Ruckenbauer, I. Burghardt, *The Journal of Chemical Physics* **2013**, *138*, 064106.

[2] A. Chenu, G. D. Scholes, *Annual Review of Physical Chemistry* **2015**, *66*, 69.

[3] C. Deibel, T. Strobel, V. Dyakonov, *Advanced Materials* **2010**, *22*, 4097.

[4] H. Uoyama, K. Goushi, K. Shizu, H. Nomura, C. Adachi, *Nature* **2012**, *492*, 234.

[5] I. Burghardt, E. R. Bittner, H. Tamura, A. Pereverzev, J. G. S. Ramon in *Energy Transfer Dynamics in Biomaterial Systems*, (Eds.: I. Burghardt, V. May, D. A. Micha, E. R. Bittner), Springer Series in Chemical Physics 93, Springer Berlin Heidelberg, **2009**, pp. 183–212.

[6] H. Gest, *Photosynthesis Research* **2002**, *73*, 7.

[7] G. D. Scholes, *ACS Nano* **2008**, *2*, 523.

[8] J. C. Tully, *The Journal of Chemical Physics* **1990**, *93*, 1061.

[9] T. J. Martinez, M. Ben-Nun, R. D. Levine, *The Journal of Physical Chemistry* **1996**, *100*, 7884.

[10] M. Ben-Nun, T. J. Martínez in *Advances in Chemical Physics*, (Eds.: I. Prigogine, S. A. Rice), John Wiley & Sons, Inc., **2002**, pp. 439–512.

[11] A. M. Virshup, C. Punwong, T. V. Pogorelov, B. A. Lindquist, C. Ko, T. J. Martínez, *The Journal of Physical Chemistry B* **2009**, *113*, 3280.

[12] R. Martinazzo, M. Nest, P. Saalfrank, G. F. Tantardini, *The Journal of Chemical Physics* **2006**, *125*, 194102.

[13] D. V. Shalashilin, I. Burghardt, *The Journal of Chemical Physics* **2008**, *129*, 084104.

[14] I. Burghardt, H.-D. Meyer, L. S. Cederbaum, *The Journal of Chemical Physics* **1999**, *111*, 2927.

[15] I. Burghardt, M. Nest, G. A. Worth, *The Journal of Chemical Physics* **2003**, *119*, 5364.

[16] G. A. Worth, H.-D. Meyer, H. Köppel, L. S. Cederbaum, *International Reviews in Physical Chemistry* **2008**, *27*, 569.

[17] G. W. Richings, I. Polyak, K. E. Spinlove, G. A. Worth, I. Burghardt, B. Lasorne, *International Reviews in Physical Chemistry* **2015**, *34*, 269.

[18] I. Polyak, C. S. M. Allan, G. A. Worth, *The Journal of Chemical Physics* **2015**, *143*, 084121.

[19] W. Domcke, D. R. Yarkony, H. Köppel, *Conical Intersections: Electronic Structure, Dynamics and Spectroscopy*, World Scientific, **2004**, 857 pp.

[20] H. Köppel, W. Domcke, L. S. Cederbaum in *Advances in Chemical Physics*, (Eds.: I. Prigogine, S. A. Rice), John Wiley & Sons, Inc., **1984**, pp. 59–246.

[21] G. A. Worth, L. S. Cederbaum, *Annual Review of Physical Chemistry* **2004**, *55*, 127.

[22] R. Binder, J. Wahl, S. Römer, I. Burghardt, *Faraday Discussions* **2013**, *163*, 205.

[23] S. Mukamel, S. Tretiak, T. Wagersreiter, V. Chernyak, *Science* **1997**, *277*, 781.

[24] S. Karabunarliev, E. R. Bittner, *The Journal of Chemical Physics* **2003**, *118*, 4291.

[25] M. H. Beck, A. Jäckle, G. A. Worth, H. D. Meyer, *Physics Reports* **2000**, *324*, 1.

[26] H. Wang, M. Thoss, *The Journal of Chemical Physics* **2003**, *119*, 1289.

[27] I. R. Craig, M. Thoss, H. Wang, *The Journal of Chemical Physics* **2007**, *127*, 144503.

[28] M. Polkehn, P. Eisenbrandt, H. Tamura, S. Haacke, S. Méry, I. Burghardt, *Proc. SPIE*, Nanophotonics VI **2016**, *9884*, 98840O.

[29] E. Schrödinger, *Annalen der Physik* **1926**, *384*, 361.

[30] M. Born, R. Oppenheimer, *Annalen der Physik* **1927**, *389*, 457.

[31] V. May, O. Kühn, *Charge and Energy Transfer Dynamics in Molecular Systems*, John Wiley & Sons, **2011**, 777 pp.

[32] A. Szabo, N. S. Ostlund, *Modern Quantum Chemistry: Introduction to Advanced Electronic Structure Theory*, Courier Corporation, **1989**, 484 pp.

[33] H. Köppel, D. R. Yarkony, H. Barentzen, *The Jahn-Teller Effect: Fundamentals and Implications for Physics and Chemistry*, Springer Science & Business Media, **2009**, 912 pp.

[34] C. A. Mead, D. G. Truhlar, *The Journal of Chemical Physics* **1982**, *77*, 6090.

[35] H. Nakamura, D. G. Truhlar, *The Journal of Chemical Physics* **2001**, *115*, 10353.

[36] H. Choi, K. K. Baeck, T. J. Martinez, *Chemical Physics Letters* **2004**, *398*, 407.

[37] Q. Ou, J. E. Subotnik, *The Journal of Physical Chemistry C* **2013**, *117*, 19839.

[38] P. Hohenberg, W. Kohn, *Physical Review* **1964**, *136*, B864.

[39] E. Runge, E. K. U. Gross, *Physical Review Letters* **1984**, *52*, 997.

[40] C. Møller, M. S. Plesset, *Physical Review* **1934**, *46*, 618.

[41] F. Jensen, *Introduction to Computational Chemistry*, John Wiley & Sons, **2013**, 733 pp.

[42] O. Christiansen, H. Koch, P. Jørgensen, *Chemical Physics Letters* **1995**, *243*, 409.

[43] J. Schirmer, A. B. Trofimov, *The Journal of Chemical Physics* **2004**, *120*, 11449.

[44] A. Dreuw, M. Wormit, *Wiley Interdisciplinary Reviews: Computational Molecular Science* **2015**, *5*, 82.

[45] S. Grimme, *The Journal of Chemical Physics* **2003**, *118*, 9095.

[46] R. J. Bartlett, M. Musiał, *Reviews of Modern Physics* **2007**, *79*, 291.

[47] W. Kohn, L. J. Sham, *Physical Review* **1965**, *140*, A1133.

[48] P. a. M. Dirac, *Mathematical Proceedings of the Cambridge Philosophical Society* **1930**, *26*, 376.

[49] J. P. Perdew, K. Burke, M. Ernzerhof, *Physical Review Letters* **1996**, *77*, 3865.

[50] J. P. Perdew, K. Burke, M. Ernzerhof, *Physical Review Letters* **1997**, *78*, 1396.

[51] A. D. Becke, *The Journal of Chemical Physics* **1993**, *98*, 5648.

[52] S. Grimme, *The Journal of Chemical Physics* **2006**, *124*, 034108.

[53] M. E. Casida in *Recent Advances in Density Functional Methods (Part I)*, Recent Advances in Computational Chemistry, World Scientific, **1995**.

[54] A. Dreuw, M. Head-Gordon, *Chemical Reviews* **2005**, *105*, 4009.

[55] T. Yanai, D. P. Tew, N. C. Handy, *Chemical Physics Letters* **2004**, *393*, 51.

[56] J.-D. Chai, M. Head-Gordon, *Physical Chemistry Chemical Physics* **2008**, *10*, 6615.

[57] E. J. Heller, *The Journal of Chemical Physics* **1975**, *62*, 1544.

[58] E. J. Heller, *Chemical Physics Letters* **1975**, *34*, 321.

[59] P. Ehrenfest, *Zeitschrift für Physik* **1927**, *45*, 455.

[60] J. L. Alonso, J. Clemente-Gallardo, J. C. Cuchí, P. Echenique, F. Falceto, *The Journal of Chemical Physics* **2012**, *137*, 054106.

[61] E. A. M. Jr, R. E. Wyatt, *The Journal of Chemical Physics* **1969**, *51*, 1253.

[62] E. A. M. Jr, R. E. Wyatt, *The Journal of Chemical Physics* **1971**, *54*, 3578.

[63] J. C. Light, I. P. Hamilton, J. V. Lill, *The Journal of Chemical Physics* **1985**, *82*, 1400.

[64] J. C. Light in Time-Dependent Quantum Molecular Dynamics, (Eds.: J. Broeckhove, L. Lathouwers), Plenum, New York, **1992**, pp. 185–199.

[65] J. C. Light, T. C. Jr, *Advanced Chemical Physics* **2000**, *114*, 263.

[66] J. Frenkel, J. I. Frenkel, *Wave Mechanics: Advanced General Theory*, Clarendon Press, **1934**.

[67] P. Kramer, M. Saraceno, *Geometry of the Time-Dependent Variational Principle in Quantum Mechanics*, Springer Berlin Heidelberg, **1981**, 101 pp.

[68] A. D. McLachlan, M. A. Ball, *Reviews of Modern Physics* **1964**, *36*, 844.

[69] A. D. McLachlan, *Molecular Physics* **1964**, *8*, 39.

[70] H. D. Meyer, U. Manthe, L. S. Cederbaum, *Chemical Physics Letters* **1990**, *165*, 73.

[71] M. D Feit, J. A Fleck Jr., A Steiger, *Journal of Computational Physics* **1982**, *47*, 412.

[72] M. D. Feit, J. A. F. Jr, *The Journal of Chemical Physics* **1983**, *78*, 301.

[73] M. D. Feit, J. A. F. Jr, *The Journal of Chemical Physics* **1984**, *80*, 2578.

[74] T. J. Park, J. C. Light, *The Journal of Chemical Physics* **1986**, *85*, 5870.

[75] P. a. M. Dirac, *Proceedings of the Royal Society of London A: Mathematical Physical and Engineering Sciences* **1930**, *126*, 360.

[76] M. Ehara, H.-D. Meyer, L. S. Cederbaum, *The Journal of Chemical Physics* **1996**, *105*, 8865.

[77] U. Manthe, *The Journal of Chemical Physics* **2008**, *128*, 164116.

[78] O. Vendrell, H.-D. Meyer, *The Journal of Chemical Physics* **2011**, *134*, 044135.

[79] D. J. Tannor, *Introduction to Quantum Mechanics: A Time-dependent Perspective*, University Science Books, **2007**, 694 pp.

[80] S.-Y. Lee, *The Journal of Chemical Physics* **1982**, *76*, 3035.

[81] I. Burghardt, K. Giri, G. A. Worth, *The Journal of Chemical Physics* **2008**, *129*, 174104.

[82] D. J. Rowe, A. Ryman, G. Rosensteel, *Physical Review A* **1980**, *22*, 2362.

[83] J. Broeckhove, L. Lathouwers, E. Kesteloot, P. Van Leuven, *Chemical Physics Letters* **1988**, *149*, 547.

[84] H. Tamura, I. Burghardt, M. Tsukada, *The Journal of Physical Chemistry C* **2011**, *115*, 10205.

[85] H. Tamura, R. Martinazzo, M. Ruckenbauer, I. Burghardt, *The Journal of Chemical Physics* **2012**, *137*, 22A540.

[86] G. A. Worth, M. A. Robb, I. Burghardt, *Faraday Discussions* **2004**, *127*, 307.

[87] R. A. Marcus, N. Sutin, *Biochimica et Biophysica Acta (BBA) - Reviews on Bioenergetics* **1985**, *811*, 265.

[88] H. Oevering, M. N. Paddon-Row, M. Heppener, A. M. Oliver, E. Cotsaris, J. W. Verhoeven, N. S. Hush, *Journal of the American Chemical Society* **1987**, *109*, 3258.

[89] A. F. Izmaylov, D. Mendive–Tapia, M. J. Bearpark, M. A. Robb, J. C. Tully, M. J. Frisch, *The Journal of Chemical Physics* **2011**, *135*, 234106.

[90] U. Manthe, A. Dell Hammerich, *Chemical Physics Letters* **1993**, *211*, 7.

[91] A. D. Hammerich, U. Manthe, R. Kosloff, H.-D. Meyer, L. S. Cederbaum, *The Journal of Chemical Physics* **1994**, *101*, 5623.

[92] G. A. Worth, H.-D. Meyer, L. S. Cederbaum, *The Journal of Chemical Physics* **1996**, *105*, 4412.

[93] J.-Y. Fang, H. Guo, *The Journal of Chemical Physics* **1994**, *101*, 5831.

[94] J. H. Mathews, *Numerical Methods Using MATLAB*, Pearson Prentice Hall, **2004**, 728 pp.

[95] *Numerical Recipes in Fortran 77: The Art of Scientific Computing*, Cambridge University Press, **1996**, 933 pp.

[96] J. Stoer, R. Bulirsch, *Introduction to Numerical Analysis*, Springer Science & Business Media, **2013**, 618 pp.

[97] M. J. Bramley, T. C. Jr, *The Journal of Chemical Physics* **1993**, *99*, 8519.

[98] E. Schmidt, *Mathematische Annalen* **1907**, *63*, 433.

[99] E. Schmidt, *Mathematische Annalen* **1907**, *63*, 473.

[100] E. W. Cheney, D. R. Kincaid, *Linear Algebra: Theory and Applications*, Jones & Bartlett Learning, **2009**, 768 pp.

[101] G. A. Worth, M. H. Beck, A. Jäckle, H.-D. Meyer, The MCTDH Package, Version 8.2, (2000). H.-D. Meyer, Version 8.3 (2002), Version 8.4 (2007). Current version: 8.5.4 (2015). See http://mctdh.uni-hd.de, University of Heidelberg, Germany.

[102] M. Schade, P. Hamm, *The Journal of Chemical Physics* **2009**, *131*, 044511.

[103] N. S. Sariciftci, L. Smilowitz, A. J. Heeger, F. Wudl, *Science* **1992**, *258*, 1474.

[104] C. J. Brabec, G. Zerza, G. Cerullo, S. De Silvestri, S. Luzzati, J. C. Hummelen, S. Sariciftci, *Chemical Physics Letters* **2001**, *340*, 232.

[105] S. De, T. Kesti, M. Maiti, F. Zhang, O. Inganäs, A. Yartsev, T. Pascher, V. Sundström, *Chemical Physics*, Femtochemistry and Femtobiology Papers associated with the 8th International Conference on Femtochemistry and Femtobiology **2008**, *350*, 14.

[106] P. Parkinson, J. Lloyd-Hughes, M. B. Johnston, L. M. Herz, *Physical Review B* **2008**, *78*, 115321.

[107] R. D. Pensack, K. M. Banyas, L. W. Barbour, M. Hegadorn, J. B. Asbury, *Physical Chemistry Chemical Physics* **2009**, *11*, 2575.

[108] R. D. Pensack, J. B. Asbury, *The Journal of Physical Chemistry Letters* **2010**, *1*, 2255.

[109] R. D. Pensack, K. M. Banyas, J. B. Asbury, *The Journal of Physical Chemistry B* **2010**, *114*, 12242.

[110] M. Tong, N. E. Coates, D. Moses, A. J. Heeger, S. Beaupré, M. Leclerc, *Physical Review B* **2010**, *81*, 125210.

[111] R. Martinazzo, K. H. Hughes, F. Martelli, I. Burghardt, *Chemical Physics* **2010**, *377*, 21.

[112] G. A. Worth, M. H. Beck, A. Jäckle, O. Vendrell, H.-D. Meyer, The MCTDH Package, Version 8.2, (2000). H.-D. Meyer, Version 8.3 (2002), Version 8.4 (2007). O. Vendrell and H.-D. Meyer Version 8.5 (2013). Version 8.5 contains the ML-MCTDH algorithm. Current versions: 8.4.12 and 8.5.5 (2016). See http://mctdh.uni-hd.de/, University of Heidelberg, Germany.

[113] G. A. Worth, K. Giri, G. W. Richings, M. H. Beck, A. Jäckle, H.-D. Meyer, The QUANTICS Package Version 1.1, (2015), University of Birmingham, Birmingham, U.K.

[114] W. Koch, D. H. Zhang, *The Journal of Chemical Physics* **2014**, *141*, 021101.

[115] T Roland, G. H. Ramirez, J Léonard, S Méry, S Haacke, *Journal of Physics: Conference Series* **2011**, *276*, 012006.

[116] T. Roland, J. Léonard, G. Hernandez Ramirez, S. Méry, O. Yurchenko, S. Ludwigs, S. Haacke, *Physical Chemistry Chemical Physics* **2012**, *14*, 273.

[117] G. H. Ramirez, PhD thesis, Université de Strasbourg, **2010**.

[118] J. Wenzel, Master Thesis, **2012**.

[119] J. Wenzel, A. Dreuw, I. Burghardt, *Physical Chemistry Chemical Physics* **2013**, *15*, 11704.

[120] A. Klamt, G. Schuurmann, *Journal of the Chemical Society Perkin Transactions 2* **1993**, 799.

[121] S. Sinnecker, A. Rajendran, A. Klamt, M. Diedenhofen, F. Neese, *The Journal of Physical Chemistry A* **2006**, *110*, 2235.

[122] A. Schäfer, C. Huber, R. Ahlrichs, *The Journal of Chemical Physics* **1994**, *100*, 5829.

[123] M. Polkehn, H. Tamura, P. Eisenbrandt, S. Haacke, S. Méry, I. Burghardt, *The Journal of Physical Chemistry Letters* **2016**, *7*, 1327.

[124] F. C. Spano, C. Silva, *Annual Review of Physical Chemistry* **2014**, *65*, 477.

[125] R. E. Merrifield, *The Journal of Chemical Physics* **1961**, *34*, 1835.

[126] M. J. Frisch, G. W. Trucks, H. B. Schlegel, G. E. Scuseria, M. A. Robb, J. R. Cheeseman, G. Scalmani, V. Barone, G. A. Petersson, H. Nakatsuji, X. Li, M. Caricato, A. Marenich, J. Bloino, B. G. Janesko, R. Gomperts, B. Mennucci, H. P. Hratchian, J. V. Ortiz, A. F. Izmaylov, J. L. Sonnenberg, D. Williams-Young, F. Ding, F. Lipparini, F. Egidi, J. Goings, B. Peng, A. Petrone, T. Henderson, D. Ranasinghe, V. G. Zakrzewski, J. Gao, N. Rega, G. Zheng, W. Liang, M. Hada, M. Ehara, K. Toyota, R. Fukuda, J. Hasegawa, M. Ishida, T. Nakajima, Y. Honda, O. Kitao, H. Nakai, T. Vreven, K. Throssell, J. A. Montgomery, Jr., J. E. Peralta, F. Ogliaro, M. Bearpark, J. J. Heyd, E. Brothers, K. N. Kudin, V. N. Staroverov, T. Keith, R. Kobayashi, J. Normand, K. Raghavachari, A. Rendell, J. C. Burant, S. S. Iyengar, J. Tomasi, M. Cossi, J. M. Millam, M. Klene, C. Adamo, R. Cammi, J. W. Ochterski, R. L. Martin, K. Morokuma, O. Farkas, J. B. Foresman, D. J. Fox, Gaussian09 Revision D.01, Gaussian Inc. Wallingford CT 2013.

[127] M. E. Köse, *The Journal of Physical Chemistry A* **2012**, *116*, 12503.

[128] J.-H. Kim, H. U. Kim, D. Mi, S.-H. Jin, W. S. Shin, S. C. Yoon, I.-N. Kang, D.-H. Hwang, *Macromolecules* **2012**, *45*, 2367.

[129] B. Gieseking, B. Jäck, E. Preis, S. Jung, M. Forster, U. Scherf, C. Deibel, V. Dyakonov, *Advanced Energy Materials* **2012**, *2*, 1477.

[130] L. Liu, P. Eisenbrandt, T. Roland, M. Polkehn, P.-O. Schwartz, K. Bruchlos, B. Omiecienski, S. Ludwigs, N. Leclerc, E. Zaborova, J. Léonard, S. Méry, I. Burghardt, S. Haacke, *Physical Chemistry Chemical Physics* **2016**, *18*, 18536.

[131] B. P. Karsten, R. K. M. Bouwer, J. C. Hummelen, R. M. Williams, R. A. J. Janssen, *The Journal of Physical Chemistry B* **2010**, *114*, 14149.

[132] F. Weigend, R. Ahlrichs, *Physical Chemistry Chemical Physics* **2005**, *7*, 3297.

[133] T. Lu, F. Chen, *Journal of Computational Chemistry* **2012**, *33*, 580.

[134] TURBOMOLE V6.4 2012, a development of University of Karlsruhe and Forschungszentrum Karlsruhe GmbH, 1989-2007, TURBOMOLE GmbH, since 2007; available from `http://www.turbomole.com`.

[135] F. Neese, *Wiley Interdisciplinary Reviews: Computational Molecular Science* **2012**, *2*, 73.

[136] S. Hirata, M. Head-Gordon, *Chemical Physics Letters* **1999**, *314*, 291.

[137] F. Sterpone, R. Martinazzo, A. N. Panda, I. Burghardt, *Zeitschrift für Physikalische Chemie* **2011**, *225*, 541.

[138] W. Paa, J. P. Yang, S. Rentsch, *Synthetic Metals*, Proceedings of the International Conference on Science and technology of Synthetic Metals **2001**, *119*, 525.

[139] M. A. Fox, J. K. Whitesell, *Organic Chemistry*, Jones & Bartlett Learning, **2004**, 1181 pp.

[140] P. M. Viruela, R. Viruela, E. Orti, *International Journal of Quantum Chemistry* **1998**, *70*, 303.

[141] A. Karpfen, C. H. Choi, M. Kertesz, *The Journal of Physical Chemistry A* **1997**, *101*, 7426.

[142] C. Li, H. Wonneberger, *Advanced Materials* **2012**, *24*, 613.

[143] C. Curutchet, A. Muñoz-Losa, S. Monti, J. Kongsted, G. D. Scholes, B. Mennucci, *Journal of Chemical Theory and Computation* **2009**, *5*, 1838.

[144] H.-M. Zhao, J. Pfister, V. Settels, M. Renz, M. Kaupp, V. C. Dehm, F. Würthner, R. F. Fink, B. Engels, *Journal of the American Chemical Society* **2009**, *131*, 15660.

[145] D. Ambrosek, H. Marciniak, S. Lochbrunner, J. Tatchen, X.-Q. Li, F. Würthner, O. Kühn, *Physical Chemistry Chemical Physics* **2011**, *13*, 17649.

[146] B. Engels, W. Liu, J. Pfister, V. Settels, H.-M. Zhao, R. Fink in *Comprehensive Nanoscience and Technology*, (Eds.: G. D. Scholes, G. P. Wiederrecht), Academic Press, Amsterdam, **2011**, pp. 1–22.

[147] W. Liu, V. Settels, P. H. P. Harbach, A. Dreuw, R. F. Fink, B. Engels, *Journal of Computational Chemistry* **2011**, *32*, 1971.

[148] V. Settels, W. Liu, J. Pflaum, R. F. Fink, B. Engels, *Journal of Computational Chemistry* **2012**, *33*, 1544.

[149] U. C. Singh, P. A. Kollman, *Journal of Computational Chemistry* **1984**, *5*, 129.

[150] B. H. Besler, K. M. Merz, P. A. Kollman, *Journal of Computational Chemistry* **1990**, *11*, 431.

[151] J. A. M. Jr, M. J. Frisch, J. W. Ochterski, G. A. Petersson, *The Journal of Chemical Physics* **1999**, *110*, 2822.

[152] J. A. M. Jr, M. J. Frisch, J. W. Ochterski, G. A. Petersson, *The Journal of Chemical Physics* **2000**, *112*, 6532.

[153] A. Weller, *Zeitschrift für Physikalische Chemie* **1982**, *133*, 93.

[154] W. M. Haynes, *CRC Handbook of Chemistry and Physics, 93rd Edition*, CRC Press, **2012**, 2657 pp.

[155] K. Ando, *The Journal of Chemical Physics* **1997**, *107*, 4585.

[156] H. J. Kim, J. T. Hynes, *The Journal of Chemical Physics* **1992**, *96*, 5088.

[157] D. N. LeBard, M. Lilichenko, D. V. Matyushov, Y. A. Berlin, M. A. Ratner, *The Journal of Physical Chemistry B* **2003**, *107*, 14509.

[158] C. C. Moser, J. M. Keske, K. Warncke, R. S. Farid, P. L. Dutton, *Nature* **1992**, *355*, 796.

[159] H. Wang, E. R. McNellis, S. Kinge, M. Bonn, E. Cánovas, *Nano Letters* **2013**, *13*, 5311.

[160] D. M. Adams, L. Brus, C. E. D. Chidsey, S. Creager, C. Creutz, C. R. Kagan, P. V. Kamat, M. Lieberman, S. Lindsay, R. A. Marcus, R. M. Metzger, M. E. Michel-Beyerle, J. R. Miller, M. D. Newton, D. R. Rolison, O. Sankey, K. S. Schanze, J. Yardley, X. Zhu, *The Journal of Physical Chemistry B* **2003**, *107*, 6668.

[161] A. B. Ricks, K. E. Brown, M. Wenninger, S. D. Karlen, Y. A. Berlin, D. T. Co, M. R. Wasielewski, *Journal of the American Chemical Society* **2012**, *134*, 4581.

[162] J. Qu, B. Gao, H. Tian, X. Zhang, Y. Wang, Z. Xie, H. Wang, Y. Geng, F. Wang, *Journal of Materials Chemistry A* **2014**, *2*, 3632.

[163] B.-R. Gao, J.-F. Qu, Y. Wang, Y.-Y. Fu, L. Wang, Q.-D. Chen, H.-B. Sun, Y.-H. Geng, H.-Y. Wang, Z.-Y. Xie, *The Journal of Physical Chemistry C* **2013**, *117*, 4836.

[164] P.-O. Schwartz, L. Biniek, E. Zaborova, B. Heinrich, M. Brinkmann, N. Leclerc, S. Méry, *Journal of the American Chemical Society* **2014**, *136*, 5981.

[165] L. Biniek, P.-O. Schwartz, E. Zaborova, B. Heinrich, N. Leclerc, S. Méry, M. Brinkmann, *Journal of Materials Chemistry C* **2015**, *3*, 3342.

[166] B. Grévin, P.-O. Schwartz, L. Biniek, M. Brinkmann, N. Leclerc, E. Zaborova, S. Méry, *Beilstein Journal of Nanotechnology* **2016**, *7*, 799.

[167] M. A. Polkehn, PhD thesis, Goethe Universität Frankfurt, **2017**.

[168] K. Schwinn, Master Thesis, Goethe Universität Frankfurt, **2017**.

Scientific contributions

Publications

1. P. Eisenbrandt, M. Ruckenbauer, S. Römer, I. Burghardt, "*Gaussian-based multiconfiguration time-dependent Hartree: A two-layer approach. III. Non-Adiabatic Dynamics*", J. Chem. Phys., **2017** *submitted*

2. P. Eisenbrandt, M. Ruckenbauer, S. Römer, I. Burghardt, "*Gaussian-based multiconfiguration time-dependent Hartree: A two-layer approach. II. Implementation and Application to Intramolecular Vibrational Energy Transfer*", J. Chem. Phys., **2017** *submitted*

3. L. Liu, P. Eisenbrandt, T. Roland, M. Polkehn, P.-O. Schwartz, K. Bruchlos, B. Omiecienski, S. Ludwigs, N. Leclerc, E. Zaborova, J. Léonard, S. Méry, I. Burghardt, S. Haacke, "*Controlling charge separation and recombination by chemical design in donor–acceptor dyads*", Phys. Chem. Chem. Phys **2016**, 18, 18536-18548

4. M. Polkehn, H. Tamura, P. Eisenbrandt, S. Haacke, S. Méry, I. Burghardt, "*Molecular Packing Determines Charge Separation in a Liquid Crystalline Bisthiophene-Perylene Diimide Donor-Acceptor Material*", J. Phys. Chem. Lett., **2016**, 7, 1327-1334

5. M. Polkehn, H. Tamura, P. Eisenbrandt, S. Haacke, S. Méry, I. Burghardt, "*Ultrafast excitonic and charge transfer dynamics in nanostructured organic polymer materials*", Proc. SPIE 9884, Nanophotonics IV, **2016**, 7, 98840O

6. S. Habermehl, P. Mörschel, P. Eisenbrandt, S. M. Hammer, M. U. Schmidt, "*Structure determination from powder data without prior indexing, using a similarity measure based on cross-correlation functions*", Acta Cryst. B, **2014**, 70, 347-359

7. S. Knippenberg, P. Eisenbrandt, L. Šištík, P. Slaviček, A. Dreuw, "*Simulation of Photoelectron Spectra Using the Reflection Principle in Combination with Unrestricted Excitation ADC(2) to Assess the Accuracy of Excited-State Calculations*", ChemPhysChem, **2011**, 12, 3180-3191

Poster contributions to conferences

1. "*Gaussian-based multiconfiguration time-dependent Hartree: A two-layer approach*", The International Workshop "Quantum Dynamics: From Algorithms to Applications", Alfred Krupp Wissenschaftskolleg, Greifswald, Germany, **2016**

2. "*Gaussian-based multiconfiguration time-dependent Hartree: A two-layer approach*", CECAM Workshop "Molecular Quantum Dynamics Methods: Benchmarks and State of the Art", Lausanne, Switzerland, **2015**

3. "*Gaussian-based multiconfiguration time-dependent Hartree: A two-layer approach*", 50^{th} Symposium on Theoretical Chemistry (STC 2014) Vienna, Austria, **2014**

4. "*Gaussian-based multiconfiguration time-dependent Hartree: A two-layer approach*", CECAM Workshop "Recent progress in adiabatic and non-adiabatic methods in quantum dynamics", Lausanne, Switzerland, **2014**

Oral presentations

1. Weekly seminar of the Institute of Physical and Theoretical Chemistry, Goethe University, **2016**

2. Internal group seminar, **2014**

3. Annual seminar of the Institute of Physical and Theoretical Chemistry, Goethe University, Hirschegg/Austria, **2013**

Danksagung

Ohne die Unterstützung der folgenden Personen wäre diese Arbeit in ihrer vorliegenden Form nicht möglich gewesen oder entstanden. Daher möchte ich mich bedanken bei

- Meiner Betreuerin und Vorgesetzten Prof. Dr. Irene Burghardt für das Bereitstellen der interessanten und abwechslungsreichen Themen, sowie die stetige Unterstützung bei Unklarheiten und unzähligen Fragen während der gesamten letzten 5 Jahre.
- Dr. Sarah Römer für das Beantworten von vielen Fragen zu den verschiedenen MCTDH-Methoden, sowie besonders der 2L-G-MCTDH-Methode und die Unterstützung bei weiteren Fragen mathematischer Natur.
- Dr. Matthias Ruckenbauer für die Unterstützung und zahlreiche Diskussionen rund um Probleme mit Fortran und die Implementierung der 2L-G-MCTDH Methode.
- Dr. Rainer Hegger für das Beantworten von unzähligen Fragen und der Unterstützung bei einigen Themen dieser Arbeit.
- Prof. Dr. Stefan Haacke für die Kooperation im Rahmen der Untersuchungen des Donor-Akzeptor Bisthiophene-Perylenediimid Projektes, sowie die zahlreichen Diskussionen zur Interpretation der experimentellen und simulierten Ergebnisse.
- Meinen ehemaligen Büronachbarn Robert, Jan und Konstantin für die gemeinsame und unterhaltsame Zeit, zahlreichen Diskussionen und Korrekturvorschlägen zu dieser Arbeit.
- Dem restlichem Arbeitskreis Burghardt inkl. ehemaliger Mitglieder für die nette Atmosphäre und gemeinsamen Unternehmungen.
- Meinen Eltern, Großeltern und meiner Tante, die mich nicht nur während den letzten 5 Jahren in meiner Promotion, sondern auch schon die Zeit davor unterstützt und immer an mich geglaubt hat.
- Meiner Freundin Claudia, die jederzeit für mich da war, in allen Situationen unterstützt hat und mich trotz ihrer eigenen Arbeit immer aufgebaut, an mich geglaubt und mich im Zweifel motiviert hat.

Eidesstattliche Erklärung

Ich versichere an Eides statt durch meine eigene Unterschrift, dass ich die vorstehende Arbeit selbständig und ohne fremde Hilfe angefertigt und alle Stellen, die wörtlich oder annähernd wörtlich aus Veröffentlichungen genommen sind, als solche kenntlich gemacht habe. Die Versicherung bezieht sich auch auf in der Arbeit gelieferte Zeichnungen, Skizzen, bildliche Darstellungen und dergleichen.

Ort, Datum	Unterschrift